Asilomar's legacy, 50 years later pp. 454, 468, & 480

What happens when Trump uproots a research agency? p. 464

Scratching stimulates mast cell immunity pp. 473 & 489

Science

$15
31 JANUARY 2025
science.org

AAAS

LIVING WITH TIGERS

Restoring a top predator across India p. 505

TRILLIONS OF MICROBES ONE ESSAY

The NOSTER *Science* Microbiome Prize is an international prize that rewards innovative research by investigators who have completed their terminal degree in the last 10 years and are working on the functional attributes of microbiota. The research can include any organism with the potential to contribute to our understanding of human or veterinary health and disease, or to guide therapeutic interventions. The winner and finalists will be chosen by a committee of independent scientists chaired by a senior editor of *Science*. The first prize includes complimentary membership to AAAS, an online subscription to *Science*, and USD 25,000. Submit your research essay today.

Kazuki Nagashima, Ph.D.
2024 Winner

NOSTER | Science
MICROBIOME
PRIZE

Apply by 14 February 2025 at www.science.org/noster

Sponsored by Noster Inc.

CONTENTS

31 JANUARY 2025
VOLUME 387
ISSUE 6733

464

NEWS

IN BRIEF

IN DEPTH

FEATURES

INSIGHTS

POLICY FORUM

PERSPECTIVES

BOOKS *ET AL.*

LETTERS

454, 468, & 480

CREDITS: (ILLUSTRATION) A. MASTIN/*SCIENCE*; (PHOTO) ALBUM/ALAMY STOCK PHOTO

RESEARCH

IN BRIEF

RESEARCH ARTICLES

Synthetic biology

491
The neural representation of sociality in fruit bats

DEPARTMENTS

ON THE COVER

Cultural reverence toward tigers (*Panthera tigris*) has fostered tolerance and permitted coexistence with humans in India. Ecological restoration, socioeconomic policies, and political stability have facilitated the recovery of tigers within their historical range, despite high human densities. This tigress has reclaimed the ancient fort within Bandhavgarh Tiger Reserve and made it her home. See page 505. *Photo: Yashpal Rathore*

PHOTO: YUVAL BARKAI

SCIENCE (ISSN 0036-8075) is published weekly on Friday, except last week in December, by the American Association for the Advancement of Science, 1200 New York Avenue, NW, Washington, DC 20005. Periodicals mail postage (publication No. 484460) paid at Washington, DC, and additional mailing offices. The title SCIENCE is a registered trademark of the AAAS. Domestic individual membership, including subscription (12 months): $165 ($74 allocated to subscription). Domestic institutional subscription (51 issues): $2865; Foreign postage extra: Air assist delivery: $135. First class, airmail, student, and emeritus rates on request. Canadian rates with GST available upon request, GST #125488122. Publications Mail Agreement Number 1069624. **Printed in the U.S.A.**
Change of address: Allow 4 weeks, giving old and new addresses and 8-digit account number. **Postmaster:** Send change of address to AAAS, P.O. Box 96178, Washington, DC 20090–6178. **Single-copy sales:** $15 each plus shipping and handling available from backissues.science.org; bulk rate on request. **Authorization to reproduce** material for internal or personal use under circumstances not falling within the fair use provisions of the Copyright Act can be obtained through the Copyright Clearance Center (CCC), www.copyright.com. The identification code for *Science* is 0036-8075. *Science* is indexed in the *Reader's Guide to Periodical Literature* and in several specialized indexes.

EDITORIAL

Viewing Asilomar from the Global South

Shobita Parthasarathy is a professor of public policy and director of the Science, Technology, and Public Policy program at the Gerald R. Ford School of Public Policy, University of Michigan, Ann Arbor, MI, USA. shobita@umich.edu

To many in the scientific community, the 1975 Asilomar Conference on Recombinant DNA stands as a singular achievement. This experiment in governance seemed to demonstrate that citizens could trust scientists to anticipate their fields' risks and propose sensible ways to regulate themselves. Over the past half-century, similar efforts have been made to govern controversial areas of research, from geoengineering to artificial intelligence. However, when viewed from a global perspective, Asilomar did not address concerns in the way that many assume. The conference's output may have made it more difficult for scientists to take seriously global public concerns about emerging technologies, which has impeded governance and eroded trust in science.

Despite its historical importance, Asilomar was a narrow affair. Conference organizers and most of the 140 participants were life scientists from the United States and United Kingdom who were likely to work in the new field. They focused on a limited set of environmental and occupational risks and wrote guidelines accordingly, despite ethical, socioeconomic, and national security concerns about the genetically modified organisms (GMOs) that recombinant DNA (rDNA) research would create. As a result, the conference reinforced the idea that only those with relevant scientific expertise should guide regulations for controversial new technologies, and that physical risks should be the primary concern. This guided both the US National Institutes of Health's policies on rDNA research and the Coordinated Framework for the Regulation of Biotechnology that the US government issued a decade later.

> "Despite its historical importance, Asilomar was a narrow affair."

However, the rDNA controversies that emerged around the world in subsequent years were more extensive and complex than the Asilomar scientists anticipated. In low- and middle-income countries in particular, many scientists, farmers, civil society groups, and government officials responded with concern. Despite possible higher yields and nutritional benefits, GMOs came with patents, licenses, and other legal restrictions that seemed like new—even neocolonial—extensions of Western power and control, which many in the Global South worried would limit the rights and autonomy of small-scale farmers, reduce crop biodiversity, and dull the flavor on their plates. Global South countries also saw the new organisms as part of larger technological packages that included pesticides and herbicides that could harm humans and animals and disrupt ecosystems. The United States exerted pressure on these nations to adopt the GMOs, but they questioned the quality of US regulatory oversight.

This triggered new governance experiments across the Global South. Informed by different understandings of the problem than those of the Asilomar scientists, civil society groups and think tanks convened deliberations among small-scale farmers who expressed skepticism that was grounded in their experience with the Green Revolution and other agricultural technologies. Farmers asked for local field trials and comprehensive impact evaluations, and questioned whether the technologies would make rural livelihoods more secure. Meanwhile, governments of the Global South contested patents on genetically modified crops and fought for different licensing terms, arguing that they had developed similar native cultivars over centuries. As policy-makers and courts decided whether the fruits of these technologies should be grown, imported, or sold in their countries, they assembled a range of experts to conduct toxicological, socioeconomic, and ecological assessments. This led to different expectations for approval, and in some cases even moratoria and bans.

Too frequently, Western governments, scientists, and journalists characterized these efforts as ignorant and dangerous. Echoing the Asilomar framing, the West argued that experts had found biotechnology safe, rather than viewing Global South efforts as rooted in different historical experiences and understandings of the technology and its effects. Just last year, the US government successfully challenged Mexico's ban on GMO imports (corn) due to cultural, health, and environmental concerns, saying that the decision was unscientific.

These responses missed the opportunity to see broader connections between technology, politics, economics, culture, health, and the environment, an approach that likely would have enhanced public trust in postcolonial countries as well as in the Western world. This failure provides important lessons. Good governance of emerging technologies requires inclusion of a variety of experts from the outset, and decision-makers—including scientists—must understand that concerns that may seem ignorant or irrelevant may actually represent different, but valid, understandings of the problem. Ultimately, this approach will achieve more trustworthy and responsible science, technology, and related public policies.

–Shobita Parthasarathy

10.1126/science.adw2511

Climate déjà vu

As in his earlier term, US President Donald Trump's misguided announcement that the US will withdraw from the Paris Agreement on climate continues a long history of confusion—mostly created intentionally—over the intersection of climate science and US climate policy. The tactics and consequences are no different from what opponents of climate science and action have been using for almost 50 years. For decades, political discourse on climate has blurred the lines between scientific reality and political ideology, treating established facts like debatable opinions, providing shifting reasons for making decisions, and turning what should be reasoned policy debates into ideological battlegrounds.

In the 2025 executive order, as well as in his comments in 2017, Trump said that the rationale for pulling out of the Paris Agreement is a straightforward matter of economics—a bad and unfair deal that would lead to a "massive redistribution of United States wealth to other countries." Never mind that some consider the bad deal fine for developing countries that are being asked to forgo energy sources—coal and oil—that propelled the West to economic dominance. But it is clear from his hundreds of comments and social posts that even though some of his nominees are willing to discuss the importance of climate change, Trump himself also questions the very veracity of climate change and whether it is caused by humans. The result is a slippery mess that provides multiple paths to oppose climate change, none of which are based on science. Maybe that passes as clever politics, but it is more important than ever that citizens see through the political smokescreen so that decisions can be made against a background of robust research.

> **"...it is more important than ever that citizens see through the political smokescreen..."**

Climate change became a partisan issue in the 1980s when President Ronald Reagan—who was later called the "most environmental governor in California history"— prioritized his disdain for government regulation over his previous environmental views. Instead of accepting the science and then debating whether government regulation was the appropriate solution, conservatives sought to cast doubt on the research and scientists and create confusion in the minds of the public. This was a way around acknowledging that they valued commerce over the environment. Sensing real concern and a political opportunity, Democratic politicians, especially Vice President Al Gore, adopted as a platform climate change and the need for a solid government response, cementing the battle lines. Little has changed since, and so scientists who sign up to work on climate change knowingly enter a political theater where the rhetoric and policy oscillate with each political change.

For years, the Pew Research Center has shown that although trust in science is generally high compared with many institutions, such as elected officials and business leaders, a substantial majority of Democrats believe that scientists should "take an active role in public policy debates about scientific issues," whereas a similar majority of Republicans prefer that scientists "focus on establishing sound scientific facts and stay out of policy debates." UK Prime Minister Winston Churchill was perhaps in the middle when he said that science should be "on tap, but not on top." Nearly all scientists would concede that other issues, like the economy and national security, should be weighed along with science when government leaders are making decisions, and many would also agree that science itself should rise above any political agenda. But would those who say scientists should stay out of policy debates agree that nonscientist policy-makers should, conversely, stay out of the execution and judgment of scientific research?

Scientists and politicians are people with both facts and opinions. But unlike politicians, scientists' opinions usually—and optimally—are clearly marked to differentiate them from the conclusions of their research. By contrast, many politicians, especially Trump, pursue their goals by mingling facts, falsehoods, and opinions. He can post hundreds of tweets attacking the facts of climate change and then add on another layer of his opinions about the economic terms of the Paris Agreement—all without acknowledging the dangers to people and the planet or the degree to which his opinions are supported by robust research.

Withdrawing from the Paris Agreement is a bad idea. And many scientists will continue to express that opinion in appropriate ways, because the steady progress on describing the details and dangers of climate change will continue.

–H. Holden Thorp

PHOTO: CAMERON DAVIDSON

H. Holden Thorp
Editor-in-Chief,
Science journals.
hthorp@aaas.org

Published online 21 January 2025; 10.1126/science.adw1532

NEWS

IN BRIEF

Edited by **Jeffrey Brainard**

ILLUSTRATION: STEPHAN SCHMITZ/FOLIOART

TRUMP TRACKER

New administration upends U.S. science

Following through on his vows to shake up the U.S. government, President Donald Trump's new administration quickly issued a flurry of executive orders and other decisions, some with big implications for research and global health, sowing worry and confusion among many scientists.

GRANTS CLAMPDOWN In an unprecedented move, the administration said it would freeze huge chunks of federal spending, including for research, so that political appointees at every agency can determine whether the funds "conform with administrative priorities." But on 28 January, a federal judge postponed the implementation. Historically, federal science agencies have dispersed grants based on recommendations by peer-review panels in a process overseen by career employees. Following its 27 January announcement of the policy, the White House added that the pause might last as little as a day for some programs and that the review involves spending related to government activities prohibited by Trump's recent executive orders, which include "Marxist equity, transgenderism, and Green New Deal social engineering policies." Critics say the pause, of whatever duration, opens the door to the politicization of scientific grants. "It is hard to see how this [policy] doesn't grind biomedical research to a halt very quickly … given the sheer numbers of NIH [National Institutes of Health] grants potentially affected," says Carrie Wolinetz, a former NIH official who is now a lobbyist.

BANNING GENDER A separate executive order prohibits the use of "gender" in government publications, potentially interfering with many research grants. It inaccurately defines gender as a male-female binary and states that gender identity has no basis in "biological reality." The order also bans the funding of grants that "promote gender ideology." Researchers who have NIH grants to study health in people who identify as neither male nor female say they are fearful such grants would be permanently canceled. *Science* identified at least 400 of these grants totaling $235 million, funded by almost every NIH institute. Nearly half involve HIV/AIDS, and many are focused on transgender youth (see related story, p. 458).

DEI DEMOLITION Another order ended government programs promoting diversity, equity, and inclusion (DEI), signaling the demise of long-running university projects designed to broaden the scientific workforce by recruiting underrepresented minorities. Several U.S. research agencies quickly canceled existing grant programs and solicitations for future awards. The terminations will extend beyond racial distinctions, as DEI programs also support researchers who are disabled or come from economically disadvantaged backgrounds. Trump's order calls DEI efforts "illegal and immoral discrimination programs." Some scientists

told *Science* they plan to continue the work without using DEI terminology to try to skirt the crackdown—even as the government has asked whistleblowers to report such attempts.

NIH WHIPLASH Last week the administration halted external communications, travel, purchasing, and new experiments by NIH employees, to enable a review. Past presidents have made some similar restrictions. But the breadth of those under Trump, which included meeting cancellations, bewildered researchers who said they could stall in-house research and clinical trials at the $47.4 billion biomedical agency and impede its administration of external grants. Days later, on 27 January, newly appointed acting Director Matthew Memoli, a longtime influenza researcher at NIH, issued a memo describing circumstances under which NIH would make exceptions during this "pause," which will allow "the new team to set up a process for review and prioritization."

AI DO-OVER Another executive order nullified former President Joe Biden's blueprint, issued in October 2023, to foster the use of safe, secure, and trustworthy artificial intelligence. Echoing criticisms by technology industry leaders of the Biden administration plan, Trump's order asserts it would have "hindered innovation and imposed onerous and unnecessary government control." Trump has asked aides for a new plan within 180 days that would promote economic competitiveness and national security and sustain U.S. leadership in the field.

HIV HELP AT RISK Trump's administration paused all foreign assistance pending an 85-day review, an edict that could disrupt the ability of a key U.S.-funded program to provide lifesaving anti-HIV drugs on a timely basis to 21 million people in 55 countries. The President's Emergency Plan for AIDS Relief uses contractors based in the United States and other nations to distribute money.

New Zealand remakes funding

POLICY | New Zealand's research community is cautiously welcoming a major shake-up of the country's science infrastructure meant to promote economic growth. Among the changes, announced last week by the government, the biggest will consolidate the country's seven Crown Research Institutes. Starting later this year, the institutes will be reorganized into three new "public research organizations" focused on earth sciences, biological sciences, and health and forensic sciences, respectively. A fourth, new entity will concentrate on developing artificial intelligence, quantum computing, and synthetic biology, among other technologies. All will seek increased investments from the private sector; another new agency, Invest New Zealand, will work to tap foreign investment for this research. Some scientists worry the plan lacks adequate government funding, will create unreasonable expectations for fast economic returns, and will spur additional job losses in the research sector. In 2024, several Crown Research Institutes laid off hundreds of staff members.

Irregular mowing helps insects

ECOLOGY | Cutting grass in curves—rather than straight lines—and varying their paths over time benefit pollinators, a study has found. Industrial agriculture makes meadows less welcoming to insects, in part because most fields are mowed completely all at once, lessening their habitat diversity. Mowing just part of a field at a time can help a lot, but how it's done matters, a research team discovered. During 3 years of experiments, farmers cut sinuous shapes across some fields twice per year, each time keeping a two-to-one ratio of mown to unmown areas. The diversity of butterflies and bees was up to 30% and 40% higher, respectively, in those fields than in ones in which grass was mowed in straight lines and the two-to-one ratio was maintained. The curvy method requires more training, time, and effort for farmers. It could also benefit urban parks and even small residential yards, the team reported last week in *Agriculture, Ecosystems & Environment*.

Adding wiggles when mowing fields can boost the abundance and diversity of bees and butterflies.

PHOTO: NICHOLAS KLEIN/ALAMY

Institute head settles lawsuit

WORKPLACE | Rena D'Souza, the embattled director of the dental research institute at the U.S. National Institutes of Health (NIH), will retire as of 31 January, the agency told employees in an email last week. NIH placed D'Souza on paid administrative leave in April 2024 during a probe of her workplace behavior as head of the $520 million National Institute of Dental and Craniofacial Research. She had sued the secretary of the Department of Health and Human Services (HHS), NIH's parent department, in 2023, alleging race, sex, color, and national-origin discrimination after NIH placed her on two shorter, unpaid leaves. D'Souza said both the lawsuit and HHS proceedings against her ended last week when she and the agency signed a settlement agreement with undisclosed terms. D'Souza, 70, was born in India and in 2020 became was the first woman of color to direct an NIH institute.

AI expert falls victim to AI

LEGAL AFFAIRS | A U.S. judge in Minnesota this month tossed expert testimony by a researcher who specializes in artificial intelligence after he submitted a statement containing two references, generated by AI, to nonexistent papers. According to the ruling, Jeff Hancock of Stanford University admitted the bogus references resulted from using GPT-4o to prepare his testimony, which discussed the hazards to democracy posed by AI-generated content. Minnesota's attorney general had tapped Hancock to help defend a state law that bans using AI-generated "deepfake" content to damage a political candidate. In her order excluding Hancock's testimony, District Court Judge Laura Provinzino wrote, "The irony. Professor Hancock, a credentialed expert on the dangers of AI and misinformation, has fallen victim to the siren call of relying too heavily on AI—in a case that revolves around the dangers of AI, no less."

IN DEPTH

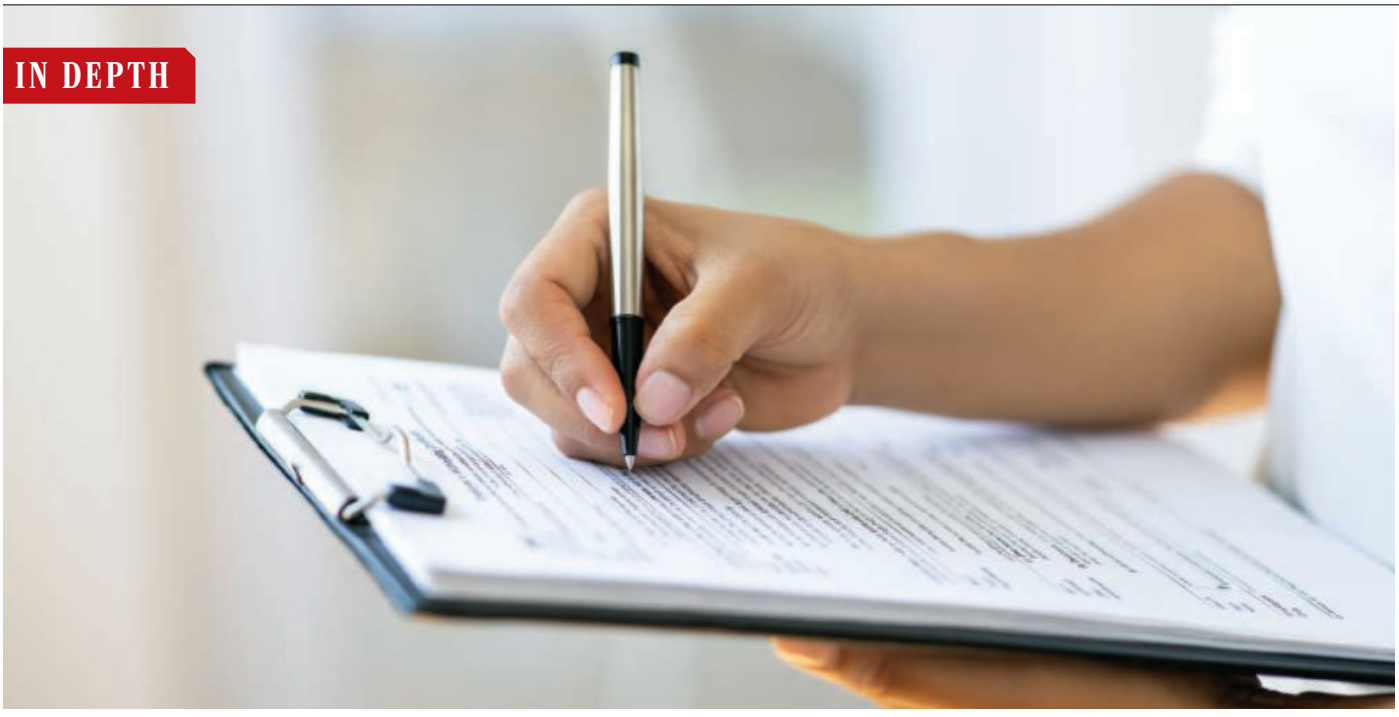

U.S. POLITICS

Trump gender order upends federal surveys

Move would ban data collection on transgender and nonbinary people

By **Jeffrey Mervis**

President Donald Trump's executive order banning "gender ideology," issued last week, has alarmed researchers studying gender minorities as well as people who fear their own gender identity could put them at risk. It also promises to upend a key resource for social scientists: federal surveys on topics that include health, education, housing, adolescent behavior, political engagement, and criminal justice.

The 20 January order, called "Defending women from gender ideology extremism and restoring biological truth to the federal government," directs federal agencies to use the term sex, not gender, in all policies and documents. Male and female are the only permissible options when asking about an individual's sex. That assertion ignores reality, note social scientists, whose surveys routinely include questions about gender that depart from that strict dichotomy.

"The directive seems to be saying, 'Thou shalt not collect information on gender identity because trans people and nonbinary people don't really exist,'" says retired federal statistician Nancy Bates, who led a 2022 National Academies of Sciences, Engineering, and Medicine (NASEM) study that made the case for asking about gender identity on all federal population surveys. "But of course they do." In the meantime, agency heads and researchers are in limbo until the White House explains how the order will be implemented.

Over the past 2 decades, the federal government has been slowly updating federal surveys to move away from only giving respondents the option of selecting male or female. One example came in 2016 when LGBTQ advocates persuaded the Department of Justice to add questions about gender identity and sexual orientation to its National Crime Victimization Survey.

> **"The directive seems to be saying ... trans people and nonbinary people don't really exist."**
>
> **Nancy Bates**
> retired federal statistician

"That was one of our earliest successes" in adding such questions to federal surveys, says American University political scientist Andrew Flores, lead author on a seminal 2022 paper that used the crime survey data. The data confirmed advocates' belief that sexual and gender minorities are crime victims more often than the general U.S. population, showing the community is 2.7 times more likely to be victimized.

In 2022, the NASEM study found that 30 federal surveys included gender options such as transgender and nonbinary. The list includes the massive All of Us project by the National Institutes of Health, which aims to improve personalized medicine, and the American National Election Studies surveys, which analyze how voters choose their leaders.

The tally is growing. Last year, the National Science Foundation (NSF) began to offer a new question with a broader range of gender identity options on its annual survey of newly minted Ph.D.s. And starting in 2027, the Census Bureau planned to include expanded options in its flagship American Community Survey, an annual survey designed to provide a more timely picture of national trends than the decennial survey can give.

Bates says removing those questions will degrade the quality of the surveys and the data available to policymakers for addressing important societal trends. "If those questions are dropped," Bates says, "many of the most reputable data collections in

PHOTO: BYMURATDENIZ/ISTOCK PHOTO

our country, with the most valid sample sizes and data collection procedures and methods, would simply disappear."

Charles Rothwell, a retired federal public health official, was head of the National Center for Health Statistics, which includes questions about gender identity on several surveys. He worries about the loss of information that could be used to understand and track the health outcomes of people of different genders. "We just want a way to measure those differences," he says.

The White House Office of Management and Budget (OMB) must approve every federal survey before it can be used to collect data, so it will call the shots on how the new executive order is implemented. That won't be easy, given the work that has already gone into planned surveys.

Long before a survey is approved, agencies thoroughly test each question and the sequence in which they are asked to remove ambiguities and ensure the validity of the results. The new executive order seems to ignore how that process works, says Nancy Potok, chief statistician of the United States during the first Trump administration.

"It's not simply a matter of printing a new form," says Potok, who led the OMB office that vets such surveys. "There's a huge amount of reprogramming and testing that has to take place if you start pulling questions off. It's also very expensive."

And that's not just at the federal level, she adds. State and local governments, which supply data for many federal surveys, will also have to rework their instruments to abide by the new directive. Potok worries OMB might use the increased cost as a rationale to get rid of some surveys that conservative groups have targeted because they see the questions as an invasion of privacy. (OMB officials didn't respond to a request for comment.)

Legal challenges to the executive order may be coming, anticipates Jon Freeman, a Columbia University psychologist who has pushed NSF to collect more data on LGBTQ scientists. Gender identity is a "protected" characteristic under federal civil rights laws, he explains, and that designation can't simply be erased with the stroke of a pen. "Collecting data on federal surveys is a key way to safeguard these protections by tracking disparities and developing solutions to prevent discrimination," Freeman says.

Flores is hoping OMB will provide an exemption that would allow agencies to continue to ask about gender identity on ongoing and approved surveys. "That's the best case," he says. "The worst case is a ban. Because then you're completely erasing nonbinary, gender-diverse people." ■

PHYSICS

Laser-powered accelerators, compact and cheap, get real

Encouraging lab results bolster plans to harness a new kind of particle accelerator in x-ray sources

By **Adrian Cho**

An elegant new concept may be about to revolutionize the technology of particle acceleration, which animates huge atom smashers and x-ray sources. For decades, some physicists have strived to develop an accelerator powered by laser light that would be much smaller and cheaper than existing machines. Recent progress suggests laser plasma accelerators (LPAs) may soon realize that bright promise.

Most recently, physicists at Lawrence Berkeley National Laboratory (LBNL) used the approach to boost electrons to an energy of 9.2 giga-electron volts (GeV) over just 30 centimeters, as they reported in December 2024 in *Physical Review Letters*. That's more than twice the energy achieved by a new 1-kilometer-long, $1.1 billion linear accelerator (linac) at SLAC National Accelerator Laboratory. Although LPAs still produce relatively ragged electron beams, physicists around the world are already racing to put them to work.

"We're moving from a phase in which the plasma accelerator is the object of study to one in which it's doing something useful," says Simon Hooker, a laser physicist at the University of Oxford. LPAs can't yet deliver the exquisitely tuned beams that physicists prize, but the much cheaper machines could find niches where beam quality isn't so crucial, says Samuel Barber, an accelerator physicist at LBNL. "You can develop a more bespoke machine."

In a conventional accelerator, charged particles such as electrons gain energy by surfing on the electric fields in radio waves resonating within long evacuated cavities. The 80-year-old approach has a limitation: If the radio waves are too intense, they'll create sparks in the cavities. The effect limits the accelerating field and means a high-energy accelerator must be kilometers long.

Physicists can generate far stronger accelerating fields by blasting an intense pulse of laser light into low-pressure hydrogen gas. The light ionizes the gas and, like a speedboat, pushes the wispy electrons aside, leaving a region of positively charged ions. After the light passes, the electrons surge back into the positive region, creating a negatively charged wake that trails the laser pulse through the gas.

Traveling at 99.99% of light speed, that wake resembles the wave produced by fans in a sports stadium when they raise their hands in turn, notes Marlene Turner, an accelerator physicist at CERN, the European particle physics laboratory. "There's this wave of electrons that is moving forward, but it's never the same electrons." Yet it produces an electric field 1000 times higher than a conventional accelerator, which other electrons can surf to reach astounding energies. In 2006, multiple groups boosted electrons to 1 GeV in just a few centimeters.

But the laser pulse quickly diverges, limiting the electrons' maximum energies. To counter that spreading, Anthony Gonsalves, an accelerator physicist at LBNL; Howard Milchberg, a laser plasma physicist at the University of Maryland; and colleagues hit gas spewing from a bladelike nozzle with not one laser pulse, but two. A special mirror focused the weaker first flash into a bright line across the wide gas jet, creating a channel of low-density plasma narrower than a human hair. Acting as an optical fiber, the channel guided the second pulse, which arrived nanoseconds later.

Others had tried guiding a pulse by using an electric current to ionize the gas in tiny glass capillaries, Turner notes. The technique didn't as effectively guide the drive pulse, which would vaporize the glass if it hit it. In contrast, the laser-created channel is "made of entirely of plasma, so it's immune to damage," Milchberg says. With it, researchers got the drive pulse to glide 30 centimeters, they reported last month.

The resulting energy fell just short of a record set by Manuel Hegelich, a laser plasma physicist at the University of Texas at Austin, and colleagues. In November 2023, they reported reaching 10 GeV in an unguided scheme, albeit using more laser power. But the LBNL group also managed to reduce the spread of energies yielded by previous LPAs, which picked up stray electrons in the plasma more or less randomly.

The key was to mix nitrogen into the gas. The guide laser would strip a nitrogen atom of most of its electrons, but the last two would pop loose only when the most intense part of the drive pulse arrived. "The electrons that get ionized then happen to slip right into the accelerating portion of that [plasma] bubble," says Alexander Picksley, an accelerator physicist at LBNL. By injecting the nitrogen at only one point along the nozzle, researchers controlled how far the electrons surfed and how much energy they gained.

"All the elements of this experiment have been known for some time," says Brigitte Cros, a plasma physicist with CNRS, the French national research agency. "But they have succeeded in putting everything together." There's still lots of room for improvement, Milchberg says. The petawatt lasers that drive LPAs currently can only fire once a second or so, and the pulses can vary widely from one to the next, he notes. "Aside from the plasma or anything else, we need to improve the laser technology."

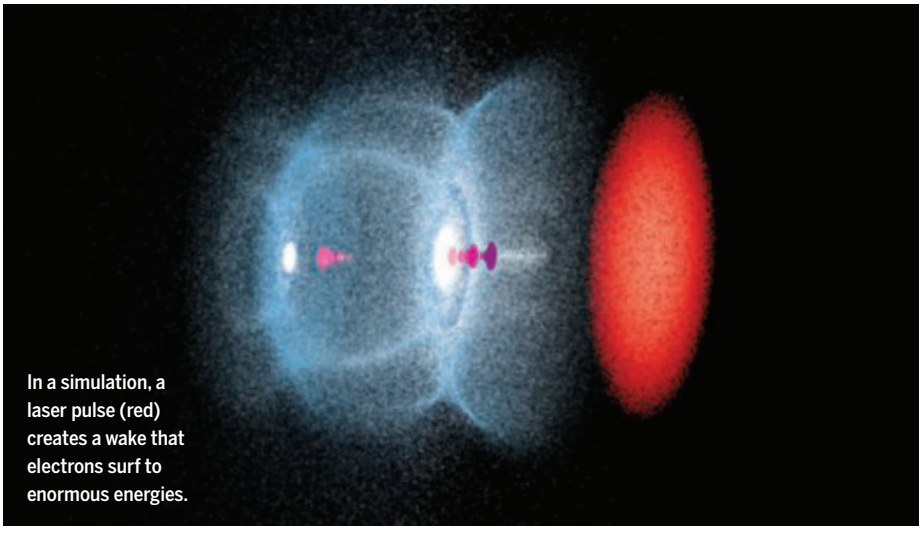

In a simulation, a laser pulse (red) creates a wake that electrons surf to enormous energies.

Still, researchers are already thinking about a killer app: using an LPA to power a free-electron laser (FEL), a machine that generates potent x-rays by shooting a finely tuned electron beam through a long magnet that makes it slalom from side to side. The swerving electrons emit light that, in a feedback loop, separates them into tiny bunches that radiate in chorus. The result is a laser beam of x-rays, a powerful tool for studying molecules and materials.

SLAC's new giant linac powers an FEL, but physicists could make such machines far smaller and cheaper by replacing the linac with an LPA. There's a global race to do just that. In 2021, physicists at the Shanghai Institute of Optics and Fine Mechanics used an LPA to drive an FEL shining at ultraviolet wavelengths. However, it produced laser light on only 10% of its shots. Last year, Barber's team at LBNL upped that figure to 90% with its LPA. To reach useful x-ray wavelengths, however, developers will need higher energy electrons, which will likely require techniques like those combined in the new result from LBNL.

Europe is also betting big on this application. This year, as part of an effort called the European Plasma Research Accelerator with Excellence in Applications, officials will choose the site for a facility costing hundreds of millions of euros that will deploy FELs driven by LPAs. The facility aims to serve researchers and speed the development of LPAs, Cros says. "We have never been able to build a real accelerator operating all day, every day of the year, based on these techniques."

LPAs might also work in concert with other accelerators. For example, PETRA-III, a ring-shaped accelerator at the German laboratory DESY, circulates 6-GeV electrons to generate x-rays. Currently, electrons reach that energy by first passing through a linac and two smaller rings. Andreas Maier, a plasma accelerator physicist at DESY, and colleagues hope to supplement or replace all of that with a single LPA when the facility is upgraded in 2030, using the techniques demonstrated by the LBNL group. "For us, it's a very encouraging result," he says.

Some physicists think LPAs are already good enough to make money. Hegelich, for example, has founded a company called TAU Systems that is completing an LPA facility in Carlsbad, California, to serve customers. NASA's Jet Propulsion Laboratory has signed up to test whether electronics can stand up to the radiation environment in space, Hegelich says. The facility will also serve as a showroom, he adds. "You can go there and see the machine. And if you want one yourself, we'll build you one." ■

AIR POLLUTION

In India, a debate over the benefits of gas stoves

Surprise finding of few health payoffs complicates push to replace biomass fuel

By **Vaishnavi Chandrashekhar**

On a cloudy morning in October 2024, researchers visited a small home in Karyalur, a village in south India, to take the measure of a 5-year-old girl named Dhanashree. They recorded her blood pressure, weight, and height, and tested her skills with games that involved kicking a ball or building with blocks. The reason for their visit sat in a corner: a cooking stove connected to a large red cylinder of liquefied petroleum gas (LPG).

The stove and cylinder had been given to Dhanashree's family as part of a large four-nation study, funded by the U.S. National Institutes of Health and the Bill & Melinda Gates Foundation, called the Household Air Pollution Intervention Network (HAPIN) trial. Launched in 2018, it aimed to discover whether the health of children improved in homes that replaced traditional, smoky stoves that burn biomass such as wood and dung with stoves fueled by cleaner burning LPG. Now, the results of the HAPIN trial are fueling a debate among researchers over whether India and other nations should aggressively expand the use of gas cooking stoves to curb air pollution.

Supporters of expanding LPG use say it is critical to improving air quality—especially indoor air quality—in a nation with some of the world's worst air pollution. They note that researchers have found biomass stoves used for cooking and heating produce 25% to 50% of the smog that chokes some regions of India for parts of each year. "Clean residential energy is key to delivering healthful air on multiple scales," says Chandra Venkataraman, a senior climate researcher at the Indian Institute of Technology Bombay.

Skeptics, however, point to the HAPIN trial's puzzling outcome: It found no statistically significant health benefits for children living in houses with LPG stoves. They add

IMAGE: CARLO BENEDETTI

that LPG is a relatively expensive fossil fuel that is subject to global market turmoil. "If LPG can't deliver on health outcomes, we should try something else," says epidemiologist Thomas Clasen of Emory University, a leader of the HAPIN trial. Expanding access to electricity, ideally from renewable sources, would benefit both health and the environment, he and others say.

Biomass stoves, used by an estimated one-third of the world's population, pose a clear threat to human health. The stoves produce fine soot particles, less than 2.5 micrometers in diameter (PM2.5), that contribute to respiratory and other health problems and millions of premature deaths.

For decades, researchers have tried to design "smokeless" biomass stoves, with little success. More recently, they turned to replacing biomass fuels with natural gas (methane) or LPG (often propane or butane), especially after the World Health Organization endorsed them as clean fuels in 2014 and the United Nations made access to energy a sustainable development goal in 2015. In recent years, the World Bank has helped promote gas stoves in Africa, and countries such as Indonesia have expanded access to LPG.

Advocates of gas stoves say they are good for the climate as well as air quality. Studies by Venkataraman, for example, have found that the soot and other pollutants given off by biomass stoves are potent warming compounds. A study by the Council on Energy, Environment and Water (CEEW), a nonprofit research institute in India, also found that one LPG cylinder can replace 178 kilograms of firewood, leading to a net reduction in warming emissions due to unsustainable wood harvesting practices.

Researchers thought the HAPIN trial would make an unequivocal case for LPG's health benefits. It enrolled some 3200 poor households in India, Guatemala, Peru, and Rwanda, including 800 pregnant women and their 800 infants. Half of the households received LPG stoves, which the researchers hypothesized would reduce pollution exposures and childhood pneumonia, and improve maternal blood pressure, infant birth weight, and growth rates. But the primary results, reported in three papers published in *The New England Journal of Medicine* in 2022 and 2024, were decidedly mixed. Median PM2.5 exposure dropped by two-thirds in homes with the stoves. But for birth weight, stunting, and pneumonia, there was no statistically significant difference after 18 months between children living in households using LPG and those burning biomass.

Several factors might explain the results, the researchers say. The intervention may have started too late in the gestation period—most mothers enrolled in their second trimester, and the few who enrolled earlier seemed to see better results. Benefits might also appear later; ongoing follow-up studies of children like Dhanashree could reveal long-term effects. But the most likely reason, Clasen says, is that when a population faces multiple environmental risks, as most poor communities do, a single intervention such as a clean stove may be "necessary but not sufficient" to improve health.

India has been promoting stoves fueled by liquefied petroleum gas, such as this one in a home in Uttar Pradesh.

PHOTO: T. NARAYAN/BLOOMBERG VIA GETTY IMAGES

This point is also emphasized by health researcher Kalpana Balakrishnan, who led the HAPIN trial in India. "We could give them free LPG, but we couldn't give them free food," says Balakrishnan, who is dean of research at the Sri Ramachandra Institute of Higher Education and Research. "Perhaps it was naïve to think we can undo with a short intervention what they have already been exposed to, the course they were already on."

The findings have left researchers divided over the wisdom of expanding the use of LPG. Balakrishnan says the demonstrated pollution reductions justify pushing ahead. But Clasen thinks policymakers should be wary of spending more public funds on the fuel without definitive evidence of health benefits. "The oil and gas industry like people to think that [LPG] is a virtuous fuel," he says. But alternatives, such as expanding access to electricity, could offer broader benefits, such as providing lighting and stimulating economic activity.

Yet a large-scale "leapfrog" to electricity, especially from renewable sources, may be unrealistic in India. Although its grid is expanding—and solar is also being promoted—the system isn't ready to handle the increased demand, says analyst Abhishek Kar of CEEW. Instead, he sees the path followed by Ecuador as a potential model for transitioning India away from biomass. There, the government promoted subsidized LPG and then, when gas prices started to rise, scaled up the use of electric stoves by offering financial incentives.

In India, LPG use has a long way to go. In 2016, the government launched an initiative to connect 100 million poor households to subsidized fuel supplies. By 2020, 62% of households were using LPG as their primary cooking fuel, but the share is much lower in rural areas. And surveys have found that only 30% of homes cook exclusively with gas; the rest either use biomass or charcoal exclusively or alongside LPG.

This "fuel stacking" was evident in Dhanashree's home. Anita, her mother, received free LPG during the HAPIN trial, spanning her pregnancy and Dhanashree's first year. But after that she reverted to using mostly wood. Cooking with gas is quicker and not smoky, Anita said, but the family can't afford to frequently refill cylinders, even at subsidized prices.

Advocates of expanding LPG use hope India's new national air pollution plan, which could be finalized this year, will address household air pollution and help increase subsidies for gas. And Venkatraman says a government plan to boost the production of biogas from waste could also contribute to a transition away from biomass fuels. "We need a basket of fuels for rural energy transitions," Venkataraman says. "But you have to start somewhere." ■

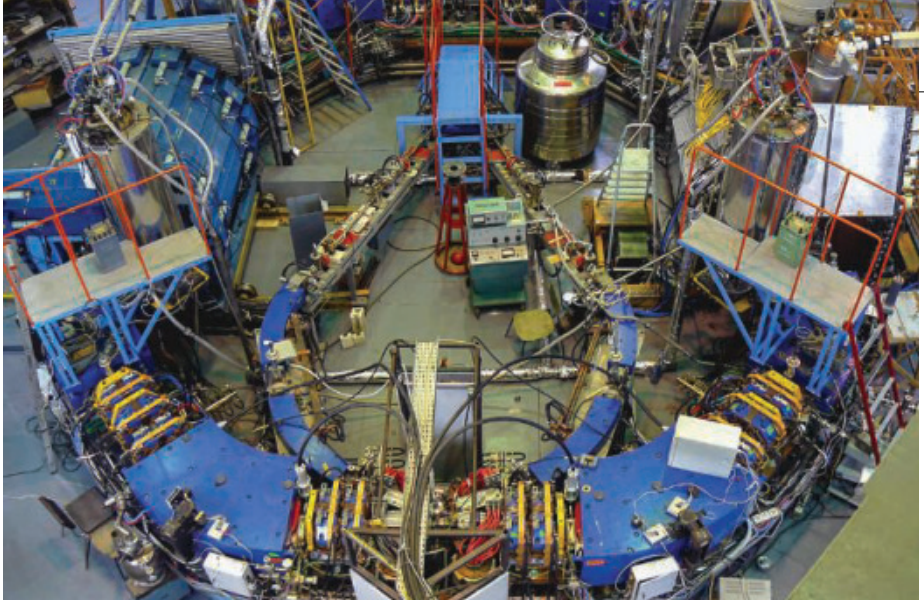

An electron-positron collider at Russia's Budker Institute could be a new focus of research efforts.

PHOTO: PETER BAGRYANSKY/WIKIMEDIA COMMONS

PHYSICS

Banished from CERN, Russian physicists regroup

Breakdown in collaboration leads many scientists to look to domestic projects—and to China

By ***Science*** **News Staff**

In the dead of the Russian winter, many of the nation's physicists are feeling a particular chill. Banished since late last year from Europe's CERN, the world's largest particle physics laboratory, and increasingly isolated by trade sanctions that have complicated purchases of scientific equipment, many Russian physicists are having to dramatically reorient their work—with some looking to China for collaboration.

Some scientists have found ways to sustain their connections to CERN and other institutions in Europe and the United States. But they have faced pressure from Russian officials to sever ties.

The breakdown in collaborations, catalyzed by Russia's full-scale invasion of Ukraine in 2022, is producing "obvious losses" for all sides, says Alla Skovorodina, a spokesperson for the Budker Institute of Nuclear Physics (BINP), a leading Russian research center. Researchers from the institute had worked with CERN for decades, she notes, a collaboration that "has always been mutually beneficial." Russian scientists played a significant role, for example, in building and operating the Compact Muon Solenoid, one of two key particle detectors fed by the world's largest atom smasher, CERN's Large Hadron Collider (LHC), which discovered the Higgs boson.

But several hundred Russian scientists were forced to end their work at CERN on 30 November 2024, after the laboratory terminated its partnership agreements with institutes operated by the governments of Russia and Belarus, Russia's close ally. At least 90 Russian researchers sidestepped the ban by reaffiliating with institutes in other nations, according to a CERN spokesperson. The ban also did not apply to scientists affiliated with the Joint Institute for Nuclear Research (JINR) near Moscow, which is operated by a coalition of more than a dozen nations and has its own agreement with CERN.

More Russian researchers might have attempted to reaffiliate if not for opposition from prominent Russian officials, says Andrey Seryakov, a Russian physicist who in recent years had spent up to 3 months a year at CERN. For example, when researchers attempted to establish a new organization, based outside Russia, that would have enabled Russian scientists to continue working at CERN, they faced fierce criticism from physicist Mikhail Kovalchuk, president of the Kurchatov Institute nuclear energy research center, who is known for his ties to Russian President Vladimir Putin. "Given that most Russian scientists working at CERN have their main place of work in Russian universities and research centers, most of them were forced to refuse to cooperate," Seryakov says.

Although Seryakov can no longer work at CERN, he says he is still analyzing data he collected at the laboratory while he looks for a job. (He lost a post at St. Petersburg State University because of political activism.)

Other Russian physicists who have lost access to CERN say they will turn to domestic projects, such as the Nuclotron-based Ion Collider Facility under construction at JINR, which will create fleeting puffs of fundamental particles called a quark-gluon plasma, and a pair of small electron-positron colliders at BINP. The larger of the two produces a particle called the tau lepton, a fleeting heavier cousin of the electron. The smaller, just 24 meters in circumference, has pioneered a new technique to produce round particle beams, which are more compact and stable than the usual flat, ribbonlike ones. That should enable a collider to run longer before refilling the beams. "These are worthy projects, although they are not as advanced as the LHC," says physicist Fedor Ratnikov of the Laboratory of Methods for Big Data Analysis at the National Research University Higher School of Economics in Moscow.

At BINP, another "promising direction is China," Skovorodina says. China has ambitious plans for a next-generation collider that could surpass the LHC in energy, she notes, "and our institute plans to participate."

In the meantime, Russian physicists continue to struggle with trade sanctions that have made it difficult to obtain electronics and other high-tech gear from the U.S. and Europe, and ongoing pressure from Ukraine and its allies to expel Russia from other collaborations. For example, a BINP researcher says Russian contributions to a nuclear physics experiment called PANDA at the Facility for Antiproton and Ion Research, a large accelerator project currently under construction in Germany, have been largely frozen.

Such ruptures trouble Anatoli Romaniouk, a Russian physicist who has worked at CERN since 1990 and was not directly affected by the ban. "Science is a bridge that allows people to communicate and exchange both intellectual and moral products," he says, adding that he will try to maintain some communication with colleagues in Russia, in part because he thinks it is important to "give young scientists the opportunity to participate and develop in the global scientific community." But he's not optimistic that U.S. and European institutions will become more welcoming to Russia anytime soon. "I do not foresee any significant changes in attitudes towards Russian scientists in the next decade," he says. "And perhaps longer." ■

With reporting by Andrey Feldman and Eugene Gerden.

CONSERVATION BIOLOGY

Global study shows species are losing diversity

Even in some common species, the genetic variation key to resilience is slipping away

By **Elizabeth Pennisi**

Variety is more than just the spice of life. Genetic variation is what allows a species to adapt as climate changes, new diseases arise, and novel predators come on the scene. A slightly different genetic makeup can ensure at least some individuals will still do OK in times of crisis. But just as the number of species is declining worldwide, so, too, is the genetic diversity within many species, an international team reports this week in *Nature*.

"This paper is a big leap forward in helping us understand the extent of genetic diversity loss," says Chris Funk, a conservation geneticist at Colorado State University who was not involved with the work.

Conservationists were already worried about declines in the genetic diversity of threatened species, which tend to have populations that are small and isolated. But the new study indicates some animals and plants whose populations seem healthy are also losing genetic diversity as their numbers or ranges shrink because of pressures such as development or climate change.

Deborah Leigh, a conservation geneticist at Goethe University Frankfurt and the Senckenberg Research Institute and Natural History Museum who was also not involved with the study, calls this diversity loss "the silent extinction" because the change is not obvious. She notes that when many people think of biodiversity, they picture the rich flora and fauna of a tropical jungle or the colorful inhabitants of a coral reef. "But biodiversity also includes all the differences within each species in that jungle or that coral reef," Leigh explains.

Until 2022, governments interested in protecting the environment were concerned mostly with keeping species from disappearing. That year, however, when updating the United Nations's Convention on Biological Diversity treaty, participating countries agreed to start to look at genetic diversity as well. "For the first time, countries agreed to protect diversity in wild species," says David Bravo Nogues, a biogeographer at the University of Copenhagen.

The first step toward slowing the trend is understanding it. Conservation biologist Catherine Grueber from the University of Sydney and scores of colleagues assembled 882 papers written between 1985 and 2019 that traced diversity changes within individual species by analyzing their DNA at at least two time points. Of the 628 species discussed, 70 were birds, 134 were mammals, 131 were bony fish, and 72 were flowering plants. The team used sophisticated statistical analyses to make the data comparable, enabling them to identify trends and correlate loss of genetic diversity with floods, habitat destruction, or other disturbances. They also tracked what happened in the face of various conservation measures, such as legally protecting a species or setting aside and protecting habitats.

The critically endangered kākāpō has low genetic diversity.

PHOTO: TUI DE ROY/MINDEN PICTURES

Two-thirds of the populations analyzed exhibited a decline in diversity, Grueber and her colleagues report. That included species already known to be at risk, such as the kākāpō, a ground-living New Zealand parrot that suffers from inbreeding and infertility. It also included more common species such as the black-tailed prairie dog and the house sparrow. The implication is that those species may be less resilient than expected during environmental change, says Alicia Mastretta-Yanes, a conservation geneticist at the Royal Botanic Gardens, Kew. "We must halt the loss of genetic diversity."

Some conservation efforts, such as ecological restoration or reducing pests, didn't help much, the analysis found. "This failure is not surprising," Nogues says. "Many conservation tools were not fine-tuned for [protecting] genetic diversity." But certain actions did seem to help, such as efforts to expand and protect habitat, introduce new individuals to dwindling populations, or connect two isolated populations. For example, in Western Australia, conservationists have been able to stabilize the genetic diversity of golden bandicoots by transferring some individuals from an island with a large population onto two other islands.

"It was pretty impressive they were able to track what human disturbance and conservation actions had done," says Moisés Expósito Alonso, an evolutionary geneticist at the University of California, Berkeley who authored a preprint last year indicating that protecting existing habitat won't be enough to prevent genetic diversity losses for many species. "We needed something like this," he says of the *Nature* study.

Conservation scientists emphasize the importance of continuing to monitor populations. But DNA methods aren't always practical, some note. "It is relatively hard and expensive to measure genetic diversity directly," Mastretta-Yanes says.

To get around that, Mastretta-Yanes and others published a paper in *Ecology Letters* last year that used proxy measures, such as population size, instead of DNA to evaluate genetic diversity in 919 species. The method, which only required about 3 hours of work per species, indicated that 58% of the species have populations that are too small to maintain their genetic diversity. The fact that these different approaches found declining diversity "makes both results more robust," Mastretta-Yanes says. "Finally, genetic diversity is getting the attention it deserves." ■

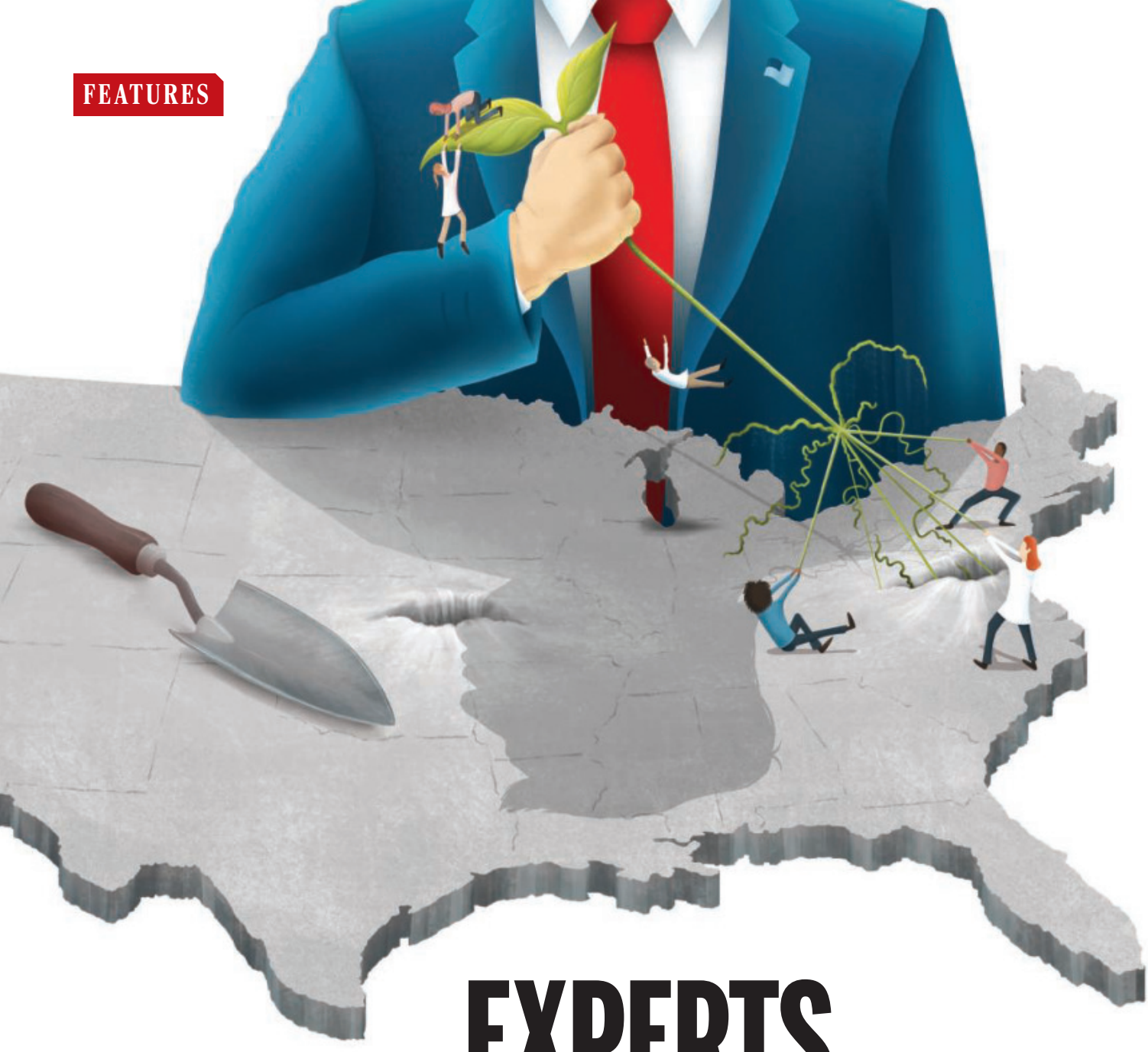

EXPERTS UPROOTED

A small statistical agency within the U.S. Department of Agriculture was torn apart under Trump—and then rebuilt. What did it lose, and what can other U.S. research agencies learn from it? *By* **Jeffrey Mervis**

On an unseasonably cold day in March 2019, hundreds of agricultural economists were herded into a conference room in Washington, D.C., to learn their fate.

The previous August, Secretary of Agriculture Sonny Perdue had announced that the U.S. Department of Agriculture's Economic Research Service (ERS), a small but well-regarded statistical agency, would be relocating somewhere outside of the nation's capital to allow USDA "to provide more streamlined and efficient services." One by one, a USDA official read the job descriptions of the 76 of 329 ERS positions that would remain in town. The rest would move.

"It was awful the way they told us," recalls one of several economists who requested anonymity because they still work at ERS. "People not on the list started crying."

That day was part of a seismic upheaval at an agency that essentially serves as USDA's in-house think tank, analyzing and

ILLUSTRATION: A. MASTIN/*SCIENCE*

anticipating trends in agriculture, food and nutrition, natural resources, and the rural economy. Nearly one-half of its employees jumped ship between when Perdue announced the move and October 2019, when ERS opened its new office in Kansas City, Missouri, barely 3 months after the city won a nationwide competition to host the agency. (Kansas City also snared USDA's National Institute of Food and Agriculture [NIFA], which distributes some $1.5 billion in grants and contracts.)

"I calculated that more than 2000 years of ERS experience vanished in 3 months," says agricultural economist Marca Weinberg, a senior manager who took early retirement and then was rehired as acting head of the agency for the first year in its new location. "We lost the vast majority of our institutional knowledge and expertise, and it decimated the ranks of middle management." Only a dozen or so ERS economists actually moved from Washington, D.C., to Kansas City.

Yet those departures have not destroyed ERS. Congress ignored then-President Donald Trump's repeated requests to slash the agency's $87 million annual budget and staff in conjunction with the move. Those fiscal votes of confidence enabled ERS to go on a hiring spree and return to its pre-move size by 2022. The COVID-19 pandemic that hit in the spring of 2020 also helped repopulate ERS, making it possible for researchers unwilling to move to Kansas City to work remotely.

"That timing really saved our asses," says Daniel Hellerstein, a longtime ERS researcher who retired in 2019 but was hired back as a manager of its conservation and environment branch, which shrank from 15 to eight economists before rebounding. "After COVID we could say, 'You don't have to move here. You can stay where you are.'"

Although the agency survived the battering, it was diminished. "It is very, very disruptive to move the headquarters of an agency to a different city," says Michelle Amante of the Partnership for Public Service. "It's disruptive to the workforce, disruptive to the programming, and it decreases collaboration." The rebuilt staff is much younger and less experienced (see graphic, right). And ERS watchers say some topics have fallen off its radar because of a lack of expertise and because its researchers are less inclined to tackle controversial issues.

Those lessons have new, broader relevance now that Trump has returned to the White House with a promise to shrink the entire federal workforce and replace up to 100,000 civil servants with political loyalists. "When you politicize the whole merit-based civil service, it has dramatic impacts on the ability for public service to be impartial, to provide advice and expertise without fear of retribution," Amante says.

Even the rhetoric takes a toll. "It's very hard to know how much of this is just designed to scare or threaten us," one ERS economist says of Trump's attacks on government workers, including scientists. "But that by itself will lead to attrition. It's very difficult to keep going when you're being vilified."

WHEN JIM MACDONALD was looking for a job in 1980, ERS offered everything a newly minted industrial organization economist could want. "You're expected to publish, so you're interacting with academic economists," MacDonald says. "But at the same time you're working on policy-related stuff for a broader audience. And you get to work with a bunch of other people with similar skills and interests. All of that was very appealing."

Over the next 4 decades at ERS, MacDonald conducted seminal studies on how structural changes in the U.S. and global economies have affected agriculture. He traced the impacts of railroad deregulation and the consolidation of the livestock industry, and he documented the sharp rise of the prophylactic use of antibiotics in farm animals before it became a major policy issue. "Jim is that perfect blend of an amazing researcher and an amazing mentor," Weinberg says.

But Perdue's decision to move ERS forced veterans like MacDonald to rethink their future at the agency. Staff whose jobs were not on the "stay" list unveiled in March 2019 were given four options. "We were told you can move, or you can quit, be fired, or retire," remembers Catherine Greene, the agency's go-to research economist on organic agriculture.

Greene chose to retire after a 35-year career at ERS. So did roughly 100 of her colleagues, including MacDonald. "There was no way I was going to Kansas City," he says.

Perdue had said in 2018 that moving ERS and NIFA would allow the agencies to attract and retain top talent, bring them closer to their "customers," and save the government $300 million over 15 years. But a 2022 report by the Government Accountability Office (GAO), the congressional watchdog agency, poked holes in all those arguments.

USDA made an "unreliable estimate of savings" because it "did not include costs associated with expected employee attrition [and other] economic effects associated with a relocation," GAO found. Factoring in those elements, the Agricultural & Applied Economics Association calculated the move could actually cost taxpayers as much as $182 million.

Younger staff

The Economic Research Service's (ERS's) move to Kansas City, Missouri, led to an exodus of experienced researchers. They have been replaced over time by a much younger cohort, most of whom have been working remotely following the onset of the pandemic.

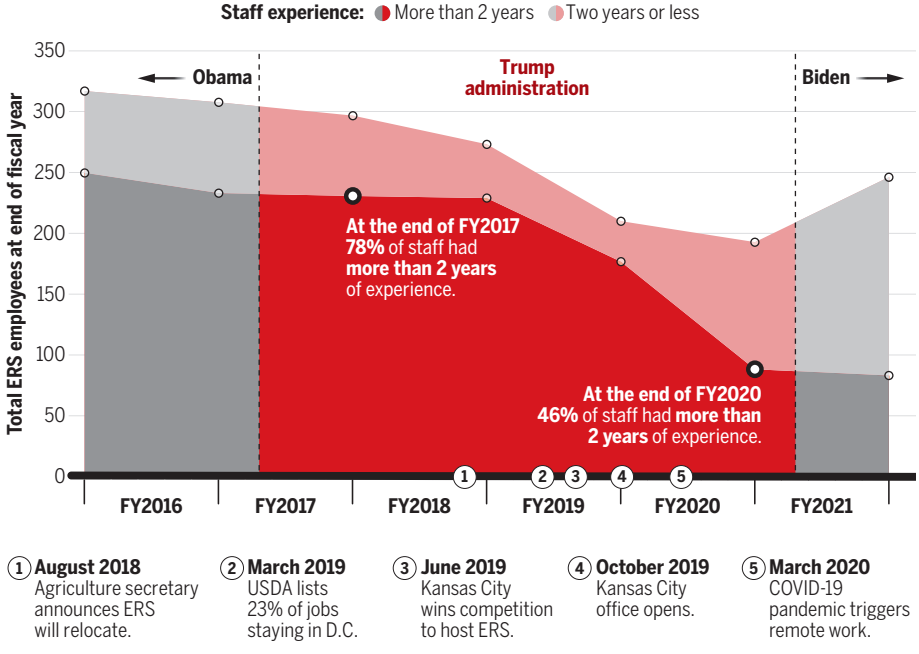

The U.S. fiscal year starts on 1 October of the previous calendar year and ends on 30 September.

CREDITS: (GRAPHIC) V. PENNEY/*SCIENCE*; (DATA) GOVERNMENT ACCOUNTABILITY OFFICE, GAO-23-104709 (2022)

Perdue's assertion that moving ERS out of Washington, D.C., would allow it to hire researchers at lower salaries was never realistic, says Gregory Pompelli, who served as associate ERS administrator for 10 years but left shortly after the move for a job at Texas A&M University. "The market for agricultural economists is national, not regional," he explains. "Even the ag econ programs at universities in the [Kansas City] area were hiring people at higher salaries than we could pay them at ERS."

Nor did the city realize the promised economic bonanza from hosting hundreds of well-paid professionals. ERS occupies just part of one floor of a downtown office building it shares with NIFA. Fewer than a dozen ERS staffers show up on a typical day, a fraction of the 40 or so who were given office space after pledging to come in at least 2 days per pay period.

Weinberg thinks a more likely reason for Perdue's decision was his desire to be "a good soldier" in carrying out Trump's assault on the federal workforce. Soon after Kansas City was chosen, White House Office of Management & Budget Director Mick Mulvaney explained that the desire to downsize was the impetus for the move.

"It's nearly impossible" to fire federal workers, Mulvaney told a meeting of Republican loyalists. But moving them to the nation's heartland, he explained, is "a wonderful way to streamline government."

ERS's mission to provide rigorous analyses of federal agricultural policies had historically made it an attractive target. Its predecessor agency, the Bureau of Agricultural Economics (BAE), provided data former President Franklin Roosevelt used to carry out his New Deal programs, which helped lift the country out of the Great Depression. At the time, "That work pissed off Republicans and some Democrats" opposed to social welfare programs, MacDonald recalls. "Then it began working on segregation and discrimination in agriculture, which pissed off some very powerful southern Democrats." Former President Dwight Eisenhower actually dismantled BAE, but former President John F. Kennedy Jr. reconstituted it in its present form in 1961.

Over the past 6 decades, ERS's independent analyses have continued to rankle those in power. In 2004, for example, it published an article exploring alternative ways to distribute some $22 billion in agriculture grants to the states. The goal was to find approaches that might improve environmental practices or boost economies, instead of simply stimulating greater production of commodities such as soybeans and corn.

Some senior USDA officials objected to the proposals, which might have hurt large commodity producers. "I had to sit through a whole lot of meetings, some in the secretary's office, getting berated by political appointees about what ERS should and shouldn't be allowed to publish," recalls the paper's lead author, agricultural economist Susan Offutt, who was ERS administrator from 1996 to 2006. "But the undersecretaries for research never caved. They said, 'That's what ERS is supposed to do.'"

Two more recent ERS studies may have helped trigger Perdue's decision. They found that the wealthiest farmers reaped most of the benefits from Trump's 2017 tax cuts and that those at the bottom of the income scale actually paid more in taxes. The studies, presented at the premier conference of U.S. economists in January 2018, were written up by *The New York Times* the day before Trump spoke at the American Farm Bureau Federation's annual convention.

"[Perdue] got blindsided," Weinberg says. "And if all [Perdue] knows about us is the pain points, then it's easier for him to say, 'Let's just get rid of ERS.'"

ERS EMPLOYEES TRIED TO FIGHT BACK. Just hours before the August 2018 announcement that the agency would be relocated, Perdue transferred its leader, economist Mary Bohman, to another USDA unit. With no one to speak up for the agency as events unfolded, a group of ERS employees decided to take matters into their own hands and seek representation by a labor union.

"The idea was that, after we became unionized, perhaps we could get a collective bargaining agreement in time to bar relocation," says one researcher who was active in the effort. ERS staff voted overwhelmingly to join Local 3403 of the American Federation of Government Employees, but they couldn't block the move. "That was probably wishful thinking, but for a time it injected some optimism," the researcher says.

Having failed to stop the relocation, many staffers decided to leave. MacDonald, for instance, joined the faculty at the University of Maryland. Its gain is ERS's loss, according to Weinberg. "We've been trying to fill his position for years," she says. "But you can't replace Jim MacDonald."

The huge number of departures has greatly altered the demographics of the agency. The number of ERS staffers with more than 2 years of experience plunged from 177 to 88, according to GAO. And the workforce became less racially diverse, with the number of Black or African Americans staff falling from 22% (60) in 2018 to 9% (21) in 2021.

Out of loyalty, Greene agreed to come back for 1 year as a contractor to finish a massive study of how organic agriculture has evolved since the government issued its first regulations in 2000. The goal was to provide a baseline for future analyses. "The idea was to transfer institutional knowledge that I had created on organic agriculture," Greene explains. But the organics team is now a shadow of its former self, she says. "The program was essentially killed. So who are you transferring this knowledge to?"

Offutt believes the same vacuum exists across the agency. "I don't want to cast aspersions on the current staff," she says, "but when you lose people who have decades of experience, know a lot of people in Washington, and understand how to do policy analysis, it takes a long time to rebuild that human capital."

At the same time, the relocation was a boon to other employers, both inside and outside the government. "The ERS community of researchers had no problem finding good jobs," Hellerstein says. "The thinking was, if you work for ERS, you must be good."

Dan Bigelow, an agricultural economist who left ERS for a faculty position

Fewer articles

The massive turnover from ERS's relocation, announced in 2018, caused a sharp drop in the number of journal articles and research reports. USDA has prioritized outlook reports, which are mandated by Congress.

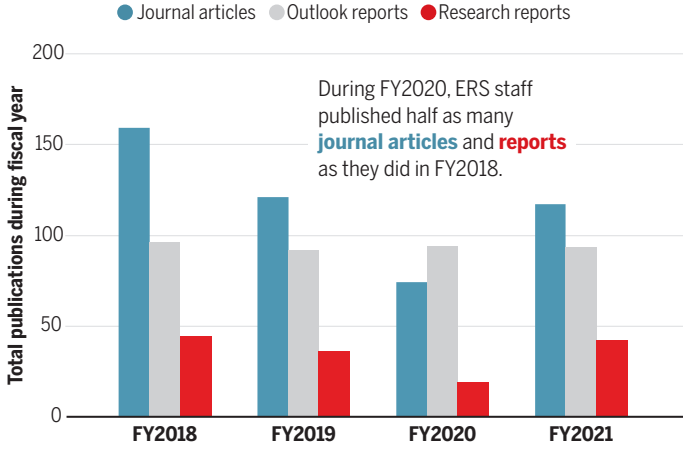

The U.S. fiscal year starts on 1 October of the previous calendar year and ends on 30 September.

CREDITS: (GRAPHIC) V. PENNEY/*SCIENCE*; (DATA) GOVERNMENT ACCOUNTABILITY OFFICE, GAO-23-104709 (2022)

at Montana State University and is now at Oregon State University, says he applied to 20 places and "got 15 initial interviews and eight or nine fly-out offers," an unusually positive response to an academic job search. "There's no way I would have been that successful had I not spent those 3 years at ERS," he says.

But landing on your feet is not always the same thing as pursuing your passion. "Leaving ERS marked an abrupt end to my research program, which I felt was just picking up steam at the time," says one former ERS economist who has remained in the government. Since then, "I've had a new job every year and a half or so," the economist says, explaining, "If you can't do what you really want to do, you might as well move up the [federal pay scale]." At the same time, "I'm trying to publish what's probably the last paper I'll ever write."

TEN MONTHS AFTER THE MOVE to Kansas City, the Trump administration named agricultural economist Spiro Stefanou as permanent ERS administrator with a remit to rebuild the staff. Stefanou, an expert on productivity measures, declined a request for an interview. But Weinberg and others say he has managed to attract both promising early-career scientists and more seasoned researchers by upholding the agency's high standards and sense of mission.

"I interviewed for academic jobs, government jobs, and consulting jobs," says one newly minted Ph.D. economist who started at ERS several months after the agency relocated. "But I'm really drawn to public service and to doing research that will help alleviate poverty. I guess I'm biased, but I think ERS is still the premier place to do work in this area."

ERS has also hired back a few dozen researchers who fled because of the chaos and uncertainty accompanying the move. "I wasn't interested in a job in Kansas City, but fortunately, a position doing exactly the same thing I had been doing opened up in D.C., and I was happy to take it," says one economist who asked to remain anonymous.

But the nature of the work has changed, the economist adds. They mention the need to spend more time mentoring younger staff and sharing ERS's institutional culture with new arrivals. "I think we're having success, but there's only so much of that you can do along with your regular job."

Those added duties could help explain why the number of peer-reviewed journal articles from ERS staff dropped sharply in the first 2 years after the move before recovering to previous levels, according to GAO. It found that ERS did a better job of pumping out its forecast reports, which are mandated by Congress. But MacDonald, who like Weinberg and Hellerstein has been working part time for ERS as a USDA contractor, thinks the quality of both the required reports and the journal articles has suffered.

"We're not as imaginative in what we're doing, because we don't quite understand as deeply what we're digging into," MacDonald says. "The new people don't have that long history with working with previous reports or with other agencies," he adds, citing as an example the agency's reduced focus on antibiotics.

Behavioral economics is another area where ERS has lost its edge, according to Weinberg. Running randomized, controlled trials to learn whether farmers respond to economic incentives to adopt more environmentally friendly practices is difficult and expensive under the best of circumstances, she says, and ERS has lost most of the experimental economists trained to do that work. "I think it will come back, but it makes me sad," she says about the program.

Offutt sees a more profound difference in the reconstituted ERS. She thinks the agency is less willing to stick out its neck by tackling issues that are politically sensitive.

"You don't see things about the distribution of payments," she says. "You don't see things about whether conservation programs are effective, or what fertilizer flowing off Iowa does to oxygen levels in the Gulf of Mexico. And the stuff they're doing on climate change is mostly descriptive."

"So yes, they're back to what looks like full strength, and the number of reports may be the same," Offutt continues. "But the nature of the output has changed. It's less relevant to policy."

WITH TRUMP BACK in the White House, Weinberg says she's been telling the staff to "keep their heads down and just do your work. It's good for your mental health, and it's also good in case you decide to go on the job market."

Even so, the recent upheaval has affected morale and culture. "It still feels like we're in limbo," a current ERS economist based in Kansas City said last month, referring to widespread speculation that the Trump administration would try to end remote work. "Everything seems so fragile." Adds one Washington, D.C.–based ERS economist, "Everybody is under a lot of stress." (Just before this article went to press, Trump ordered federal employees to return to the office.)

MacDonald is blunt when asked what it would mean to decimate ERS again. "Without ERS, USDA would be left with relying on commodity trade groups and advocacy groups to make stuff up," he asserts. "The information would be lower quality, and it would be packed with lies." ■

"I calculated that more than 2000 years of ERS experience vanished in 3 months."
Marca Weinberg
former acting ERS administrator

"Without ERS, [the U.S. Department of Agriculture] would be left with relying on commodity trade groups and advocacy groups to make stuff up."
Jim MacDonald
University of Maryland

PHOTOS: (TOP TO BOTTOM) MARCA WEINBERG; JIM MACDONALD

INSIGHTS

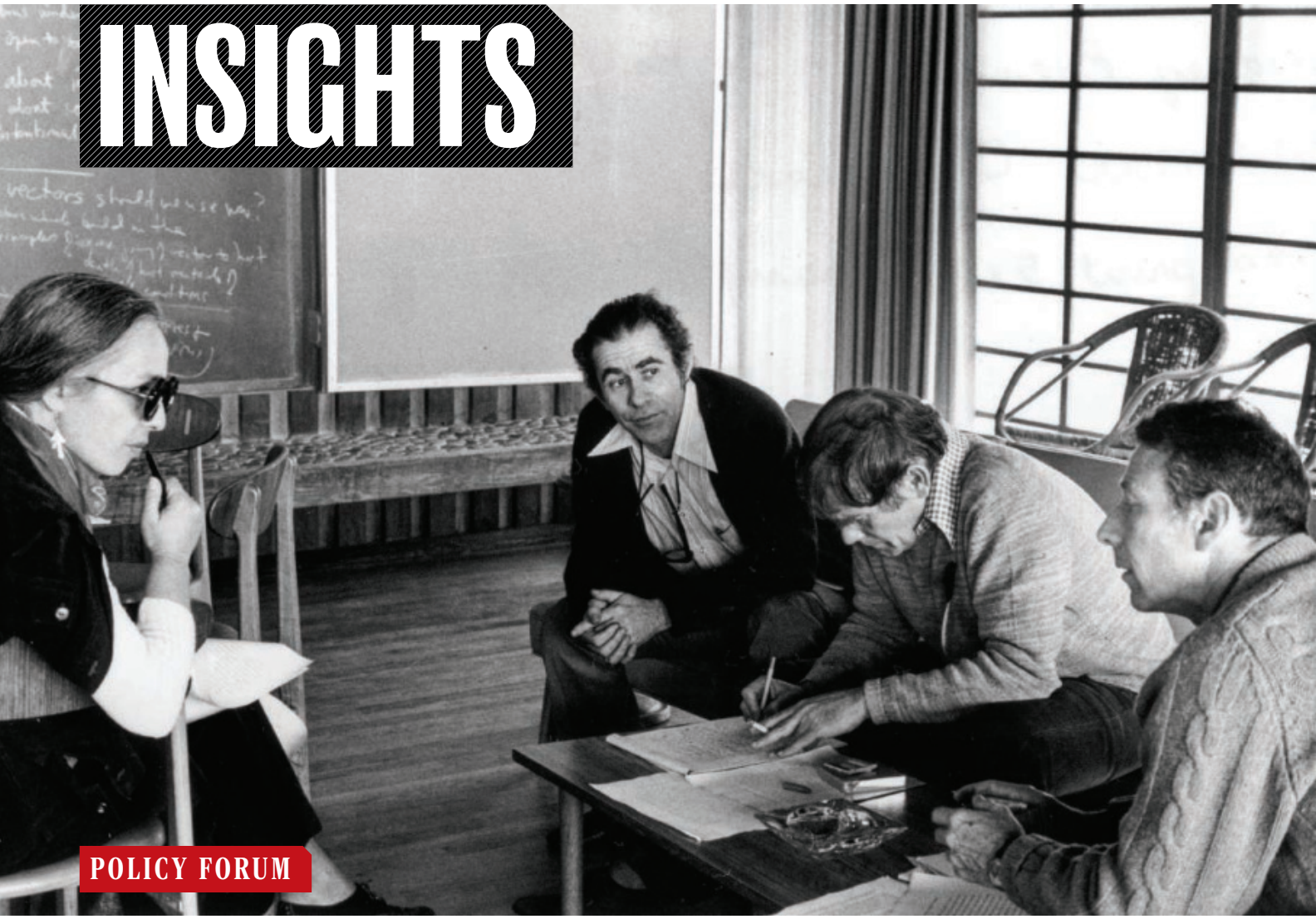

POLICY FORUM

SCIENCE AND DEMOCRACY

Taking responsibility: Asilomar and its legacy

A reappraisal of the constitutional position of science in American democracy is needed

By **J. Benjamin Hurlbut**

In February 1975, leading molecular biologists gathered at the Asilomar conference center on the California coast to evaluate risks of the emerging technology of recombinant DNA and to establish guidelines to govern research. The meeting is remembered as a defining moment in the making of molecular biology. Yet its legacy lies not in specific rules it developed but in the approach to scientific self-regulation that it crystallized. Five decades later, this near-mythic "meeting that changed the world" is held up as a precedent to celebrate and a model to emulate: Scientists take responsibility for governing themselves, solidifying public trust while securing future benefits of technology for society. But although this may elicit public acquiescence and secure scientific autonomy in the short run, ultimately it has engendered reactive distrust. The 50th anniversary affords a moment for taking stock of Asilomar's legacy and its implications for science and democracy. Its lessons are difficult.

The Asilomar meeting is held up as an exemplar of how scientists can navigate between the Scylla of technological risk and the Charybdis of public reaction and overregulation (*1*). The Asilomar myth encourages scientists to define what is at stake in emerging science and technology and whether and when those stakes require democratic attention (*2*). It invites them to draw upon the public credibility of science as a source of disinterested expertise to set the terms of debate and frame problems and solutions, thereby influencing (or dissuading) policy-makers who do not want to be seen as ignorant or scientifically regressive. This approach empowers technical experts to define appropriate societal concerns while discouraging disagreement on the ground that premature or ill-informed democratic engagement will inhibit innovation and deny society its benefits. This science-first, ethics-later paradigm construes democratic oversight as a potential threat to science because

PHOTO: ALBUM/ALAMY STOCK PHOTO

Maxine Singer, Norton Zinder, Sydney Brenner, and Paul Berg participated in the Asilomar Conference, February 1975.

only science is positioned to separate real risks from imagined concerns and hence to see into the technological future.

CONTAINING CONTROVERSY

In 1974, molecular biologists recognized that emerging recombinant DNA experiments might generate new biohazards. In an unprecedented move, they adopted a voluntary (if controversial) moratorium. The Asilomar meeting aimed to develop consensus recommendations for safely resuming research. It gathered dozens of leading scientists in the emerging field of molecular biology, a small handful of lawyers and social scientists, and a few journalists.

Molecular biologist and conference co-chair David Baltimore opened Asilomar by explaining that the focus would be "unusual for a scientific meeting." The assembled scientists would ask: "What should be done? What should we know before doing certain things?" [(*3*), p. 148]. Discussion focused on the potential for recombinant experiments to create dangerous new pathogens, but another risk also loomed large for participants: the possibility that public nervousness might lead to governmental overreaction and needless restrictions.

Some objected to any systematic regulation of research, voluntary or otherwise, as an abrogation of scientific freedom. But Sydney Brenner, a conference co-organizer, repeatedly warned that failure to act would result in public condemnation and governmental interference. Self-regulation, he said, would protect the autonomy of science.

Brenner was heard. The scientists produced consensus recommendations for the National Institutes of Health's (NIH's) recently formed Recombinant DNA Advisory Committee (RAC) to administer. Consequently, research was governed not by formal regulations but by flexible guidelines, implemented and updated primarily by researchers. In short, Asilomar successfully kept research governance in the hands of science.

Yet, decades later, Asilomar is remembered as a victory for both democracy and science. It remains a touchstone for good regulation wherein experts take responsibility on behalf of society for assessing risks and guiding development of emerging technology. Paul Berg, the primary organizer of the meeting who later won the Nobel Prize for fundamental contributions to recombinant DNA, said Asilomar marked "the beginning of an exceptional era for science and for the public discussion of science policy" [(*1*), p. 290]. On the meeting's 25th anniversary, Donald Fredrickson, NIH director in 1975, proclaimed: "from the awesome promise of Asilomar has come a new science, a new medicine, and a new industry." For Fredrickson, Asilomar's primary achievement was not containing risks, overestimated in retrospect, he believed, but as an experiment in democracy. The engagement of "science, public, government, and industry with questions about the meaning of the social compact" was "an entry point into the future [(*4*), p. 181].

Thus, the heart of the Asilomar myth became a "social compact" in which scientific self-regulation stands in for democratic governance. Numerous meetings rearticulating this understanding have been held at Asilomar—on geoengineering, embryonic stem cell research, artificial intelligence; rituals of reenactment to recapture an original power.

The connecting thread is the perceived risk of public challenges to scientific sovereignty. By acting first, experts seek to assuage public anxieties, showing that someone is in charge and paying attenton, even when they might otherwise dismiss concerns as unfounded. Taking responsibility is performative as well as preemptive. By reframing problems of governance as essentially technical matters within their sole jurisdiction, experts assert their competence to serve public needs better than any nonexpert democratic institutions.

MAKING POLICY IN PRIVATE

Yet already in 1975, some saw that the scientists at Asilomar had claimed not just the ability but also the authority to govern a powerful new technology for transforming life. Senator Edward Kennedy (D-MA) objected to Asilomar, not because he doubted the scientists' integrity or expertise, but as a usurpation of democratic authority: "They were making public policy, and they were making it in private" [(*5*), p. 188].

If the meeting was an expression of scientific responsibility, it was also an exercise in control. The scientists claimed that a complex, technical domain must be governed by those who knew it best—who understood what is known and unknown, and thus "what should be done" to regulate this emerging technology. A less noticed corollary, however, was that by asserting the right to define what needs governing, scientists also circumscribed the issues to technical considerations within their scope of expertise. Recombinant DNA emerged against a backdrop of heightened concern about science's contributions to environmental degradation, military technology, and human research abuses like Tuskegee (*6*). Yet Baltimore began the meeting by declaring issues of biosecurity and social and ethical issues out of bounds because they were "peripheral," raising "complicated questions of what's right and what's wrong" that were secondary to deciding "what should be done" [(*3*), pp. 148–149].

The Asilomar scientists delimited questions of governance largely to physical containment. In so doing, they also limited the uncertainties they had to address, waving off concerns about social, ethical, economic, and environmental risks as too speculative, downstream, irrelevant, or irresolvable, even as they preached the vast potential of a new biotechnology. In short, they abdicated responsibility for the social and ethical dimensions of a technology even as scientists asserted that it was for the good of society. This move neatly restricted the perspectives, both expert and public, that needed to be addressed: If engineered products could be kept contained in labs, then so too could questions of how to govern them.

Scientists positioned themselves as custodians of the public good as well as their own sovereign territory. In 1977, 137 molecular biologists wrote an open letter to Congress warning that "the benefits of recombinant DNA will be denied to society by unnecessarily restrictive legislation" [(*3*), p. 266]. Not wanting to defy expert's predictions, Congress dropped recombinant DNA from the legislative agenda.

In sum, Asilomar crystallized an image of science and democracy in which society's institutions can only inhibit, not guide or govern, science at its frontiers. Indeed, in congressional hearings on human cloning 20 years later, NIH director Harold Varmus invoked Asilomar to educate on the virtues of democratic inaction: "Much deliberation was given to the question raised by the cloning of DNA…the consequence of not having legislation to prevent such research is directly linked to the fact that we now have an extremely vibrant and benefit-generating biotechnology industry in this country" [(*7*), p. 23]. The lesson for governance: "Science and legislation frequently do not mix very well" [(*7*), p. 24].

These moves—treating risk as knowable and governable by scientific experts while construing the frontier of future technological benefits as endless only if democratic institutions get out of the way—are all too common. Paradoxically, nondemocratic governance was seen at Asilomar and beyond as essential for the public good. Yet, the consequence of dismissing public worries as premature, reactionary, ignorant, or irresponsible was to focus narrowly on scientifically assessable risks of immediate next steps that scientists could imagine—on the isolated experiment rather than where a line of research might lead and what challenges it might create.

School of Life Sciences, Arizona State University, Tempe, AZ, USA. Email: bhurlbut@asu.edu

This displaced opportunities for democratic articulation of visions of the good that could (and should) orient agendas of research and innovation. It delayed deliberation on what kinds of technological futures society wants until after enormous barriers to altering course were already erected—technologies developed, intellectual property acquired, capital invested, companies established. Any attempts to intervene earlier were seen as an abrogation of scientific freedom and a threat to the economic and social benefits of innovation.

SCIENCE FIRST, ETHICS LATER

The notion that governance must begin with expert-driven risk assessment and standard setting—safety first, ethics later—enshrines expert governance as primary, and sometimes as all the governance that is needed. Asilomar's categorical prohibition of field release of genetically modified organisms (GMOs), for example, silenced debate about what environmental release means—ethically, culturally, economically, and legally, as well as in terms of safety and health. When the time came for the RAC to evaluate a proposed field release, it followed the Asilomar playbook and treated the field like a laboratory rather than shared public space. Seeing minimal risk, RAC summarily dropped the prohibition, thereby setting loose a fierce controversy over GM agriculture that persists to this day (*8*).

When the world learned in late 2018 that children with edited genomes had been born in China, the presidents of the US National Academy of Sciences and National Academy of Medicine, and the Chinese Academy of Sciences responded by condemning the experiment and calling for "research guidelines" and "specific standards and criteria" to control how such experiments should be done safely. Yet it was (and remains) a matter of considerable ethical concern whether heritable human genome editing will ever be acceptable. Claiming jurisdiction to "convene needed international expertise and to help foster broad scientific consensus on the responsible pursuit of human genome editing research and clinical applications," the presidents noted that "the model of Asilomar offers important lessons" (*9*). The lesson in question is that when it comes to the governance of science and technology, what is right and responsible is first a matter for "scientific consensus," and only then for societal judgment. Society needs science to show what it means to be responsible. Science should act first, and society should follow.

This pattern is an inheritance of Asilomar: Experts treat the advent of new technology as the warrant for writing new rules of the road, as if prior thought and norms are suddenly obsolete. Genome editing becomes an entirely new concern, even if the ethical issues at stake—the responsibilities of procreation and parenting—have been subjects of thought for millennia. This foregrounding of technological novelty limits the forms of expertise recognized as relevant: Much is opined about molecular risks, little about cultural, legal, and religious encroachments on the integrity of human life. The emphasis on scientific consensus silences voices with much to contribute and handicaps the capacity for robust deliberation while it authorizes science to set the terms of debate.

Notably, this is precisely the logic that drove He Jiankui to create the "CRISPR babies" in the first place. "If we are waiting for society to reach a consensus…," he said, "it's never going to happen. But once one or a couple of scientists make first kid, it's safe, healthy, then the entire society including science, ethics, law, will be accelerated. Speed up and make new rules" [(*10*), pp. 229–230].

"This way of doing business not only flouts democracy but is contrary to science."

In the distributed environment of global science, making policy in private, expert settings on matters that concern all of humanity—whether by "rogue" scientists or scientific academies—has become the norm. When a professional scientific organization like the International Society for Stem Cell Research (ISSCR) convenes a closed-door committee to define (or abandon) limits on experimentation on forms of human life that a vast number of people globally consider inviolable, it is making public policy in private. ISSCR guidelines inform ethical standards for universities, companies, and scientific journals. Yet its ingrown processes radically constrain the range of thought that is brought to bear, producing policies that are parochial, partisan, and underdeveloped, to the point of alienating publics who justifiably view the process with skepticism.

Such secluded policy-making wraps professional self-interest in the mantle of scientific expertise. This exploits the essential role that science plays as a source of disinterested knowledge in guiding public judgment. Thus, it risks doing damage to the public credibility of science. It hardens reasonable disagreement into oppositional dissent, expressed in political and legislative arenas where grandstanding can displace nuance and deliberation.

Societies that buck the Asilomar model of scientific self-governance, imposing their own limits through public law and regulation, risk being marked as scientifically regressive and falling behind. Others on the fence shrug off their ambivalence on the theory that because someone somewhere will do the problematic research, it's better to stay competitive and forge ahead responsibly at home.

For science, the pill of regulation is less bitter when deliberation focuses on technical matters—ensuring safety and efficacy or reducing off-target effects—and does not demand thinking too hard about what kind of society innovation might bring into being. This is an approach to global governance that turns the race to international scientific and technological leadership into an ethical race to the bottom.

This way of doing business not only flouts democracy but is contrary to science. Keeping the doors closed, constraining the terms of debate, and excluding perspectives deemed to be unreasonable or inconvenient cuts against the spirit of scientific inquiry. It suppresses questions rather than encouraging them. It discourages disagreement and dissent, including within the scientific community itself. And it encodes limited imagination and norms of neglect into practices of research and innovation, virtually guaranteeing future controversy.

THE POWER OF CONSENSUS

Sydney Brenner and his colleagues believed consensus was essential for Asilomar's public credibility. To speak truth to power, science needed to speak univocally. That performance of "scientific consensus" is still seen as central to the political authority of expertise. It is no surprise, then, that scientists fear expressions of ambivalence within the community will unleash public skepticism.

Scientific communities often discourage expressions of disagreement about "what should be done" from within their own ranks. As a science and technology studies scholar who studies the nexus of science and ethics, I have had many conversations in which scientists expressed ethical discomfort with research in their own fields, sometimes even within their own labs. Yet almost without fail, these conversations happen in hushed voices during conference coffee breaks or some similarly private setting. My scientist-interlocutors worry that raising any suggestions of limits will be seen as legitimating public distrust and could jeopardize their professional standing. In my experience, this applies no less to elite scientists—National Academies members and candidates for the Nobel Prize—than to vulnerable assistant professors and graduate students.

Freedom to disagree is the lifeblood of scientific inquiry just as it is of democracy. Debates within science should center no less

Since the 1975 conference, similar events have been held at Asilomar on geoengineering, embryonic stem cell research, and artificial intelligence—"rituals of reenactment to recapture an original power."

on ideas of value and virtue that underwrite its projects of inquiry than on the knowledge and technologies science produces. Yet for a profession that insists on defining its own limits, discussion of limits is notably rare.

As a consequence, internal scientific consensus on matters of wider social concern tends to be overstated, whereas those who raise questions get accused of being ideological or "anti-science." This asymmetry warps deliberation on matters where knowledge and values are inevitably intertwined and must necessarily be resolved together. Instead, democratic scrutiny of expertise—essential to the health of both science and democracy—transmutes into a politics (of both right and left) of tarring particular experts and institutions as politically motivated. This form of criticism valorizes the political authority of science in the abstract—power should defer to "real" science—even as it hollows out the credibility of actual scientific experts and expert institutions. If "scientific consensus" decides "what should be done," science becomes the focus of political disagreement, producing dissensus and fracture.

SETTING LIMITS

Could it be otherwise? *Science* recently published an exception that proves the rule. Nearly 40 leaders in biotechnology took the rare step of calling for prohibiting some forms of basic research that might facilitate development of a potentially dangerous technology known as "mirror life" (*11*). But imposing limits should not be limited to areas that, like this one, may have the potential to destroy life on Earth. Fifty years after Asilomar, we have capacities to fundamentally transform life, both human and nonhuman; to engineer planetary systems; to deploy digital agents to control, manipulate, or militarize our social and technological infrastructures. Limits are a democratic imperative.

Further, the mirror life statement is notable for its outcome, but not for its process, which followed the conventional pattern of expert deliberation on risk and safety. The authors rightly call for broader discussion. But decades of discouraging deliberation at the frontiers of science have produced a deficit of public capacity. As a leader in innovation, the US has an obligation to foster deliberative capacity, yet it has done so poorly. For instance, no national bioethics council has existed in the United States since the end of the Obama administration—a result of bipartisan neglect. The National Academies have stepped into the breech, but even when they act at Congress's behest, their members define the parameters of deliberation, decide what perspectives and forms of expertise should be included, and conduct closed door deliberations designed to produce consensus. The outputs of these Asilomar-like processes, though often technically excellent, are a poor substitute for deliberative democracy.

Neither is academic bioethics or investment in ethical, legal, and social issues (ELSI) research alone a corrective to this democratic deficit in science governance. Bioethics too can be swayed by Asilomar's mythology. In 2010, several of the "mirror life" authors raised concerns to Obama's bioethics commission about synthetic biology governance. To their frustration, the commission invoked Asilomar to shift responsibility back to the scientists, asserting that at "this early stage of research," they should self-regulate because they "typically are the first to notice the laboratory door ajar."

ELSI research is often embedded in the science-first paradigm, not least because that is how it is funded: responding to downstream implications of ethically fraught science and technology, rather than critically assessing the contexts—the institutions, processes, culture, and configurations of power and authority—that generate them, or the causes of social controversy or breakdown that they may elicit.

How might things have looked different if the legacy of Asilomar had been a serious commitment to fostering democratic capacity to reflect on the collective moral understandings and commitments that should guide scientific and technological projects? Would a more open, deliberative, and capacious approach to governance

PHOTO: ALAMY

have avoided the corrosive politics of distrust we are now facing?

WHY THE LEGACY MATTERS

In 1976, Asilomar's legacy looked uncertain. Controversy had erupted. Cambridge, Massachusetts, home to Harvard and the Massachusetts Institute of Technology (MIT), was contemplating a ban on recombinant DNA research.

In a contentious City Council hearing (archived by MIT at https://archivesspace.mit.edu/repositories/2/archival_objects/303079), Councilman David Clem asked NIH molecular biologist and Asilomar co-organizer Maxine Singer: "Dr Singer, do you believe, personally, that there should be civilian control over the military?" Singer, nonplused and perplexed, responded: "That is a very difficult question for me to answer…it is something unexpected and not right on the topic."

The exchange offers an important lesson. Singer's response reveals the deficit at the heart of Asilomar. Whereas for Singer, good governance meant deference to expertise—following the science—Clem saw an essentially constitutional problem of power and authorization. Clem rejoined: "I think it is on the topic because I think that is, in fact, the fundamental issue here…I don't have the expertise to analyze or investigate any type of laboratory facility at Harvard University. But…there…is an important principle in this country that the people who have a vested interest in certain types of activity shouldn't be the ones who are charged with not only promulgating it but regulating it."

For Singer and her colleagues, the answer to Baltimore's question "what should be done?" was Asilomar: democratic deference to the technical judgment of a carefully limited group of experts whose knowledge, however incomplete, was sovereign. Clem wanted something more durable: a constitutional guarantee that governance by experts should be by delegation, not appropriation.

WHAT SHOULD BE DONE?

A half-century into the biotechnology revolution, we need a reappraisal of the constitutional position of science in American democracy (*8*). We need to valorize ambivalence alongside certitude, affirming that questions of what should be done and what must be known are inevitably and inextricably intertwined—and thus must be asked repeatedly and inclusively (*12*). To be truly progressive achievements, science and technology must be informed by and in the service of society's values. Technological progress thus understood is first a democratic project of collective moral imagination.

Asilomar's legacy inhibits this kind of constitutionalism. It robs democracy of the difficult yet essential task of determining what should be done and what must be known—and who must be empowered to know—for a technologically advanced society to govern itself well.

The inheritance of Asilomar is better understood in Clem's terms, not Singer's. Its legacy is not the long-since obsolete consensus that scientists assembled over three and a half days in 1975, but a de facto constitutional settlement that was never properly subjected to democratic ratification—exclusionary in its politics, suppressive of the democratic imagination, and lacking in checks and balances. It prioritizes technical expertise, discourages public deliberation, and truncates our collective capacity for asking "what should be done?" Instead, publics are shunted to a slower track that says: Keep out till science tells you what is justifiable to deliberate on."

"…a constitutional guarantee that governance by experts should be by delegation, not appropriation."

The time is ripe for change—for a "second enlightenment" that enhances the role of science in public reasoning by rethinking its place in democracy (*13*). A new enlightenment requires more than minor correctives to established patterns of scientific self-governance. Tacking on a formal process—a citizen's jury or a bioethical consultation—that ticks a box on the linear path of self-governing innovation is more opiate than cure.

Fortunately, there are glimmers of change. Agenda-setting organizations like the Organization for Economic Cooperation and Development, long committed to purely technocratic and economic conceptions of innovation, are awakening to the need to center the question of responsibility in structuring regimes of innovation (*14*). The Steering Committee on Bioethics of the Council of Europe has foregrounded capacity building for public debate as essential for protecting human rights in biomedicine. Even efforts to foster deliberation in the tradition of Asilomar like the three international summits on human genome editing have taken steps to broaden deliberation. But displacing old habits and building capacity that fosters new and better ones takes time, practice, and often-uncomfortable self-critique (*15*).

This spring, the Global Observatory on Genome Editing (of which I am a co-director), itself an experiment in deliberation, will host a summit that, contra Asilomar, radically expands the range of questions and perspectives that societies should take into account. It will begin with diverse understandings of the meaning of being human—cultural, legal, religious, and scientific—and explore their implications for projects in biotechnology. The hope is to start laying the groundwork for a genuinely global social compact that contends with the distribution of benefits and harms and the asymmetries in power and resources that order global science and technology. It will eschew the drive for scientific consensus in favor of cosmopolitan deliberation that affirms disagreement and aspires to mutual understanding and humility over artificial univocality.

That projected meeting is but one small step on a winding pathway. Traveling it requires abandoning Asilomar's ideology of linear progress. We must ask anew what experiments should be done—not merely in the enclaves of science and technology but in the laboratories of democracy worldwide—such that our scientific and technological projects can more truly align with democratically articulated imaginations of the good. Let us celebrate this 50th anniversary of Asilomar by relegating it to the past where it belongs and embracing the hard task of democratic renewal that lies before us. ■

REFERENCES AND NOTES

1. P. Berg, *Nature* **455**, 290 (2008).
2. S. Jasanoff, J. B. Hurlbut, K. Saha, *Issues Sci. Technol.* **32**, 25 (2015).
3. S. Wright, *Molecular Politics: Developing American and British Regulatory Policy for Genetic Engineering, 1972-1982* (Univ. of Chicago Press, 1994).
4. D. S. Fredrickson, *Perspect. Biol. Med.* **44**, 170 (2001).
5. B. J. Culliton, *Science* **188**, 1187 (1975).
6. J. H. Evans, *Playing God?: Human Genetic Engineering and the Rationalization of Public Bioethical Debate* (Univ. of Chicago Press, 2002).
7. US Senate, Committee on Labor and Human Resources, *Scientific Discoveries in Cloning: Challenges for Public Policy*, HRG-1997-LHR-0005, 12 March 1997.
8. S. Jasanoff, *Designs on Nature* (Princeton Univ. Press, 2005).
9. V. J. Dzau, M. McNutt, C. Bai, *Science* **362**, 1215 (2018).
10. J. B. Hurlbut, "Advancing Progressively Backwards: Guiding and Governing Heritable Genome Editing" in *The Promise and Peril of CRISPR*, N. Baer, Ed. (Johns Hopkins Univ. Press, 2024), p. 219.
11. K. P. Adamala *et al.*, *Science* **386**, 1351 (2024).
12. National Research Council, *Understanding Risk: Informing Decisions in a Democratic Society* (National Academies Press, 1996), https://doi.org/10.17226/5138.
13. S. Jasanoff, *Energy Res. Soc. Sci.* **35**, 11 (2018).
14. OECD Framework for Anticipatory Governance of Emerging Technologies, OECD Science, Technology, and Industry Policy Papers, no. 165 (2024); https://doi.org/10.1787/0248ead5-en.
15. K. Saha *et al.*, *Trends Biotechnol.* **36**, 741 (2018).

10.1126/science.adv3132

NEUROSCIENCE

Scratching more than an itch

Enhanced antibacterial skin inflammation is an adaptation of the itch-scratch cycle

By **Aaron Ver Heul**

Many people can relate to feeling the urgent need to scratch an itch. As the primary barrier surface and largest organ in the body, the skin has evolved a vast repertoire of immune and sensory functions that can manifest as inflammatory rashes and sensations such as pain and itch to protect the host (*1*, *2*). The capacity to both sense itch and behaviorally respond by scratching evolved hundreds of millions of years ago. Yet, the possible survival advantages conferred by the itch-scratch reflex remain unclear. On page 489 of this issue, Liu *et al.* (*3*) report the identification of a neuroimmune circuit whereby scratching engages signaling pathways that enhance immune cell–mediated antibacterial skin inflammation. This may have implications for understanding and treating a range of conditions with an itch-scratch component.

Skin is densely innervated by distinct populations of sensory neurons that respond to a variety of different stimuli. Classically, neurons have been defined by morphology and function, including by their axon thickness and the velocity at which they conduct electrical signals. Sensations of itch (pruriception) and pain (nociception) are primarily transmitted by neurons with thin, unmyelinated, and slowly conducting axons that are generally classified as C fibers (*4*). Most C fibers express transient receptor potential cation channel subfamily V member 1 (TRPV1) ion channels, which convert peripheral chemical and physical stimuli to sensory signals that are perceived as burning pain (*5*). Yet, both itch-responsive neurons (pruriceptors) and pain-responsive neurons (nociceptors) can express TRPV1, which has led to debate about whether itch and pain represent distinct sensations. When TRPV1 was ablated from all cells in mice except neurons expressing the pruritogen receptor Mas-related G protein–coupled receptor member A3 (MrgprA3), the animals exhibited itch behavior rather than pain behavior in response to an intradermally administered TRPV1 agonist, thus establishing MrgprA3-expressing neurons as bona fide pruriceptors (*6*).

It is increasingly appreciated that C fibers do not simply send sensory signals, such as itch, to the central nervous system but that they can also transmit stimuli toward the periphery by releasing neuropeptides that potently modulate the local tissue environment (*1*, *2*). C fibers bearing TRPV1 play key roles in coordinating inflammation in response to a variety of infectious and environmental insults. Indeed, activation of TRPV1 neurons in mouse skin by optogenetics, even in the absence of inflammatory stimuli, induces them to release calcitonin gene–related peptide (CGRP). Dermal dendritic cells respond to neuronal CGRP by recruiting interleukin-17–producing gamma delta T cells that subsequently confer protection from cutaneous infection with the fungus *Candida albicans* (*7*). Conversely, *Streptococcus pyogenes*, an organism that causes necrotizing fasciitis, hijacks TRPV1 neurons to release CGRP, which suppresses nearby bacteria-killing neutrophils, allowing more-severe tissue infection (*8*). In allergic skin conditions, the protease activities of certain allergens, such as those from house dust mites, can stimulate TRPV1 neurons to release substance P (*9*), a factor that drives local inflammation by stimulating mast cell degranulation (the release of proinflammatory substances, including histamine, cytokines, and proteases) (*9*, *10*). Substance P released by protease-activated TRPV1 neurons also causes dermal dendritic cell migration from the skin to initiate type 2 adaptive immune responses that can contribute to the development of allergies (*11*, *12*).

Liu *et al.* build on these observations in two important ways. They identify a circuit involving distinct neuronal populations in the mouse dermis whereby itch sensation is decoupled from neuron-induced inflammation. A population of pruriceptive neurons that express MrgprA3 but not TRPV1 can detect allergic inflammation and signal itch, whereas a separate population of neurons that express TRPV1 but not MrgprA3 releases substance P to boost local inflammation in response to scratching (see the figure). This adds a new dimension to prior findings that demonstrated direct activation of TRPV1 neurons drives neurogenic inflammation. Liu *et al.* also show that this is not mediated through a local tissue signaling axis but rather depends on scratching behavior coordinated through the central nervous system. In addition to the classical explanation of scratching as a defensive adaptation to remove parasites and toxins, these findings provide a physiologic and molecular explanation for conserved pathways requiring the itch-scratch cycle to complete a neuroimmune circuit.

Immunoglobulin E (IgE) antibodies likely evolved to protect against parasites and toxins, but they also contribute to en-

Scratching enhances skin defense

Allergens and bacteria that breach the skin barrier can trigger dermal mast cells to activate itch-specific neurons. This directs scratching behavior to the affected area, provoking other neurons to enhance local inflammation and host skin defense.

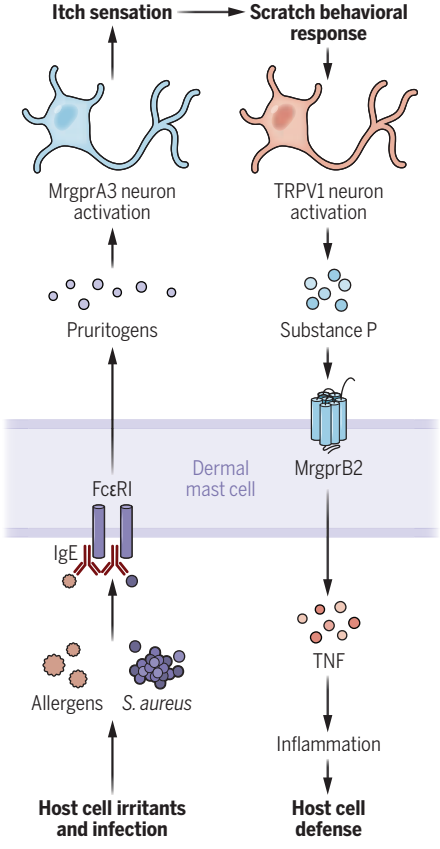

FcεRI, Fc epsilon receptor 1; IgE, immunoglobulin E; MrgprA3 or MrgprB2, Mas-related G protein–coupled receptor member A3 or B2; *S. aureus*, *Staphylococcus aureus*; TNF, tumor necrosis factor; TRPV1, transient receptor potential cation channel subfamily V member 1.

GRAPHIC: A. MASTIN/*SCIENCE*

Divison of Allergy and Immunology, John T. Milliken Department of Medicine, Washington University School of Medicine in St. Louis, St. Louis, MO, USA. Email: averheul@wustl.edu

Neuroimmune circuits may underlie a purpose for itch sensation inducing scratching.

vironmental allergies. Mast cells are the primary tissue-resident cells that mediate IgE responses by expressing Fc epsilon receptor 1 (FcεRI), the high-affinity receptor for IgE (*13*). Additionally, neuropeptides, such as substance P, can activate the mast cell–specific receptor MrgprB2 in mice (or MRGPRX2 in humans) to drive neurogenic inflammation (*9*, *10*). Notably, mast cells are the central immune mediators in the circuit identified by Liu *et al.*, triggering enhanced inflammation in the setting of simultaneous stimulation by allergen- or bacteria-specific IgE and substance P. The involvement of IgE responsiveness greatly expands the range of inputs that can drive itch-induced neurogenic inflammation. Rather than direct activation of TRPV1 neurons through a limited number of germ line–encoded receptors as in prior studies, any antigen recognized by IgE (generated through adaptive immune responses) can activate mast cells to elicit itch-scratch behavior and feed into the newly identified neuroimmune circuit. Maladaptive conditions associated with exaggerated type 2 immune responses often begin with itchy skin inflammation and proceed in an "atopic march" to include additional conditions, such as asthma and food allergies (*14*). Given increasing evidence that neurogenic inflammation can drive IgE sensitization to allergens (*11*, *12*), it is possible that the itch-scratch neuroimmune circuit characterized by Liu *et al.* contributes to the progression of allergic sensitizations underlying the atopic march.

Prurigo nodularis (PN) is a highly debilitating condition that can develop after chronic activation of the itch-scratch cycle (*15*). Although the pathogenesis remains poorly understood, neuronal dysfunction leading to severe itch followed by exaggerated neurogenic inflammation in the setting of intense scratching are hallmarks of PN. In addition to allergic skin conditions such as atopic dermatitis, systemic illnesses such as diabetes and chronic kidney disease are strongly associated with PN. The notion of an itch-scratch circuit that evolved to control cutaneous infections by synergistically activating mast cells may more broadly inform mechanistic understanding of other conditions, such as PN. Perhaps diabetic neuropathy can aberrantly activate pruriceptors to initiate the itch-scratch process, or elevated endogenous opioids in chronic kidney disease can synergistically drive mast cell–mediated neuroinflammation instead of IgE. Notably, the mast cell–depleting therapeutic monoclonal antibody barzolvolimab showed marked efficacy in a recent phase 1 clinical trial for PN (NCT04944862). Thus, beyond defining a previously unidentified neuroimmune itch-scratch circuit, the findings of Liu *et al.* may lay a foundation for discoveries to help people suffering from chronic itch. ■

REFERENCES AND NOTES

1. M. Tamari, A. M. Ver Heul, B. S. Kim, *Annu. Rev. Immunol.* **39**, 369 (2021).
2. S. Udit, K. Blake, I. M. Chiu, *Nat. Rev. Neurosci.* **23**, 157 (2022).
3. A. W. Liu *et al.*, *Science* **387**, eadn9390 (2025).
4. E. S. J. Smith, G. R. Lewin, *J. Comp. Physiol. A Neuroethol. Sens. Neural Behav. Physiol.* **195**, 1089 (2009).
5. M. J. Caterina *et al.*, *Nature* **389**, 816 (1997).
6. L. Han *et al.*, *Nat. Neurosci.* **16**, 174 (2013).
7. J. A. Cohen *et al.*, *Cell* **178**, 919 (2019).
8. F. A. Pinho-Ribeiro *et al.*, *Cell* **173**, 1083 (2018).
9. N. Serhan *et al.*, *Nat. Immunol.* **20**, 1435 (2019).
10. B. D. McNeil *et al.*, *Nature* **519**, 237 (2015).
11. C. Perner *et al.*, *Immunity* **53**, 1063 (2020).
12. C. H. Flayer *et al.*, *Nature* **634**, 440 (2024).
13. J. M. McDonnell, B. Dhaliwal, B. J. Sutton, H. J. Gould, *Annu. Rev. Immunol.* **41**, 255 (2023).
14. A. S. Paller, J. M. Spergel, P. Mina-Osorio, A. D. Irvine, *J. Allergy Clin. Immunol.* **143**, 46 (2019).
15. L. Misery, *Br. J. Dermatol.* **187**, 464 (2022).

10.1126/science.adv1573

BIOCHEMISTRY

Catching carbon fixation without fixing

Structural snapshots of an enzyme complex reveal missing pieces of a biological process

By **Xiang Feng**[1,2] *and* **Douglas C. Rees**[1,2]

Biological carbon fixation is a process in which living organisms convert atmospheric carbon dioxide (CO_2) into metabolically usable organic compounds, such as sugars or acetate. This not only forms the foundation of the food chain but is also vital for regulating the global carbon cycle. The fixation of CO_2 involves many enzymes and cofactors. Although important features of the six known biological carbon fixation pathways have been established (*1*, *2*), the sizes and transient natures of protein complexes have complicated the capture of intermediate states using structural methods such as x-ray crystallography and nuclear magnetic resonance spectroscopy. On page 498 of this issue, Yin *et al.* (*3*) report high-resolution snapshots of the Wood-Ljungdahl pathway (WLP), which is one of the most efficient carbon fixation mechanisms, using cryo–electron microscopy (cryo-EM). The results reveal the dynamics of key enzymes and could contribute to designing such pathways for carbon capture and biofuel production (*4*).

The WLP, which is also known as the reductive acetyl–coenzyme A (acetyl-CoA) pathway, accounts for an estimated 20% of biological carbon fixation (*2*). In this mechanism, two CO_2 molecules are converted to acetyl-CoA, a key metabolic intermediate for carbohydrates, proteins, and lipids. The WLP involves two enzymes: carbon monoxide dehydrogenase (CODH), which performs a reversible conversion of CO_2 to carbon monoxide (CO), and acetyl-CoA synthase (ACS), which produces acetyl-CoA. Two copies each of CODH and ACS associate to form the CODH/ACS complex. Carbon fixation by

[1]Division of Chemistry and Chemical Engineering, Howard Hughes Medical Institute, California Institute of Technology, Pasadena, CA, USA. [2]Howard Hughes Medical Institute, California Institute of Technology, Pasadena, CA, USA. Email: dcrees@caltech.edu; xfeng2@caltech.edu

PHOTO: M-GUCCI/ISTOCK PHOTO

the WLP requires a coordinated delivery of two CO_2 intermediates, CO and methyl (CH_3), to the A-cluster ($[Fe_4S_4]$-Ni-Ni) of ACS, where acetyl-CoA is synthesized. CODH coordinates two C-clusters, which are the active sites for CO_2 reduction to CO. A functional corrinoid iron-sulfur protein (CoFeSP) produces CH_3 from CO_2. However, it remains to be clarified how conformational changes within the CODH/ACS complex orchestrate the sequence of these reactions to produce acetyl-CoA.

The work of Yin *et al.* provides a comprehensive framework by visualizing missing conformations of the WLP intermediates using cryo-EM. The A-cluster serves as a hub, which is connected to three branches that deliver CO, CH_3, and acetyl-CoA. The CO branch transfers electrons from an iron-sulfur protein (ferredoxin) to the C-cluster of CODH, where CO_2 is reduced to CO. The CO subsequently diffuses through a gas tunnel from the C-cluster into ACS, where it ultimately binds to the A-cluster. The CH_3 branch generates a methylcobalamin (vitamin B12) species from CO_2 reduction on the CoFeSP protein that subsequently delivers the CH_3 group to the A-cluster. The combined binding of CO and CH_3 creates the acetylated A-cluster, which further reacts with the thiol (SH) group of CoA to release acetyl-CoA.

Yin *et al.* showed a critical design feature of ACS that explains how the protein conformation changes for efficient carbon fixation. Three domains (A1, A2, and A3) are connected by flexible linkers (see the figure). A1 forms the interface to the CODH enzyme, and A3 contains the A-cluster. This modular construction protects the A-cluster and sequesters intermediates while executing the reaction sequence to release the product. ACS can adopt a folded conformation in which the A3 domain docks to A1. This connects the A-cluster to a gas tunnel that enables receipt of CO from CODH. After CO binds to the A-cluster, the domains of ACS swing outward by more than 30 Å to expose the A-cluster to the CH_3-donating CoFeSP protein. During this transition, "gate" residues close the gas channel, preventing the escape of CO from the enzyme (*5*). After the release of acetyl-CoA, the ACS domains reset to their original conformations for the subsequent catalytic reaction. Reversing the order of receiving CO then CH_3 has been shown to yield the same product (*6*).

Yin of A-cluster *et al.* prepared the CODH/ACS complex under anaerobic conditions and in the presence of different combinations of CO, ferredoxin, or methylated CoFeSP substrates to capture transient intermediates of the WLP. By avoiding chemical fixation of the samples, the captured states of the proteins closely resemble their physiological forms. Visualizing a series of sequential conformational changes underscores the advantages of using cryo-EM to study transient protein states under conditions that closely mimic those of the cellular environment. In contrast to x-ray crystallography, which requires a crystalline arrangement of molecules, cryo-EM can take snapshots of multiple reaction states of proteins in solution. Advances in analysis software allow for detailed analysis of conformational heterogeneity within cryo-EM datasets (*7*). Additionally, improvements in the cryo-EM sample preparation technique can shorten the timescale to the millisecond range (*8*). Together, these developments are expanding the range of biochemical reactions that can be investigated with cryo-EM.

The findings of Yin *et al.* highlight some of the challenges in predicting protein structure changes, which are associated with the rapid evolution of microorganisms and fast adaptation to different physiological environments. The conservation of ACS domains across different microorganisms suggests that similar large conformational changes should occur in related organisms. However, the interface between ACS and CODH is not conserved (*9*). For example, a substantial change in this interface has been observed in *Moorella thermoacetica* (*10*) and *Carboxydothermus hydrogenoformans* (*11*) compared with *Clostridium autoethanogenum*, which Yin *et al.* studied. These alterations in the CODH/ACS complex through evolution complicate predictions of structural changes by comparing protein sequences. In addition, evolution can vary the combination of proteins in functional modules that are used for various molecular mechanisms. This process may also repurpose different enzymes for alternative biochemical pathways (*12*), which could further complicate the protein structure predictions. The integration of cryo-EM with other structural and computational techniques will address these challenges and elucidate the complex dynamics of biological systems. ■

Carbon fixation mechanism

The Wood-Ljungdahl pathway is one of the most ancient and efficient carbon fixation mechanisms in microorganisms. The structural changes of a protein complex that is involved in this process at intermediate stages were visualized by cryo–electron microscopy. Conformational changes in the protein fold enable binding of carbon monoxide (CO) and methyl (CH_3) to the active site (A-cluster). This process converts carbon dioxide to acetyl–coenzyme A (acetyl-CoA), which is a key metabolic intermediate to carbohydrates, proteins, and lipids. The reaction sequence can be 1-2-3-4 or 1′-2′-3-4.

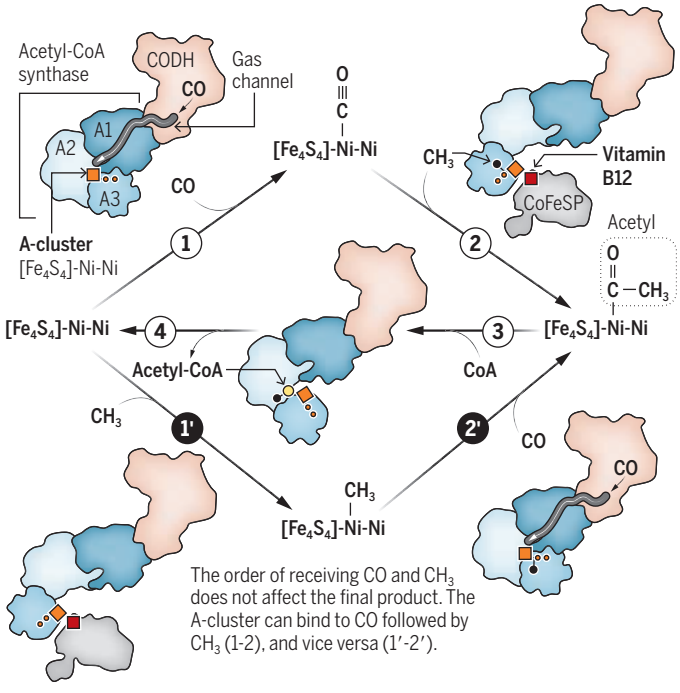

CODH, carbon monoxide dehydrogenase; CoFeSP, corrinoid iron-sulfur protein.

GRAPHIC: K. HOLOSKI/*SCIENCE*

REFERENCES AND NOTES

1. G. Fuchs, *Annu. Rev. Microbiol.* **65**, 631 (2011).
2. L. G. Ljungdahl, *Annu. Rev. Microbiol.* **63**, 1 (2009).
3. M. D. Yin *et al.*, *Science* **387**, 498 (2025).
4. A. M. Appel *et al.*, *Chem. Rev.* **113**, 6621 (2013).
5. J. Ruickoldt *et al.*, *Angew. Chem. Int. Ed.* **63**, e202405120 (2024).
6. M. Can *et al.*, *J. Am. Chem. Soc.* **145**, 13696 (2023).
7. W. S. Tang, E. D. Zhong, S. M. Hanson, E. H. Thiede, P. Cossio, *Curr. Opin. Struct. Biol.* **81**, 102626 (2023).
8. S. J. Amann, D. Keihsler, T. Bodrug, N. G. Brown, D. Haselbach, *Structure* **31**, 4 (2023).
9. A. Biester, D. A. Grahame, C. L. Drennan, *Proc. Natl. Acad. Sci. U.S.A.* **121**, e2410995121 (2024).
10. S. E. Cohen *et al.*, *ACS Catal.* **10**, 9741 (2020).
11. O. N. Lemaire, T. Wagner, *Biochim. Biophys. Acta Bioenerg.* **1862**, 148330 (2021).
12. G. J. Schut *et al.*, *Front. Microbiol.* **13**, 946711 (2022).

10.1126/science.adv2071

NEUROSCIENCE

Replaying off the beaten path

Before the hippocampus goes down memory lane, it takes a detour

By **Masahiro Takigawa** *and* **Daniel Bendor**

Buried deep within the medial temporal lobe of the human brain is the hippocampal formation, possessing the "superpower" to mentally time-travel—replaying past experiences or imagined future scenarios. Hippocampal replay is thought to perform several cognitive roles, including route planning and the consolidation and updating of memories. With this potential functional flexibility, it is unclear what determines or guides what the hippocampus will replay. On page 541 of this issue, Mallory *et al.* (*1*) provide new insights on this question: The hippocampus initially favors replaying an upcoming navigational route before switching its bias toward replaying past experiences. These findings uncover a surprising role for external input and neuronal adaptation in guiding replay content, bringing neuroscience one step closer to understanding how humans can mentally time-travel.

Knowledge about replay has largely come from observing freely moving rodents while performing electrophysiological recordings from spatially tuned hippocampal neurons known as place cells. Replay typically takes the form of a spontaneous reactivation of neuronal activity, forming a distinct sequence that represents previously taken or soon-to-be-taken spatial trajectories by the animal. When hippocampal replay was discovered in sleeping rodents more than 30 years ago, it was initially thought to consolidate recent episodic experiences into long-term memories (*2*, *3*). However, further experiments clarified that this phenomenon was more widespread, occurring during brief pauses or periods of inactivity in the awake animal, when memory consolidation is not believed to occur (*4*). Awake replay has been linked to a broad range of cognitive functions (*5*–*7*), but its potential role in planning has garnered great attention because in goal-directed behavior, replay can be observed originating from the animal's current location and propagating in the direction of the intended goal location (prospective replay) (see the figure) (*7*). Alternatively, replay can also reactivate along the recently taken path (retrospective replay), or along the path avoided by the animal (paradoxical replay), the latter more commonly observed in behavioral tasks such as a multiarm maze with a fixed goal location and aversive conditioning (*8*, *9*). Why would replay switch from being goal directed to anti–goal directed, and what does this say about what replay is really doing?

Taking a closer look at what may influence a replayed trajectory, Mallory *et al.* discovered an intriguing switch in the ongoing bias between prospective replay and retrospective replay in rats. On both a linearized track and within an open arena, replay that occurred within the first 3 seconds of stopping within the reward zone was biased toward prospective replay (referred to as forward replay on a linearized track). By contrast, after 3 seconds, reactivations shifted preferentially to replay retrospectively (referred to as reverse replay on a linearized track). That said, one must question whether prospective replay during this early window is due to a preference for future paths or an avoidance of past paths. The authors investigated a subset of stopping epochs in which an animal's past path (before stopping) overlapped with the future path (after stopping). Strikingly, the bias toward prospective replay was absent in such a scenario, suggesting that early replay tends to avoid recently experienced paths rather than actively preferring the soon-to-be-taken future path.

Mallory *et al.* further demonstrated that early avoidance of past paths during replay can be explained by spike frequency adaptation—a feedback mechanism whereby neurons become temporarily less active after firing. This adaptation suppressed neurons encoding the most recent path, leading the hippocampus to avoid recruiting these neurons during replay. This was not only limited to a path previously traversed by the animal; the hippocampus also avoided replaying again the most recent trajectory reactivated, albeit on a shorter timescale.

When spike frequency adaptation no longer causes replay to avoid the most recent trajectory, why does retrospective replay become the most prominent? Mallory *et al.* investigated the involvement of the medial entorhinal cortex (MEC), a major source of input to the hippocampus that is also reciprocally connected with the hippocampus. Disruption of the MEC input removed this bias in retrospective replay without affecting prospective replay, demonstrating a direct role for cortical input in shaping replay content. The shift in replay bias coincided with an increase in delta power (1 to 6 Hz), an oscillatory band implicated in cortico-hippocampal coupling (*10*). These observations add further weight to

Replay dynamics

When the animal stops, replay can be both prospective (in the direction of the intended goal location) and retrospective (reactivating the path previously taken by the rat) (top). In some behavioral tasks, paradoxical replay becomes more prominent, activating the path avoided by the animal (bottom).

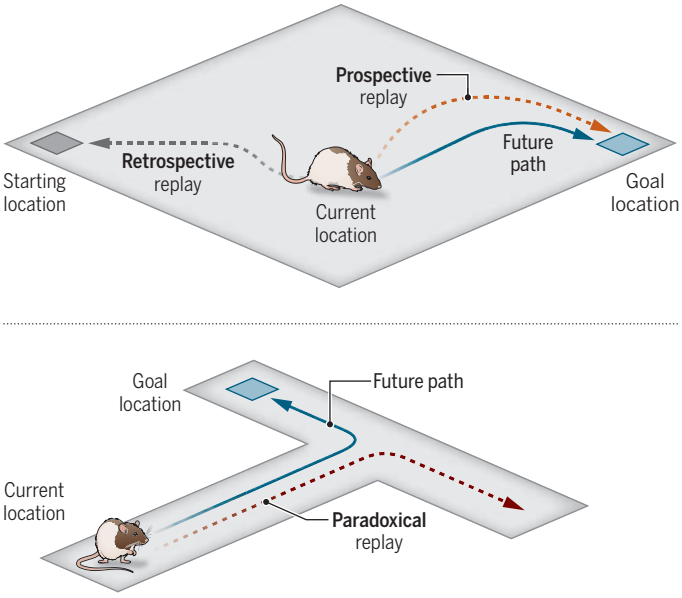

GRAPHIC: N. BURGESS/*SCIENCE*

Institute of Behavioural Neuroscience, University College London, London, UK. Email: masahiro.takigawa.17@ucl.ac.uk; d.bendor@ucl.ac.uk

the notion that cortical input can bias what the hippocampus ultimately replays (*11, 12*).

The study of Mallory *et al.* also provides a key insight into the puzzling observation that replay appears to vary with the behavioral task. A bias for prospective replay has been reported predominantly in foraging-homing tasks, in which the goals of past and future trials are typically in opposing directions and experience is balanced (*7*). By contrast, when the goal location is unchanged across trials within a block (i.e., experience is unbalanced), prospective and retrospective trajectories likely overlap as the animal runs a singular trajectory repeatedly. In such cases, if replay avoids the most recently traversed path, it would avoid both future and past trajectories, favoring the replay of an alternative path, a possible explanation for the surprising observation of "paradoxical replay" (*8*).

These exciting findings now unlock further questions. Does this shift in replay bias between avoiding versus mirroring the most recent trajectory serve a functional role, or is it simply a constraint of neuronal dynamics? Furthermore, given the similarity between reverse replay (on a linear track) and retrospective replay (in an open field), should we be considering these to be the same phenomenon? If so, rather than focusing on what trajectory gets replayed, should we shift our thinking to whether replay is incorporating neurons that have recently fired or were quiet? Intriguingly, neurons active in both future and past paths (i.e., bidirectional cells) are not modulated by spike-frequency adaptation in the same way as directionally tuned neurons solely encoding future or past paths, hinting at a more complicated framework governing replay dynamics. ■

REFERENCES AND NOTES

1. C. S. Mallory, J. Widloski, D. J. Foster, *Science* **387**, 541 (2025).
2. M. A. Wilson, B. L. McNaughton, *Science* **265**, 676 (1994).
3. G. Girardeau, K. Benchenane, S. I. Wiener, G. Buzsáki, M. B. Zugaro, *Nat. Neurosci.* **12**, 1222 (2009).
4. D. J. Foster, M. A. Wilson, *Nature* **440**, 680 (2006).
5. M. G. Mattar, N. D. Daw, *Nat. Neurosci.* **21**, 1609 (2018).
6. M. Huelin Gorriz, M. Takigawa, D. Bendor, *Nat. Commun.* **14**, 8157 (2023).
7. B. E. Pfeiffer, D. J. Foster, *Nature* **497**, 74 (2013).
8. A. A. Carey, Y. Tanaka, M. A. A. van der Meer, *Nat. Neurosci.* **22**, 1450 (2019).
9. C.-T. Wu, D. Haggerty, C. Kemere, D. Ji, *Nat. Neurosci.* **20**, 571 (2017).
10. I. Zutshi, G. Buzsáki, *Curr. Biol.* **33**, 3648 (2023).
11. D. Bendor, M. A. Wilson, *Nat. Neurosci.* **15**, 1439 (2012).
12. G. Rothschild, E. Eban, L. M. Frank, *Nat. Neurosci.* **20**, 251 (2017).

ACKNOWLEDGMENTS

The authors acknowledge support from the Medical Research Council (MR/N013867/1 for M.T.) and the Biotechnology and Biological Sciences Research Council (BB/Y010345/1 for D.B.)

10.1126/science.adv1570

GENOMICS

Genome recombination on demand

Large genome rearrangements in mammalian cells can be generated at scale

By **Marta Seczynska**[1] *and* **Lars M. Steinmetz**[1,2,3]

The human genome consists of more than 3 billion base pairs, among which only 1% encode proteins. These coding regions are small islands within a sea of noncoding and repetitive sequences. It remains unclear which DNA has a function or regulatory role and what the functional relevance of such genome architecture is. Advances in genome editing and functional genomics have facilitated the systematic interrogation of gene sequence and function. Yet there is little understanding of how gene order, orientation, and spacing affect gene expression and encode biological functions. On pages 487 and 488 of this issue, Koeppel *et al.* (*1*) and Pinglay *et al.* (*2*), respectively, present approaches for generating large genome rearrangements in mammalian cells at unprecedented scale. These technologies pave the way for large-scale functional analyses of genome organization, structural variants, noncoding DNA, and the design of mammalian cell lines with evolved properties.

The importance of genome structure, order, and content can be probed by engineering diverse genome configurations and comparing how they behave in cells. In yeast, such shuffling of the genome has provided valuable insights into genome function, revealing how gene context influences isoform selection (*3*), revealing how rearrangement patterns correlate with chromatin structure (*4*), and identifying rearrangements beneficial for selected traits (*5*). This was achieved by incorporating hundreds of loxP recombination sites into the yeast genome (*5*). These sites are targets for *Cre* recombinase enzyme, enabling the excision or rearrangement of DNA segments to generate diverse deletions, inversions, translocations, and extrachromosomal circular DNAs (ecDNAs).

[1]Department of Genetics, School of Medicine, Stanford University, Stanford, CA, USA. [2]Stanford Genome Technology Center, Stanford University, Palo Alto, CA, USA. [3]European Molecular Biology Laboratory (EMBL), Genome Biology Unit, Heidelberg, Germany. Email: lars.steinmetz@stanford.edu

Although this approach has proven feasible in yeast, adapting it for studying more complex and larger mammalian genomes has presented substantial challenges. The incorporation of recombination sites in yeast has been achieved through de novo genome synthesis, but the synthesis of the mammalian genome—or even a single chromosome—has been out of reach because of its large size. Also, the larger size and more complex genome architecture mean a greater combination of potential rearrangements. Inefficient or costly methods for variant recovery and mapping, such as isolating individual clones and sequencing entire genomes, have been major barriers to high-throughput studies in mammalian cells. Consequently, the impact of genomic rearrangements on the mammalian genome has primarily been studied by inducing rearrangements at individual loci or examining naturally occurring rearrangements in human populations (*6*) and cancer patients (*7*), scenarios that represent a strongly selected set of variants.

Koeppel *et al.* and Pinglay *et al.* describe complementary approaches to induce thousands of structural variants in a pool of cultured mammalian cells (see the figure). As in yeast, these rely on inserting a large number of recombination sites into the genome and expressing an enzyme that facilitates recombination between the sites. Although simultaneous insertion of multiple sequences into the genome is not trivial, Koppel *et al.* leveraged long-interspersed element-1 (LINE-1) repetitive elements, which comprise 21% of the human genome (*8*). Using prime editing technology, the authors integrated hundreds of loxP sites into conserved LINE-1 sequences in two human cell lines, overcoming issues of toxicity associated with manipulation of numerous loci and achieving a broad distribution of insertion across all chromosomes. Taking a different approach, Pinglay *et al.* randomly integrated recombination sites flanked by sequences that barcode each integration and allow its mapping to a specific genomic location. Expression of a recombinase induces recombination between these sites and reshuffles the ini-

tial barcodes. By sequencing new barcode combinations, genomic rearrangements can be detected and quantified without the need to sequence the entire genome. This method, which Pinglay *et al*. call Genome-Shuffle-seq, relies on in vitro transcription of barcodes to detect rearrangements alongside single-cell transcriptomes and thus enables the study of how structural variants affect cellular transcriptomes in a heterogeneous cell population.

The ability to generate cell lines with structural variants at scale also allows for the systematic study of how gene expression and chromatin state change when manipulating the order and position of nearby sequences. With the strategic use of barcodes and in vitro transcription, Genome-Shuffle-seq is designed to study the impact of structural variants at the single-cell level, establishing a foundation for large-scale single-cell screens, analogous to CRISPR screens with single-cell transcriptome readouts. This approach addresses a major gap in functional genomics: Methods for studying structural variants have long lagged behind those for other types of human genetic variation, such as single-nucleotide variations and insertion-deletion events, even though structural variants are known to cause Mendelian disorders, contribute to genetic diversity and complex disease risk, and often have larger phenotypic effects than those from single-nucleotide variants (*9*). By enabling the systematic study of the causal relationships between structural variants and gene expression, Genome-Shuffle-seq may help accurately interpret pathogenic variants and their role in disease.

Rearranging genomes

Thousands of loxP or attB sites can be inserted into the mammalian genome through prime editing or random integration. Cre or Bxb1 recombinases induce recombination between these sites, generating structural variants (SVs). Tracking the resulting heterogeneous cell population over time allows for probing selective pressure on SVs and the essentiality of the noncoding genome. Transcriptome sequencing reveals how SVs influence gene expression.

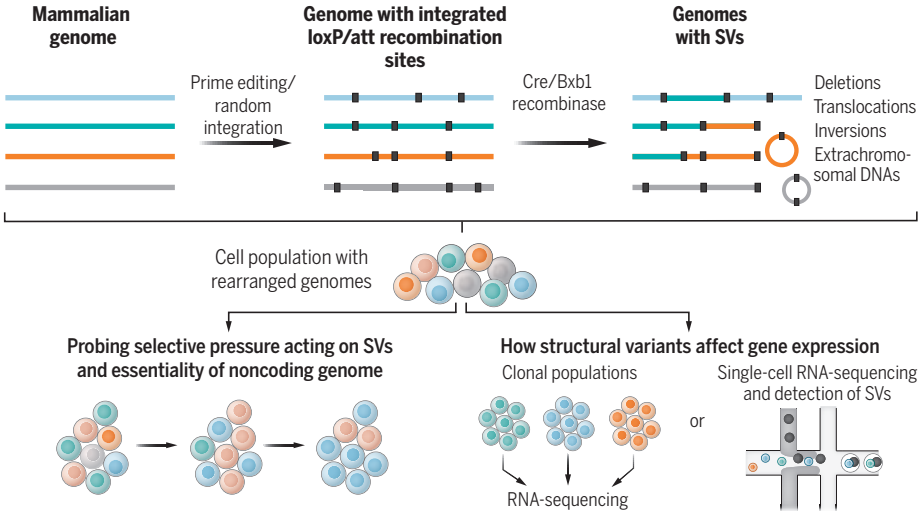

The ability to induce genome recombination on demand provides a means to address questions that are otherwise difficult to tackle. It allows assessment of selective pressure that acts on different types of rearrangements. By tracking variant abundance over time, Koeppel *et al*. and Pinglay *et al*. identified characteristics of tolerated structural variation: shorter inversions and deletions that avoided essential genes were better tolerated, and surviving variants were enriched in heterochromatic regions. Despite the general trend toward shorter variants, some megabase-scale deletions could nevertheless survive in haploid genomes, demonstrating that substantial amounts of DNA are dispensable for growth, at least in vitro. Application of these methods to assay genome-wide sequence essentiality could be the first step toward a minimal human genome—the core genetic elements required for the propagation of mammalian cell lines, with potential applications in cell-based therapies and biological drug manufacturing.

In addition, the technologies leveraged by Koeppel *et al*. and Pinglay *et al*. allow for the study of how structural rearrangements drive cellular and evolutionary adaptations. On-demand recombination generates hundreds of ecDNAs, which are particularly important in the context of cancer, in which they frequently drive oncogene amplification and are associated with poor patient prognosis (*10*). Investigating how ecDNAs are generated and selected could reveal mechanisms of cancer initiation and progression. Moreover, coupling high-throughput, on-demand structural variant generation with phenotypic selection should enable the isolation of cell lines with desired properties, a strategy already successfully applied to yeast with synthetic chromosomes (*11*, *12*).

The broad applicability of these methods is evident, but they do have certain limitations. Both studies observed rapid depletion of all types of variants within the cellular pool within a week, regardless of whether cells were haploid, diploid, or triploid, an effect predominantly driven by the well-documented toxicity of *Cre* expression. An orthogonal method that used Bxb1 recombinase and asymmetrical attB/P recombination sites yielded more stable rearrangements, but the proportion of cells carrying variants was low (4%). Interrogating a large number of diverse rearrangements would therefore require an enormous experimental scale. Also, the ability to causally link variants to gene expression changes remains limited because of either the need to isolate clonal populations first or the low recovery of variant identity in inherently sparse single-cell RNA-sequencing data. Improving the efficiency of these methods will depend on increasing variant formation and survival by modulating recombinase expression and DNA-damage responses and incorporating selection markers reconstituted upon recombination to select cells with variants. Looking ahead, improving the efficiency and scale of inserting sequences into the mammalian genome by means of prime editing or homology-directed repair will be central to unlocking the full potential of the technology. This will not only make high-throughput experiments more feasible but also enable more focused, high-resolution interrogation of genomic regions, which will ultimately be key to the mechanistic understanding of genome architecture. ■

REFERENCES AND NOTES

1. J. Koeppel *et al*., *Science* **387**, eado3979 (2025).
2. S. Pinglay *et al*., *Science* **387**, eado5978 (2025).
3. A. N. Brooks *et al*., *Science* **375**, 1000 (2022).
4. S. Zhou *et al*., *Natl. Sci. Rev.* **10**, nwad073 (2023).
5. J. S. Dymond *et al*., *Nature* **477**, 471 (2011).
6. P. H. Sudmant *et al*., *Nature* **526**, 75 (2015).
7. J. R. Dixon *et al*., *Nat. Genet.* **50**, 1388 (2018).
8. S. J. Hoyt *et al*., *Science* **376**, eabk3112 (2022).
9. C. Chiang *et al*., *Nat. Genet.* **49**, 692 (2017).
10. C. Bailey *et al*., *Nature* **635**, 193 (2024).
11. W. Liu *et al*., *Nat. Commun.* **9**, 1936 (2018).
12. G. F. Gowers *et al*., *Nat. Commun.* **11**, 868 (2020).

10.1126/science.adt0750

GRAPHIC: N. CARY/*SCIENCE*

BOOKS *et al.*

Humans have long made monsters out of those they fear, becoming monsters themselves in the process.

IMAGE: BILWISSEDITION LTD. & CO. KG/ALAMY STOCK PHOTO

SCIENCE AND SOCIETY

The monster in the room

A historian interrogates the mythical creatures we create to dehumanize and devalue others

By **Ed Finn**

The world is full of monsters, most of our own making. Throughout history, humans have conjured the supernatural from natural origins, turning species such as bears or wolves into something dangerous and otherworldly or making a vindictive god out of a winter storm. People are even more adept at dehumanizing their fellow *Homo sapiens*, othering minorities, outsiders, and the disadvantaged to excuse everything from petty prejudice to the most horrific acts of violence imaginable.

Despite these dark shadows, monsters are a familiar, almost intimate, part of our cultural lives—a way to engage our fears and fantasies through fairy tales, stories, and role-play. At least some of the time, our need for monsters comes not from a desire to push the world away but to draw it closer, giving us a means for domesticating our deepest worries. Historian Surekha Davies plumbs these depths in *Humans: A Monstrous History*, drawing together a broad tapestry of humanity's long tradition of naming, shaming, and blaming others by turning them into something monstrous.

This book is not really a comprehensive history, except perhaps in the classical sense of *historia*, offering stories and accounts of how societies across time have created monsters. And what stories they are: They include portraits and harrowing tales of people whose perceived physical, cognitive, or cultural differences caused them to be labeled witches, devils, animals, and worse.

The book is at its best when Davies invites readers to imagine the lives of historical monsters and to empathize with their often-wretched treatment. She writes, for example, about Petrus Gonsalvus, a 16th-century man with a genetic condition that caused excessive body hair growth. Gonsalvus was captured in the Canary Islands and brought back to Europe to live out his days as a kind of honored prisoner and living curiosity. He married and had children, who were in turn frequently poked, prodded, undressed, and examined by the cognoscenti. Davies asks what it must have felt like to live that way, in a body that was ceaselessly objectified and dehumanized.

From colonial Spain to the Third Reich, history repeatedly reminds us that the seemingly scientific construction of monsters is often more dangerous than plain superstition, because it dresses up our fears in the robes of knowledge and offers easy rationales for brutality. Pseudoscientific ideas about race, for example, remain a throughline from the ancient world to contemporary debates about the nation-state, immigration, citizenship, and belonging.

Monsters haunt not only our past but also our future. The global competition to develop new forms of artificial intelligence (AI) frequently devolves into a race to see who can dehumanize people the fastest. This occurs when algorithms abstract away the individuality and context of billions of people whose creative outputs and personal information have been fed into large language models and other machine learning platforms—usually without their informed consent. The narratives embedded in many AI products also brush aside the intrinsic value of the individual by suggesting, directly or indirectly, that the amalgamated average is superior to the messiness of specific humans. A friend recently sent me a photo of an advertisement posted at his bus station for a company that claimed that their AI "won't complain about work-life balance."

Davies spends most of the book criticizing all of the terrible things humans have done in the name of battling monsters, but there is less reflection on why we need monsters so badly. To be sure, humanity must practice empathy and a politics of care—but how do we become more thoughtful and accepting of the monsters we make and the monsters we become?

Humans: A Monstrous History
Surekha Davies
University of California Press, 2025. 336 pp.

I would propose to add a new head to the splendid many-limbed creature Davies has unleashed in this volume. To do this, we need to lean into the monster business rather than (ahem) monstrifying it. Monster literacy and a deeper understanding of why humanity clutches its greatest fears close might help us flex our imaginations and build some immunity against the demagogues and xenophobes who invoke monsters to try to rile up a mob. Think of it as a kind of species-level civics education, embarked on to help us better understand who we are and how we overlap with other people and our world. If we can truly learn to love our monsters, we may, in turn, learn to love ourselves and greet the world with hope instead of fear. ■

The reviewer is at the Center for Science and the Imagination, Arizona State University, Tempe, AZ, USA, and is co-editor of *Frankenstein: Annotated for Scientists, Engineers, and Creators of All Kinds* (MIT Press, 2017). Email: edfinn@asu.edu

10.1126/science.adu8851

Scientists have regularly revisited Asilomar, literally and figuratively, over the past 50 years.

PHOTO: LUIS CAMPOS

HISTORY OF SCIENCE

Invoking Asilomar

The historic meeting's legacy resists simple lessons

By **Luis A. Campos**

Early correspondence about an important meeting to take place in February 1975 left department secretaries and others struggling to capture the name: Selmar? Sylomar? Asimolar? A portmanteau of "refuge" and "sea" in Californian Spanish, the Asilomar conference on recombinant DNA that took place in February 1975 soon became a mythical event. Within a few years, it was already being recalled as having ignited a "firestorm" and as "a milestone in the relationships between science and society. It is a milestone, however, whose legend is difficult to decipher" (*1*).

Thoughtful and eloquent critics have described the meeting as narrow-minded, a poor model, and a politically dangerous precedent—or, even more strongly, as notorious, wrongheaded, and even an unmitigated disaster (*2*). These powerful critiques are far from new—they recapitulate criticisms first offered by scientists, then by activists and civil society groups, and later by journalists and scholars. What can we learn from the fact that, over time, the same sorts of claims have been made by radically different people, for different reasons?

Just what Asilomar meant, and what its lessons were, has always been contested. Even before the meeting, some Stanford University scientists bemoaned the "small, self-appointed groups of scientists" who pronounce "on problems of great fundamental importance and complexity without providing for an adequate basis of thought and discussion" (*3*). The Asilomar organizers likewise acknowledged that their meeting was a small, "not necessarily representative" group, but biologist David Baltimore understood himself and his colleagues as "public advocates" (*4*).

For their part, the activist group Science for the People denounced the meeting in an open letter as akin to "asking the tobacco industry to limit manufacture of cigarettes" (*5*). One group member—biologist Jonathan King—praised Asilomar in its aftermath as "an unprecedented event in public responsibility of science" (*6*) (for which the scientists "should be applauded," he told Congress) but observed that "the scientists at Asilomar were *experts* in the production of recombinant organisms; but they were *amateurs* in the assessment of hazard and in the establishment of safe procedures and regulations."

"WHATEVER THE 'PUBLIC' MAY BE"

What would a better process look like? These issues were also raised in the meeting itself by several invited legal experts. Harold Green noted that "explicit consideration is being given over and above the question of risk, and the means for minimizing that risk, to broader questions of social and moral responsibility. In this context, this conference will hopefully serve as a precedent, an example, and a model." After the meeting, Green proposed that rather than worrying about how to "involv[e] the 'public' (whatever the 'public' may be)…the real question is the extent to which, and how, the decisions of administrators should and could be made to reflect the aspirations, concerns, and values of the community rather than merely the scientific merit and potential benefits of a proposed line of research" (*7*).

Questions of science, ethics, and public interest intensified after Asilomar. Co-organizer Maxine Singer engaged in a testy exchange with a director of the Hastings Institute, arguing that "it is not certain that those who are specifically trained in matters of morality and politics are any more likely to reflect the public view than are the scientists" (*8*). Singer invoked Asilomar's legacy, writing that "if scientists are to participate responsibly in the ethical debate (and we believe that they should), they must have some appreciation of the values that the public deems relevant." This complexity in the historical record challenges the notion that there are simple, uncontested "lessons" from Asilomar.

"IS MY MEMORY FAULTY?"

At the conclusion of the long and involved process of transforming Asilomar's recommendations into National Institutes of Health guidelines, co-organizer Paul Berg declared that the final version was "a faithful translation of the spirit of Asilomar." But a year and a day after the meeting, one correspondent wrote to him, saying: "It appears that my recollection of the 'sense or spirit of Asilomar' which is so often invoked is somewhat different from yours. Is my memory faulty?" (*9*).

There are surprising points of agreement as well. In subsequent decades, the meeting has come to be widely understood as though it were fundamentally only about technical issues—despite "ethics" and "public policy" appearing on the conference agenda, the organizers at the start of the meeting having identified "legal, and moral and ethical aspects" as a major fourth area of focus, and the ever-present language of moral responsibility pervading

discussions before, during, and after Asilomar.

Ironically, the renarration of the meeting as solely technical became a mainstay both of many scientists' later recollections and of critics, who maintained that the gathering was elitist, exclusionary, and technocratic. For many scientists, this retreat from the realm of the ethical into the refuge of the technical was an increasingly favored response to media coverage and political attention generated by others claiming the mantle of public advocacy. And so, despite serving distinctly different interests, a powerful myth about Asilomar was enacted—jointly by scientists and critics—that severed scientific discussions from larger concerns and motivations.

Understanding the effects of this dynamic seems crucial to understanding the stories we tell about Asilomar. Sometimes it matters less what is said, it seems, than who said it and when.

THERE COULD NEVER BE ANOTHER

Other shifts emerged. By 2006 (and again in 2013), Baltimore now felt that the Asilomar participants "were not pretending to speak for the public" and that another Asilomar would be "impossible" or "counterproductive" if it were focused on ethical and moral issues (*10*). In such a setting, scientists would "have something to offer, but a much wider public would have to be involved." He felt, by contrast, that a meeting more focused on "scientific" aspects, such as those related to biowarfare, would be feasible.

Paul Berg, for his part, reflected that the "oft-voiced criticism" of Asilomar as overlooking ethical and legal dimensions was "due neither to oversight nor to the unawareness of the issues" but because "it was premature to consider applications that were so speculative and certainly not imminent." He noted, decades after the meeting, moreover, that commercial interests would now be an obstacle to any attempt to have "another Asilomar" (*11*). These doubts have not stopped scientists from returning time and again, physically and spiritually, to Asilomar—where it is invoked in fields ranging from geoengineering and nanotechnology to artificial intelligence and cultivated meat and seafood.

This legacy of history, memory, and invocation suggests that the question of representing larger public interests and concerns continues to evolve. Political philosophers have long noted that a fundamental condition of democracy and other kinds of collective solidarities is that no one can represent "the public" forever. Or as Roger Dworkin—one of the legal experts present at Asilomar—later observed, "criticism of the Asilomar organizers for not adequately involving the 'general public' may be meant as a moral criticism; but properly understood, it is simply a criticism of six scientists for lacking the same transcendent social wisdom that all humanity has lacked throughout its history" (*12*).

THE SPIRIT OF ASILOMAR

Rather than looking to emulate a singular "Asilomar process" or counterposing favored myths and origin stories, a more fruitful approach might be to invoke its "spirit." In a sense, even critiques of Asilomar echo the same sorts of ethical motivations and sensed obligations to larger publics that were the very basis of the call to meet at Asilomar—and of the meeting itself

The "spirit of Asilomar" can therefore be seen as a moral and collective call to action that has resonated down the decades. Indeed, a little more than a year after the meeting, this spirit was invoked by others grappling with subsequent developments: "I hope you will hold another meeting to deal with moral and social considerations of the work. This issue should be dealt with openly rather than having it come back to haunt us," wrote one Harvard University biologist to another in April 1976 (*13*).

And yet, it is true—there could never be another Asilomar. Powerful critiques have changed how Asilomar might be invoked nowadays. A major summit organized today on the future of biotechnology could not have only a handful of women in attendance, for example, or proceed without the participation of younger researchers. Such discussions also require the inclusion of a much broader group of stakeholders and would also include humanists, social scientists, journalists, legal and policy experts, and artists, among larger publics. Broader societal concerns and critiques would also have to be recognized, with differing viewpoints invited to engage in constructive discussion. It would also have to be openly acknowledged that the very act of assembling any such finite group is inherently subject to criticism. And one could certainly not have such a meeting dominated by primarily American concerns or without committing substantial funding to enable participation from around the world.

The organizers of February's "The Spirit of Asilomar and the Future of Biotechnology" summit—of which I am one—are attempting to bring these insights to bear on our current moment (*14*). Our aim is to take advantage of the original meeting's 50th anniversary not only to discuss areas left unexplored at the original conference and new ones that seem well within its "spirit"—bioweapons and pathogens research, new uses of artificial intelligence, frontiers of synthetic cells, and deploying engineered organisms into environments and bodies—but also to highlight the ever-present questions of public benefit, social relations, and human (and more-than-human) flourishing.

This latest invocation of Asilomar is not a cover for predetermined interests, corrosive (or justified) skepticism, or unbridled hope for a better world but rather an experiment in convening a discussion about matters of concern among more-diverse constituencies. History shows that the spirit of Asilomar is surprisingly capacious and can be invoked by each new generation attempting to grapple with familiar questions about unfamiliar technologies and the worlds they hope for.

Contestations over the meaning of Asilomar are in some sense what Asilomar has always been about. But if even opposing voices in the past have oddly found themselves coming to share meaningful myths, maybe we can endeavor to gather anew to find points of common cause and shared truths too. If there is a lesson worth learning from this historic meeting, that may be it. ■

The author is a co-organizer of "The Spirit of Asilomar and the Future of Biotechnology" summit. He is the 2025 Cain Conference Fellow of the Science History Institute and Baker College Chair for the History of Science, Technology, and Innovation in the Department of History, Rice University, Houston, TX, USA. Email: lc@rice.edu

REFERENCES AND NOTES

1. J. Rodgers, *Mosaic* **12**, 19 (1981).
2. See, for example, C. Weiner, *Perspect. Biol. Med.* **44**, 208 (2001); W. F. May, *Newsl. Sci. Technol. Human Values* **23**, 34 (1978); S. Wright, *Molecular Politics* (Univ. of Chicago Press, 1994), pp. 157–159; J. B. Hurlbut, in *Dreamscapes of Modernity*, S. Jasanoff, S.-H. Kim, Eds. (Univ. of Chicago Press, 2015), chap. 6; S. Jasanoff, K. Saha, J. B. Hurlbut, *Issues Sci. Tecnol.* **32** (2015); and S. Parthasarathy, *Ethics Biol. Eng. Med.* **6**, 305 (2015).
3. David Korn to Roy Curtiss, 3 September 1974, Box 39, Folder 609, MC100, MIT Distinctive Collections.
4. D. Baltimore to Sen. Kennedy, 1 December 1975, Box 2, Folder 1a, Paul Berg Papers, Stanford University.
5. J. Beckwith *et al.*, "Open letter to the Asilomar conference on hazards of recombinant DNA" in J. D. Watson, J. Tooze, *The DNA Story* (W. H. Freeman and Co., 1981), Doc. 2.6, p. 49.
6. J. King, *New Sci.* **16**, 634 (1977).
7. H. Green, "A Public Policy Perspective," remarks at Asilomar. H. Green to P. Berg, 2 September 1975, Box 14, "Kennedy Hearings, Cambridge Controversy" binder, Paul Berg Papers, Stanford University.
8. Maxine Singer to Willard Gaylin, 30 April 1975, Box 32, Folder 3, Maxine Singer Papers, Library of Congress. D. M. Singer, M. F. Singer, *Am. Biol. Teach.* **37**, 528 (1975).
9. N. Wade, *Science* **190**, 1175 (1975). Donald Brown to Paul Berg, 27 February 1976, Box 40, Folder 619, MC100, MIT Distinctive Collections.
10. D. Baltimore, keynote address, Synthetic Biology 2.0 Conference, Univ. of California, Berkeley, 20 May 2006.
11. Chemical Heritage Foundation, "The Emergence of Biotechnology: DNA to Genentech," Symposium on the Emergence of Biotechnology, June 1997, Philadelphia, PA. P. Berg, *Nature* **455**, 290 (2008).
12. R. B. Dworkin, *South. Calif. Law. Rev.* **51**, 1471 (1978).
13. Richard Goldstein to Daniel Branton, 15 April 1976, Folder 20, MC100, MIT Distinctive Collections.
14. The Spirit of Asilomar and the Future of Biotechnology, Pacific Grove, CA, 23 to 26 February 2025; http://spiritofasilomar.org.

10.1126/science.adv7574

Worldwide, important cultural heritage sites, such as this historic lighthouse in the Outer Banks, are put at risk by rising sea levels.

PHOTO: JOHN GREIM VIA GETTY IMAGES

LETTERS

Edited by **Jennifer Sills**

Rising seas endanger maritime heritage

In coastal regions, anthropogenic sea level rise, extreme weather, and coastal erosion have led to mass migrations (*1*), leaving cultural heritage sites behind. Coastal heritage resources preserve humanity's long history of maritime dispersals, adaptations, cultural diversity, and resilience. Communities, institutions, and governments worldwide must work to monitor and protect these valuable sources of information.

Coastal heritage resources are already at risk (*2*, *3*) under conservative Intergovernmental Panel on Climate Change (IPCC) predictions of sea level rise by 2100, which range from 0.29 to 1.1 m (*4*). Global sea level rise averaged 0.48 cm per year over the past decade and reached 0.81 cm in 2023 (*5*), more than quadrupling the 1993 rate (*5*). Other projections range from 2.3 to more than 4 m (*1*, *6*). A collapse of the Greenland and Antarctic ice sheets could lead to even greater sea level rise in the decades and centuries to come.

Endangered coastal heritage sites range from historic lighthouses to iconic cultural centers such as Hawai'i's Pu'uhonua o Hōnaunau National Historic Park (*7*, *8*). Marine erosion has already damaged invaluable coastal archaeological sites such as South Africa's Middle Stone Age shell middens, Gorham's Cave in Gibraltar, and, in the United States, Daisy Cave on California's Channel Islands and massive Native American shellmound complexes in Florida and Georgia (*7*).

Heritage resources provide ancestral cultural connections to Indigenous and descendant communities and contain invaluable scientific information. Cultural heritage sites provide insight into human survival and sustainability in dynamic island and coastal settings, including earlier periods of rapid sea level rise, as well as the nature of ancient ecosystems and the organisms they contained (*9*). These data can be used to help restore modern ecosystems and conserve endangered species (*9*).

Global stakeholders must do more to reduce greenhouse gas emissions and atmospheric carbon dioxide levels and work with descendant communities to help protect priceless coastal heritage. Effective programs such as Florida's Heritage Monitoring Scouts and Scotland's Coastal Archaeology and the Problem of Erosion (SCAPE) Trust partner academics, agencies, and volunteers to evaluate and mitigate the effects of sea level rise and coastal erosion on heritage resources (*10*, *11*). Along North America's Pacific Coast, archaeologists have worked extensively with descendant communities, government agencies, and nongovernmental organizations to record, monitor, and carbon-14 date endangered archaeological sites (*7*). Expanding these efforts and initiating similar collaborations in vulnerable regions can help save coastal and maritime heritage resources.

Jon M. Erlandson[1]*, Scott M. Fitzpatrick[1,2], Kristina M. Gill[1], Patrick V. Kirch[3], John T. Ruiz[4], Victor D. Thompson[5], Jason Younker[2,6]

[1]Museum of Natural and Cultural History, University of Oregon, Eugene, OR, USA. [2]Department of Anthropology, University of Oregon, Eugene, OR, USA. [3]Department of Anthropology, University of Hawai'i at Manoa, Honolulu, HI, USA. [4]Southern Owl Clan, Coastal Band of the Chumash Nation, Santa Barbara, CA, USA. [5]Department of Anthropology, Georgia Museum of Natural History, University of Georgia, Athens, GA, USA. [6]Coquille Indian Tribe, North Bend, OR, USA.
*Corresponding author. Email: jerland@uoregon.edu

REFERENCES AND NOTES

1. United Nations (UN), "Surging seas in a warming world: The latest science on present-day impacts and future projections of sea-level rise" (UN Technical Brief, UN, 2024).
2. M. J. Rowland, *Aust. Archaeol.* **34**, 29 (1992).
3. L. A. Reeder-Myers, *J. Isl. Coast. Archaeol.* **10**, 436 (2015).
4. IPCC, "Climate change 2023: Synthesis report, Contribution of Working Groups I, II and III to the Sixth Assessment Report of the Intergovernmental Panel on Climate Change," Core Writing Team, H. Lee, J. Romero, Eds. (IPCC, 2023).
5. G. C. Johnson, R. L. Lumpkin, *Bull. Am. Meteorol. Soc.* **105**, S156 (2024).
6. J. T. Overpeck *et al.*, *Science* **311**, 1747 (2006).
7. J. M. Erlandson, *J. Coast Conserv.* **16**, 137 (2012).
8. A. Johnson, L. Marrack, S. Dolan, *Hawai'i J. Isl. Coast. Archaeol.* **10**, 232 (2015).
9. S. M. Fitzpatrick, J. M. Erlandson, K. M. Gill, Eds., *Sustainability in Ancient Island Societies: An Archaeology of Human Resilience* (Univ. Press Florida, 2024).
10. S. E. Miller, E. J. Murray, *Conserv. Manag. Archaeol. Sites* **20**, 234 (2018).
11. T. Dawson, J. Hambly, A. Kelley, W. Lees, S. Miller, *Proc. Natl. Acad. Sci. U.S.A.* **117**, 8280 (2020).

10.1126/science.adu0717

International commitment to safe nuclear reactors

In their Policy Forum "The weapons potential of high-assay low-enriched uranium" (7 June 2024, p. 1071), R. S. Kemp *et al.* describe the potential misuse of high-assay low-enriched uranium (HALEU). The American Nuclear Society (ANS)—a professional nuclear science and technology society representing more than 10,000 members worldwide—acknowledges the importance of continually evaluating the proliferation risks associated with nuclear materials. However, we disagree with Kemp *et al.*'s implied recommendation that the United States decide international nuclear security policy by unilaterally redefining HALEU enriched above 10% as "weapons usable." ANS's position on HALEU aligns with the stance of the United Nations' International Atomic Energy Agency (IAEA): HALEU enriched up to 20% is not considered "direct-use" material (*1*).

Kemp *et al.*'s implication that the United States should unilaterally decide international nuclear security policy ignores the comprehensive assessments and effectiveness of existing international safeguards as well as country-specific controls on possession and export of special nuclear material, which have been developed in cooperation with international partners. For more than 60 years, research reactors all over the world have been fueled by HALEU with no evidence of attempted diversion or misuse. There is no evidence indicating that the safeguards programs implemented by the IAEA, which include rigorous inspections, material accounting, and physical protection, are anything short of effective and transparent in ensuring that HALEU is used solely for peaceful purposes (*2*).

Kemp *et al.*'s definition of weapons-usable material, based solely on having a finite critical mass, does not fully address the complex engineering and materials handling challenges involved in weaponization, particularly in the case of advanced reactor fuels. Definitions and restrictions associated with uranium enrichment were established by the international community through the IAEA, which carefully considered the real risks associated with uranium at all levels of enrichment (*3*).

A unilateral approach to establishing a domestic policy contrary to international consensus would impair the ability of the United States and its allies to meet their collective nuclear nonproliferation objectives. It is vitally important that any reevaluation of what constitutes weapons-usable or direct-use material be developed with international cooperation and in consultation with the IAEA.

Instead of focusing on inflammatory descriptions, as *Science* did in its selection of the pull quote characterizing countries with HALEU of being "only days away from a bomb" and its subhead accusing proponents of new reactors of "disregard[ing] decades-old concerns about nuclear proliferation," we encourage policy-makers to remain optimistic and committed to deploying new advanced reactors, focusing on practical rather than theoretical risks. Effective policies can manage these risks while supporting our transition to a cleaner, sustainable future.

Lisa Marshall
President, American Nuclear Society, Washington, DC, USA. Email: lisa.marshall@ans.org

REFERENCES AND NOTES

1. ANS, "Safeguards and security for advanced reactors using HALEU" (Position Statement 84, ANS, 2023).
2. US Government Accountability Office (GAO), "Nuclear nonproliferation: Efforts are underway to address factors affecting the International Atomic Energy Agency's safeguards program" (GAO-24-106296, GAO, 2024).
3. National Academies of Sciences, Engineering, and Medicine, in *Merits and Viability of Different Nuclear Fuel Cycles and Technology Options and the Waste Aspects of Advanced Nuclear Reactors* (National Academies Press, 2023), chap. 6.

10.1126/science.adt3020

Response

In her Letter on behalf of the American Nuclear Society (ANS), Marshall suggests that the United States should not unilaterally determine security policy with regard to high-assay low-enriched uranium (HALEU). However, it is established by international treaty that nuclear security is the sovereign responsibility of individual states (*1*). It is also incumbent on the United States to help inform the development of international standards by carrying out early studies. This has historically been the case, as, for example, when the United States initially established standards to restrict the dissemination of HALEU to quantities less than the amount sufficient to make a nuclear weapon (*2*).

Marshall also errs in arguing that the international safeguards system maintained by the International Atomic Energy Agency (IAEA) should be assumed sufficient for the widespread use of HALEU. The existing standards were developed in an era when HALEU was used only in small quantities for research reactors. It is important to reevaluate these standards now that power reactors propose to use weapon-relevant quantities and, if necessary, adjust the standards to accommodate this change. The safeguards system has been updated before to address emerging threats and performance deficiencies, such as when the IAEA failed to detect the covert Iraqi and Iranian nuclear weapons programs (*3*, *4*).

In contrast to Marshall's assertion, the safeguards programs implemented by the IAEA do not include "physical protection." The IAEA has no authority over physical protection for state-controlled nuclear materials (*1*).

Our prediction of weapon usability is not based "…solely on having a finite critical mass…" as Marshall claims. Rather, we incorporated results from previous technical studies (*5*); our own analysis using open-source data, codes, and relationships for weapon hydrodynamics and yields; and testimony from a US nuclear weapons designer (*6*). All of this research and discussion indicate that HALEU has direct and practicable explosive potential. Marshall does not explicitly challenge this central point but asserts that we did not take into account the challenges involved in weaponizing HALEU. Our Policy Forum points out that because the technical barriers to weapons design have gone down over time, a new, formal assessment of those challenges is needed.

We understand that the ANS has lobbied for HALEU programs [e.g., see (*7*)], but we hope that they choose to put the security of the nation first. If the ANS is confident in the sufficiency of present standards, then we suggest that they produce the technical basis for their view. Otherwise, the only defensible position is to support our call for an expert study to find the answer.

R. Scott Kemp[1]*, Edwin S. Lyman[2], Mark R. Deinert[3], Richard L. Garwin[4], Frank N. von Hippel[5]
[1]Department of Nuclear Science and Engineering, Massachusetts Institute of Technology, Cambridge, MA, USA. [2]Union of Concerned Scientists, Washington, DC, USA. [3]Nuclear Science and Engineering Program, Department of Mechanical Engineering, Colorado School of Mines, Golden, CO, USA. [4]IBM Thomas J. Watson Research Center, Yorktown Heights, NY, USA. [5]Program on Science and Global Security, Princeton University, Princeton, NJ, USA.
*Corresponding author. Email: rsk@mit.edu

REFERENCES AND NOTES

1. IAEA, "Amendment to the Convention on the Physical Protection of Nuclear Materials" (INFCIRC/274/Rev.1/Mod. 1, IAEA, 2021), para. 5.2.
2. National Security Council, in *Foreign Relations of the United States, 1952–1954, Volume II, Part 2, National Security Affairs*, W. Z. Slany *et al.*, Eds. (1984), Doc. 238.
3. IAEA, Additional protocol; https://www.iaea.org/topics/additional-protocol.
4. Garry B. Dillion, *IAEA Bull.* **44-2**, 13 (2002).
5. L. R. Hafstad, "Research reactors for foreign application, Report to the general manager by the director of reactor development" (Atomic Energy Commission, 1954).
6. "Conversion of research and test reactors to low-enriched uranium (LEU) fuel," Hearing before the US House of Representatives, 98th Congress of the United States, 25 September 1984, p. 77.
7. ANS, Letter to the Office of Nuclear Energy, US Department of Energy, 14 February 2022.

10.1126/science.adv1245

RESEARCH

IN *SCIENCE* JOURNALS

Edited by **Michael Funk**

Polar bears, such as this individual in Hudson Bay, Canada, are starving due to loss of sea ice, which is their primary hunting habitat.

PHOTO: TOM MANGELSEN/NPL/MINDEN PICTURES

ENERGETICS

Understanding polar bear declines

It has been well documented that polar bear populations have declined over the past 50 years as the extent of sea ice has decreased. Using data collected from polar bears in the western Hudson Bay Area over nearly all of that time, Archer *et al.* built an individual-based bioenergetic model that hindcasts population dynamics and successfully predicts patterns of abundance and reproduction. Energetic patterns at the individual level successfully predicted larger-scale population dynamics. A single driver, energy limitation, emerged as being responsible for the population decline, confirming that polar bears face food shortages due to the loss of ice. —Sacha Vignieri *Science* p. 516, 10.1126/science.adp3752

ANCIENT DNA

Untangling the woolly origins of sheep

Sheep have provided key resources for human society through their domestication, most iconically wool for making textiles; however, the origins of sheep are still not entirely clear. Daly *et al*. sequenced 118 ancient genomes from Eurasian domestic and wild sheep samples spanning the past 12,000 years. They found that a Neolithic Turkish population likely represents a basal lineage to modern domesticated sheep, but other wild varieties such as a steppe-derived group contributed a large degree of diversity to modern populations. This study explores some of the complex dynamics that played a role in sheep domestication and reveals some potential parallels with human migrations. —Corinne Simonti

Science p. 492, 10.1126/ science.adn2094

MICROBIOLOGY

A familiar immune system in bacteria

Caspases are proteases that are crucial in human innate immunity and cell death, with emerging evidence of similar roles in bacteria. Rousset *et al*. investigated a bacterial immune system involving a TIR-domain protein and a caspase-like protease that defends against phage infection. They discovered that during phage invasion, the TIR protein produces a previously unknown signaling molecule derived from nicotinamide adenine dinucleotide that activates a bacterial caspase-like protease. This protease then indiscriminately degrades cellular proteins, including the elongation factor Tu, effectively halting phage replication. The defense system, called type IV Thoeris, was found to be abundant across bacterial and archaeal species and provides population-level protection against viral invasion. —Di Jiang

Science p. 510, 10.1126/science.adu2262

INFLUENZA

Boost for broadly neutralizing antibodies

Antibodies have long been used in influenza therapy, a practice accelerated by the development of broadly neutralizing monoclonal antibodies (bnAbs). Monoclonal antibody therapy has been used successfully against lower respiratory infections with respiratory syncytial virus. Kanekiyo *et al*. tested prophylaxis and treatment regimens against the highly pathogenic avian H5N1 influenza in nonhuman primate models. The authors infused a single dose of 30 milligram per kilogram of a bnAb that recognizes the conserved stem of the

viral hemagglutinin molecule. Animals were infected 3 days later, and serious respiratory disease was averted, a protective effect that the authors estimate could last for up to 8 weeks. —Caroline Ash

Science p. 534, 10.1126/science.ado6481

IMMUNOTHERAPY

Tracking T cells after transplantation

Acute graft-versus-host disease (aGVHD) driven by T cells after allogeneic hematopoietic stem cell transplantation (HCT) can occur in several different organs and tissues. Omdahl *et al*. sought to understand how post-HCT T cell responses are shaped in two commonly affected organs, the lungs and the liver, using a cohort of nonhuman primates that underwent allogeneic HCT. T cells from the different tissues acquired distinct transcriptional programs and phenotypes. This was true even for T cells carrying the same T cell receptor, hinting that the environment is the driver of the divergent phenotypes. These data suggest that T cell–targeting treatments for aGVHD could be tailored based on the affected organs. —Courtney Malo

Sci. Transl. Med. (2025) 10.1126/scitranslmed.ads1298

PHASE TRANSITIONS

Tracking rapid phase interconversions

The η-to-θ phase transition of bulk alumina is unidirectional and retains crystal orientation; however, when occurring in nanoparticles, it is a rapid stochastic process that loses orientation memory. Sakakibara *et al*. used transmission electron microscopy to observe the stochastic appearance of η and θ structures of alumina nanoparticles on the surface of bulk alumina before the formation of a stable crystalline phase. Millisecond time resolution allowed measurement of the interconversion rate at different temperatures, which revealed that the barrier to interconversion was almost entirely entropic. —Phil Szuromi

Science p. 522, 10.1126/science.adr8891

MOLECULAR BIOLOGY

Histone modification on the fly

Eukaryotic genomes are organized into chromatin, in which a strand of DNA is wrapped compactly around histone proteins to form nucleosomes. Nucleosomes can be chemically modified by epigenetic marks to regulate gene expression. Trimethylation of histone H3 at lysine 36 (H3K36me3) is critical for active transcription, splicing, and genomic stability. Using cryo–electron microscopy, Markert *et al*. determined the mechanism by which the enzyme SETD2 deposits H3K36me3 by recognizing and binding to nucleosomes partially unwrapped by the transcription machinery. This finding provides a structural basis for how some histone modifications are established co-transcriptionally. —Di Jiang

Science p. 528, 10.1126/science.adn6319

CANCER IMMUNOLOGY

Immunotherapy for relapsed leukemia

Hematopoietic stem cell transplantation represents the only potential cure for patients with aggressive myeloid leukemia. Donor lymphocyte infusion (DLI) is used to treat patients experiencing leukemia relapse after this procedure, but why some patients respond better than others to DLI immunotherapy remains unclear. Using single-cell and spatial transcriptomics, Maurer *et al.* analyzed longitudinal bone marrow samples from patients with relapsed acute myeloid leukemia. Response to DLI was associated with the expansion of a particular subset of cytotoxic T cells, which were mostly derived from the DLI product and formed complex cellular networks with other bone marrow immune cells. —Claire Olingy

Sci. Immunol. (2025) 10.1126/sciimmunol.adr0782

IN OTHER JOURNALS

Edited by **Corinne Simonti** *and* **Jesse Smith**

Hurricane Isaac arriving on Grande Riviere, Trinidad

HURRICANES

Temperature first

What is the most important ingredient in tropical cyclogenesis? Bercos-Hickey and Patricola performed regional model simulations to determine which of the two well-known causal agents, sea surface temperature (SST) or the strength of the African easterly wave (AEW) from which a hurricane arises, is the dominant factor. The authors found that SST plays a larger role than AEW strength in driving the frequency of tropical cyclones in the North Atlantic. Their conclusion reinforces the well-understood idea that SST is the primary factor in the development of tropical cyclones. —Jesse Smith

Geophys. Res. Lett. (2025) 10.1029/2024GL112002

SIGNAL TRANSDUCTION

Information theory and oncogenic signaling

Although signaling proteins are often thought of as switches, they likely have more complex properties that maximize information transfer. Madsen *et al.* explored how oncogenic mutations affect signaling by phosphoinositide 3-kinase. Improved methods for single-cell quantitative measurements of signaling at high temporal resolution showed effects beyond simple increases in signaling. They confirmed that cells respond to pathway activation in a probabilistic rather than a deterministic manner. Furthermore, the fidelity with

Fossils show that insect damage to *Eucalyptus* plants has remained the same for millions of years.

PALEOECOLOGY

Consistent interactions across epochs

Eucalyptus trees dominate wet forests in Australia and provide food for up to 20,000 species of insects. Insect herbivores, including those of *Eucalyptus*, employ myriad feeding strategies, including leaf mining, galling, and piercing and sucking. Giraldo *et al*. investigated whether feeding types and insect species have been consistent over large spatial and temporal spans by comparing signs of herbivory from modern Australasian *Eucalyptus* herbarium samples against those found in the oldest known *Eucalyptus* fossils from Argentinian Patagonia. All 28 of the leaf damage types found in the fossils were also present in herbarium samples, showing consistent plant-insect interactions across 52 million years. —Bianca Lopez

New Phytol. (2024) 10.1111/nph.20316

GENE THERAPY

A clinical trial improves vision

Leber congenital amaurosis 1 (LCA1) is a rare congenital eye disease caused by mutations in a gene called *GUCY2D* (*guanylate cyclase 2D*). LCA1 appears within the first few months of birth and results in blindness in affected individuals. Yang *et al.* conducted a phase 1/2 clinical trial to test the safety and efficacy of a gene therapy approach for 15 patients with LCA1. Different doses of gene therapy were tested in patients, with individuals receiving either low, middle, or high levels of ATSN-101. Patients receiving the highest dose noted improvements usually within 1 month of treatment, and the progress was sustained during the 12 months of the study. —Priscilla N. Kelly

Lancet (2024)
10.1016/S0140-6736(24)01447-8

CELL ADHESION

Sponge proteins for self-recognition

The cells of multicellular organisms require molecular strategies to recognize and stick to other self cells during development and regeneration. Ruperti *et al.* used proteomics and in silico protein structure prediction to explore the properties of an extracellular glycoprotein complex that mediates this self-recognition process in sponges. They found that many of these proteins adopt conserved folds known to mediate cell-cell interactions in other animals, consistent with a deep evolutionary origin of the protein domains involved in these processes. —Michael A. Funk

Proc. Natl. Acad. Sci. U.S.A. (2024)
10.1073/pnas.2409125121

which cells interpreted signals from multiple growth factors was disrupted. Better understanding of such signaling dynamics may allow more effective pharmacological interventions that help to restore information transfer. —L. Bryan Ray

Mol. Syst. Biol. (2024)
10.1038/s44320-024-00078-x

SEASONALITY

The microbial year

In natural ecosystems, microorganisms will display seasonality, and, because of rapid generational turnover among many species, seasonality can be accompanied by significant evolution. Rohwer *et al.* and Zhou *et al.* examined real-time microbial ecology and evolution in a 20-year time series of freshwater samples from Lake Mendota in Wisconsin. Phenological bacterial abundance patterns showed a consistent seasonal pattern of changing strain composition reflecting ecological processes. Changes in strain composition, especially among Nanopeligicale bacteria and Caudoviricetes viruses, could also signal species invasions and the ecological impact of climate change, which may have profound effects on freshwater food webs. —Caroline Ash

Nat. Microbiol. (2025)
10.1038/s41564-024-01888-3;
10.1038/s41564-024-01876-7

POLITICAL SCIENCE

Military service reduces prejudice

Random assignment to US military service under the Vietnam Draft Lotteries led white men to express more positive attitudes toward Black people. Green and Hyman-Metzger drew upon General Social Survey data from 1978 to 2021 that were augmented to reflect draft status. Being drafted into service, and thus into prolonged, cooperative, interracial contact, led white men years later to express more support for policies intended to benefit Black people compared with men who were in the lottery but did not ultimately serve. Being drafted did not appear to affect broader political identities and preferences. —Brad Wible

Am. Polit. Sci. Rev. (2024)
10.1017/S0003055424001266

PHOTO: L. GIRALDO *ET AL.*, NEW PHYTOLOGIST (2024)

RESEARCH ARTICLE SUMMARY

SYNTHETIC BIOLOGY

Randomizing the human genome by engineering recombination between repeat elements

Jonas Koeppel†, Raphael Ferreira†, Thomas Vanderstichele, Lisa Maria Riedmayr, Elin Madli Peets, Gareth Girling, Juliane Weller, Pierre Murat, Fabio Giuseppe Liberante, Tom Ellis, George McDonald Church*, Leopold Parts*

INTRODUCTION: Only about 1% of the human genome contains protein-coding sequences. Studying the dispensability of the vast remaining noncoding DNA for expressing genes and cellular survival remains challenging. Genome engineering techniques can induce deletions, inversions, and translocations to offer insights into genome organization. However, these methods have largely been confined to individual sites rather than applied to the entire human genome. Natural genomic rearrangements, such as those observed in cancer, illustrate potential configurations and adaptability after surviving selection, but they only permit a limited view into the impact of large-scale variation on noncoding sequences and miss the variants that are too disruptive for cell survival.

RATIONALE: An innovative method developed in yeast with synthetic genomes endowed each gene with a DNA handle for recombining with every other gene to generate sequence diversity. However, genome synthesis is currently impractical for the larger human genome. We used the recently developed prime editing technology to insert recombinase sites into the human genome at scale, targeting repetitive DNA sequences. By creating cell lines with thousands of such insertions and subsequently inducing rearrangements by using a recombinase, we could randomize the human genome. In contrast to naturally occurring structural variants that have already been shaped by selection, we could observe and compare the initially generated variants to the surviving ones to map the acting selection pressures and to explore the resulting gene expression changes. This innovative strategy allows genome manipulation on an unprecedented scale and advances our understanding of genome expression and integrity.

RESULTS: We leveraged prime editing of the high-copy-number, long interspersed nuclear element-1 (LINE-1) retrotransposon to engineer incorporation of thousands of Cre-recombinase sites into the genomes of two human cell lines. We demonstrated the feasibility of large-scale prime editing and explored how chromatin, target mismatch, and replication-timing influence the making of successful edits. These engineered cell lines served as a starting point to induce thousands of distinct recombinations upon treatment with recombinase. The variants we generated in a single experiment covered the human genome threefold; affected all chromosomes; and encompassed deletions, inversions, extrachromosomal DNAs, fold backs, and translocations. On average, every cell in the resulting pool carried more than 130 structural variants, many likely leading to inviable outcomes. The majority of cells with rearrangements disappeared from the population over 2 weeks. Yet we found that several megabase-scale deletions affecting tens of genes were viable in haploid cells for growth in culture. More broadly, we defined the characteristics of tolerated structural variation by contrasting features of generated and surviving variants and found that the latter avoided essential genes and mutation-constrained DNA. Last, we characterized clones with several large rearrangements by means of paired whole-genome and RNA-sequencing and observed that variants strongly affected gene expression when they modified copy number but did not influence the expression of nearby genes. Similarly, reshuffling the relative location of genes through inversions or translocations did not influence their expression in our clones.

CONCLUSION: Randomizing the genome by scrambling can simultaneously affect numerous genes and large noncoding regions, exploring a broader mutational space than use of single-nucleotide variants. The randomized genomes can produce new cell lines with evolved traits or optimized cellular properties and offer insights into genotype-phenotype relationships. Such approaches have already been successful in yeast and can aid in understanding drug resistance and improving biomanufacturing in mammalian cells. The random large deletions also allow genome-wide sequence essentiality assays, creating essentiality maps that help interpret pathogenic variants and understand genome structure and function, and could lay the groundwork for the engineering and synthesis of minimal mammalian genomes. ■

The list of author affiliations is available in the full article online.
*Corresponding author. Email: leopold.parts@sanger.ac.uk (L.P.); gchurch@genetics.med.harvard.edu (G.M.C.)
†These authors contributed equally to this work.
Cite this article as J. Koeppel *et al.*, *Science* **387**, eado3979 (2025). DOI: 10.1126/science.ado3979

READ THE FULL ARTICLE AT
https://doi.org/10.1126/science.ado3979

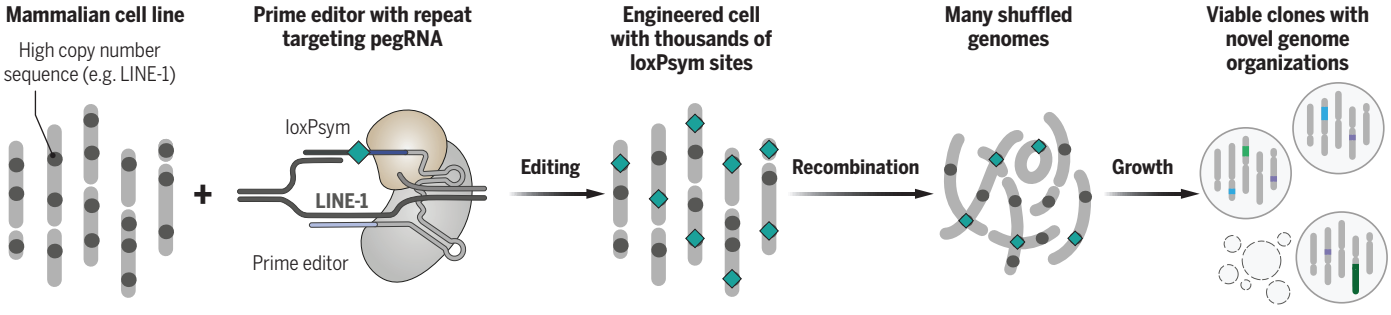

Randomizing the human genome. Prime editing can insert recombination handles into repetitive elements in human cells, which can subsequently be induced to rearrange, generating many random genomes. The surviving cells give a view into viable organizations of the human genome and the role of noncoding DNA in maintaining cell integrity and fitness. pegRNA, prime editing guide RNA; loxPsym, symmetrical loxP site.

RESEARCH ARTICLE SUMMARY

SYNTHETIC BIOLOGY

Multiplex generation and single-cell analysis of structural variants in mammalian genomes

Sudarshan Pinglay*, Jean-Benoît Lalanne, Riza M. Daza, Sanjay Kottapalli, Faaiz Quaisar, Jonas Koeppel, Riddhiman K. Garge, Xiaoyi Li, David S. Lee, Jay Shendure*

INTRODUCTION: The structural variants (SVs) present in mammalian genomes include deletions, insertions, inversions, duplications, translocations, extrachromosomal DNA circles (ecDNAs), and complex rearrangements. In an individual human genome, SVs collectively affect more nucleotides than any other class of genetic variation and have been associated with myriad rare and common diseases as well as normal phenotypic variation. However, it has been very challenging to study the functional consequences of SVs at scale, largely because methods to generate, map, and characterize SVs in model systems (e.g., mammalian cell lines) are grossly underdeveloped.

RATIONALE: To address this challenge, we developed Genome-Shuffle-seq, a method designed for the multiplex generation, mapping, and characterization of several major SV classes (deletions, inversions, translocations, and ecDNAs) throughout a mammalian genome. Genome-Shuffle-seq leverages barcoded, genomically integrated "shuffle cassettes" whose design facilitates: (i) bp resolution, genome-wide mapping of the coordinates of shuffle cassette integrations, through T7 in vitro transcription; (ii) site-specific recombination of shuffle cassettes with one another, mediated by recombinases such as Cre or Bxb1; (iii) conversion of barcodes from parental to novel pairings upon recombination, with each novel pair reflecting the breakpoints and class of event that generated it; and (iv) a co-assay of mRNAs and barcode pairings by coupling of T7 in situ transcription and single-cell RNA-seq. These design attributes are intended not only to generate a diversity of SVs in a single experiment, but also to facilitate their efficient and cost-effective mapping and quantification, i.e., forgoing the need for cell line cloning or whole-genome sequencing.

RESULTS: In this proof of concept, we applied Genome-Shuffle-seq to mouse embryonic stem cells and human cancer cells, generating and mapping hundreds to thousands of SVs per experiment. We find that cells in which SVs are generated through Cre-mediated recombination of symmetric loxP sites are rapidly depleted, potentially due to toxicity of Cre and/or of the SVs themselves. By contrast, cells in which SVs are generated by Bxb1-mediated recombination at asymmetric attB/P sites are stable to propagation. This stability enabled us to investigate selection pressures acting on different classes of Bxb1-induced SVs, as well as to begin characterizing their functional consequences. First, we find that cells bearing large deletions, but not inversions, are preferentially lost from a proliferating cellular population and that this is partly attributable to intolerance for centromere loss. Second, we observe that although balanced translocations are tolerated in vitro, unbalanced translocations, particularly those that are acentric, are rapidly depleted. Finally, by co-assaying the transcriptome and shuffle cassette barcode pairings in a bottlenecked population of genome-shuffled cells, we demonstrate that we can measure the consequences of specific, induced SVs on gene expression.

CONCLUSION: Genome-Shuffle-seq is a straightforward method that unlocks the possibility of pooled cellular screens to quantify the functional consequences of SVs spanning the entire human genome on fitness, gene expression, chromatin state, and three-dimensional nuclear architecture. Such data may (i) facilitate the interpretation and mechanistic investigation of SVs associated with human phenotypes; (ii) advance our understanding of the functional architecture of mammalian genomes; and (iii) inform efforts to design and construct a minimal human genome. ■

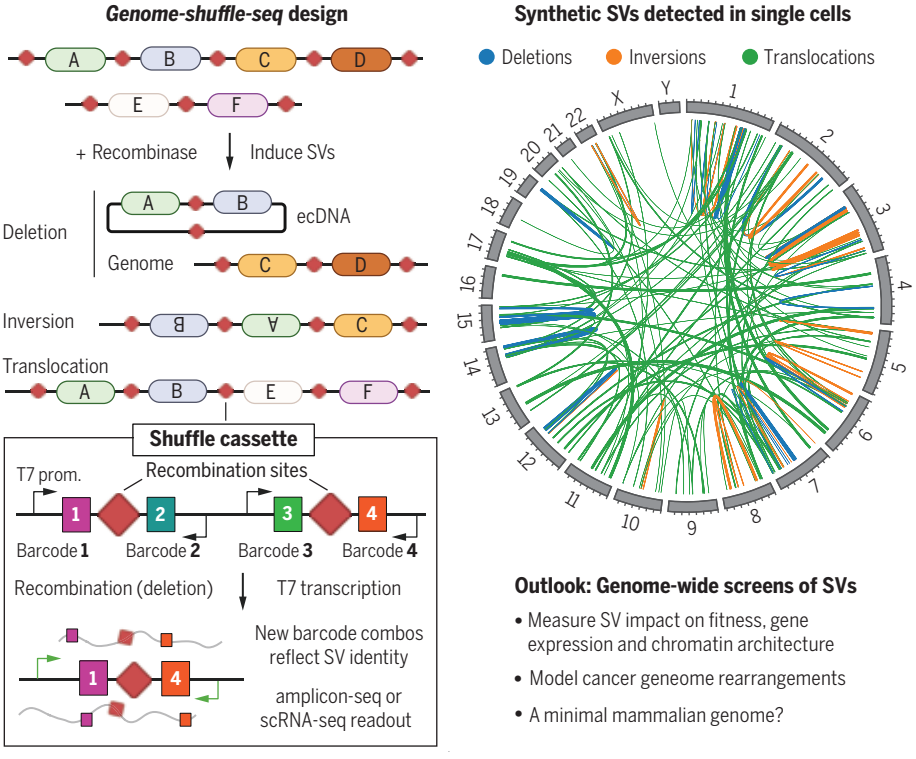

Genome-shuffle-seq enables the generation and characterization of thousands of structural variants (SVs) in mammalian genomes, even at single-cell resolution. The method uses "shuffle-cassettes" containing site-specific recombinase sites, unique DNA barcodes, and phage T7 promoters. Recombination between shuffle cassettes results in novel barcode combinations that reflect SV identity, which is detectable in bulk through polymerase chain reaction–amplicon sequencing or with single-cell RNA-seq after T7 transcription. BioRender.com was used to create some schematics in this figure.

The list of author affiliations is available in the full article online.
*Corresponding author. Email: pinglay@uw.edu (S.P.); shendure@uw.edu (J.S.)
Cite this article as S. Pinglay *et al.*, *Science* **387**, eado5978 (2025). DOI: 10.1126/science.ado5978

READ THE FULL ARTICLE AT
https://doi.org/10.1126/science.ado5978

RESEARCH ARTICLE SUMMARY

IMMUNOLOGY

Scratching promotes allergic inflammation and host defense via neurogenic mast cell activation

Andrew W. Liu, Youran R. Zhang, Chien-Sin Chen, Tara N. Edwards, Sumeyye Ozyaman, Torben Ramcke, Lindsay M. McKendrick, Eric S. Weiss, Jacob E. Gillis, Colin R. Laughlin, Simran K. Randhawa, Catherine M. Phelps, Kazuo Kurihara, Hannah M. Kang, Sydney-Lam N. Nguyen, Jiwon Kim, Tayler D. Sheahan, Sarah E. Ross, Marlies Meisel, Tina L. Sumpter, Daniel H. Kaplan*

INTRODUCTION: Scratching is an often irresistible, stereotypical, and evolutionarily conserved behavioral response to the sensation of cutaneous itch. In many common skin diseases, such as dermatitis (eczema), protracted itching—or pruritus—is the dominant symptom and represents a substantial source of morbidity. Scratching in response to itch is clinically well recognized to exacerbate dermatitis and is pathogenic in some diseases. However, scratching an itch is often a pleasurable sensation and does not trigger avoidance behavior, which suggests that it may provide some benefit to the host.

RATIONALE: In the skin, activated dermal mast cells mediate hallmarks of the cutaneous allergic response, including hives and itch, which results in scratching behavior. They also recruit inflammatory cells and promote host defense against *Staphylococcus aureus*. Mast cells can be activated through a variety of mechanisms, including allergens, that cross-link preformed complexes of immunoglobulin E (IgE) antibodies bound to the FcεRI receptor or via ligands for the MrgprB2 receptor, including substance P (SP)—a neuropeptide released by pain-sensing neurons. The functional consequence of mast cell activation through different receptors, how scratching promotes cutaneous inflammation, and whether scratching provides benefit to the host all remain poorly explored.

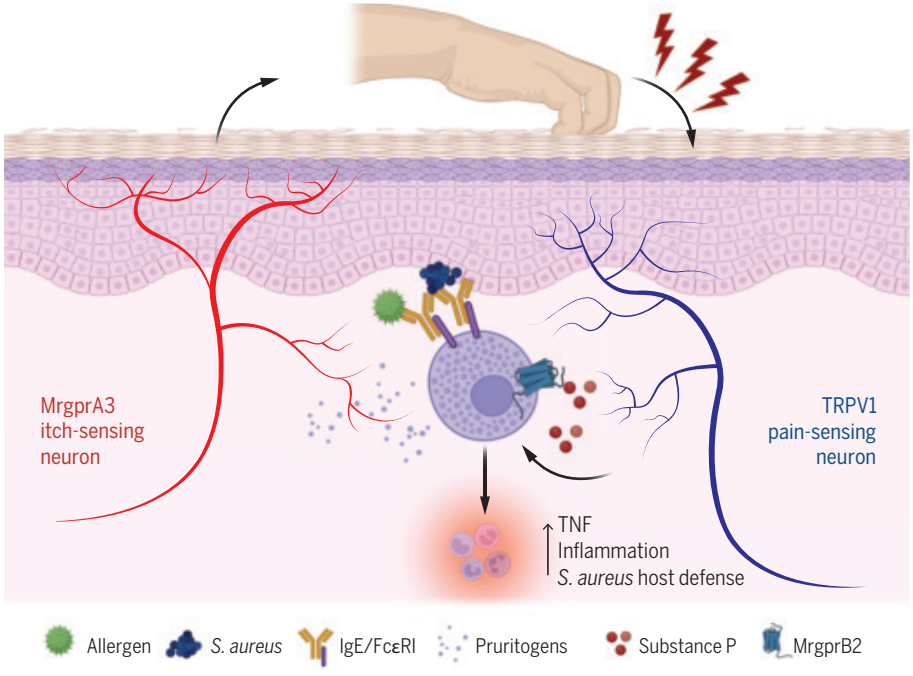

Scratching synergizes with FcεRI mast cell activation to drive allergic skin inflammation. Cross-linking of FcεRI or IgE on mast cells by allergens or *S. aureus* activates mast cell release of pruritogens (itch-inducing factors) that are sensed by MrgprA3-expressing neurons. Scratching resulting from itch sensation activates Trpv1-expressing neurons to release the neurotransmitter SP. SP acting through MrgprB2 on mast cells synergizes with FcεRI to enhance mast cell release of TNF, resulting in enhanced cutaneous inflammation and increased *S. aureus* host defense. [Figure created with BioRender.com]

RESULTS: To explore the relationship between itch, scratching, and inflammation, we generated mice that allow for the selective and inducible ablation of the nonpeptidergic 2 (NP2) subset of itch-sensing neurons, characterized by the expression of MrgprA3 (called Mrgpra3^{DTR}). We found that MrgprA3-expressing neurons were required for scratching and inflammation in models of type 2 contact hypersensitivity and FcεRI-mediated mast cell activation. In both cases, scratching augmented mast cell degranulation, tumor necrosis factor (TNF) expression, and recruitment of neutrophils. Scratching was not required for increased expression of the alarmins thymic stromal lymphopoietin (TSLP) and interleukin-33 (IL-33), which are known to activate mast cells. Rather, we found that scratching was sufficient to trigger release of SP from Trpv1-expressing neurons that synergized with FcεRI cross-linking, resulting in maximal TNF release from mast cells. This was confirmed using mice with a genetic ablation of MrgprB2 or the gene encoding SP (*Tac1*) and by chemogenetic inhibition of Trpv1-expressing neurons. Inflammation in mice prevented from scratching could be rescued by exogenous activation of Trpv1-expressing neurons. Finally, we found that scratching reduced cutaneous microbial diversity and, in an epicutaneous *S. aureus* infection model, both inflammation and host defense required scratching.

CONCLUSION: The itch-scratch cycle is a pathogenic process in allergic skin rashes, such as dermatitis, or arthropod reactions. In this cycle, itch and scratching increase inflammation and disease exacerbation. Our data suggest that scratching activates cutaneous Trpv1-expressing neurons, which are a major source of SP in the skin. Coordinated activation of mast cells by both MrgprB2 and FcεRI agonism synergistically augments inflammation, in part through increased recruitment of neutrophils. Thus, dermal mast cells occupy a central node in cutaneous inflammation and are capable of integrating both adaptive and innate neuroimmune triggers. Moreover, inflammation-induced scratching can reduce the abundance of certain members of the cutaneous commensal community and, in the context of superficial *S. aureus* infection, inflammation triggered by scratching provides enhanced host defense. These data exemplify how scratching can both exacerbate disease and benefit the host through a neuroimmune axis and reconciles the seemingly paradoxical role of scratching as a pathological process and evolutionary adaptation. ■

The list of author affiliations is available in the full article online.
***Corresponding author. Email: dankaplan@pitt.edu**
Cite this article as A. W. Liu *et al.*, *Science* 387, eadn9390 (2025). DOI: 10.1126/science.adn9390

READ THE FULL ARTICLE AT
https://doi.org/10.1126/science.adn9390

RESEARCH ARTICLE SUMMARY

NANOMATERIALS

Transforming achiral semiconductors into chiral domains with exceptional circular dichroism

Thomas J. Ugras, River B. Carson, Reilly P. Lynch, Haoyang Li, Yuan Yao, Lorenzo Cupellini, Kirt A. Page, Da Wang, Arantxa Arbe, Sara Bals, Louisa Smieska, Arthur R. Woll, Oriol Arteaga, Tamás Jávorfi, Giuliano Siligardi, Gennaro Pescitelli, Steven J. Weinstein, Richard D. Robinson*

INTRODUCTION: The creation of mesoscale chiroptic materials from nanoscale achiral building blocks has been previously realized through exciton coupling in organic supramolecular assemblies and with plasmons in inorganic metal nanoparticle assemblies, but extending excitonic chirality to inorganic semiconducting systems has remained elusive. Among the many challenges to achieving this goal is the need for degenerate excited electronic states, which are difficult to obtain in nanocrystals with nonzero size distributions, and the requirement for aligned transition dipoles, an unlikely characteristic in spherical nanocrystals that lack a distinct axis. This goal is consequential, as introducing chirality into the band structure of semiconductors enables simultaneous control over light, spin, and charge, key capabilities for driving innovations in next-generation photonic, optoelectronic, and spintronic technologies.

RATIONALE: We hypothesized that magic-sized nanoclusters could overcome these obstacles to form an exciton-coupled chiroptic inorganic assembly. Magic-sized nanoclusters are atomically and electronically identical, enabling greater wavefunction overlap and coupling between neighboring nanoclusters. And they need not be spherical, allowing for anisotropic arrangements of their transition dipoles through dipole-dipole interactions during solution processing. Additionally, the bandgap, composition, and size of semiconducting magic-sized clusters can be rationally synthesized to tailor the chiroptic responses over a range of wavelengths.

RESULTS: Following our hypothesis, we found that three different species of nanoclusters [cadmium sulfide (CdS), cadmium selenide (CdSe), and cadmium telluride (CdTe)] could be assembled through meniscus-guided evaporative processing into films with strong circular dichroic (CD) responses. Films made from CdS achieved dissymmetry factors, the CD figure of merit, as large as 1.30 for unpatterned, drop-cast films and 1.06 for patterned assemblies, values that approach the theoretical maximum. CD maps collected with Mueller matrix polarimetry showed that controlling the evaporative processing geometry enabled the creation of millimeter-scale homochiral domains that continuously transition between left- and right-handed, with their spatial organization adjustable through processing parameters. The mechanism behind these organized assemblies is elucidated through linear dichroism (LD), small-angle x-ray scattering (SAXS), and in situ microscopy, which reveal that the meniscus guides highly concentrated fibrous solutions, aligning their transition dipoles within fibrous bands as they deposit on a substrate. These bands are subsequently twisted by fluid flows, generating homochiral domains.

CONCLUSION: We report on a method to form chiral films of three different inorganic semiconductor nanocrystals, with near-limit dissymmetry factors and large homochiral domains. Our results for the three different semiconducting nanocluster systems demonstrate the generality of the method, suggesting the applicability to other nanocluster species or colloidal nanoplatelets. Our experiments uncovered the key mechanisms for achieving these chiroptic films by the meniscus-guided deposition process, including the alignment of transition dipoles of the constituents and the fluid flows responsible for twisting the fibers, and make a connection to emergent chiral properties. Harnessing methods to form chiral films from achiral, solution-processable semiconductors offers an opportunity in the design and fabrication of complex chiroptical metamaterials in ways that are both scalable and versatile. Beyond nanocluster films, this study provides valuable insights into the complexities of hierarchical assembly found in nature and offers a pathway to extend these principles to other chiral molecules and nanomaterials for engineering sophisticated, twisted structures. ■

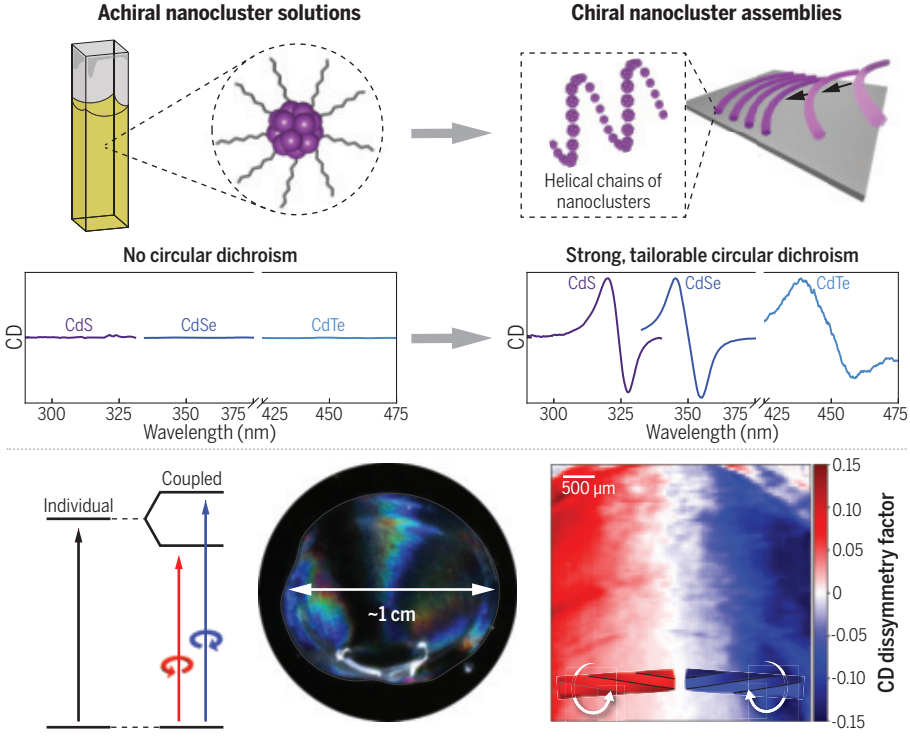

Chiral assemblies from achiral nanoclusters. Semiconducting magic-sized nanoclusters can form helical assemblies through meniscus-guided deposition. Degenerate excited states split into nondegenerate states upon coupling, producing exciton couplets in CD spectra. Controlling the evaporation geometry produces high-fidelity films with handedness imparted onto the fibers, forming various domain shapes and sizes with homochiral domains exceeding 6 mm^2 that transition smoothly between left- and right-handed chirality.

The list of author affiliations is available in the full article online.
*Corresponding author. Email: rdr82@cornell.edu
Cite this article as T. J. Ugras *et al.*, *Science* **387**, eado7201 (2025). DOI: 10.1126/science.ado7201

READ THE FULL ARTICLE AT
https://doi.org/10.1126/science.ado7201

RESEARCH ARTICLE SUMMARY

COGNITIVE MAPS

Hippocampal coding of identity, sex, hierarchy, and affiliation in a social group of wild fruit bats

Saikat Ray, Itay Yona, Nadav Elami, Shaked Palgi, Kenneth W. Latimer, Bente Jacobsen, Menno P. Witter, Liora Las*, Nachum Ulanovsky*

INTRODUCTION: Social animals live in groups and interact volitionally in complex ways. To perform real-life social behaviors, the brain needs to code other individuals' identities, represent various types of social interactions, and encode key social factors such as the sex, dominance hierarchy, and social affiliation of multiple other individuals. However, our understanding of how the brain deals with such diverse requirements stems from constrained laboratory experiments in which an animal typically exhibits one specific behavior with one other animal in one particular task. This leaves the fundamental question unexplored: How does the brain actually represent the real world with its complex, multianimal settings?

RATIONALE: To understand natural social coding in the mammalian brain, we studied Egyptian fruit bats (*Rousettus aegyptiacus*), which are highly social mammals, and focused on the hippocampus, a brain area that in previous studies has been shown to be important for memories of social identities, episodic events, and spatial locations. We hypothesized that in natural scenarios, when all of these disparate aspects occur simultaneously, hippocampal neurons would bind together all of these different types of information. To create a naturalistic environment, we established a laboratory-based "cave," housing mixed-sex groups of five to 10 wild-caught bats. The bats lived together continuously (24/7) for several months, engaging in natural social behaviors without any imposed tasks. During this time, we conducted wireless neural recordings from the dorsal hippocampus area CA1 of both male and female bats and tracked their positions, head directions, and social interactions with each other.

RESULTS: The freely behaving bats formed a stable social network and displayed three key behaviors: (i) flying between two nets located at opposite corners of the setup, (ii) engaging in social interactions, and (iii) being active on the net and observing each other. We found that hippocampal "place cells," neurons known to represent the animal's own position, were modulated during flight by the social context, i.e., whether the bat was flying to meet another bat or to be alone. These cells also encoded the identities of other bats. This identity coding was invariant to the bat's flight direction. We also found that many hippocampal cells encoded social-interaction events, with different neurons typically encoding distinct types of social interactions such as affiliative grooming or aggressive boxing. During active observation on the nets, we used methods from machine learning and game theory to reveal that neurons encoded the bat's own position and head direction, together with the positions, directions, and identities of multiple other individuals. Identity-coding neurons encoded the same specific bat across different locations and different behavioral states, both in-flight and on the net, providing another example of social invariance. The strength of identity coding was modulated by the sex, dominance hierarchy, and social affiliation of the other bats.

CONCLUSION: Our use of a naturalistic social colony allowed us to discover that the classical hippocampal cognitive map of space also integrates rich social information, forming a sociospatial cognitive map. We found neurons that encoded social interaction events, identities and sex of other individuals, dominance hierarchy, and social affiliation, along with the position and direction of both self and others. These findings combine the historically disparate views on hippocampal function, which suggested that the hippocampus is important for encoding memory, social identity, or spatial maps. Here, we have shown that all of these factors are represented together in the same neural network. ■

Experimental setup

Mixed-sex 24/7 colony of wild fruit bats

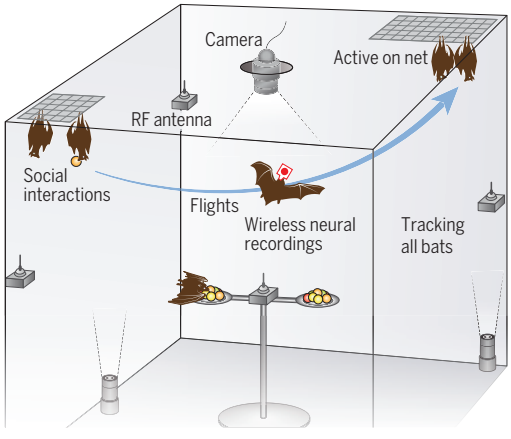

Findings

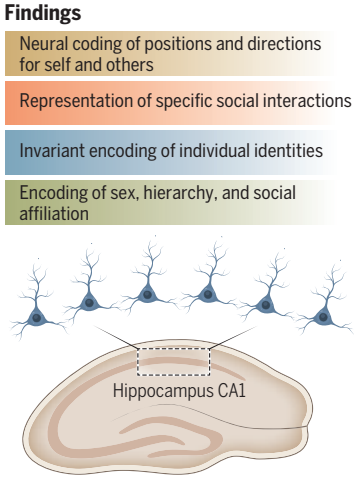

Conclusions

Hippocampal place cells also encode social information, forming a sociospatial cognitive map. In a naturalistic mixed-sex colony of freely behaving wild Egyptian fruit bats, hippocampal CA1 neurons encoded social interactions with other bats and represented the identity, sex, dominance hierarchy, and social affiliation of other individuals. [Map illustrations: Juliana Brykova/Shutterstock]

The list of author affiliations is available in the full article online.
*Corresponding author. Email: nachum.ulanovsky@weizmann.ac.il (N.U.); liora.las@weizmann.ac.il (L.L.)
Cite this article as S. Ray *et al.*, *Science* **387**, eadk9385 (2025). DOI: 10.1126/science.adk9385

READ THE FULL ARTICLE AT
https://doi.org/10.1126/science.adk9385

RESEARCH ARTICLES

ANCIENT DNA

Ancient genomics and the origin, dispersal, and development of domestic sheep

Kevin G. Daly[1,2]†, Victoria E. Mullin[1]†, Andrew J. Hare[1]†, Áine Halpin[1], Valeria Mattiangeli[1], Matthew D. Teasdale[3], Conor Rossi[1], Sheila Geiger[4], Stefan Krebs[5], Ivica Medugorac[6,7], Edson Sandoval-Castellanos[4,7], Mihriban Özbaşaran[8], Güneş Duru[9], Sevil Gülcür[8], Nadja Pöllath[6,10], Matthew Collins[11,12], Laurent Frantz[4,13], Emmanuelle Vila[14], Peter Zidarov[15], Simon Stoddart[16], Bazartseren Boldgiv[17], Ludovic Orlando[18], Mike Parker Pearson[19], Jacqui Mullville[20], Igor V. Askeyev[21], Arthur O. Askeyev[21], Oleg V. Askeyev[21], Dilyara N. Shaymuratova[21], Youri Van den Hurk[22], Andrea Zeeb-Lanz[23], Rose-Marie Arbogast[24], Helmut Hemmer[25], Hossein Davoudi[26], Sarieh Amiri[26], Sanaz Beizaee Doost[26], Delphine Decruyenaere[27,28], Homa Fathi[26], Roya Khazaeli[26], Yousef Hassanzadeh[29], Alireza Sardari[30], Johanna Lhuillier[31], Mostafa Abdolahi[32], Geoffrey D. Summers[33,34], Catherine Marro[14], Veli Bahshaliyev[35], Rémi Berthon[27], Canan Çakirlar[22], Norbert Benecke[36], Amelie Scheu[37], Joachim Burger[37], Eberhard Sauer[38], Liora Kolska Horwitz[39], Benjamin Arbuckle[40], Hijlke Buitenhuis[22,41], Lionel Gourichon[42], Jelena Bulatović[43], Terry O'Connor[44], David Orton[44], Mindia Jalabadze[45], Stephen Rhodes[46], Michael Chazan[46,47], Vecihi Özkaya[48], Melinda Zeder[49], Levent Atıcı[50], Marjan Mashkour[26,27], Joris Peters[4,6,10]*, Daniel G. Bradley[1]*

The origins and prehistory of domestic sheep (*Ovis aries*) are incompletely understood; to address this, we generated data from 118 ancient genomes spanning 12,000 years sampled from across Eurasia. Genomes from Central Türkiye ~8000 BCE are genetically proximal to the domestic origins of sheep but do not fully explain the ancestry of later populations, suggesting a mosaic of wild ancestries. Genomic signatures indicate selection by ancient herders for pigmentation patterns, hornedness, and growth rate. Although the first European sheep flocks derive from Türkiye, in a notable parallel with ancient human genome discoveries, we detected a major influx of Western steppe–related ancestry in the Bronze Age.

Numbering 1.2 billion worldwide (Food and Agriculture Organization, 2020), sheep were initially domesticated from the Asiatic mouflon (*Ovis gmelini*), which ranged from Türkiye to eastern Iran (*1*–*3*). Along with meat, skin, and fat, their lifetime (secondary) products, including milk (*4*) and dung (*5*), have played a major role in human societies. Wool, in particular, was a sought-after commodity and source of warm, breathable, water resistant textiles, which was intertwined through the economies of early complex societies in fourth to third millennium BCE Southwest Asia and later in Bronze Age Europe (*6*, *7*).

The origins of sheep management and husbandry can be traced to the mid–ninth millennium BCE in the northern Fertile Crescent. Among Early Neolithic sites in the upper Euphrates basin and Central Türkiye, faunal remains reveal the emerging new relationship between humans and sheep through shifts in species composition, age profiles, diet, the occurrence of bone pathologies, evidence of fetal and neonatal deaths on site, and progressive size reduction compared with earlier hunted assemblages (*8*–*11*). One millennium later, caprine pastoralism was consolidated more widely across Southwest Asia with smaller, phenotypically domestic sheep populating landscapes well beyond the natural distribution of wild sheep (*12*–*14*).

To investigate the origins, dispersal, and development of sheep, we analyzed 118 newly sequenced ancient sheep genomes spanning 12,000 years (Fig. 1A) with a mean coverage of 0.85× (~0.01× to 5.38×; figs. S2 and S3 and tables S1 to S5), supplemented with five published ancient genomes (*15*, *16*). Their geographic range stretches from Mongolia to Ireland (fig. S1), with a particular focus on Southwest Asia (N = 70 sheep genomes) (Fig. 1B). We analyzed these with 73 modern *Ovis* genomes (table S4), including 57 domestic *Ovis aries* from Asia, Europe, and Africa; 12 *O. gmelini* from Iran; and 4 Iranian urials (*Ovis vignei*).

Ancient wild genomes point away from domestication in the east of the Fertile Crescent

Eight of our ancient genomes are from wild *Ovis*. Three Iranian samples from Tappeh Sang-e Chakhmaq (~6000 BCE; Fig. 1) (*17*, *18*) are identifiable as urial (*O. vignei*) by their segregation with modern urials in principal components analysis (PCA; PC3 in fig. S4 and table S6), *D* statistics (fig. S5 and table S7), and their mitochondrial DNA (mtDNA) sequences (fig. S6 and table S1). Four specimens with genomic affinity with wild Eurasian mouflon (*O. gmelini*; fig. S4) derived from Nachcharini Cave (Lebanon) and Körtik Tepe (Türkiye), dating to mid-10th

[1]Smurfit Institute of Genetics, Trinity College Dublin, Dublin, Ireland. [2]UCD School of Agricultural and Food Science, University College Dublin, Belfield, Ireland. [3]Bioinformatics Support Unit, Faculty of Medical Sciences, Newcastle University, Newcastle upon Tyne, UK. [4]Institute of Palaeoanatomy, Domestication Research and the History of Veterinary Medicine, LMU Munich, Munich, Germany. [5]Laboratory for Functional Genome Analysis (LAFUGA), Gene Center, LMU Munich, Feodor-Lynen-Straße 25, Munich, Germany. [6]ArchaeoBioCenter, LMU Munich, Munich, Germany. [7]Population Genomics Group, Department of Veterinary Sciences, LMU Munich, Martinsried, Germany. [8]Prehistory Department, Faculty of Letters, Istanbul University, Istanbul, Türkiye. [9]Department of Archaeology, Mimar Sinan Fine Arts University, Şişli/İstanbul, Türkiye. [10]Bavarian Natural History Collections, State Collection of Palaeoanatomy Munich, Munich, Germany. [11]Globe Institute, Faculty of Health and Medical Sciences, University of Copenhagen, Copenhagen, Denmark. [12]McDonald Institute for Archaeological Research, University of Cambridge, West Tower, Downing Street, Cambridge, UK. [13]School of Biological and Behavioural Sciences, Queen Mary University of London, London, UK. [14]CNRS-UMR 5133, Maison de l'Orient et la Méditerranée, Université Lumière Lyon 2, Lyon, France. [15]Institute of Prehistory, Early History and Medieval Archaeology, Eberhard-Karls Universität Tübingen, Tübingen, Germany. [16]Department of Archaeology, University of Cambridge, Cambridge, UK. [17]Laboratory of Ecological and Evolutionary Synthesis, Department of Biology, School of Arts and Sciences, National University of Mongolia, Ulaanbaatar, Mongolia. [18]Centre for Anthropobiology and Genomics of Toulouse (CNRS UMR 5288), Université Paul Sabatier, Toulouse, France. [19]Institute of Archaeology, University College London, London, UK. [20]School of History, Archaeology and Religion, Cardiff University, Cardiff, Wales, UK. [21]Laboratory of Biomonitoring, The Institute of Problems in Ecology and Mineral Wealth, Tatarstan Academy of Sciences, Daurskaya Street, 28, Kazan, Russia. [22]Groningen Institute of Archaeology, University of Groningen, Groningen, Netherlands. [23]Generaldirektion Kulturelles Erbe Rheinland-Pfalz, Dir. Landesarchäologie, Speyer, Germany. [24]UMR 7044, ARCHIMEDE, University of Strasbourg, Strasbourg, France. [25]Anemonenweg 18, Mainz, Germany. [26]Bioarchaeology Laboratory, Central Laboratory, Archaeozoology section, University of Tehran, Tehran, Iran. [27]Archéozoologie et Archéobotanique: Sociétés, Pratiques et Environnements UMR 7209 du Centre national de la recherche scientifique (CNRS) et Muséum national d'Histoire naturelle (MNHN), Paris, France. [28]Department of History and Cultural Heritage, Silk Road University of Tourism and Cultural Heritage, 17 University Boulevard, Samarkand, Uzbekistan. [29]National Museum of Iran, Tehran, Iran. [30]Iranian Center for Archaeological Research, Research Institute of Cultural Heritage and Tourism, Tehran, Iran. [31]Laboratoire Archéorient, UMR 5133 (CNRS), Maison de l'Orient et de la Méditerranée, Lyon, France. [32]Department of Archaeology, Dezful Branch, Islamic Azad University, Khuzestan, Iran. [33]ENSA Nantes, Nantes, Mauritus. [34]Institute for the Study of Ancient Cultures, West Asia & North Africa (ISAC), Chicago University, Chicago, IL, USA. [35]Nakhchivan Branch of the Azerbaijan National Academy of Sciences, Nakhchivan, Azerbaijan. [36]German Archaeological Institute, Central Department, Im Dol 2-6, Berlin, Germany. [37]Palaeogenetics Group Institute of Organismic and Molecular Evolution (iomE), Johannes Gutenberg University Mainz, Mainz, Germany. [38]School of History, Classics and Archaeology, University of Edinburgh, Edinburgh, UK. [39]National Natural History Collections, Hebrew University, Jerusalem, Israel. [40]Department of Anthropology, University of North Carolina at Chapel Hill, Chapel Hill, NC, USA. [41]ArcheoSupport B.V., Postbus 41091, CB Groningen, Netherlands. [42]Université Côte d'Azur, CNRS, CEPAM, Nice, France. [43]Department of Historical Studies, University of Gothenburg, Box 200, Gothenburg, Sweden. [44]BioArCh, Department of Archaeology, Environment Building, University of York, Heslington, York, UK. [45]Georgian National Museum, 3 Shota Rustaveli Ave, Tbilisi, Georgia. [46]Department of Anthropology, University of Toronto, 19 Ursula Franklin Street, Toronto, Ontario, Canada. [47]Evolutionary Studies Institute, University of the Witwatersrand, 1 Jan Smuts Avenue, Braamfontein, Johannesburg, South Africa. [48]Department of Archaeology, Dicle University, Diyarbakır, Türkiye. [49]Smithsonian Institution, Washington, DC, USA. [50]Department of Sociology and Anthropology, NC State University, Raleigh, NC, USA.

***Corresponding author. Email: joris.peters@lmu.de (J.P.); dbradley@tcd.ie (D.G.B.)**

†These authors contributed equally to this work.

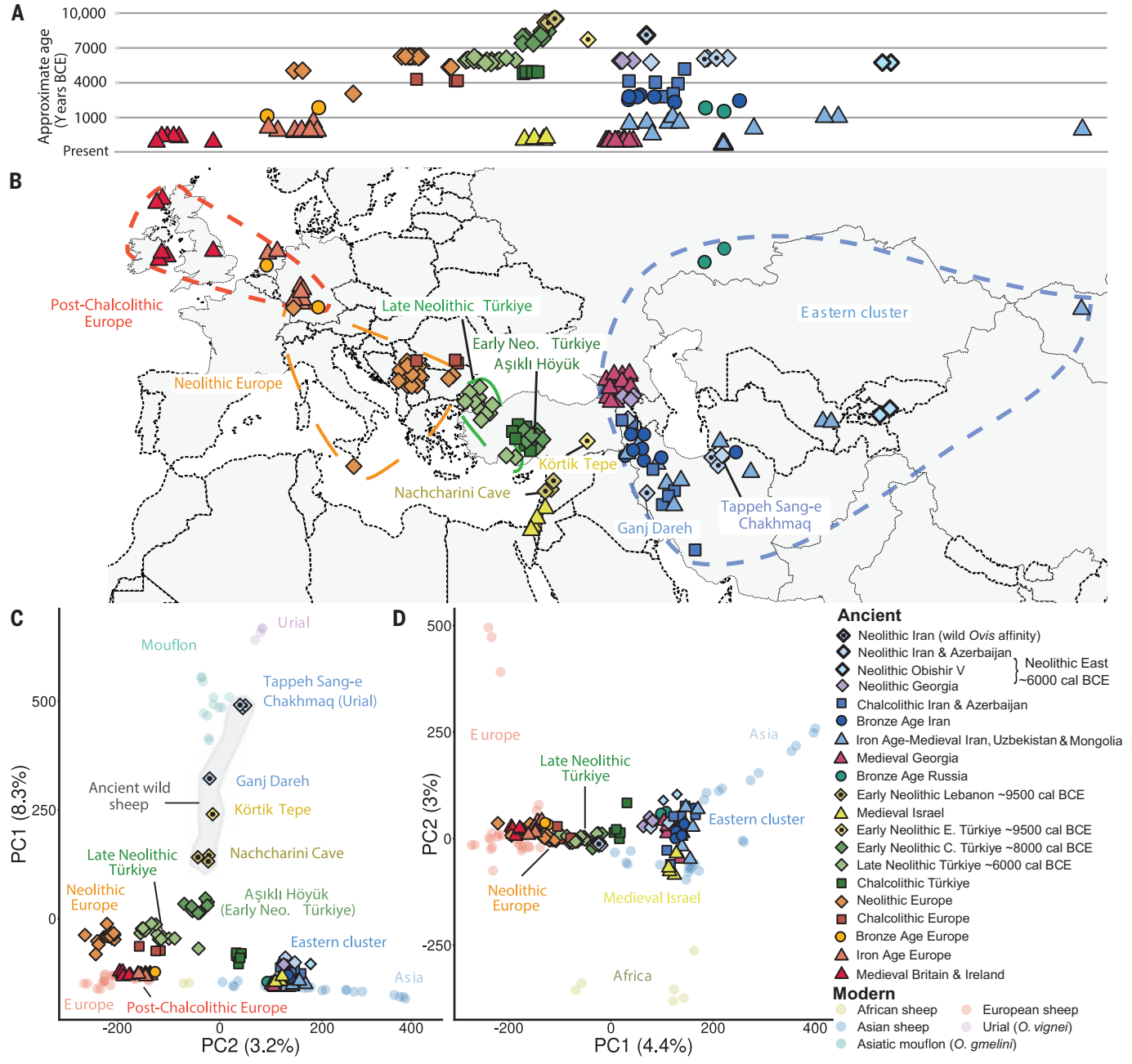

Fig. 1. Provenance and principal components analysis of 123 ancient wild and domestic sheep genomes (118 reported in this study) projected onto modern *Ovis* diversity. (**A**) Approximate sample date plotted versus (jittered) longitude [corresponding to positions in (B)]. Symbols with dots indicate ancient wild genomes. (**B**) Provenance and cultural period of sampled genomes. (**C**) Plot of PC1 and PC2 with symbol and color key as in the map; clear separations between hunted wild (samples from Tappeh Sang-e Chakhmaq, Ganj Dareh, Körtik Tepe, and Nachcharini Cave) and human-managed sheep and also between eastern and western locations are visible. The "Eastern cluster" designation encompasses ancient sheep from Georgia, Iran, Azerbaijan, Uzbekistan, Kyrgyzstan, and Mongolia. (**D**) Plot of PC1 and PC2 calculated with modern wild genomes removed, which shows geographic separation by continent. Cal, calibrated; C., central; E., eastern.

millennium BCE. Both assemblages lack demographic indicators of management (*13*, *19*) and predate evidence of sheep management (*2*, *20*). A final wild mouflon genome is from ~8000 BCE Ganj Dareh (Iran), where sheep (in contrast to contemporaneous herded goats) show a demographic profile typical of hunted populations (*21*). In PCA, when we project our ancient data on a framework of modern sheep and wild *Ovis* genomes (Fig. 1C, fig. S4, and tables S3 and S4), these ancient wild samples clearly separate from those representing managed, domestic assemblages on PC1; this, along with other analyses, were tested for robustness with respect to sequencing error and selection of variant sites (*22*).

Among the ancient wild sheep (Fig. 1, B and C), those which plot closest to domesticates on PC1 are the three more western mouflon genomes from Nachcharini Cave in Lebanon (~9700 to 9000 BCE), followed by those from Körtik Tepe [2σ (σ, standard deviation) C_{14} age: 9873 to 9453 BCE] in Southeast Türkiye, and then Ganj Dareh (2σ C_{14} age: 8279 to 7960 BCE) in the Iranian Zagros toward the eastern side of the wild *Ovis* range (Fig. 1C). This hierarchy within wild versus domesticated

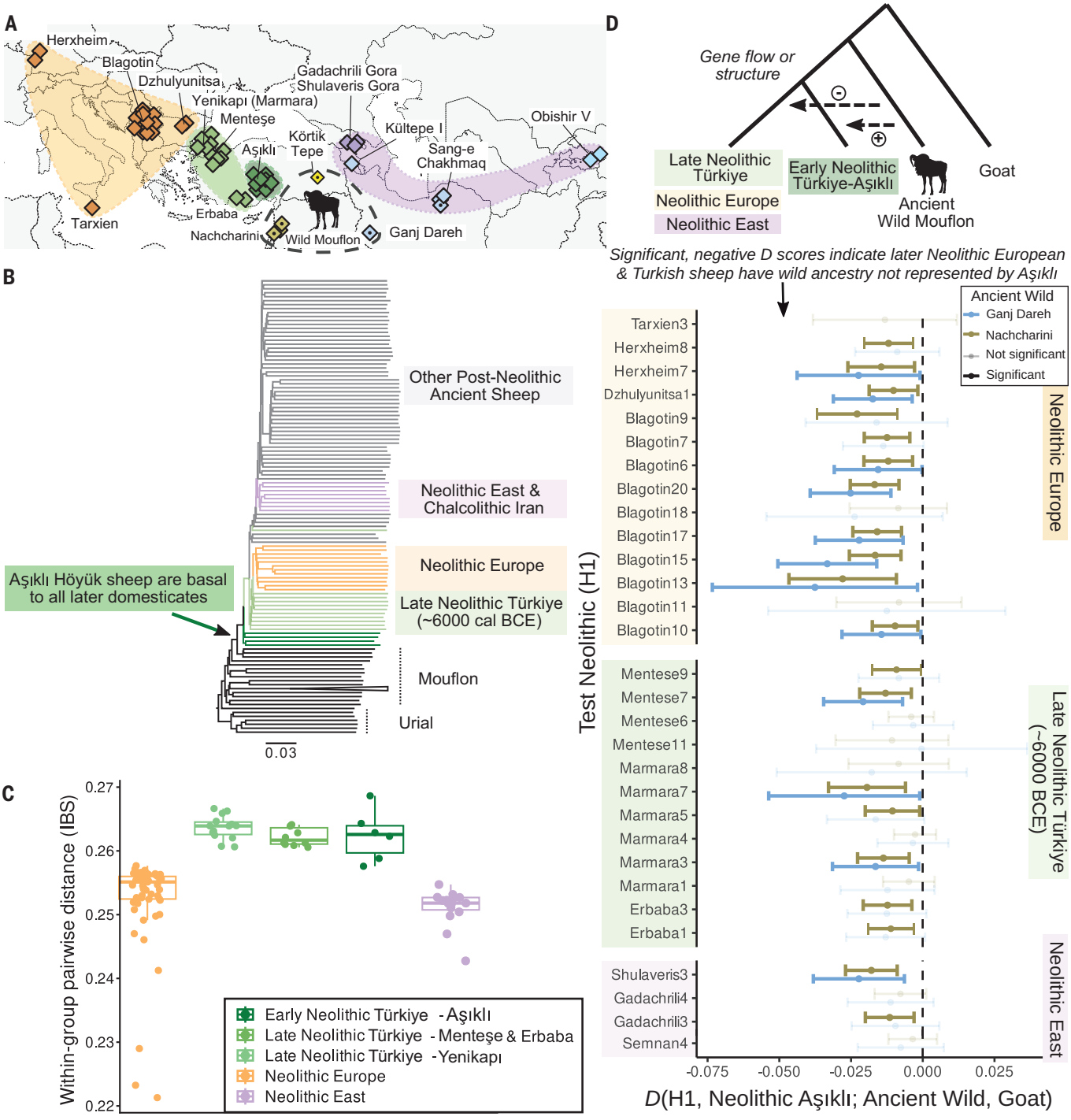

Fig. 2. Patterns of Neolithic sheep diversity. (**A**) The groupings of Neolithic samples compared in (B), with sampled sites also indicated. (**B**) Neighbor-joining tree based on IBS data of ancient and modern *Ovis*. Aşıklı Höyük sheep are basal to all later domesticates. The Late Neolithic Türkiye sample grouping away from others (Marmara8) is an outlier with regards to eastern ancestry (see Fig. 3B). Neolithic East refers to genomes from ~6000 BCE Iran, Azerbaijan, Georgia, and Kyrgyzstan, highlighted in purple in (C). The outgroup goat is not shown, and a clade of modern Iranian mouflon is collapsed; see fig. S9 for individually labeled phylogeny. Samples Pie10 and Pie11 from Măgura Gorgana, Romania, were excluded owing to higher sequencing error rates (table S1). (**C**) Comparative plots of diversity among Neolithic groups using within-group pairwise IBS distance. (**D**) Error-corrected *D* statistics testing whether the pairing of Early Neolithic Central Turkish (Aşıklı Höyük) and individuals from Late Neolithic (~6000 BCE) sites retains integrity when ancient wild sheep groups are considered as introgressors; group level tests are presented in table S7, and tests with Aşıklı individuals, in fig. S16.

affinity is supported by identity-by-state phylogenetic analysis, where the Lebanese mouflon form the closest ancient outgroup to all domesticate genomes, and Ganj Dareh, the most distant (fig. S6). Additionally, later Iranian domestic sheep cannot be modeled (qpWave; table S10) as stemming from the Ganj Dareh mouflon genome. This evidence points away from a core area of sheep domestication at the east of

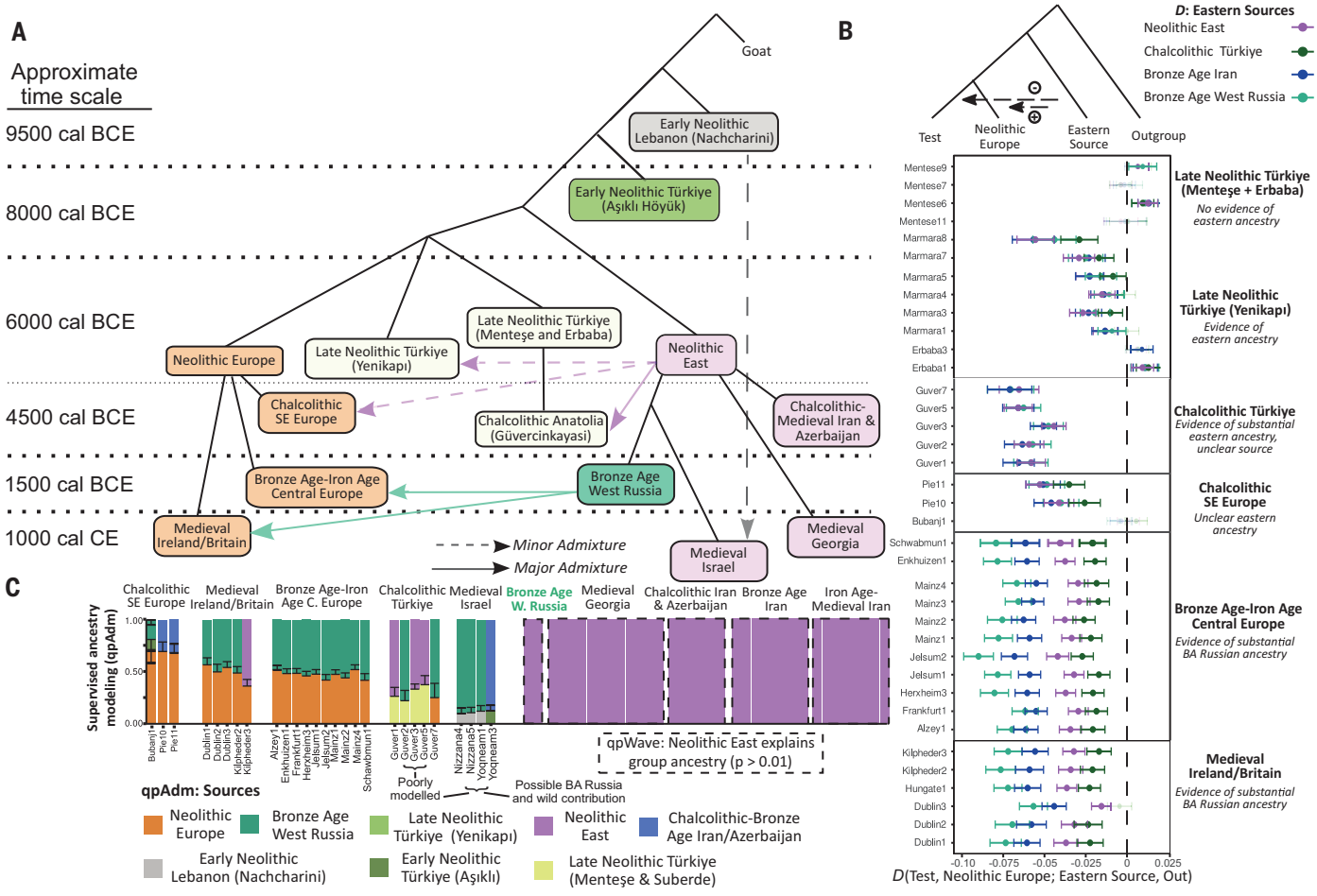

Fig. 3. An admixture history of domestic sheep. (**A**) Phylogenetic scheme based on recurrent features emerging in Admixtools2 exploration, with topology supported by a Treemix analysis (figs. S12 and S15). Dashed arrows denote minor (<25%) and solid arrows show major (>25%) secondary admixtures. Vectors involving the Medieval Israel, Medieval Georgia, and (combined for illustration) Chalcolithic-Medieval Iran-Azerbaijan groups were grafted to the model based on qpWave, qpAdm, and Treemix results. (**B**) Error-corrected *D* statistics testing for admixture from different eastern sources (see color key) with Neolithic European genomes as a reference. The strongest introgression signals are from a Neolithic East–related source in earlier time periods, with stronger signals from Bronze Age West Russia in later Europeans. Non–error-corrected group and individual tests are shown in figs. S20 and S21. (**C**) Supervised ancestry modeling of post-Neolithic genomes; the color key denotes the potential sources considered. Models with the highest *P* values are shown (*35*), with alternative fitting models in table S11. Fitting models for Chalcolithic Türkiye samples always comprise western and eastern mixture, but a range of alternate eastern sources are accepted, suggesting that their source is not well represented in our data; we similarly fit a range of models for the Medieval Israel sheep.

the mouflon range in the Zagros and accords with an origin in the western range of southwest Asia. It also aligns with the archaeofaunal record evidencing that domestic sheep phenotypes and management occurred later in that region, around 7000 BCE (*12*, *23*). By contrast, by around 8000 BCE, goats in Iran had already begun a demographic and genetic transition toward the domesticated state (*21*), indicating uncoupled early domestication processes in the two small livestock species in the eastern arc of the Fertile Crescent.

Early Neolithic Aşıklı Höyük are a basal population but do not fully represent domestic ancestry

PC1 also distributes samples of herded populations in order of archaeological age (Fig. 1C), stretching from Early Neolithic Aşıklı Höyük (8300 to 7500 BCE) through later Neolithic genomes (Fig. 2A) and subsequent periods to medieval and, lastly, modern genomes. The Aşıklı Höyük genomes, represented by a mixture of shotgun and whole-genome enrichment data (we restrict key analyses to shotgun data only), are from close in time to the beginnings of sheep domestication. There, herd management is reflected in the culling of young males, slaughtering near habitations, and accumulation of dung and urine in sediments, indicating the stabling of livestock on site (*8*, *24*). However, sheep at this time did not yet have the reduced size and altered morphology typical of later domesticates (*25*). When we modeled the ancient sheep phylogeny using either individuals with identity by state (Fig. 2B and fig. S9) or admixture graph exploration with genomes grouped into the major geographic-temporal PCA clusters (Fig. 3A, figs. S10 to S15, and tables S8 and S9), Aşıklı Höyük holds a basal position among domesticates [inferred by using shotgun but excluding genome-enriched sequencing data (*22*)]. This is consistent with that population being genetically proximal to the origins of domestic sheep.

However, our Late Neolithic samples (here defined as ~6000 BCE) are likely not a simple derivation of this early Central Turkish diversity. *D* statistics with either the wild Ganj Dareh or Nachcharini sheep as outgroups to test the integrity of Aşıklı Höyük–Late Neolithic genome clade pairings point toward the latter having a broader wild ancestry than the flocks raised at Aşıklı Höyük (Fig. 2D and fig. S16; although

tests with different Aşıklı individuals produce a mixture of positive, indeterminate, and negative results, fig. S17). Moreover, these later populations cannot be modeled as deriving from the Aşıklı sheep alone (by using qpWave to evaluate the fit of single ancestry streams, table S10). This could arise from local wild genomes being incorporated in their population histories after a common origin (*26*). Alternatively, a broader mosaic of wild diversity gave rise to the founder herds, not all of which are represented in our Aşıklı Höyük sample. Genomic sampling of additional ninth millennium BCE assemblages within the natural habitat of the mouflon, including from the Northern Levant and upper Euphrates basin in the center of the Fertile Crescent, would distinguish these scenarios.

Migrations and admixture shaped ancient sheep populations

In PC space, western Neolithic sheep appear highly structured (Fig. 1C). There are distinct clusters of genomes deriving from Turkish and European Neolithic sites. By contrast, ~6000 BCE Neolithic sheep genomes which are geographically dispersed among Georgia, Azerbaijan, eastern Iran, and Kyrgyzstan sites (*15*) cluster tightly genetically; we refer to this group as "Neolithic East" in subsequent analyses. Relative homogeneity of these eastern genomes is supported by pairwise identity-by-state (IBS) values (Fig. 2C) and a cladal relationship (along with Chalcolithic Iran) in an IBS-based phylogeny (Fig. 2B).

When we calculated PC1 and PC2 without modern wild genomes, three poles of variation, marked by trends in ancient and modern European, Asian, and African animals (Fig. 1D), became apparent. Ancient Turkish sheep trend toward the European pole, Iranians toward the Asian population, and, although less pronounced, medieval genomes from Israel toward African sheep today, implying roles in the foundations of the respective continental herds. Supported by *D* statistics and qpAdm modeling (fig. S18 and tables S7 and S11), these separate continental affinities of the three corners of the Fertile Crescent have parallels in ancient goat and cattle genomes (*27*, *28*). However, there are additional complexities in the trajectories of these sheep populations.

To explore the role of gene flow in the development of ancient sheep, we explored phylogenetic relations using admixture graph exploration and Treemix (fig. S12) and constructed a summary schema (Fig. 3A). This retained the most frequent features within best-fitting solutions [(*22*); tables S8 and S9] and explicitly modeled inferred population mixtures with qpAdm (Fig. 3B and table S11). The primary divide in the Late Neolithic (~6000 BCE) and subsequent periods is between east and west (Figs. 1, C and D, and 3A). The earliest admixture between these involves sheep from Late Neolithic Yenikapı on the western shore of the Bosphorus, showing additional minor eastern ancestry relative to neighboring sheep populations (qpAdm: 17 to 20% with one outlier, Marmara8, at 53 ± 16%; fig. S19 and table S11). Late Neolithic Turkish populations have been noted to exhibit reduced mtDNA diversity, which is modeled as the result of a population bottleneck occurring as founder flocks migrated from the region of domestication (*29*, *30*). mtDNA diversity does not similarly decline in the Neolithic East (table S1). Although we saw reduced autosomal diversity (assessed as levels of pairwise allele sharing; Fig. 2C) in the Neolithic European and Eastern populations, this was not the case in our Late Neolithic Turkish sheep. This contrast between maternal and whole genome patterns may be at least partly explained by secondary directional admixture (mediated largely by choice of sires), which, in herded stock, can leave mtDNA diversity unchanged (*28*). There were distinct routes and events during dispersal from the initial domestication region throughout coastal and inland Türkiye (*26*, *31*), with likely ongoing exchange of animals within Neolithic Southwest Asia.

We found little evidence of discontinuity after the foundation of the eastern population: sheep from the Chalcolithic and later periods can be modeled entirely by the Neolithic East group (qpWave, table S10) according with their close clustering in PCA and despite a wide geographical provenance. Conversely, both the European and Central Turkish Chalcolithic show differences relative to their Neolithic counterparts, clearly indicated by *D* statistics (Fig. 3B and figs. S19 to S23) and unsupervised ancestry modeling (fig. S24). Within central Türkiye, in a discontinuity with Neolithic genomes, Chalcolithic Güvercinkayası sheep are a mix of western and eastern ancestry (57 to 70%, from all fitting group-level qpAdm models with a range of possible eastern sources; table S11). At Güvercinkayası, decorated pottery, stamped seals, and seal impressions point to connections to Mesopotamian Ubaid culture sites (*32*), which were known to practice large-scale, mobile sheep pastoralism (*33*). Notably, the signals of east-to-west gene flow in Southwest Asian sheep have resonance with a wider recurring pattern of westward movements from the Caucasian, Iranian, or northern Mesopotamian cultural sphere that is paralleled in both material culture and human genetics (*34*). Substantial Iranian or Caucasus ancestry influx into Anatolian and Mediterranean human populations also occurred in the Chalcolithic and has been postulated to correlate with the spread of Anatolian languages basal to Indo-European tongues (*35*). Eastern input extends into Southeast European Chalcolithic sheep (18.7 to 32.3% for best-fitting models, but qpAdm allows several possible sources; table S11), according with multiple postulated cultural shifts between the Early Neolithic Starčevo horizon (represented here by the Blagotin assemblage, Fig. 2A) and the Chalcolithic period [fig. S1, (*36*)].

Steppe-related sheep migration to Europe

The most dramatic east to west genome introgression, both in distance traversed and extent of influence, is that which transformed Bronze Age and subsequent European sheep. Supervised ancestry modeling, likelihood-based graph exploration [Treemix (*37*); figs. S12 to S15), and *D* statistics (Fig. 3B; variation in *D* scores were observed by using individual Neolithic European sheep rather than groups; see fig. S21 and table S6) favor Late Bronze Age sheep sampled from the Russian Volga–Ural steppe as the best-fitting source. With qpAdm, we estimate that 44 to 61% of the individual ancestry of European sheep from the Bronze Age onwards derives from Western steppe–related admixture (Fig. 3C). Post-Neolithic translocations of steppe sheep into Europe fit studies of modern genetic markers (*38*) and are hinted at by ancient mtDNA data (*39*).

One of the most substantial findings from ancient human genomics is strong evidence for a massive steppe-derived population turnover in Europe around 3000 to 2700 BCE (*40*, *41*). We infer that, in the frame of this cultural process, sheep populations were transformed by a translocation from the steppe into central and western Europe by the mid–second millennium BCE. This was likely motivated by the lifeways and dietary preferences of the third millennium BCE Yamnaya culture, i.e., primarily sheep-herding, migratory pastoralists of the Pontic-Caspian steppe that depended on small livestock for dairy products (*42*, *43*).

Ancient signals of selection and sheep production traits

To test which traits may have undergone selection in prehistory, we focused on the two clusters of genomes in our data with the best sampling and genome coverage (Fig. 1C): Neolithic southeast Europe (restricted to genomes from the ~6000 BCE assemblage of Blagotin-Poljna, Serbia) and Bronze Age–to–medieval European sheep (pooled across assemblages dating to ~1400 BCE to ~1100 CE). We used these two groups comprising 6 (mean 1.37X coverage) and 13 genomes (mean 1.69X coverage) and compared them with 17 modern wild sheep genomes (*44*) to calculate pairwise fixation indices in genome-wide windows. This is summarized in population branch statistics (*45*) within which we identified 50-kb windows with excessive divergence and located these signals on the respective trajectories of the Neolithic or post-Chalcolithic groups (fig. S25).

On the branch leading to the ~6000 BCE Neolithic population, it is notable that, within the 10 most-elevated signal peaks, a majority contain genes with prior evidence for phenotype consequence and/or selection history in

modern sheep. The strongest genome-wide peak is adjacent to the genes *PDGFRA* and *KIT* [a locus implicated in selection and coat color, e.g., piebaldism, in multiple species (*27*, *46*); fig. S25]). The fourth-ranked region contains *MC1R*, which has also had variation linked to coloration in multiple studies (*47*, *48*). This suggests that, within the first two millennia of sheep husbandry and mirroring results from ancient goat genomes (*27*), herders had strong preferences for coat colors and patterns. This may have aided identification within communally herded flocks, resulted from pleiotropy with behavior (*49*), or reflected value for decoration or textile production, although systemic use of animal-based textiles does not occur until later periods (*50*). Alternately, domestic animals possess strong symbolic and aesthetic value, and it is possible that herders simply favored the beautiful and unusual. Other outlier Neolithic signals contain genes suggesting early selection for growth rate [*GHR* (*51*)], wool morphology [*SHCBP1* (*52*)], and climate adaptation [*TBC1D12* (*53*)].

Selection in later ancient Europe

By the Bronze Age, sheep began to play a more central economic role in Europe, demonstrated by the appearance of larger breeds, higher proportions of polled (i.e., hornless) animals, and wool as a key textile and traded commodity (*54*, *55*). In the post-Chalcolithic European branch, the strongest signals include *RXFP2*, the major determinant of horn shape and the polled trait (*56*). We did not find strongly outlying signals associated with wool trait loci, although the occurrence of several within the top 1% of genome windows may concord with a more diffuse selection process (table S12). These include *IRF2BP2*, which has a 3′ untranslated region–derived variant associated with fleece fiber (*57*) that shows an increase from 50 to 91% (P = 0.012, binomial test) between our Neolithic European sheep and those bred in the Iron Age and medieval periods (fig. S26).

We have shown that herds in the wool-enriched economies of Bronze Age and later Europe were transformed by a major influx from the Western steppe. Within these sheep herds, we see some indication of selection at fleece-related genes. However, as coarse yarns continued to be used for textiles, the adoption of wool was probably a spatially and temporally heterogeneous process, rendering human exploitation of this lifetime product more akin to an evolution than a revolution (*55*).

REFERENCES AND NOTES

1. J. Peters, D. Helmer, A. von den Driesch, M. Saña Segui, *Paéorient* **25**, 27–48 (1999).
2. J. Peters, A. von den Driesch, D. Helmer, in *First Steps of Animal Domestication: New Archaeozoological Approaches*, J.-D. Vigne, J. Peters, D. Helmer, Eds. (Oxbow Books, 2005), pp. 86–124.
3. C. Her *et al*., *Anim. Genet.* **53**, 452–459 (2022).
4. J.-D. Vigne, D. Helmer, *Anthropozoologica* **42**, 9–40 (2007).
5. A. Bogaard *et al*., *Proc. Natl. Acad. Sci. U.S.A.* **110**, 12589–12594 (2013).
6. C. C. Lamberg-Karlovsky, G. Algaze, *J. Interdiscip. Hist.* **25**, 662 (1995).
7. C. Breniquet, C. Michel, Wool Economy in the Ancient Near East and the Aegean: From the Beginnings of Sheep Husbandry to Institutional Textile Industry, vol. 17 of Ancient Textile Series (Oxbow Books, 2014), pp. 1–11.
8. M. I. Zimmermann, N. Pöllath, M. Özbaşaran, J. Peters, *J. Archaeol. Sci.* **92**, 13–27 (2018).
9. M. C. Stiner, N. D. Munro, H. Buitenhuis, G. Duru, M. Özbaşaran, *Proc. Natl. Acad. Sci. U.S.A.* **119**, e2110930119 (2022).
10. S. Lösch, G. Grupe, J. Peters, *Am. J. Phys. Anthropol.* **131**, 181–193 (2006).
11. N. Pöllath *et al*., *J. Archaeol. Sci.* **130**, 105344 (2021).
12. M. Zeder, "*Archaeozoology of the Near East VIII: Proceedings of the 8th International Symposium on the Archaeozoology of Southwestern Asia and Adjacent Areas*, **vol. 49** of Travaux de la Maison de l'Orient, E. Vila, L. Gourichon, A. M. Choyke, and H. Buitenhui, Eds. (Maison de l'Orient et de la Méditerranée, 2008), pp. 243–277.
13. B. S. Arbuckle, L. Atici, *Levant* **45**, 219–235 (2013).
14. J.-D. Vigne, L. Gourichon, D. Helmer, L. Martin, J. Peters, in *Quaternary of the Levant. Environments, Climate Change, and Humans*, Y. Enzel, O. Bar-Yosef, Eds. (Cambridge Univ. Press, 2017), pp. 753–760.
15. W. T. T. Taylor *et al*., *Nat. Hum. Behav.* **5**, 1169–1179 (2021).
16. C. Rossi *et al*., *Biol. Lett.* **17**, 20210222 (2021).
17. M. Mashkour *et al*., in *The First Farming Village in Northeast Iran and Turan: Tappeh Sang-E Chakhmaq and Beyond*, A. Tsuneki, Ed. (Univ. of Tsukuba, 2014), pp. 27–32.
18. K. Roustaei, M. Mashkour, M. Tengberg, *Antiquity* **89**, 573–595 (2015).
19. S. Rhodes, E. B. Banning, M. Chazan, *PLOS ONE* **15**, e0227276 (2020).
20. M. A. Zeder, *Proc. Natl. Acad. Sci. U.S.A.* **105**, 11597–11604 (2008).
21. K. G. Daly *et al*., *Proc. Natl. Acad. Sci. U.S.A.* **118**, e2100901118 (2021).
22. Materials and methods are available as supplementary materials.
23. D. de Groene, R. Bendrey, G. Müldner, A. Coogan, R. Matthews, *J. Archaeol. Sci. Rep.* **49**, 103936 (2023).
24. J. T. Abell *et al*., *Sci. Adv.* **5**, eaaw0038 (2019).
25. H. Buitenhuis *et al*., in *The Early Settlement at Aşıklı Höyük. Essays in Honor of Ufuk Esin*, M. Özbaşaran, G. Duru, M. C. Stiner, Eds. (Ege Yayınları, 2018), pp. 281–323.
26. B. S. Arbuckle *et al*., *PLOS ONE* **9**, e99845 (2014).
27. K. G. Daly *et al*., *Science* **361**, 85–88 (2018).
28. M. P. Verdugo *et al*., *Science* **365**, 173–176 (2019).
29. E. Yurtman *et al*., *Commun. Biol.* **4**, 1279 (2021).
30. E. Sandoval-Castellanos *et al*., *Sci. Adv.* **10**, eadj0954 (2024).
31. M. A. Zeder, in *Human Dispersal and Species Movement: From Prehistory to the Present* (Cambridge Univ. Press, 2017), pp. 261–303.
32. S. Gülçur, P. Çaylı, I. Demirtaş, B. Eser, V. İndere, in *Anatolian Metal VIII: Eliten - Handwerk - Prestigegüter*, Ü. Yalcin, Ed. (Verlag Marie Leidorf, 2018), pp. 43–56.
33. C. A. Makarewicz, B. S. Arbuckle, A. Öztan, in *Isotopic Investigations of Pastoralism in Prehistory*, A. R. Ventresca Miller, C. A. Makarewicz, Eds. (Routledge, 2017), pp. 113–122.
34. D. Koptekin *et al*., *Curr. Biol.* **33**, 41–57.e15 (2023).
35. I. Lazaridis *et al*., *Science* **377**, eabm4247 (2022).
36. D. Borić, in *Neolithic and Copper Age between the Carpathians and the Aegean Sea. Chronologies and Technologies from 6th to 4th Millennium BCE*, **vol. 31** of Archäologie in Eurasien, S. Hansen, P. Raczky, A. Anders, A. Reingruber, Eds. (Verlag Marie Leidorf, 2015), pp. 177–237.
37. J. K. Pickrell, J. K. Pritchard, *PLOS Genet.* **8**, e1002967 (2012).
38. B. Chessa *et al*., *Science* **324**, 532–536 (2009).
39. S. Sabatini, S. Bergerbrant, L. Ø. Brandt, A. Margaryan, M. E. Allentoft, *Archaeol. Anthropol. Sci.* **11**, 4909–4925 (2019).
40. M. E. Allentoft *et al*., *Nature* **522**, 167–172 (2015).
41. W. Haak *et al*., *Nature* **522**, 207–211 (2015).
42. S. Wilkin *et al*., *Nature* **598**, 629–633 (2021).
43. A. Scott *et al*., *Nat. Ecol. Evol.* **6**, 813–822 (2022).
44. F. J. Alberto *et al*., *Nat. Commun.* **9**, 813 (2018).
45. X. Yi *et al*., *Science* **329**, 75–78 (2010).
46. J. W. Kijas *et al*., *PLOS Biol.* **10**, e1001258 (2012).
47. E. García-Gámez *et al*., *PLOS ONE* **6**, e21158 (2011).
48. Q. Zhou *et al*., *J. Anim. Sci.* **101**, skad084 (2023).
49. A. S. Wilkins, R. W. Wrangham, W. T. Fitch, *Genetics* **197**, 795–808 (2014).
50. J. McCorriston, *Curr. Anthropol.* **38**, 517–535 (1997).
51. J. Cheng *et al*., *Anim. Biotechnol.* **34**, 2546–2553 (2023).
52. G.-W. Ma, S.-Z. Wang, N. Wang, H. Li, H. Yang, *Biochem. Genet.* **61**, 551–564 (2023).
53. F.-H. Lv *et al*., *Mol. Biol. Evol.* **31**, 3324–3343 (2014).
54. K. Kristiansen, M. L. S. Sørensen, S. Sabatini, S. Bergerbrant, *Wool in the Bronze Age. Concluding reflections. The Textile Revolution in Bronze Age Europe* (Cambridge Univ. Press, 2019), pp. 317–332.
55. E. A. Strand, M.-L. Nosch, in *The Textile Revolution in Bronze Age Europe: Production, Specialisation, Consumption*, S. Sabatini, S. Bergerbrant, Eds. (Cambridge Univ. Press, 2019), pp. 15–38.
56. S. E. Johnston *et al*., *Nature* **502**, 93–95 (2013).
57. F.-H. Lv *et al*., *Mol. Biol. Evol.* **39**, msab353 (2022).
58. K. G. Daly, Scripts_for_sheep_paper, Zenodo (2024); https://zenodo.org/records/13152045.

ACKNOWLEDGMENTS

We acknowledge the following persons and institutions without which this work and manuscript would not be possible: A. Ben-Tor, M. T. Atayi, S. Beath, E. Gladyr, I. Haciyev, M. Khasanov, L. Kistler, The University of Manchester, The Manchester Museum, F. McCormick, M. J. Nokandeh, H. Omrani, F. Özer, J. Roodenberg, S. A. Roodenberg, B. Sitch, M. Somel, and I. Wiechmann. We are grateful to the Research Institute for Cultural Heritage and Tourism of Iran (RICHT), The National Museum of Iran, the Bioarchaeology Laboratory of the Central Laboratory at the University of Tehran (BALUT), and the French Laboratory of Archéozoolgie et Archéobotanique (AASPE-UMR 7209) of the CNRS and the Muséum National d'Histoire Naturelle for having funded the archaeological expeditions for the Iranian sites and the conservation of the bioarchaeological material and their study. We also thank the ATM project ORIENTSPREAD (2017) of the MNHN and the University of Tsukuba and JSPS for their support. The sheep specimens reported in this study are under the curatorship of coauthors detailed in table S1, with the associated sample-level ENA accession numbers; sample contacts are also provided in the supplementary materials. **Funding:** This work was supported by the European Research Council under the European Union's Horizon 2020 research and innovation program (grant nos. 885729-AncestralWeave, 295729-CodeX, 295375-Persia and its Neighbors; K.G.D., V.E.M., A.J.H., Á.H., V.M., C.R., M.D.T., D.G.B., E.S.) and was supported in part by a grant from Science Foundation Ireland under grant no. 21/PATH-S/9515 (K.G.D.), Government of Ireland Postdoctoral Fellowship GOIPD/2020/605 (V.E.M.), and the CNRS International Research Project AnimalFarm. J.P. is supported by Deutsche Forschungsgemeinschaft (DFG) grant no. 165831460. B.B. was supported by the Taylor Family-Asia Foundation Endowed Chair in Ecology and Conservation Biology. C.Ç. was funded by the Institute for Aegean Prehistory (INSTAP). **Author contributions:** Conceptualization: D.G.B. and J.P. with input from J.B. and M.C.; Data curation: K.G.D., A.J.H., and Á.H.; Formal analysis: K.G.D., V.E.M., A.J.H., and Á.H.; Funding acquisition: D.G.B., M.C., and J.P.; Investigation: K.G.D., V.E.M., A.J.H., Á.H., V.M., M.D.T., C.R., Sh.G., and I.M.; Resources: M.Ö., G.D., Se.G., N.P., L.F., P.Z., S.S., B.B., L.O., M.P.P., J.M., I.V.A., A.O.A., O.V.A., D.N.S., Y.V.d.H., A.Z.-L., R.-M.A., H.H., H.D., Sa.A., S.B.D., D.D., H.F., R.K., Y.H., Al.S., J.L., M.A., G.D.S., C.M., V.B., R.B., C.Ç., N.B., Am.S., J.B., E.S., L.K.H., B.A., H.B., L.G., J.B., T.O.C., D.O., M.J., S.R., M.C., V.Ö., M.Z., L.A., M.M., and J.P.; Supervision: D.G.B.; Visualization: K.G.D., V.E.M., and Á.H.; Writing – original draft: D.G.B., K.G.D., V.E.M., and J.P.; Writing – review and editing: All authors. **Competing interests:** The authors declare that they have no competing interests. **Data and materials availability:** Raw reads and mitochondrial sequences have been deposited at the European Nucleotide Archive (ENA) with project number: PRJEB61808. Custom code generated for this study are available at Zenodo (*58*).

SUPPLEMENTARY MATERIALS

science.org/doi/10.1126/science.adn2094
Materials and Methods
Figs. S1 to S26
Tables S1 to 12
References (*59*–*233*)

Submitted 8 December 2023; resubmitted 10 May 2024
Accepted 3 December 2024
10.1126/science.adn2094

METALLOENZYMES

Conformational dynamics of a multienzyme complex in anaerobic carbon fixation

Max Dongsheng Yin[1]†, Olivier N. Lemaire[2]†, José Guadalupe Rosas Jiménez[3,4], Mélissa Belhamri[2], Anna Shevchenko[5], Gerhard Hummer[3]*, Tristan Wagner[2,6]*, Bonnie J. Murphy[1]*

In the ancient microbial Wood-Ljungdahl pathway, carbon dioxide (CO_2) is fixed in a multistep process that ends with acetyl–coenzyme A (acetyl-CoA) synthesis at the bifunctional carbon monoxide dehydrogenase/acetyl-CoA synthase complex (CODH/ACS). In this work, we present structural snapshots of the CODH/ACS from the gas-converting acetogen *Clostridium autoethanogenum*, characterizing the molecular choreography of the overall reaction, including electron transfer to the CODH for CO_2 reduction, methyl transfer from the corrinoid iron-sulfur protein (CoFeSP) partner to the ACS active site, and acetyl-CoA production. Unlike CODH, the multidomain ACS undergoes large conformational changes to form an internal connection to the CODH active site, accommodate the CoFeSP for methyl transfer, and protect the reaction intermediates. Altogether, the structures allow us to draw a detailed reaction mechanism of this enzyme, which is crucial for CO_2 fixation in anaerobic organisms.

The most ancient pathway for carbon dioxide (CO_2) fixation, the Wood-Ljungdahl pathway, also known as the reductive acetyl–coenzyme A (acetyl-CoA) pathway, is also the most efficient natural CO_2 fixation pathway in terms of adenosine triphosphate (ATP) input (*1*, *2*). This strictly anaerobic process, performed by a wide range of acetogenic bacteria and methanogenic archaea (*3*), is also used in biotechnology (*4*–*6*). In this pathway, the methyl branch transforms CO_2 into a methyl group bound to a cobalamin derivative (hereafter simplified as B12), and the carbonyl branch reduces CO_2 to carbon monoxide (CO). The latter reaction is catalyzed by an Fe-[Ni-3Fe-4S] cluster (C-cluster) in the carbon monoxide dehydrogenase subunit of the bifunctional carbon monoxide dehydrogenase/acetyl-CoA synthase complex (CODH/ACS) (*7*–*17*). The branches converge at the Ni-Ni-[4Fe-4S] cluster (A-cluster) localized in the ACS subunit (fig. S1) to generate acetyl-CoA from CO, the methyl group, and CoA (*8*, *9*, *18*). Subsequently, acetyl-CoA can be converted to acetate for energy conservation or assimilated into cellular carbon (*19*, *20*). Other microbes use the same enzyme for the reverse process of acetyl-CoA decarbonylation (*11*, *21*, *22*).

Structural insights into the catalytic reactions of CODH and ACS have been obtained from standalone enzymes and bifunctional CODH/ACS complexes, including those from *Moorella thermoacetica*, *Carboxydothermus hydrogenoformans*, and *Clostridium autoethanogenum* (*Mt*, *Ch*, and *Ca*, respectively) (*8*, *9*, *12*, *15*–*18*, *23*, *24*). However, the overall molecular mechanism of acetyl-CoA synthesis is still not fully understood owing to the complexity of the reaction, which requires several additional actors and substantial structural rearrangements of the ACS.

In one of the accepted scenarios, the reaction begins with CO_2 reduction at the C-cluster, which requires electron transfer from a ferredoxin (*25*). The electrons are first transferred to a solvent-exposed [4Fe-4S] cluster (D-cluster, alternatively a [2Fe-2S] cluster) (*7*, *12*, *14*, *26*–*28*) located on the symmetry axis of the CODH dimer before being transferred to the C-cluster through an intermediate [4Fe-4S] cluster (B-cluster). Once produced, CO is channeled to the A-cluster through a hydrophobic internal tunneling network and covalently binds as a carbonyl group to the proximal Ni (Ni_p) (*8*, *16*, *23*, *29*). Subsequently, the methyl-Co(III)-B12, carried by the corrinoid iron-sulfur protein (CoFeSP), interacts with ACS to transfer a methyl cation to the A-cluster (*30*, *31*). The methyl and carbonyl groups react to generate an acetylated A-cluster (*32*), which promotes the formation of acetyl-CoA through its reaction with the thiol group of CoA.

This reaction mechanism requires flexibility of the ACS as a prerequisite for complete turnover because the ACS must undergo sequential reactions dependent on ferredoxin, gas trafficking, CoFeSP, and CoA. The ACS is composed of three functional domains (A1, A2, and A3, from the N terminus to C terminus) separated by linkers that allow interdomain flexibility. Multiple conformational arrangements of the ACS have been shown through x-ray crystallography and negative-stain electron microscopy (*8*, *9*, *15*–*18*, *24*, *33*). However, high-resolution structures of the CODH/ACS complex with its partners or ligands are lacking.

In this study, we aimed to capture the CODH/ACS in action by visualizing the missing conformations in various protein-protein interaction or ligand-bound states. All presented results are derived from proteins anaerobically isolated from the biotechnologically relevant syngas converter *C. autoethanogenum*, an acetogen that we cultivated heterotrophically on fructose in the presence of H_2 and CO_2, as reported previously (*16*). Previous studies have shown that CODH/ACS from *C. autoethanogenum* catalyzes reversible CO oxidation with artificial electron acceptors or ferredoxin as the physiological partner and methylates the A-cluster with methylcobinamide (*16*, *34*, *35*) (see methods). In this work, to structurally characterize the mechanism of acetyl-CoA synthesis, we prepared solutions of CO-treated CODH/ACS-ferredoxin and iodomethane-treated CoFeSP. The solutions were mixed and rapidly plunge-frozen for cryo–electron microscopy (cryo-EM) analysis under anaerobic conditions at ~5% CO in the gas phase. The final mixture contained CODH/ACS heterotetramer, CoFeSP, and ferredoxin in a 1:2:1 molar ratio [all identified by mass spectrometry (*16*, *34*); fig. S2], with iodomethane as the methyl donor and CO as the carbonyl and electron donor. After electron microscopy imaging and initial data processing, we performed three-dimensional (3D) refinement with C_2 symmetry, yielding maps of the rigid core of the enzyme, which is composed of the CODH and A1, at resolutions reaching 1.94 Å (figs. S3 and S4A and tables S1 and S2). By further classifying the CODH/ACS into different states, we gained a detailed view of acetyl-CoA synthesis.

Ferredoxin-dependent CO_2 reduction at the C-cluster

The symmetric map of CODH/ACS exhibited an additional feature, which was not attributable to either the CODH or ACS, at the symmetry axis of CODH. It was further analyzed by focused classification and local refinement without symmetry applied, resulting in a map showing ferredoxin, harboring two [4Fe-4S] clusters, bound asymmetrically near the D-cluster on the C_2 symmetry axis (Fig. 1A and figs. S4B, S5, and S6A). The quality of the density map is substantially lower than that of the rest of the structure, which reflects the expected transient interaction. Hydrogen bonding and hydrophobic contacts stabilize the complex (fig. S6B), forming an interaction network that could be supplemented by electrostatic attraction between positively charged residues (Lys^{35}, Lys^{63}) on the flexible loops of the CODH and the negatively charged area of the ferredoxin (fig. S6C). A previous study questioned the role of the D-cluster as an electron entry or exit point owing to its midpoint potential in

[1]Redox and Metalloprotein Research Group, Max Planck Institute of Biophysics, Frankfurt am Main, Germany. [2]Max Planck Research Group Microbial Metabolism, Max Planck Institute for Marine Microbiology, Bremen, Germany. [3]Department of Theoretical Biophysics, Max Planck Institute of Biophysics, Frankfurt am Main, Germany. [4]Department of Theoretical Biophysics, IMPRS on Cellular Biophysics, Frankfurt am Main, Germany. [5]Max Planck Institute of Molecular Cell Biology and Genetics, Dresden, Germany. [6]Research Group Microbial Metabolism, Université Grenoble Alpes, CEA, CNRS, IBS, Grenoble, France.
*Corresponding author. Email: bonnie.murphy@biophys.mpg.de (B.J.M.); twagner@mpi-bremen.de (T.W.); gerhard.hummer@biophys.mpg.de (G.H.)
†These authors contributed equally to this work.

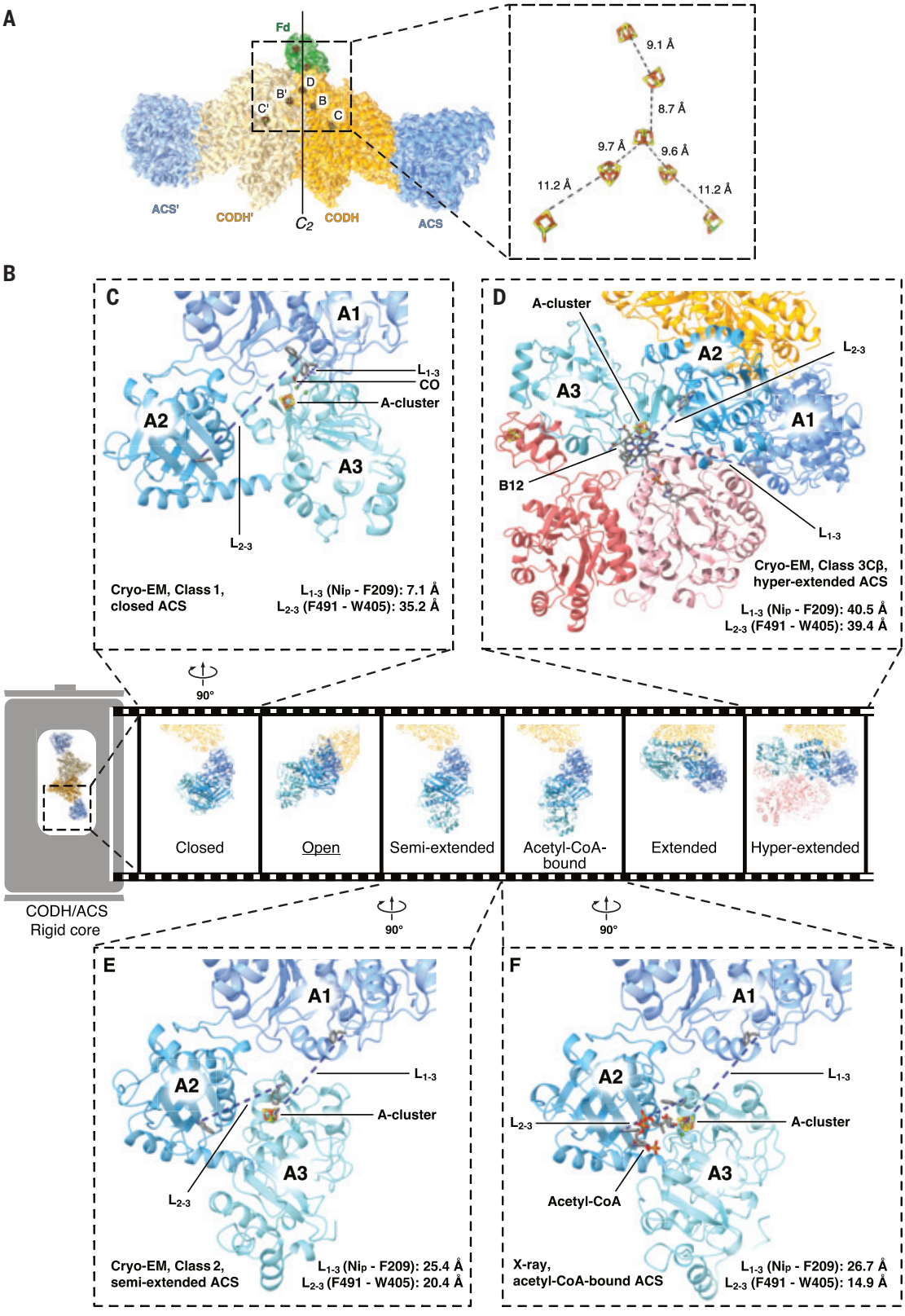

Fig. 1. Conformational gallery of the CODH/ACS. (**A**) Ferredoxin (Fd, green) docks at the C_2 symmetry axis of CODH (gold and wheat). The symmetry axis is indicated with a vertical line. A1 is displayed in blue. The cryo-EM density of the CODH/ACS-ferredoxin complex is displayed as a surface at 8.8σ, with colors matching the model. As seen in the inset, the binding conformation should allow efficient electron transfer between the [4Fe-4S] cluster of ferredoxin and the D-cluster of CODH; distances are shown as dashed lines. (**B** to **F**) The collection of flexible ACS conformations (B), with structures from this study highlighted and aligned based on the A1 domain with the open state obtained from *Mt*CODH/ACS (underlined, PDB ID 1OAO, chain D) and the extended state (*Ca*CODH/ACS, PDB ID 6YTT, chain A) of ACS. The Ni_p-F209 and F491-W405 distances (defined below as L_{1-3} and L_{2-3}, respectively) for the closed (C), hyperextended (D), semiextended (E), and acetyl-CoA–bound (F) ACS conformations are indicated by dashed lines, with the measured values provided alongside the structures. The ACS domains are shown in shades of blue, from darker at the N terminus to lighter at the C terminus, and the CoFeSP is shown in pink, with a darker shade for its large subunit. All metallocofactors are shown in stick representation. For clarity, the B12 domain of CoFeSP is omitted in (D).

the monofunctional CODH of *Rhodospirillum rubrum* (*25*, *36*). However, the observed interaction and the intercluster distance of 8.7 Å in our structure supports ferredoxin docking and electron transfer at the D-cluster (Fig. 1A) (*7*, *12*, *26*–*28*, *37*). Electrons are then transferred via the B-cluster to the catalytic C-cluster.

The experimental map at the C-cluster shows no evidence of a bound small-molecule ligand (fig. S7). An unrestrained model of the C-cluster exhibited a short distance (2.3 Å) between Ni

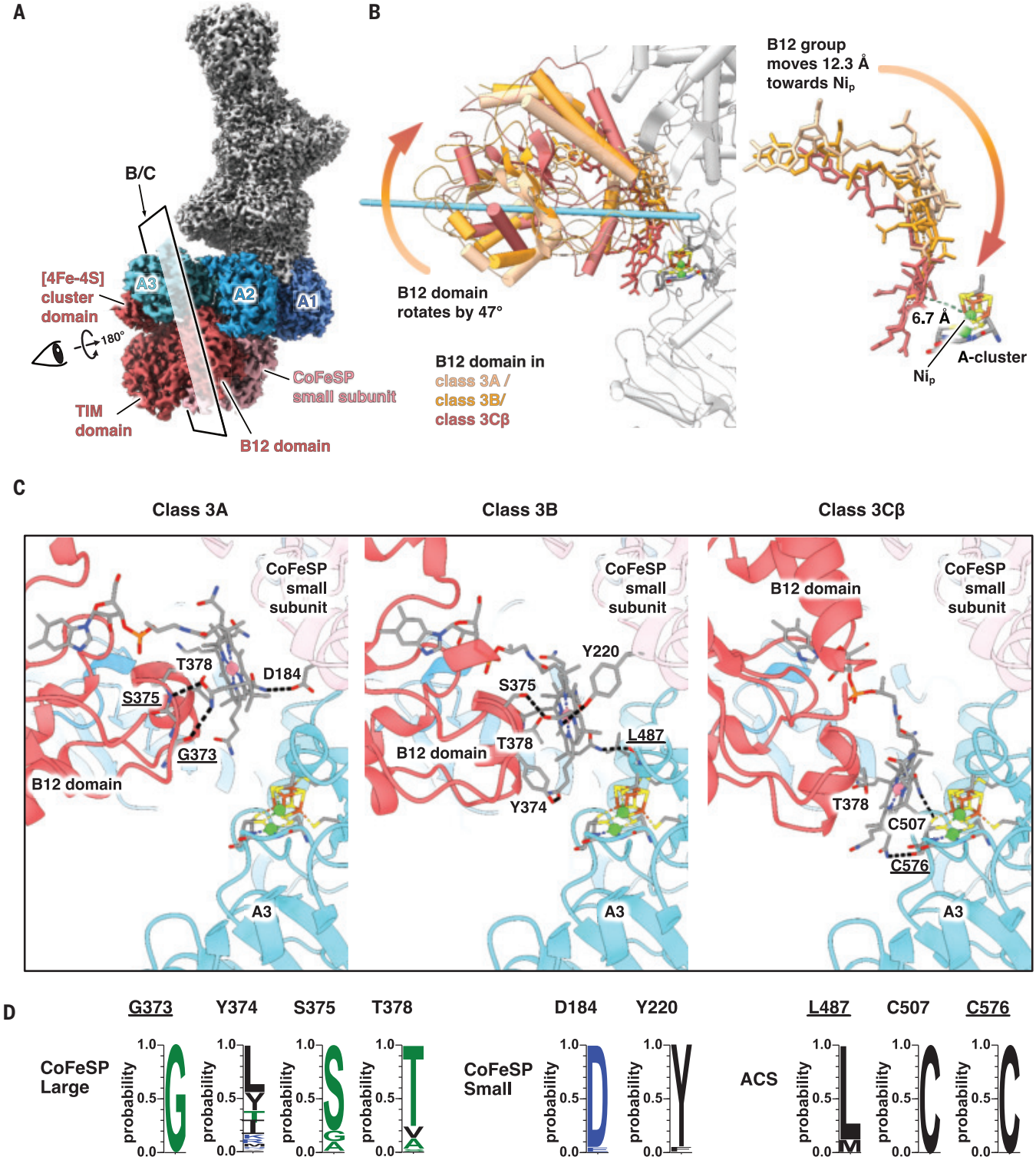

Fig. 2. In the hyperextended, CoFeSP-bound state, rotation of the CoFeSP B12 domain brings the B12 toward the Ni_p. (**A**) The cryo-EM map of the complex (class 3Cβ) showing ACS bound to CoFeSP in color, with the rest of the complex in gray. (**B**) The B12 domain undergoes a 47° rotation (the rotation axis is shown as a light blue bar) from class 3A to class 3Cβ, positioning the Co atom of B12 6.7 Å away from the Ni_p. The B12 domain and B12 are colored according to the rotational states, as indicated by the color code, and the rest of the complex is gray. (**C**) Detailed views of the three rotational states, with key hydrogen bonds indicated by dashed lines. Cofactors and residues of interest are in stick representation. In (A) and (C), the ACS domains are shown in shades of blue, from darker at the N terminus to lighter at the C terminus, and the CoFeSP is colored pink, with a darker shade for its large subunit. (**D**) Sequence conservation analysis shows that most of the B12-stabilizing residues are well conserved in bacteria and archaea. In both (C) and (D), residues involved in hydrogen bonding through their main chain atoms are underlined. Single-letter abbreviations for the amino acid residues depicted in the figures are as follows: A, Ala; C, Cys; D, Asp; E, Glu; F, Phe; G, Gly; H, His; I, Ile; K, Lys; L, Leu; M, Met; N, Asn; P, Pro; Q, Gln; R, Arg; S, Ser; T, Thr; V, Val; W, Trp; and Y, Tyr.

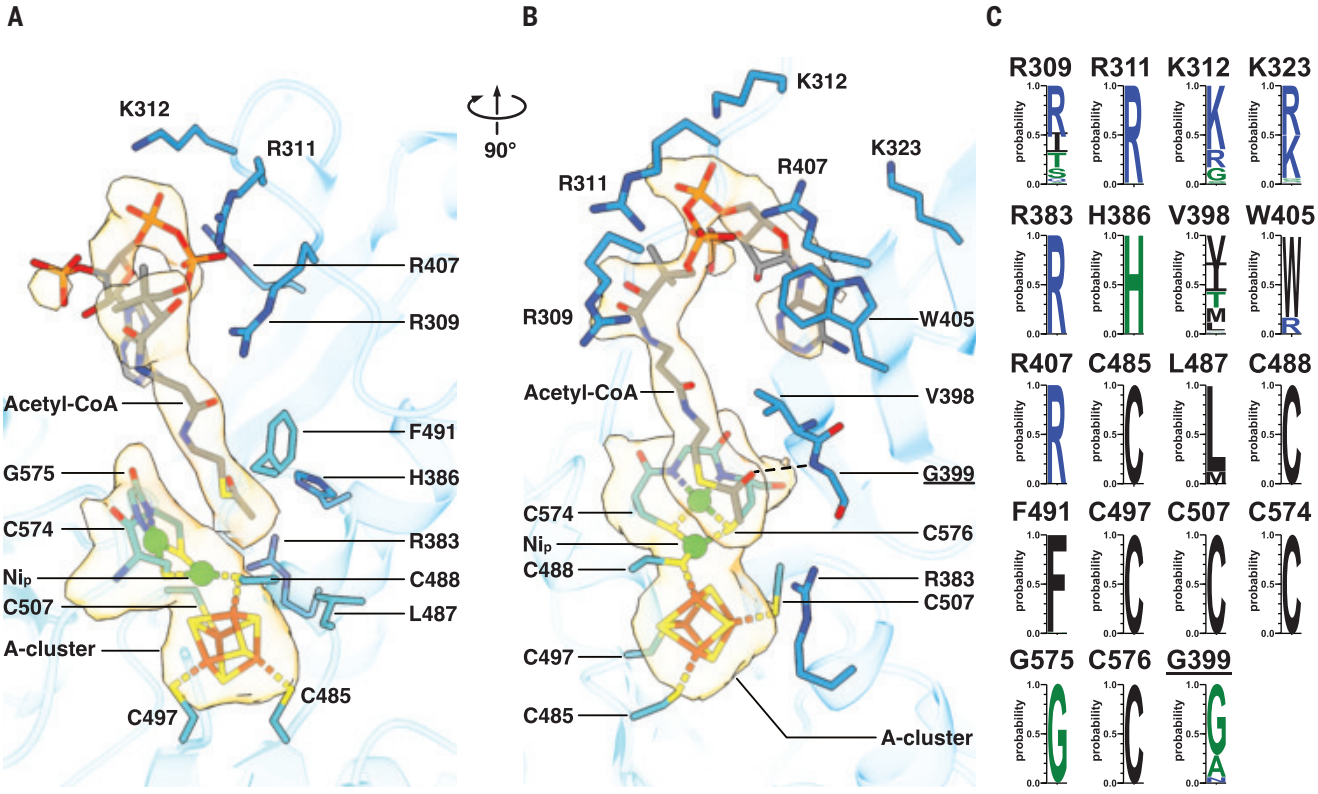

Fig. 3. Crystal structure of the CODH/ACS in the acetyl-CoA–bound state. (**A** and **B**) Close-up views of acetyl-CoA binding, highlighting key interacting residues. The electron density maps ($2F_o$-F_c) for the acetyl-CoA and the A-cluster are shown as light orange surfaces contoured at 1.1σ. A hydrogen bond is indicated by a dashed line. The crystal structure was obtained from a sample different from that used in the cryo-EM analysis. For clarity, residues 323, 398, 399, and 405 in (A) and residues 386, 487, and 491 in (B) are omitted. ACS is colored light blue; acetyl-CoA and selected residues are shown in stick representation and are colored as follows, except for acetyl-CoA carbon, which is gray: carbon in light blue, oxygen in red, nitrogen in dark blue, sulfur in yellow, phosphorus in light orange, iron in orange, and nickel in green. (**C**) Conservation of the residues in bacteria and archaea. Residues involved in hydrogen bonding through their main chain atoms are underlined.

and the pendant iron (Fe_u), both refined with partial occupancy (~50 and ~60 to 70%, respectively). The possibility of a Ni–Fe bond acting as an electron store was previously proposed (*38*), though the length of a typical Ni–Fe single bond is expected to be on the order of 2.5 Å (*39*, *40*). Mixed quantum mechanics/molecular mechanics (QM/MM) calculations using density functional theory (DFT) for the quantum region (supplementary text, figs. S8 and S9, and table S3) support this hypothesis, yielding an average Ni-Fe_u distance of 2.5 Å, which we have modeled accordingly in the C-cluster (fig. S7A).

Conformational spectrum of ACS allows A-cluster carbonylation

Poorly resolved density was present at the expected positions of domains A2 and A3. Using focused classification and refinement of symmetry-expanded datasets (fig. S10), we were able to separate two classes (named class 1 and 2 in the processing workflow, refined to resolutions of 2.83 and 3.29 Å, respectively) with clear density for A2 and A3 but without additional density attributed to CoFeSP (figs. S4, C and D, S10, and S11; and tables S2 and S4). The rearrangement of the domains can be modeled as multibody motion (*33*) with very low root mean square deviation of each domain across different conformational states and organisms (table S5). Multiple terms have been used to describe the ACS conformation in previous works, such as "open," "closed," and "extended." In this work, we introduce a reference framework for a simple comparison of these states in terms of distances between conserved sites in the three domains. In addition to the global opening and closing of the ACS owing to a highly flexible loop connecting A1 to A2 [previously shown to be highly sensitive to limited proteolysis (*16*)], the relative positions of A2 and A3 can also undergo an opening-closing movement, allowing or occluding access to the Ni_p independently of the A1 position. To best characterize this dual flexibility, we propose the distances Ni_p-F209 and F491-W405 (*Ca*ACS numbering, where F is Phe and W is Trp) as proxies of interdomain 1-3 and interdomain 2-3 spacing, respectively ($L_{1\text{-}3}$ and $L_{2\text{-}3}$, where L stands for length).

The *Ca*ACS class 1 resembles the closed conformation of *Mt*CODH/ACS and *Ch*CODH/ACS (*8*, *9*, *15*, *17*), featuring a short $L_{1\text{-}3}$ and a long $L_{2\text{-}3}$ (Fig. 1, B and C; figs. S12A and S13; and table S6). In the closed state, the A2-A3 space is opened and the A-cluster apposes the A1 surface. A predicted CO channel emanating from the C-cluster opens into a solvent-occluded space around the A-cluster (*29*). In this state, an additional density observed on Ni_p is modeled as a CO bound to the tetrahedral Ni (fig. S14, A and B). Conserved hydrophobic residues Val^{125}, Phe^{209}, and Phe^{491} are positioned similarly to their counterparts in the CO-bound state of *Mt*CODH/ACS (*15*) (fig. S14, B and C). These residues were proposed to stabilize the tetrahedral geometry of the carbonylated Ni_p, facilitate CO diffusion through internal cavities to the A-cluster, and hinder the A-cluster from adopting a methylation-compatible geometry (*15*).

In contrast, class 2 corresponds to the semi-extended state previously described in the crystallographic structure of *Ca*CODH/ACS [Protein Data Bank (PDB) ID 6YTT, chain D] (*16*) (Fig. 1, B and E, and fig. S12B). In this state, A3 is disengaged from A1 and the Ni_p is occluded by the closing of A2-A3 (fig. S13A). The resolution is too limited to describe a bound ligand on the A-cluster

(carbonyl or methyl). Class 2 likely reflects a conformation en route toward CoFeSP docking, in which the Ni_p is protected to avoid side reactions while the interdomain A1-A3 space is gradually opened (table S6).

CoFeSP interaction promotes the ACS hyperextended state

Focused classification of the flexible ACS unveiled a third class corresponding to the CODH/ACS-CoFeSP complex (Fig. 1, B and D; figs. S10, S11, and S15; and tables S2 and S4). Compared with the extended state obtained by crystallography (PDB ID 6YTT, chain A) (*16*), ACS complexed with CoFeSP maintains a long L_{1-3} and additionally opens L_{2-3} by means of a 59°

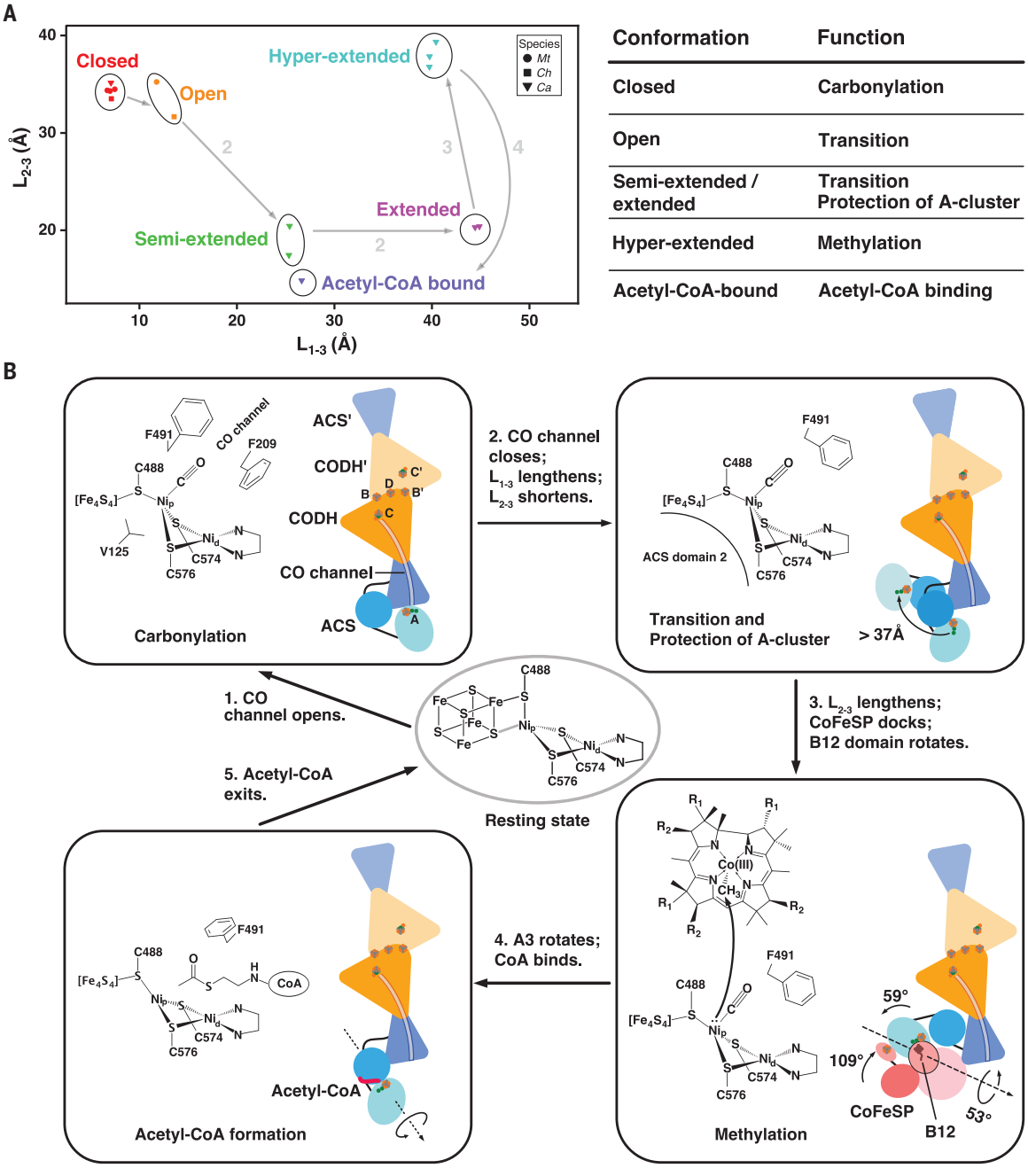

Fig. 4. A conformation-based model of acetyl-CoA synthesis. (**A**) The conformational 2D spectrum of representative structures of CODH/ACS and monomeric ACS. The L_{1-3} and L_{2-3} distances represent the separations between Ni_p and F209, and between F491 and W405 (*Ca*ACS numbering), respectively, and all measured distances are listed in table S6. One proposed reaction route, starting with carbonylation, is marked by arrows and numbered according to the model in (B). The function of each conformation is summarized in the table. (**B**) A proposed mechanism of acetyl-CoA synthesis in the sequential carbonylation-methylation scenario. Schematic representation of key CODH/ACS conformations with their functional roles, as well as the corresponding configurations of the A-cluster, are presented in the boxes. The reaction route is labeled with solid arrows, and critical domain motions during the reaction are marked by curved arrows and are further illustrated in figs. S16B, S19A, S28A, and S30. In the ligand-free resting state, the feasible Ni_p-S coordination is indicated by a gray stick. For clarity, the nucleotide tail of B12 is omitted. R_1 denotes the acetamide arm, and R_2 denotes the propionamide arm of the B12 corrin ring.

rotation of A3, leading to a hyperextended state (figs. S13C and S16 and table S6). Consequently, this is the sole state obtained in our study in which the A-cluster is fully accessible for methyl transfer.

The hyperextended state is stabilized by interactions with CoFeSP at three sites: The CoFeSP small subunit docks to both A1 and A3, the [4Fe-4S] cluster domain of the CoFeSP large subunit (residues 1 to 57) interacts with A3 (figs. S17 and S18), and the B12-binding domain (CoFeSP large subunit, residues 326 to 446) also interacts with A3, as discussed below. The distance between the [4Fe-4S] cluster and the A-cluster (32.3 Å; fig. S18) precludes electron transfer, which agrees with previous studies that indicated no direct involvement of the CoFeSP [4Fe-4S] cluster in ACS methylation (*41*, *42*). Rather, our findings support a function of this domain in stabilizing the hyperextended ACS. A comparison of our results with structures of CoFeSP from different species (*Ch*, *Mt*, *Ca*) in isolation and in interaction with the activator or methyltransferase (MeTr) protein partners showed large conformational changes of the [4Fe-4S] cluster and B12-binding domains associated with CoFeSP binding to its partner proteins (fig. S19) (*43*–*45*). Residues involved in the interaction between ACS and CoFeSP are mostly conserved among bacteria and archaea (Fig. 2D and figs. S17 and S18), suggesting a similar mode of action across microbial kingdoms.

Methyl transfer reaction through B12 domain motion

The hyperextended state of the ACS enables the bulky CoFeSP to access the A-cluster (class 3; Figs. 1D and 2), but additional motion of the CoFeSP is required to bring the B12 close enough for methyl transfer (*43*, *45*). By 3D variability analysis (3DVA) of class 3, we resolved a rotational motion of the B12-binding domain (Fig. 2B). Supervised classification using three intermediate reconstructions from 3DVA led to three subsets (3A, 3B, and 3C), with 3A and 3B refined to 2.71 and 2.65 Å, respectively (table S2). The subset 3C appeared as a mixture of two states (fig. S20). By building preliminary models for each configuration and using corresponding volumes, which were generated with the ChimeraX molmap command, for supervised classification of class 3C, we obtained two substates, 3Cα and 3Cβ, refined to 2.78 and 2.88 Å, respectively (table S2). These four states represent points along a conformational spectrum in which the B12 domain rotates, allowing B12 to approach Ni_p (Fig. 2, fig. S21, and movie S1), which is reminiscent of the motion described in the *Mt*CoFeSP complexed with its MeTr (fig. S22) (*45*). In the 3A-3B-3Cβ sequential movement, the B12 ring progressively breaks all hydrogen bonds with the CoFeSP and establishes new ones with the ACS, including with cluster-ligating cysteine residues of the A-cluster (Fig. 2C). This rotation also reduces the solvent exposure of the A-cluster [4Fe-4S] cubane. The conserved hydrogen bond–forming residues stabilize the B12 as it moves toward the A-cluster, with the shortest Co-Ni_p distance of 6.7 Å observed in 3Cβ (Fig. 2, B to D), which is nearly sufficient for direct methyl transfer. We suppose that a transient state exists with a further shortened distance that is suitable for methyl transfer, as in the CoFeSP-MeTr, but this state appears too rare to be captured by classification or 3DVA. No obvious density for a methyl or carbonyl group could be detected at either the corrinoid or the Ni_p site. We assessed the possibility of ligand loss due to radiation damage at the site by reconstructing only early frames, which corresponded to as little as 3.7 megagray (*46*), but did not observe notable differences in the density (fig. S23A).

In the structures that exhibited no external ligand at Ni_p, models consistently refined to relatively short (bonding) distances between the Ni_p and S1 sulfide of the [4Fe-4S] cluster (fig. S23B). QM/MM calculations (fig. S8, C and D, and supplementary text) indeed predicted that a strong attractive interaction with the [4Fe-4S] cluster would bring Ni_p into bonding distance (fig. S24 and table S7). Therefore, the Ni_p geometry modeled in our ligand-free cryo-EM structures is chemically reasonable, even though a low occupancy (~45 to 59%) of the Ni_p site, the moderate resolution, and the putatively mixed state may hamper the unambiguous interpretation of the Ni_p geometry and the detection of ligands from the potential map.

The acetyl-CoA complex—a snapshot of the bound reaction product

Carbonyl and methyl groups bound at Ni_p combine to form an acetyl (*32*), which is subsequently transferred to the thiol group of CoA. Despite our efforts, we could not unambiguously detect additional cryo-EM map density in CODH/ACS treated with CoA or acetyl-CoA. However, by cocrystallizing *Ca*CODH/ACS with acetyl-CoA, we obtained a 2.93-Å x-ray structure of the product-bound complex ($CODH/ACS_{AC}$; Fig. 1F and table S8). The global conformations resemble those of the as-isolated *Ca*CODH/ACS (*16*) (fig. S25). However, the previously semiextended ACS now exhibits additional density spanning the A2 surface and reaching A3, modeled as acetyl-CoA, whereas the extended ACS of the other asymmetric unit lacks such density, reflecting the requirement for a specific conformation to allow ligand binding (Fig. 3, A and B, and figs. S26 and S27).

The acetyl-CoA primarily interacts with A2 residues, with the adenine group being stabilized by Trp^{405} through π-stacking, and the diphosphate facing a positively charged patch rich in lysines and arginines (Fig. 3B and fig. S27A). The relatively high b-factors of the adenosine diphosphate moiety (fig. S27B) indicate only partial stabilization of the acetyl-CoA in the A2-A3 cleft, whose structure is restrained by the crystalline packing.

Compared with the ligand-free semiextended ACS resolved by cryo-EM, acetyl-CoA–bound ACS exhibits a 15° rotation of A3 (fig. S28A), whereas superposition with the previously obtained ligand-free crystal structure shows a more limited rotation of A3 by around 5° (fig. S29), indicating that both crystal packing and ligand binding are likely contributing to the rotation of A3. The rotation allows for additional contacts (Fig. 3), prevents potential clashes (fig. S26B) between acetyl-CoA and A3, and brings the A-cluster into closer proximity to the acetyl-CoA (fig. S28B). In this state, the acetyl-bearing sulfur atom is 4.13 Å away from the Ni_p, and the acetyl group is stabilized by a hydrogen bond between its carbonyl moiety and the main chain of Gly^{399}, as well as an interaction between its methyl moiety and His^{386} (Fig. 3, A and B). The flexible Phe^{491} swings away from the Ni_p (fig. S28C) to provide space for CoA attack. The conserved Arg^{383} and His^{386}, located near the A-cluster in the structure (Fig. 3, A and B), are likely crucial for acetyl transfer. Superposition with an acetylated A-cluster structure from a previous DFT study (*31*) indicates that Arg^{383} would be in the direct vicinity of the Ni_p-bound acetyl group, putatively stabilizing it through hydrogen bonding (fig. S28D). His^{386} is well positioned in our structure to facilitate deprotonation of the thiol group (Fig. 3A), consistent with a previous analysis (*18*). The majority of the residues involved in acetyl-CoA stabilization in the $CODH/ACS_{AC}$ were already suggested in *Mt*ACS (*18*), and most of these interacting residues are conserved among bacteria and archaea (Fig. 3C).

Discussion

In this work, we describe structural snapshots of the reaction catalyzed by CODH/ACS upon incubation with ferredoxin, CO, CoFeSP, and iodomethane. We observed a mixture of different states of the complex, which we attribute to the fact that the sample was not under turnover owing to the absence of CoA and to the transient nature of protein-protein interactions.

By providing structural insights into the electron transfer, methyl transfer, and acetyl-CoA formation steps, our work advances decades of studies on the intricate catalytic cycle of the CODH/ACS. The mechanism requires a wide conformational range of ACS mediated by interdomain flexibility, as proposed by previous studies (*25*, *33*). To simplify the nomenclature and comparison of these conformations, we introduced simple metrics based on the interdomain distances $L_{1\text{-}3}$ and $L_{2\text{-}3}$ to allow conformational states to be clustered in a 2D landscape (Fig. 4A and table S6) and to

visualize a conformation-based model of the overall reaction of the CODH/ACS (Fig. 4B). In a sequential carbonylation-methylation scenario, the reaction begins with ferredoxin docking on the D-cluster and the subsequent electron transfer to drive the formation of CO. A closed state of ACS is required to allow the controlled diffusion of CO from the C-cluster to the A-cluster for Ni_p carbonylation (*15*). To reach the methylation-compatible hyperextended state, the A-cluster–carrying A3 must undock from the A1 and move by around 37 Å (fig. S30), which could leave the reactive carbonyl-Ni_p site exposed to solvent. This appears to be mitigated by the closing of $L_{2\text{-}3}$ in the semiextended and extended states (Fig. 4A and fig. S13, A and B), which shelters the A-cluster. Upon binding of CoFeSP, the hyperextended state is stabilized, characterized by its long-distance $L_{2\text{-}3}$ and exposed A-cluster (Figs. 1D and 4A, fig. S13C, and table S6). The B12 domain of CoFeSP "waltzes" toward this open space, positioning the B12 close enough for the methyl transfer. The carbonyl and methyl groups react to a Ni_p-bound acetyl group, and CoFeSP dissociates from ACS, allowing further conformational change. Although CoA primarily interacts with A2, it must be brought near the A-cluster on A3 to further stabilize the binding and initiate acetyl transfer. Thus, acetyl-CoA formation appears to require a return to shorter $L_{2\text{-}3}$, where A3 is rotated relative to the semiextended state to finely tune the cleft between A2 and A3 for the nucleophilic attack of the thiol group of CoA (fig. S28A). CoA binding may partially drive the A3 rotation, which could explain why this conformation was not observed in our CoA-free cryo-EM sample. After acetyl-CoA release, the ACS returns to the closed conformation for another catalytic cycle.

The proposed scenario does not exclude a reverse sequential order, that is, a sequential methylation-carbonylation process, or the possibility of a random reaction mechanism. We note that among all characterized *Ca*ACS structures obtained by cryo-EM from the same sample, a carbonyl ligand is observed only in the closed state, although this may also reflect experimental limitations.

The overall architecture of *Ca*CODH/ACS differs from the model *Mt*CODH/ACS or *Ch*CODH/ACS (*16*). However, aligning all reported *Ca*ACS conformations to the rigid A1 (N-terminal domain) of *Mt*ACS does not result in any clashes with the rigid core of *Mt*CODH. This suggests that the conformational states and reaction mechanism described here could be generalized to complexes that include *Mt*CODH/ACS and *Ch*CODH/ACS, in which the N-terminal domain of ACS forms different contacts with the CODH dimer (fig. S31).

To complete the reaction landscape of ACS, several intermediate structures are still needed, including methyl-bound, CO- and methyl-bound, acetyl-bound, and CoA-bound ACS. Moreover, it will be important to clarify how large-scale conformational changes are triggered or regulated, and how these motions relate to atomic-scale rearrangements at the A-cluster, to understand this reversible and central enzyme in the global carbon cycle.

REFERENCES AND NOTES

1. M. C. Weiss *et al*., *Nat. Microbiol.* **1**, 16116 (2016).
2. N. R. Boyle, J. A. Morgan, *Metab. Eng.* **13**, 150–158 (2011).
3. O. N. Lemaire, M. Jespersen, T. Wagner, *Front. Microbiol.* **11**, 486 (2020).
4. J. K. Heffernan *et al*., *Front. Bioeng. Biotechnol.* **8**, 204 (2020).
5. R. de Souza Pinto Lemgruber *et al*., *Metab. Eng.* **53**, 14–23 (2019).
6. B. Bourgade, C. M. Humphreys, J. Millard, N. P. Minton, M. A. Islam, *ACS Synth. Biol.* **11**, 1790–1800 (2022).
7. C. L. Drennan, J. Heo, M. D. Sintchak, E. Schreiter, P. W. Ludden, *Proc. Natl. Acad. Sci. U.S.A.* **98**, 11973–11978 (2001).
8. T. I. Doukov, T. M. Iverson, J. Seravalli, S. W. Ragsdale, C. L. Drennan, *Science* **298**, 567–572 (2002).
9. C. Darnault *et al*., *Nat. Struct. Biol.* **10**, 271–279 (2003).
10. J. H. Jeoung, H. Dobbek, *Science* **318**, 1461–1464 (2007).
11. W. Gong *et al*., *Proc. Natl. Acad. Sci. U.S.A.* **105**, 9558–9563 (2008).
12. Y. Kung, T. I. Doukov, J. Seravalli, S. W. Ragsdale, C. L. Drennan, *Biochemistry* **48**, 7432–7440 (2009).
13. L. Domnik *et al*., *Angew. Chem. Int. Ed.* **56**, 15466–15469 (2017).
14. E. C. Wittenborn *et al*., *eLife* **7**, e39451 (2018).
15. S. E. Cohen *et al*., *ACS Catal.* **10**, 9741–9746 (2020).
16. O. N. Lemaire, T. Wagner, *Biochim. Biophys. Acta Bioenerg.* **1862**, 148330 (2021).
17. J. Ruickoldt, Y. Basak, L. Domnik, J. H. Jeoung, H. Dobbek, *ACS Catal.* **12**, 13131–13142 (2022).
18. A. Volbeda, C. Darnault, X. Tan, P. A. Lindahl, J. C. Fontecilla-Camps, *Biochemistry* **48**, 7916–7926 (2009).
19. K. Schuchmann, V. Müller, *Nat. Rev. Microbiol.* **12**, 809–821 (2014).
20. J. Mock *et al*., *J. Bacteriol.* **197**, 2965–2980 (2015).
21. A. Biester, A. N. Marcano-Delgado, C. L. Drennan, *Biochemistry* **61**, 2797–2805 (2022).
22. A. Biester, D. A. Grahame, C. L. Drennan, *Proc. Natl. Acad. Sci. U.S.A.* **121**, e2410995121 (2024).
23. T. I. Doukov, L. C. Blasiak, J. Seravalli, S. W. Ragsdale, C. L. Drennan, *Biochemistry* **47**, 3474–3483 (2008).
24. V. Svetlitchnyi *et al*., *Proc. Natl. Acad. Sci. U.S.A.* **101**, 446–451 (2004).
25. M. Can, F. A. Armstrong, S. W. Ragsdale, *Chem. Rev.* **114**, 4149–4174 (2014).
26. H. Dobbek, V. Svetlitchnyi, L. Gremer, R. Huber, O. Meyer, *Science* **293**, 1281–1285 (2001).
27. J. Chen *et al*., *Biochemistry* **42**, 14822–14830 (2003).
28. E. C. Wittenborn *et al*., *ACS Catal.* **10**, 7328–7335 (2020).
29. A. Biester, S. Dementin, C. L. Drennan, *J. Inorg. Biochem.* **230**, 111774 (2022).
30. W. P. Lu, S. R. Harder, S. W. Ragsdale, *J. Biol. Chem.* **265**, 3124–3133 (1990).
31. M. Can *et al*., *J. Am. Chem. Soc.* **145**, 13696–13708 (2023).
32. S. W. Ragsdale, H. G. Wood, *J. Biol. Chem.* **260**, 3970–3977 (1985).
33. S. E. Cohen *et al*., *Structure* **29**, 43–49.e3 (2021).
34. O. N. Lemaire, M. Belhamri, A. Shevchenko, T. Wagner, bioRxiv 2024.07.29.605569 [Preprint] (2024); https://doi.org/10.1101/2024.07.29.605569.
35. S. Wiley *et al*., *J. Biol. Chem.* **300**, 107503 (2024).
36. J. L. Craft, P. W. Ludden, T. C. Brunold, *Biochemistry* **41**, 1681–1688 (2002).
37. C. C. Page, C. C. Moser, X. Chen, P. L. Dutton, *Nature* **402**, 47–52 (1999).
38. P. A. Lindahl, *J. Inorg. Biochem.* **106**, 172–178 (2012).
39. E. Garcin *et al*., *Structure* **7**, 557–566 (1999).
40. H. Ogata, K. Nishikawa, W. Lubitz, *Nature* **520**, 571–574 (2015).
41. S. Menon, S. W. Ragsdale, *Biochemistry* **37**, 5689–5698 (1998).
42. S. Menon, S. W. Ragsdale, *J. Biol. Chem.* **274**, 11513–11518 (1999).
43. S. Goetzl, J. H. Jeoung, S. E. Hennig, H. Dobbek, *J. Mol. Biol.* **411**, 96–109 (2011).
44. S. E. Hennig *et al*., *Nat. Commun.* **5**, 4626 (2014).
45. Y. Kung *et al*., *Nature* **484**, 265–269 (2012).
46. L. A. Baker, J. L. Rubinstein, *Methods Enzymol.* **481**, 371–388 (2010).
47. J. G. Rosas-Jimenez *et al*., QM/MM calculations and geometry optimizations of C- and A-clusters in CODH/ACS, the key enzyme in the Wood-Ljungdahl pathway. Version v1. Zenodo (2024); https://doi.org/10.5281/zenodo.12705281.
48. O. N. Lemaire, Sequence alignments for the determination of residue conservation in ACS, CoFeSP large subunit and CoFeSP small subunit. Version v1. Zenodo (2024); https://doi.org/10.5281/zenodo.12785604.
49. A. Shevchenko, MS raw data for "Conformational dynamics of a multienzyme complex in anaerobic carbon fixation." Version v1. Edmond (2024); https://doi.org/10.17617/3.O2LZWI.

ACKNOWLEDGMENTS

The Redox and Metalloprotein research group is grateful to the Central Electron Microscopy Facility at the Max Planck Institute of Biophysics for providing cryo-EM infrastructure and technical support and to the Max Planck Society for their support. We thank R. Zimmermann for her expertise and support in the anaerobic work. The Microbial Metabolism research group thanks the Max Planck Institute for Marine Microbiology and the Max Planck Society for their continuous support. We also thank C. Probian and R. Appel for their assistance in the Microbial Metabolism laboratory. We thank the Swiss Light Source (SLS) synchrotron, especially the staff of beamline X06DA. **Funding:** This work was supported by funding from the Max Planck Society (to B.J.M., T.W., and G.H.) and the German Research Foundation (Heinz Maier-Leibnitz prize funding to B.J.M.). T.W. was additionally supported by the Deutsche Forschungsgemeinschaft priority program 1927, "Iron-Sulfur for Life" WA 4053/1-1. **Author contributions:** Conceptualization: B.J.M., T.W., M.D.Y., O.N.L.; Methodology: M.D.Y., O.N.L., J.G.R.J., A.S., G.H., T.W., B.J.M., M.B.; Investigation: M.D.Y., O.N.L., J.G.R.J., M.B., A.S.; Visualization: M.D.Y., O.N.L., J.G.R.J., A.S.; Funding acquisition: B.J.M., T.W., G.H.; Project administration: B.J.M., T.W., G.H.; Supervision: B.J.M., T.W., G.H.; Writing – original draft: M.D.Y., O.N.L., J.G.R.J., B.J.M., T.W.; Writing – review and editing: M.D.Y., O.N.L., J.G.R.J., M.B., A.S., G.H., T.W., B.J.M. **Competing interests:** The authors declare no competing interests. **Data and materials availability:** Cryo-EM structures of the CODH/ACS are available from the PDB under accession codes 9FZY (CoFeSP-bound state, class 3A), 9FZZ (CoFeSP-bound state, class 3B), 9G00 (CoFeSP-bound state, class 3Cβ), 9G01 (closed and CO-bound state), 9G02 (semiextended state), and 9G03 (ferredoxin-bound state). Maps and half-maps are available from the Electron Microscopy Data Bank (EMDB) under accession codes 50897 to 50909. The crystal structure of acetyl-CoA–bound CODH/ACS is available from the PDB under accession code 9G7I. Atomic coordinates from the QM/MM calculations are archived in Zenodo (*47*). The sequence alignment files used for the construction of figures are also archived in Zenodo (*48*). Raw mass spectrometry data are archived under accession code O2LZWI in Edmond (*49*), an open research 2data repository of the Max Planck Society.

SUPPLEMENTARY MATERIALS

science.org/doi/10.1126/science.adr9672
Materials and Methods
Supplementary Text
Figs. S1 to S31
Tables S1 to S8
References (*50*–*87*)
MDAR Reproducibility Checklist
Movie S1

Submitted 31 July 2024; accepted 25 November 2024
10.1126/science.adr9672

CONSERVATION

Tiger recovery amid people and poverty

Yadvendradev V. Jhala[1]*†, Ninad Avinash Mungi[1,2], Rajesh Gopal[3]‡, Qamar Qureshi[1]

Recovery of large yet ecologically important carnivores poses a formidable global challenge. Tiger (*Panthera tigris*) recovery in India, the world's most populated region, offers a distinct opportunity to evaluate the socio-ecological drivers of megafauna recovery. Tiger occupancy increased by 30% (at 2929 square kilometers per year) over the past two decades, leading to the largest global population occupying ~138,200 square kilometers. Tigers persistently occupied human-free, prey-rich protected areas (35,255 square kilometers) but also colonized proximal connected habitats that were shared with ~60 million people. Tiger absence and extinction were characterized by armed conflict, poverty, and extensive land-use changes. Sparing land for tigers enabled land sharing, provided that socioeconomic prosperity and political stability prevailed. India's tiger recovery offers cautious optimism for megafauna recovery, particularly in the Global South.

The Anthropocene is characterized as an epoch of species extinction and species attrition in numbers and range (*1*). Large carnivore populations across the world are most affected, with their recovery posing a formidable challenge to the modern world (*2*). Habitat loss, prey depletion, conflict with humans, and illegal demand for their body parts, combined with low densities and large space requirements for viable population, have driven large carnivores to numbers at which many have lost their functional role and some are on the brink of extinction (*3*, *4*). Losses of large carnivore populations downgrade trophic cascades, affecting ecosystem functioning, disease regulation, and socio-ecological resilience across ecosystems (*5*). Often, conservationists capitalize on the functions and charisma of these large carnivores to garner resources for restoring their populations, which entails restoring their ecosystems, and for allied services (*6*, *7*). Nonetheless, recovery of apex predators remains an exception rather than a rule, with success stories skewed to developed parts of the world (*8*, *9*) and few examples from developing countries (*10*, *11*). Recovery of large carnivores in fragmented habitats amid crowded and poverty-ridden regions of the Global South is a difficult proposition, often enforced through a dogmatic vision of separating people from predators: land sparing (*12*). The alternative—land sharing, between the people and predators (*13*)—is critiqued as unattainable, on the grounds that overlap can only exacerbate conflict (*14*). Land sparing and land sharing are looked on as opposing views; advocates of each point to the other's limitations (*8*). In this work, we demonstrated that both views of land sparing and land sharing were required for recovering tiger populations across India, suggesting that both paradigms play a part in the future of large carnivores.

The tiger acts as a charismatic flagship and an umbrella species for Asian forests but has been extirpated from more than 90% of its historic range over the past century, leaving only about 3600 wild tigers at the onset of this century (*15*). For the first time in modern history, tiger range country leaders and conservation practitioners met at St. Petersburg, Russia, in 2010 to forge the Global Tiger Recovery Program and targeted doubling the tiger population by 2022 (*16*). India achieved this target and now holds ~75% of the global population of tigers amid some of the highest human densities in the world (*16*, *17*). Key to this success are the linked scientific policies backed by governments' commitments and people's participation (*16*). However, it is crucial to evaluate socio-ecological factors that on the ground are related to persistence, recovery, and localized extinction of tigers. This evaluation becomes pertinent considering investments made for land sparing (creation of human-free protected areas through incentivized voluntary relocation of people) and land sharing (streamlining socioeconomic benefits) for tigers in this region with high poverty and the highest human densities (*18*, *19*). Although the success of tiger recovery is symbolized by its population doubling, it is critical to examine whether the population growth resonates with the intended flagship role of the tiger in conserving and increasing biodiverse areas. Hence, we explored the dynamics of tiger occupancy in India to evaluate its recovery from 2006 to 2018; evaluated the socio-ecological characteristics of local extinctions, colonization, and persistence of tigers in India; and examined the spatial association in tiger occurrence with other megafauna species.

India has monitored the distribution and abundance of tigers every 4 years since 2006 by surveying all potential tiger habitats (~381,000 km^2) for occurrence of tigers, their co-predators, prey, and habitat quality (*16*). Tiger habitat spanning 20 Indian states was delineated into ecologically meaningful sized grids of 10 by 10 km that have been fixed for sampling since 2006. Each grid cell was surveyed with multiple spatially independent search paths [mean 10 (SE 2), maximum 21] to estimate tiger occupancy and by line transects [mean 4 (SE 1), maximum 14] to estimate prey abundance. This was a large wildlife survey (*20*), conducted by ~44,000 personnel and repeated in 2006, 2010, 2014, and 2018. It covered ~2.5 million km and provided essential data for evaluating the socio-ecological facets of tiger recovery (*21*). We hypothesized that tigers would persist in protected habitats with ample prey, while becoming extinct in areas of increased human and social disturbances, and would colonize socioeconomically moderate multiuse habitats with less intensive human land use and ample prey and in proximity to source populations. We tested these hypotheses using multiseason (quadrennial) occupancy models (MSOM) of tigers for every 100-km^2 cell to account for imperfect detections and to identify socio-ecological correlates. Covariates representing socio-ecological factors that were used for

Table 1. Recovery of tiger-occupied areas in India. Habitat area where tigers were detected (naïve occupancy), areas after correcting for imperfect detections (null model occupancy), and detection corrected occupancy were modeled by using site covariates (best model occupancy). Values in parentheses are 95% confidence intervals.

Year	Naïve occupancy (km^2)	Null model occupancy (km^2)	Best model occupancy (km^2)
2006	66,389	114,562 (109,998 to 119,125)	106,332 (101,777 to 110,886)
2010	64,653	113,103 (107,734 to 118,474)	107,033 (100,938 to 113,128)
2014	77,083	113,673 (108,629 to 118,724)	117,447 (111,236 to 123,659)
2018	91,516	141,539 (136,813 to 146,308)	138,247 (131,953 to 144,541)

[1]Wildlife Institute of India, Dehradun, India. [2]Center for Ecological Dynamics in a Novel Biosphere Section of Ecoinformatics (ECONOVO), Department of Biology, Aarhus University, Aarhus, Denmark. [3]National Tiger Conservation Authority, New Delhi, India.
*Corresponding author. Email: yvjhala@gmail.com
†Present address: Indian National Science Academy, National Centre for Biological Sciences, Bengaluru, India.
‡Present address: Global Tiger Forum, New Delhi, India.

modeling occupancy, extinction, and colonization (*22*) by tigers included prey abundance (encounter rate of wild herbivores), habitat attributes (suitable habitat and land-use proportion), human impacts (forest loss, night-time lights, livestock abundance, and intensity of extractive human use), socioeconomic variables (poverty and armed conflicts), and protection status (protected areas and habitats in their proximity) (table S1). To better understand the relationship of prevailing ecological, sociological, legal, economic, and political conditions that explained dynamic tiger occupancy, we evaluated the MSOM variables using exploratory analysis and nonparametric statistical comparisons.

After correcting for imperfect detections and accounting for the socio-ecological variables, the best among competing models (table S2) estimated tiger occupancy to be increasing at 2929 (±737) km^2 per year [$P < 0.05$, coefficient of determination (R^2) = 0.83] (tables S3 and S4 and fig. S1). The modeled multiseason estimates displayed a consistent improvement over the naïve occupancy estimates (Table 1) and were statistically similar to independently modeled single-season occupancy estimates

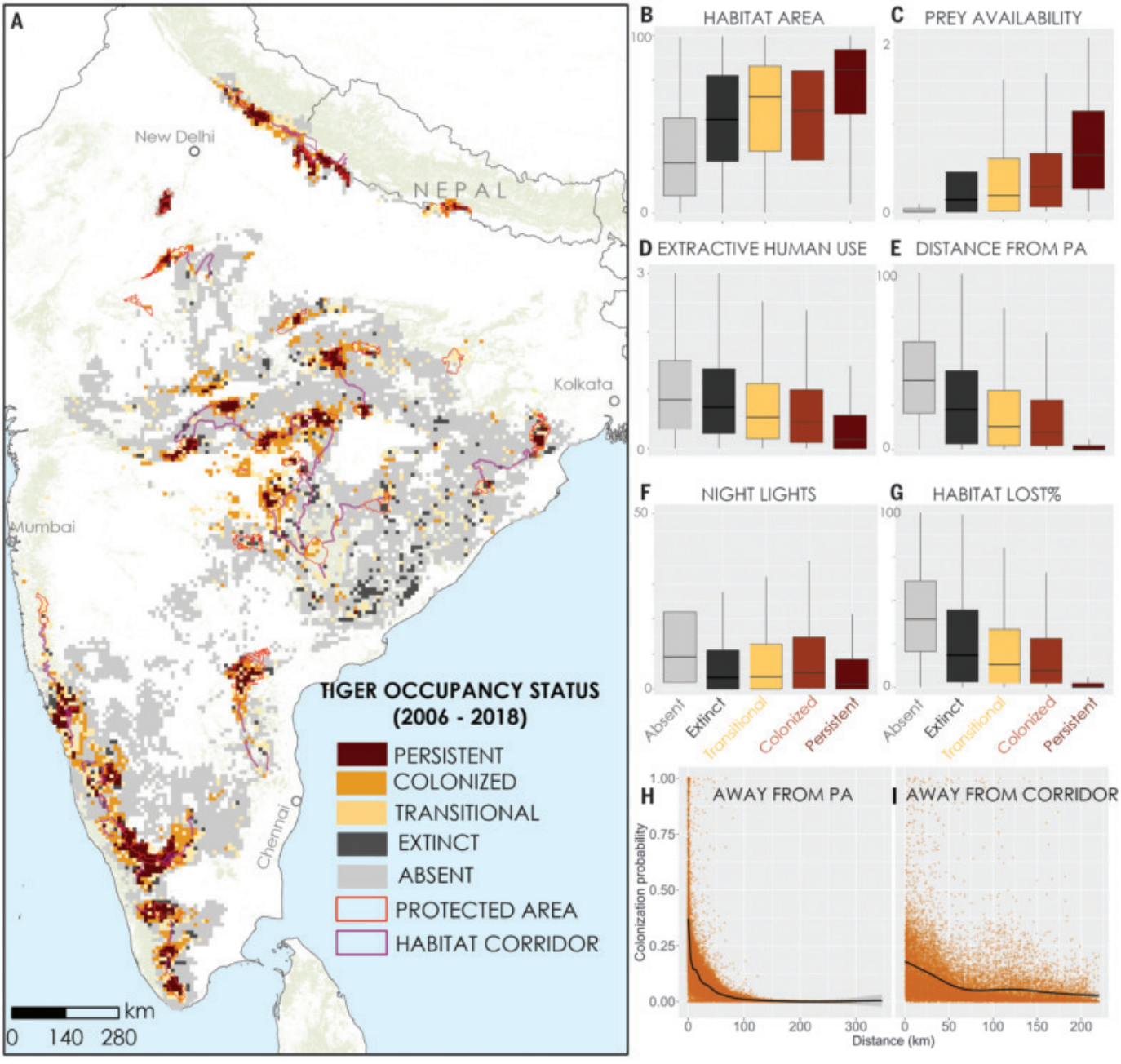

Fig. 1. Spatiotemporal trends in tiger occupancy within India and its socio-ecological covariates. (**A**) Tiger occupancy status from 2006 to 2018. (**B** to **I**) Persistent occupancy was observed within grid cells with (B) large proportion of habitat (square kilometers) and (C) higher prey availability (animals sighted/km). [(B), (C), and (E)] Colonization increased within prey-rich habitats in proximity to tiger-occupied protected areas (kilometers), and (D) tigers were absent or became extinct in areas with greater extractive human use (extraction signs per square kilometer), (F) high urbanization (night-time light radiance index), and (G) proportion of habitat loss (square kilometers). Colonization probability decreased away from (H) protected areas and (I) habitat corridors, highlighting the importance of protected areas and habitat corridors in tiger colonization. Statistical comparisons for (B) to (G) are given in table S5.

(fig. S2), strengthening the reliability of the complex multiseason occupancy models. Tigers consistently occupied 35,255-km^2 areas that were protected or were in proximity to protected areas and had high prey abundance in extensive habitats (Fig. 1 and table S4). Of the total colonized area of 41,767 km^2 in 12 years, tigers colonized 35% of new areas between 2006 and 2010, 20% between 2010 and 2014, and 45% between 2014 and 2018 (fig. S3). Overall, tiger occupancy increased by 30% over the span of the study. Colonization was higher in grid cells that were in proximity to tiger-occupied protected areas, with higher prey abundance, suitable habitats, low human density, and moderately wealthy areas (Figs. 1 and 2 and table S4). Colonization coincided spatially with proximity to protected areas [β coefficient (y) = 0.6075 × $10^{-0.01}$, R^2 = 0.58, P < 0.1] (Fig. 1H) and habitat corridors [y = −0.114ln(x) + 1.8231, R^2 = 0.20, P < 0.1] (Fig. 1I), highlighting their functionality and importance in tiger recovery. Local extinctions (17,992 km^2), spanning over 12 years, were highest (64%) between 2006 and 2010, followed by 17% between 2010 and 2014 and 19% between 2014 and 2018 (fig. S3). Grid cells that experienced tiger extinctions were characterized by isolation from protected areas, increased urbanization and infrastructure development, higher extractive human use, and a higher frequency of armed conflicts (Figs. 1 and 2 and table S4). Areas where tigers became temporarily extinct but subsequently recolonized (transitional) were proximal to either protected areas or habitat corridors. Creation of protected areas and habitat corridors connecting source populations has helped dispersal of the increasing tiger population (*17*), forming metapopulations (*23*) and increasing landscape-level tiger occupancy over the years.

Out of the 1973 grid cells occupied (persistent + colonized + transitional) by tigers, 25% were in the core area of tiger reserves or within national parks [International Union for Conservation of Nature (IUCN) protected area category II], 20% were in tiger reserve buffers or wildlife sanctuaries (IUCN category III), 10% were in tiger habitat corridors, and the remaining 45% were in human multiple-use habitats. However, out of the total consistently tiger-occupied grid cells (n = 479), 85% were within tiger reserves, national parks, and wildlife sanctuaries (IUCN categories II and III), 4% were in tiger habitat corridors, and the remaining 11% were in multiple-use mosaics of habitats and agricultural fields outside protected areas. These consistently occupied grid cells housed source populations of tigers, and model sensitivity analyses showed that extinctions in these areas would affect landscape-scale occupancy of tigers (fig. S4). Sensitivity analyses further highlighted the relevance of proximity to protected areas for increasing tiger occupancy. Like tiger extinction areas, habitats with tiger absence were mostly isolated from protected tiger source populations. These dynamics demonstrate the importance of human-free protected areas (land sparing) (*16*, *24*) for maintaining sources of

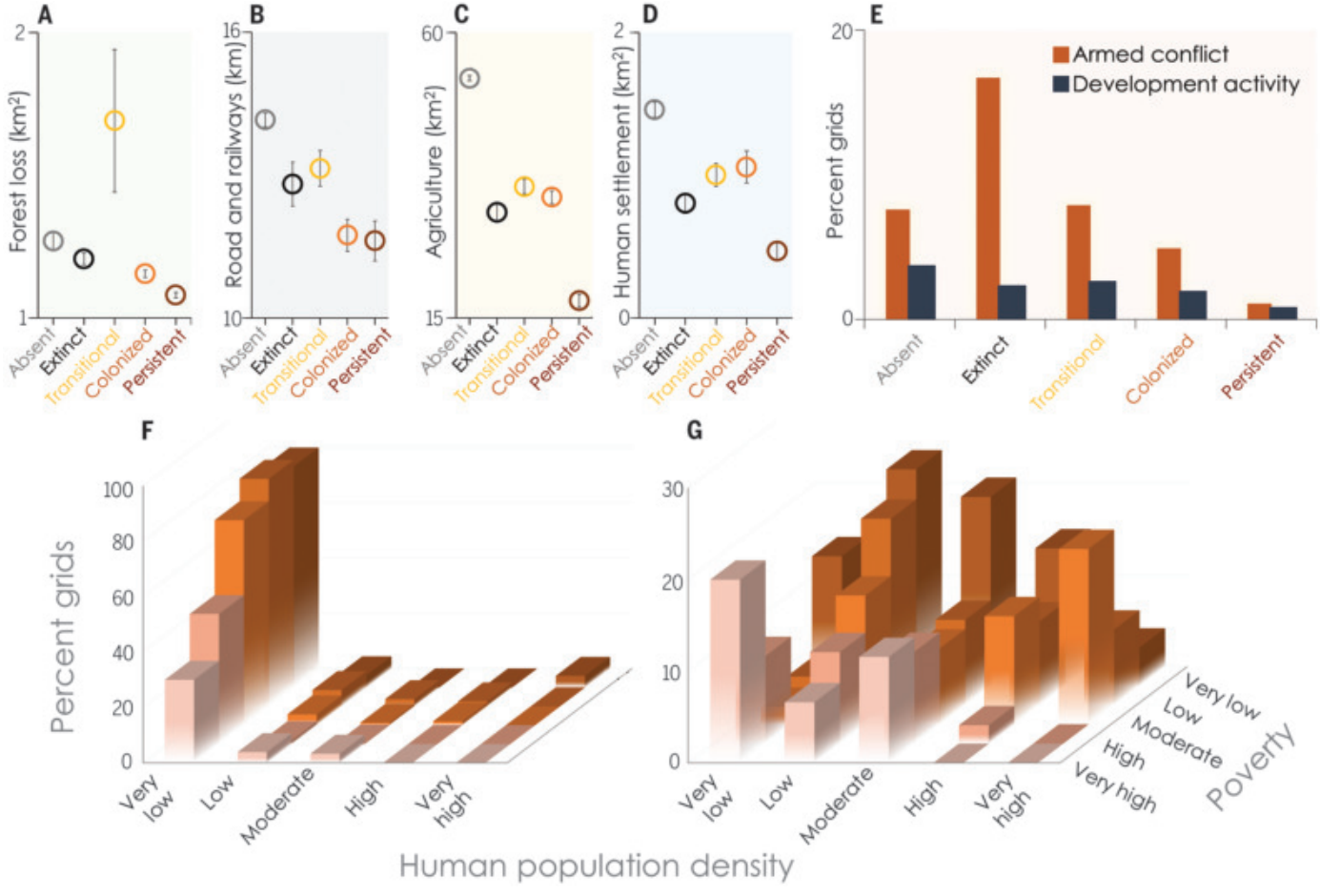

Fig. 2. Socioeconomic covariates of tiger recovery. (**A** to **E**) Threats to tiger-occupied areas are (A) summed average forest loss, (B) length of linear infrastructures per 100 km^2, (C) agricultural areas, (D) human settlement areas, and (E) percent grid cells with armed conflict and developmental activities, across tiger occupancy categories. (**F**) Grid cells with persistent tiger occupancy coincided with least populated and moderate to low rural poverty areas. (**G**) Grid cells colonized by tigers occurred across different human population density and poverty strata, except in areas with high population density and extreme poverty. Statistical comparisons are given in table S5.

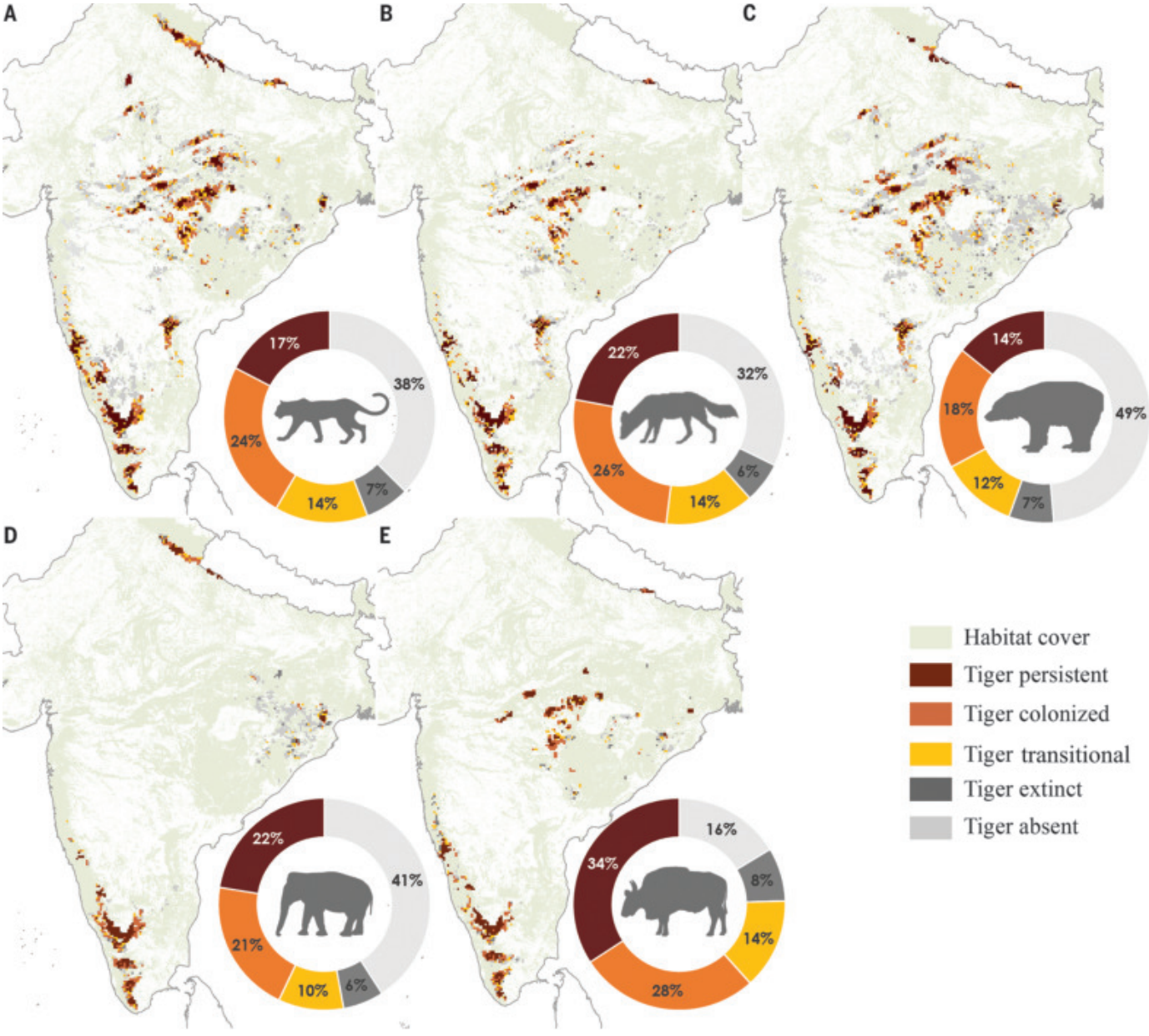

Fig. 3. Distribution of megafauna in tiger habitat of India. (**A** to **E**) Occurrence of (A) leopard (*P. pardus*), (B) dhole (*C. alpinus*), (C) sloth bear (*M. ursinus*), (D) Asian elephant (*E. maximus*), and (E) gaur (*B. gaurus*) overlapped with tiger occurrence by 62, 68, 51, 59, and 84%, respectively.

tigers and their prey. Protection of tiger source populations has permitted their occurrence in multiuse areas (land sharing). Hence, in the case of tigers, land sparing is essential to realize the benefits of land sharing.

Habitats that were devoid of tigers (157,527 km^2) were predominantly spread across the states of Chhattisgarh, Odisha, and Jharkhand. Recovery of tigers in protected areas of this region (Guru Ghasidas, Palamau, Udanti-Sitanadi, Similipal, Satkosia, and Indravati), possibly through reintroduction or supplementation, and strengthening habitat connectivity between subsequent source populations can effectively repopulate tigers in another ~10,000 km^2. However, these areas are among the poorest districts in India (Fig. 2), with high incidences of bushmeat consumption, often with the use of traps and snares that are usually indiscriminate in killing prey and predators (*16*). Biodiversity recovery in these poorer districts entails investments in socioeconomic upliftment of communities, much more so than in other areas. Such a strategy requires multisectoral synergies between governmental agencies, civil societies, and scientific institutions to ensure inclusive benefit sharing with local communities. Implementation as is done in many tiger reserves, by sharing a substantial proportion of revenues from tiger reserves with the communities in proximity (*16*), may initiate a win-win strategy for people and tiger recovery.

The frequency of armed conflicts in a grid cell significantly increased tiger extinction probability (table S4). Sociopolitical stability and wildlife conservation go hand in hand; examples abound from across the world where political instability leads to drastic wildlife declines, especially of endangered species in trade (*25*). Militants exploit wildlife products for arms, turning lawless regions into poaching havens (*26*). Within India, Manas National Park lost its greater one-horned rhinoceros (*Rhinoceros unicornis*) during the politico-ethnic conflict (*27*); Nepal's rhinoceros population was decimated

during the period of civil unrest (*28*). Therefore, it is not surprising to see tigers and their prey either absent or extirpated from regions with armed conflict (Fig. 2E). In total, 47% of grid cells that experienced tiger extinctions were in districts affected by the Naxal armed conflict (fig. S5). Tiger reserves affected by the Naxal conflict were in the states of Chhattisgarh (Indravati, Achanakmar, and Udanti-Sitanadi) and Jharkhand (Palamau). Tiger reserves where armed conflict has been recently controlled displayed recovery (Nagarjunsagar-Srisailam, Amrabad, and Similipal). Several tiger habitats in the states of Odisha, Chhattisgarh, Jharkhand, Telangana, Andhra Pradesh, and eastern parts of Maharashtra have been experiencing armed insurgencies (fig. S5), and it is in these habitats that tiger occupancy was low and extinction probability high (Fig. 2 and fig. S5). These are areas where, with greater political stability, we might expect tiger recovery.

Contrary to conventional expectation of spatial separation in humans and large carnivores, human density—although low in persistently occupied areas compared with absent areas—was not a major deterrent to tiger colonization and recovery (Fig. 2, D and G, and fig. S6). The areas that were newly colonized by tigers had an average density of 250 (±8) humans/km^2. Tigers occurred and colonized habitats interspersed with agricultural and human settlements (Fig. 2 and fig. S7). Habitats outside of tiger reserve cores and national parks are used by communities for their livelihoods (*17*). This land sharing with tigers varied across India, likely because of different sociocultural tolerances by people. Community tolerance to large carnivores in their backyards is mostly driven by economics (*29*), social settings (*30*), and cultural factors (*31*), in which India is richly diverse. Tigers shared space with people at high densities in some areas (such as Madhya Pradesh, Maharashtra, Uttarakhand, and Karnataka), whereas they became extinct or were absent from areas with a legacy of extensive bushmeat consumption or commercial poaching, even when human density was relatively low (such as in Odisha, Chhattisgarh, Jharkhand, Northeastern states of India, and most of Southeast Asia) (*28*–*30*). Thus, it is not simply the density of humans but rather their attitudes and lifestyles that determine stewardship for tiger recovery.

A large proportion of tiger-occupied habitats (45%) was shared with ~60 million people in India (fig. S6C). This co-occurrence with people coincides with relatively economically prosperous areas, many of which harness substantial financial benefits from tiger-related tourism as well as proactive government-sponsored schemes for compensating the loss caused by conflict (*16*). The rates of tiger colonization were lowest in areas of high rural poverty rate, as derived from indicators of health, education, and standard of living (fig. S6B and fig. S7) (*32*). Often, marginalized communities rely heavily on extractive use of forest resources and bushmeat for their livelihood (*33*, *34*), which is becoming unsustainable with growing human populations and declining biodiversity (*35*). Economic prosperity achieved through alternative and nonconsumptive use of ecosystems and biodiversity allows tigers and associated ecosystems to recover. However, economic prosperity usually leads to intensive land-use change, which had a negative impact on tiger occurrence (table S4). Tiger recovery is thus constrained at opposite ends of the socioeconomic spectrum, by intensive urbanization and poverty (fig. S8). Hence, adopting an inclusive and sustainable rural prosperity in place of an intensive land-use change–driven economy can be conducive for tiger recovery, aligning with India's modern environmentalism and sustainability (*36*, *37*). Investments for inclusive and equitable eco-development projects within shared landscapes would enable tiger recovery. Protected areas can also bring possibilities not only to protect biodiversity but also to alleviate poverty and secure ecosystem services by sharing benefits with local communities in the proximity (*24*, *38*).

A cornerstone to the success of tiger recovery in India would be the realization of its originally envisaged flagship role for garnering resources for biodiversity conservation. The mere presence of an apex predator usually heralds the existence of a complex ecosystem, composed of vegetation, prey, and often a functional mesocarnivore community (*7*). Naturally, tiger-occupied areas were found to be a subset of the distribution of major tiger prey such as spotted deer (*Axis axis*), sambar deer (*Rusa unicolor*), swamp deer (*Rucervus duvaucelii*) and gaur (*Bos gaurus*) (fig. S9), which had the largest contribution in explaining tiger occupancy (table S4). Moreover, the sampled region is also a subset of the historical range for many megafauna species in the region. Within the tiger's distribution range, tiger-occupied habitats spatially coincided with the distribution of co-occurring megaherbivores: Asian elephant (*Elephas maximus*; 59%) and gaur (84%) (Fig. 3). Other large carnivores such as leopard (*Panthera pardus*), dhole (*Cuon alpinus*), and sloth bear (*Melursus ursinus*) also coincided with 62, 68, and 51% tiger-occupied areas, respectively (Fig. 3). Furthermore, ecosystems protected for tiger recovery reinforced biotic resistance to biological invasions as well as contributed to carbon sequestration, benefiting the global climate (*39*, *40*). This accentuates the umbrella role of tigers in extending cobenefits to biodiversity and biosphere.

Irrespective of political parties, the government of India has shown deep-seated pride in conserving the tiger, its national animal (*16*). Conservation investments by governments—enabled through dedicated legislation in land sparing, prohibiting forest land diversions, and ensuring benefit-sharing with local communities—have largely enabled tiger recovery. These legislative instruments not only ensure tiger recovery but also can yield equitable cobenefits (*41*). Our study suggests that downgrading such existing instruments (*42*) would have far-reaching ramifications on tiger recovery and biodiversity conservation.

Carnivore-human co-occurrence is possible because of effective land-use plans and policies in vast landscapes of North America and Europe (*8*, *43*). India, despite having the world's highest human population density and only 18% of the global tiger habitat, harbors >75% of the global tiger population (~3600 tigers) (*17*). Although this sets a perfect narrative of wildlife-human co-occurrence, it is unattainable in the absence of human-free legally protected areas, embedded in socioeconomically prosperous and politically peaceful multiuse areas. The human attitude toward biodiversity, particularly large carnivores such as the tiger, is based on cultural acceptance as well as economic benefits; the latter requires meticulous governance, and the former requires conscious nurturing. The success of tiger recovery in India offers important lessons for tiger-range countries as well as other regions for conserving large carnivores while benefiting biodiversity and communities simultaneously. It rekindles hope for a biodiverse Anthropocene.

REFERENCES AND NOTES

1. R. Dirzo *et al.*, *Science* **345**, 401–406 (2014).
2. W. J. Ripple *et al.*, *Bioscience* **66**, 807–812 (2016).
3. W. J. Ripple *et al.*, *Conserv. Lett.* **12**, e12627 (2019).
4. M. Di Marco *et al.*, *Conserv. Biol.* **28**, 1109–1118 (2014).
5. J. A. Estes *et al.*, *Science* **333**, 301–306 (2011).
6. A. C. Stier *et al.*, *Sci. Adv.* **2**, e1501769 (2016).
7. W. J. Ripple *et al.*, *Science* **343**, 1241484 (2014).
8. G. Chapron *et al.*, *Science* **346**, 1517–1519 (2014).
9. K. E. Ingeman *et al.*, *Sci. Rep.* **12**, 10005 (2022).
10. J. Goodrich *et al.*, *Panthera tigris*, The IUCN Red List of Threatened Species 2015: e. T15955A50659951 (IUCN, 2015).
11. Y. V. Jhala *et al.*, *Front. Ecol. Evol.* **7**, 312 (2019).
12. P. A. Stephens, *Proc. Natl. Acad. Sci. U.S.A.* **112**, 14753–14754 (2015).
13. N. H. Carter, J. D. C. Linnell, *Trends Ecol. Evol.* **31**, 575–578 (2016).
14. A. Morales-González, H. Ruiz-Villar, A. Ordiz, V. Penteriani, *Glob. Ecol. Conserv.* **22**, e00937 (2020).
15. E. Dinerstein *et al.*, *Bioscience* **57**, 508–514 (2007).
16. Y. Jhala *et al.*, *People Nat.* **3**, 281–293 (2021).
17. Q. Qureshi, Y. V. Jhala, S. P. Yadav, A. Mallick, "Status of tigers, co-predators and prey in India 2022" (National Tiger Conservation Authority, Government of India, and Wildlife Institute of India, 2023).
18. J. Walston *et al.*, *PLOS Biol.* **8**, e1000485 (2010).
19. E. Wikramanayake *et al.*, *Conserv. Lett.* **4**, 219–227 (2011).
20. Guinness World Records, "Largest camera-trap wildlife survey" (2021); https://www.guinnessworldrecords.com/world-records/601784-largest-camera-trap-wildlife-survey.
21. Y. Jhala, N. A. Mungi, R. Gopal, Q. Qureshi, Tiger occupancy. Zenodo (2024); https://doi.org/10.5281/zenodo.13856111.
22. D. I. MacKenzie, *Occupancy Estimation and Modeling: Inferring Patterns and Dynamics of Species* (Elsevier, 2006).
23. S. Bisht, S. Banerjee, Q. Qureshi, Y. Jhala, *J. Appl. Ecol.* **56**, 1725–1740 (2019).
24. K. K. Karanth, *Biol. Conserv.* **139**, 315–324 (2007).
25. J. H. Daskin, R. M. Pringle, *Nature* **553**, 328–332 (2018).
26. M. E. Stalmans, T. J. Massad, M. J. S. Peel, C. E. Tarnita, R. M. Pringle, *PLOS ONE* **14**, e0212864 (2019).

27. R. Goswami, T. Ganesh, *Curr. Sci.* **100**, 445 (2011).
28. N. Subedi *et al.*, *Oryx* **47**, 352–360 (2013).
29. K. Banerjee, Y. V. Jhala, K. S. Chauhan, C. V. Dave, *PLOS ONE* **8**, e49457 (2013).
30. R. S. Hathaway *et al.*, *J. Urban Econ.* **3**, jux009 (2017).
31. S. Nijhawan, A. Mihu, *J. Ethnobiol.* **40**, 149–166 (2020).
32. S. Asher, T. Lunt, R. Matsuura, P. Novosad, *World Bank Econ. Rev.* **35**, 845–871 (2021).
33. N. Velho, K. K. Karanth, W. F. Laurance, *Biol. Conserv.* **148**, 210–215 (2012).
34. A. Datta, M. O. Anand, R. Naniwadekar, *Biol. Conserv.* **141**, 1429–1435 (2008).
35. T. N. E. Gray *et al.*, *Biodivers. Conserv.* **27**, 1031–1037 (2018).
36. K. S. Bawa *et al.*, *Biol. Conserv.* **253**, 108867 (2021).
37. R. Guha, *Environmental Movements in Asia* **114**, 65–82 (1998).
38. N. Sekar, *Reg. Environ. Change* **16** (S1), 111–123 (2016).
39. N. A. Mungi, Q. Qureshi, Y. V. Jhala, *J. Ecol.* **109**, 3308–3321 (2021).
40. A. Lamba *et al.*, *Nat. Ecol. Evol.* **7**, 1104–1113 (2023).
41. M. Verma *et al.*, *Ecosyst. Serv.* **26**, 236–244 (2017).
42. T. D. Gupta, *Science* **381**, 471 (2023).
43. S. A. Morrison, W. M. Boyce, *Conserv. Biol.* **23**, 275–285 (2009).

ACKNOWLEDGMENTS

We thank the National Tiger Conservation Authority, India, for funding, supporting, and coordinating the field sampling and research. We thank the State Forest Departments and the team of tiger researchers for their contribution to data collection. We thank the Wildlife Institute of India for facilitating the study and SCIENCE, Dehradun, for assistance in spatial database management. We thank P. Stephens for constructive comments on our draft manuscript. **Funding:** This work was supported by the National Tiger Conservation Authority, government of India (Y.V.J. and Q.Q.). Y.V.J. received support from the INSA senior scientist scheme while writing the manuscript. **Author contributions:** Conceptualization: Y.V.J., Q.Q., R.G., and N.A.M. Methodology: Y.V.J., Q.Q., and N.A.M. Investigation: N.A.M., Y.V.J., and Q.Q. Visualization: N.A.M., Y.V.J., and Q.Q. Funding acquisition: Y.V.J. and Q.Q. Project administration: Y.V.J., Q.Q., and R.G. Supervision: Y.V.J., Q.Q., and R.G. Writing – original draft: N.A.M. and Y.V.J. Writing – review and editing: Y.V.J., Q.Q., R.G., and N.A.M. **Competing interests:** R.G. is the director general of the Global Tiger Forum and served as director of Project Tiger and the National Tiger Conservation Authority and as field director of tiger reserves. Q.Q. is a professor at the Wildlife Institute of India. Y.V.J. was the former dean and professor at the Wildlife Institute of India. The authors declare no additional competing interests. **Data and materials availability:** Data to reproduce analyses are available on Zenodo (*21*).

SUPPLEMENTARY MATERIALS

science.org/doi/10.1126/science.adk4827
Materials and Methods
Figs. S1 to S9
Tables S1 to S6
References (*44*–*48*)
MDAR Reproducibility Checklist

Submitted 30 August 2023; accepted 27 November 2024
10.1126/science.adk4827

MICROBIOLOGY

TIR signaling activates caspase-like immunity in bacteria

François Rousset[1]†‡, Ilya Osterman[1]†, Tali Scherf[2], Alla H. Falkovich[2], Azita Leavitt[1], Gil Amitai[1], Sapir Shir[1], Sergey Malitsky[3], Maxim Itkin[3], Alon Savidor[4], Rotem Sorek[1]*

Caspase family proteases and Toll/interleukin-1 receptor (TIR)-domain proteins have central roles in innate immunity and regulated cell death in humans. We describe a bacterial immune system comprising both a caspase-like protease and a TIR-domain protein. We found that the TIR protein, once it recognizes phage invasion, produces the previously unknown immune signaling molecule adenosine 5′-diphosphate-cyclo[N7:1″]-ribose (N7-cADPR). This molecule specifically activates the bacterial caspase-like protease, which then indiscriminately degrades cellular proteins to halt phage replication. The TIR-caspase defense system, which we denote as type IV Thoeris, is abundant in bacteria and efficiently protects against phage propagation. Our study highlights the diversity of TIR-produced immune signaling molecules and demonstrates that cell death regulated by proteases of the caspase family is an ancient mechanism of innate immunity.

Caspases are proteases with central roles in innate immunity and regulated cell death in humans (*1*). The human genome harbors 12 caspase-encoding genes, with some promoting inflammation and others functioning in the execution of cell death (*1*). Inflammatory caspases, including caspases 1, 4, and 5, are recruited to activated inflammasomes following pathogen recognition, and are responsible for the proteolytic activation of cytokines and gasdermin D, promoting cell death through pyroptosis (*2*). Executioner caspases (e.g., caspases 3, 6, and 7), once activated by initiator caspases (8, 9, and 10), cleave hundreds of protein substrates to promote apoptotic cell death (*1*, *3*). Proteases of the caspase family (Pfam PF00656) also exist in prokaryotes (*4*) and were proposed to cleave bacterial gasdermins to activate immunity in response to phage infection (*5*). Bacterial proteins of the caspase family were also shown to promote cell death when activated by type III CRISPR-Cas systems (*6*–*8*). However, the molecular functions of most caspase-like proteins in bacteria remain poorly understood (*4*).

Toll/interleukin-1 receptor (TIR) domain proteins also play key roles in innate immunity. Initially described as protein-protein interaction modules in human Toll-like and interleukin-1 receptors (*9*), TIR domains in bacteria and plants were later shown to be enzymes that produce immune signaling molecules using nicotinamide adenine dinucleotide (NAD^+) as a substrate (*10*). In the bacterial defense system type I Thoeris, the TIR-domain protein, once it senses phage infection, produces the signaling molecule 1″-3′ glycocyclic adenosine 5′-diphosphate (ADP)-ribose (gcADPR) (*11*, *12*). This molecule activates an effector protein that depletes the cell of NAD^+ and aborts phage replication (*13*, *14*). The TIR-domain protein in type II Thoeris, by contrast, produces the signaling molecule histidine-ADP-ribose (His-ADPR) (*15*), which activates an effector protein that disrupts the cell membrane to abort phage propagation. A third type of Thoeris was recently proposed but its mechanism of action and molecular signaling remains unknown (*16*). In plants, TIR-derived signaling molecules are diverse and include phosphoribosyl-AMP/ADP (*17*), 1″-2′ gcADPR (*11*, *12*, *18*), di-ADPR (*19*), ATP-ADPR (*19*), and 2′,3′-cAMP/cGMP (*20*). Current evidence suggests that the repertoire of immune signaling molecules produced by TIR domains has not been fully unveiled (*10*).

In this study, we describe type IV Thoeris, a bacterial defense system encoding both a TIR-domain protein and a caspase-like protease. We show that upon phage infection, the TIR-domain protein produces the signaling molecule N7-cADPR that binds the caspase-like protease and triggers promiscuous arginine-specific protease activity. Protease activation leads to indiscriminate cleavage of multiple proteins, including elongation factor Tu (EF-Tu), thereby aborting phage infection. Our study establishes a direct functional connection between TIR signaling and caspase activation in bacterial defense against phages.

Results

A TIR-caspase operon provides anti-phage immunity.

While examining the genomic environment of caspase-like proteins in bacteria, we noticed an abundant two-gene operon encoding a short TIR-domain protein and a caspase-like protease (Fig. 1A). Operons with this gene organization were frequently encoded in the vicinity of bacterial defense systems, suggesting a defensive function (fig. S1). We synthesized and cloned two such operons, one from *Escherichia coli* 328 and the other from *Pseudomonas* sp. 1-7 and expressed these in *E. coli* K-12 MG1655 under the control of an arabinose-inducible

[1]Department of Molecular Genetics, Weizmann Institute of Science, Rehovot, Israel. [2]Department of Chemical Research Support, Weizmann Institute of Science, Rehovot, Israel. [3]Life Sciences Core Facilities, Weizmann Institute of Science, Rehovot, Israel. [4]The Nancy and Stephen Grand Israel National Center for Personalized Medicine, Weizmann Institute of Science, Rehovot, Israel.
***Corresponding author. Email: rotem.sorek@weizmann.ac.il**
†These authors contributed equally to this work.
‡Present address: CIRI, Centre International de Recherche en Infectiologie, INSERM U1111, CNRS UMR5308, Université Claude Bernard Lyon 1, Ecole Normale Supérieure de Lyon, Lyon, France.

promoter. Following a challenge by a panel of phages, we observed that the infectivity of phage T6 was substantially reduced when plated on cells expressing either of the operons, showing that this TIR- and caspase-encoding operon is a defense system (Fig. 1B). Since the *E. coli* 328 operon exhibited slight toxicity upon expression induction, we selected the *Pseudomonas* sp. 1-7 (*Ps*) homolog for further study. A sensitivity screen against phages of the BASEL collection (*21*) revealed that phages Bas18, Bas25, and Bas43 are also blocked by the defense system from *Pseudomonas* sp. 1-7 (fig. S2).

Single amino acid substitutions in the predicted catalytic sites of *Ps*TIR (E79Q) and *Ps*Caspase (C129A) proteins abolished defense (Fig. 1B), suggesting that the enzymatic activity of both proteins is required for immunity. Bacterial cells expressing the system were able to survive when infected with T6 in liquid culture at a low multiplicity of infection (MOI) but died when infected at a high MOI (Fig. 1C). In addition, infected cells expressing the system did not release phage progeny (Fig. 1D). These results suggest that this defense system functions through regulated cell death or dormancy (*22*) and provides population-level protection. Homology-based searches in a database of ~38,000 prokaryotic genomes revealed that this defense system is found in hundreds of bacteria and archaea belonging to diverse phyla (Fig. 1E and table S1).

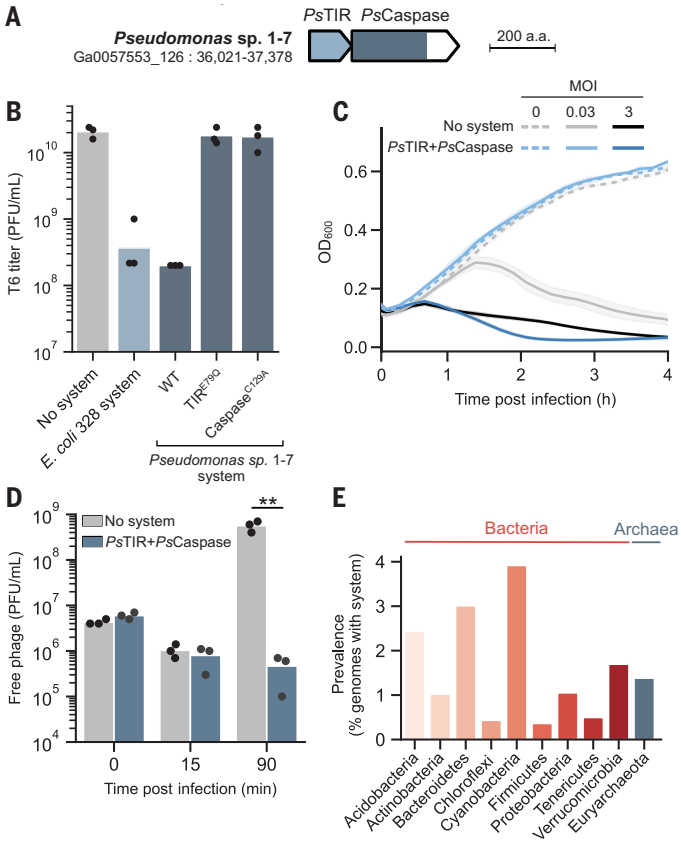

Fig. 1. A genetic system encoding a TIR-domain protein and a caspase-like protease provides anti-phage defense. (**A**) Genetic architecture of a system from *Pseudomonas* sp. 1-7. IMG (*44*) genome ID and gene coordinates are displayed below strain name. TIR and caspase-like domains are shown as blue shades. (**B**) Quantification of phage infection efficiency through plaque assays. Tenfold serial dilutions of phage T6 were spotted on a lawn of *E. coli* K-12 MG1655 cells expressing an empty vector (no system), the system from *E. coli* 328, or the system from *Pseudomonas* sp. 1-7, either wild type or mutated in the predicted active sites of the TIR (E79Q) or caspase-like protease (C129A). Bars show the mean of three replicates with individual data points overlaid. (**C**) Growth curves of *E. coli* K-12 MG1655 cells expressing an empty vector or the system from *Pseudomonas* sp. 1-7, infected by phage T6 at an MOI of 0.03 or 3 (or 0 for uninfected cells). Curves show the mean of three replicates with the standard deviation indicated by the shaded area. (**D**) Plaque-forming units of phage T6 sampled from the supernatant of *E. coli* K-12 MG1655 cells expressing an empty vector or the system from *Pseudomonas* sp. 1-7. Cells were infected at an MOI of 0.1. Bars represent the mean of three replicates with individual data points overlaid. Stars show significance of a two-sided *t*-test (**$P < 0.01$). (**E**) Detection of the defense system in prokaryotic genomes, shown for phyla with at least 50 genomes and where at least one system was detected.

Caspase cleaves EF-Tu during phage infection

TIR domains were described as NAD^+-degrading effectors in diverse families of defense systems, including Pycsar, CBASS, and prokaryotic argonautes, where their function is to deplete cells of NAD^+ once triggered by phage infection (*23*–*26*). Bacterial caspase-like proteases, on the other hand, were suggested to cleave bacterial gasdermins into active pore-forming effectors to induce cell death following infection (*5*). For this reason, we initially hypothesized that *Ps*Caspase would cleave *Ps*TIR into an active NAD^+-depleting form during infection. However, we did not detect any change in the molecular weight of *Ps*TIR during T6 infection (fig. S3A). In addition, we observed only mild reduction in NAD^+ levels during infection of cells expressing the system, which contrasts with the >95% reduction typically observed in NAD^+-depleting defense systems (*13*, *25*–*29*) (fig. S3B). These results suggest that *Ps*TIR is unlikely to be an NAD^+-depleting effector activated by *Ps*Caspase.

In Thoeris defense systems, bacterial TIR domains have an alternative role that does not involve NAD^+ depletion. In these systems, TIR domains generate signaling molecules that activate downstream effectors (*10*). We therefore hypothesized that *Ps*TIR may produce a signaling molecule during infection, and that this signaling molecule would bind and activate the effector *Ps*Caspase. Under this hypothesis, *Ps*Caspase is expected to cleave cellular or phage target proteins and halt phage infection.

To explore possible target proteins of *Ps*Caspase, we chemically labeled NH_2 groups in proteins present in lysates of T6-infected cells and subjected the labeled proteins to mass spectrometry (MS). This technique enables the identification of new protein N-termini specifically found in cells expressing the defense system as compared with control cells. A preliminary MS analysis following free amine tagging identified multiple candidate *Ps*Caspase targets, including the elongation factor Tu (EF-Tu), a highly abundant cellular protein essential for protein translation, which was previously shown to be the target of the Lit protease (*30*) (fig. S4). To verify that EF-Tu is a target of *Ps*Caspase, we co-expressed the TIR-caspase system with a C-terminally tagged copy of EF-Tu in an *E. coli* K-12 strain in which *lit* was deleted, and monitored EF-Tu cleavage during phage infection by Western blot (Fig. 2A). Two EF-Tu cleavage products were visible in cells expressing the defense system following T6 infection (Fig. 2B). These cleavage products were absent when the catalytic cysteine in *Ps*Caspase or the catalytic glutamate in *Ps*TIR were mutated to alanine, showing that EF-Tu cleavage requires both caspase and TIR activities (Fig. 2B). The molecular weight of cleavage products and the exploratory MS data suggested that EF-Tu is cleaved after two specific arginine residues (R45 and R59) (Fig. 2, C and D), which was confirmed by the loss of EF-Tu cleavage upon mutation of these two residues into glutamines (Fig. 2B). Taken together, our results suggest that *Ps*Caspase is specifically activated during phage infection and cleaves EF-Tu downstream of arginine residues at positions 45 and 59.

Caspase activity is triggered by a TIR-derived signaling molecule

We then investigated whether, as in the Thoeris family of defense systems, *Ps*TIR produces a

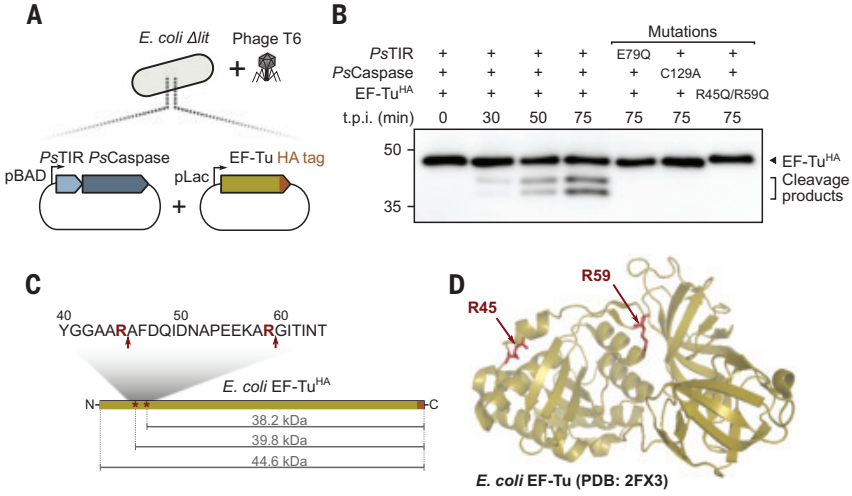

Fig. 2. EF-Tu is a target of *Ps*Caspase during phage T6 infection. (**A**) *E. coli* K-12 MG1655Δ*lit* cells co-expressing the *Pseudomonas* sp. 1-7 defense system and an HA-tagged copy of EF-Tu were infected with phage T6. (**B**) Western blot analysis of infected cells co-expressing WT or mutated *Ps*TIR and *Ps*Caspase, and WT or mutated HA-tagged EF-Tu. t.p.i., time post infection. (**C**) and (**D**) Locations of cleavage sites in the EF-Tu protein sequence (C) and structure (D) are indicated with red arrows.

signaling molecule that activates *Ps*Caspase during infection. To do so, we collected lysates from cells expressing *Ps*TIR only and filtered these lysates with a 3-kDa cutoff to retain small metabolites. We then tested the ability of these metabolite extracts to activate EF-Tu cleavage by *Ps*Caspase (Fig. 3A). EF-Tu cleavage was visible when lysates from cells expressing both *Ps*Caspase and tagged EF-Tu were incubated with metabolite extracts derived from infected *Ps*TIR-expressing cells (Fig. 3B). By contrast, EF-Tu cleavage was absent when the metabolites were extracted from infected cells expressing red fluorescent protein (RFP) or *Ps*TIR^{E79Q} instead of *Ps*TIR, or from uninfected *Ps*TIR-expressing cells (Fig. 3B). These results suggest that *Ps*TIR produces a *Ps*Caspase-activating signaling molecule during infection.

To develop a more streamlined assay for *Ps*Caspase activation, we used a synthetic five amino acid peptide comprising the residues preceding the target cleavage site in EF-Tu (positions 55 to 59, EEKAR) fused to 7-amino-4-methylcoumarin (AMC). In this assay, which is similar to assays previously used to study human caspases (*31*) and caspase-like proteins in bacteria (*8*), peptide cleavage downstream of the arginine is expected to release free AMC and emit a fluorescence signal (Fig. 3C). *Ps*Caspase was able to cleave the synthetic EEKAR-AMC peptide when incubated with metabolites derived from infected cells expressing *Ps*TIR, but not when incubated with metabolites extracted from infected RFP-expressing control cells (Fig. 3D). *Ps*Caspase activity was even more pronounced upon incubation with metabolites derived from infected cells expressing the TIR protein from the *E. coli* 328 TIR-caspase system (*Ec*TIR) (Fig. 3D), suggesting that in the experimental conditions used here, *Ec*TIR produces higher amounts of signaling molecule than *Ps*TIR. Together, these results demonstrate that the caspase-like protein is activated by a small molecule specifically produced by the TIR-domain protein during phage infection. We therefore name this defense system type IV Thoeris.

*Ps*Caspase is a promiscuous arginine-specific protease

We then investigated the substrate specificity of the caspase-like protein using synthetic peptides with mutations in the wild-type (WT) EF-Tu sequence (EEKAR). Activated *Ps*Caspase was able to cleave EEAAR-AMC and EEKLR-AMC but not EEKAA-AMC peptides, indicating that the arginine residue at the P1 position is strictly required for cleavage, but other residues are not (fig. S5). These results suggest that *Ps*Caspase does not specifically recognize EF-Tu but might rather be a promiscuous protease.

To systematically search for additional cellular targets of *Ps*Caspase beyond EF-Tu, we incubated lysates of *Ps*Caspase-expressing *E. coli* cells with metabolites extracted from infected *Ec*TIR-expressing cells (Fig. 3E). SDS-PAGE analysis revealed the loss of multiple abundant proteins in the presence of *Ec*TIR-derived metabolites, combined with the presence of a smear of low-molecular weight protein products, suggesting massive *Ps*Caspase-dependent protein degradation (Fig. 3F). We subjected these lysates to chymotrypsin digestion and mass spectrometry analysis to identify cleavage sites in a systematic manner. This analysis revealed that peptides starting directly downstream of arginine, or ending with arginine, were strongly enriched upon incubation with *Ec*TIR-derived metabolites (Fig. 3G), indicating that cleavage occurs downstream of arginine residues. Cleavage events were observed in multiple essential proteins of *E. coli* (Fig. 3H), with a strict requirement for an arginine in the P1 position and a slight preference for small nonpolar residues surrounding the cleavage site (Fig. 3I). We confirmed the cleavage of one of these target proteins, ribosomal protein RplE, by Western blot using cell lysates incubated with *Ec*TIR-derived metabolites (Fig. 3J). Altogether, our results show that *Ps*Caspase is a promiscuous arginine-specific protease that cleaves multiple target proteins once activated by the *Ps*TIR-derived signaling molecule.

Type IV Thoeris produces signaling molecule N7-cADPR

We next examined the properties of the *Ps*Caspase-activating signaling molecule produced by type IV Thoeris. For this, we sought to take advantage of previously described phage proteins that sequester specific Thoeris-derived signaling molecules as a means to inhibit bacterial defense. Thoeris anti-defense 1 (Tad1) from phage SBSphiJ7 and Tad2 from phage SPO1 are known to sequester the 1″-3′ gcADPR signaling molecule produced by type I Thoeris (*12*, *32*), and Tad2 from *Myroides odoratus* (ModTad2) sequesters His-ADPR molecules and inhibits type II Thoeris (*15*). However, co-expression of Tad1, Tad2, or ModTad2 with type IV Thoeris did not inhibit the defensive activity of the system (Fig. 4A), suggesting that type IV Thoeris does not utilize the same molecule as types I or II Thoeris. Furthermore, incubation of metabolites derived from *Ec*TIR-expressing infected cells with purified Tad proteins did not affect the ability of these metabolites to activate *Ps*Caspase in our reporter assay, suggesting that Tad proteins are unable to sequester the signaling molecule of type IV Thoeris (fig. S6A). Finally, purified 1″-3′ gcADPR, 1″-2′ gcADPR, ADPR, and cyclic-ADPR molecules were unable to activate *Ps*Caspase (Fig. 4B), and conversely, *Ec*TIR-derived metabolites were unable to activate the ThsA NADase effector of type I Thoeris (*13*) in vitro (fig. S6B). Together, these results indicate that the signaling molecule of type IV Thoeris is distinct from that of type I and type II Thoeris.

To further examine the nature of the signaling molecule produced by type IV Thoeris, we used HPLC fractionation to purify the molecule from lysates of phage-infected *Ec*TIR-expressing

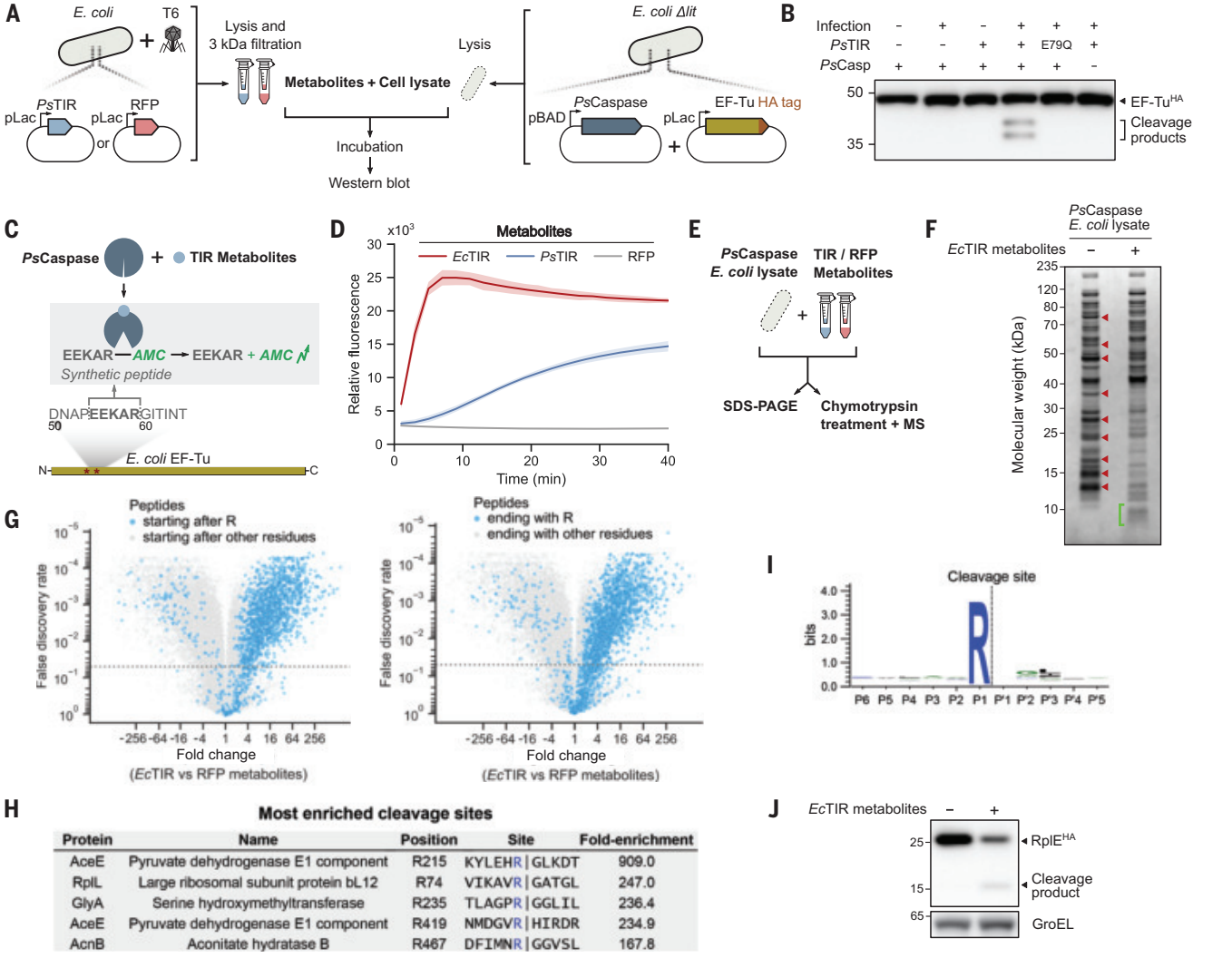

Protein	Name	Position	Site	Fold-enrichment
AceE	Pyruvate dehydrogenase E1 component	R215	KYLEHR | GLKDT	909.0
RplL	Large ribosomal subunit protein bL12	R74	VIKAVR | GATGL	247.0
GlyA	Serine hydroxymethyltransferase	R235	TLAGPR | GGLIL	236.4
AceE	Pyruvate dehydrogenase E1 component	R419	NMDGVR | HIRDR	234.9
AcnB	Aconitate hydratase B	R467	DFIMNR | GGVSL	167.8

Fig. 3. A TIR-derived signaling molecule triggers *Ps*Caspase arginine-specific proteolytic activity. (**A**) Experimental setup to test for *Ps*Caspase activation by small molecules. Lysates of T6-infected cells expressing *Ps*TIR or RFP were passed through 3-kDa filters to collect small molecules. Separately, *E. coli* K-12 MG1655Δ*lit* cells co-expressing *Ps*Caspase and a C-terminally HA-tagged copy of EF-Tu were lysed and incubated with the small molecules collected from infected *Ps*TIR- or RFP-expressing cells. Reactions were resolved by SDS-PAGE and western blot. (**B**) Western blot analysis shows EF-Tu cleavage only in the presence of metabolites derived from infected *Ps*TIR-expressing cells. (**C**) Schematic representation of the *Ps*Caspase reporter assay. A peptide comprising the residues preceding one of the cleavage sites in EF-Tu (EEKAR, positions 55 to 59) fused to 7-amino-4-methylcoumarin (AMC) was synthesized. The synthetic peptide was incubated with lysates from *Ps*Caspase-expressing *E. coli* K-12 MG1655Δ*lit* cells and small molecules collected from infected TIR- or RFP-expressing cells. *Ps*Caspase activation leads to peptide cleavage downstream of the arginine residue, thereby releasing the free fluorophore. (**D**) *Ps*Caspase reporter assay with small molecules collected from infected *Ec*TIR-, *Ps*TIR- or RFP-expressing cells. Curves show the mean of three replicates with the standard deviation shown as a shaded area. (**E**) Schematic of the in vitro cleavage assays, using lysates from *E. coli* K-12 MG1655Δ*lit* cells that express *Ps*Caspase, incubated with small molecules collected from T6-infected cells that express either *Ec*TIR or RFP. (**F**) SDS-PAGE of in vitro reactions followed by Coomassie staining. Red arrows indicate protein bands that are depleted in the presence of *Ec*TIR metabolites. Green bracket indicates a smear of low molecular weight fragments that are enriched in the presence of *Ec*TIR metabolites. (**G**) Volcano plots showing differential abundance of peptides in *Ps*Caspase cell lysates following incubation with *Ec*TIR-derived small molecules or with small molecules from control RFP-expressing cells. Peptides starting directly after an arginine residue (left) or ending with an arginine residue (right) are marked in blue. (**H**) Peptides enriched >fivefold in the *Ec*TIR sample, and depleted >twofold when incubated with RFP versus *Ec*TIR metabolites were selected for motif analysis (*n* = 83 peptides from 70 proteins). Shown are the five strongest hits. Fold enrichment relates to peptides starting at the position after arginine. (**I**) Sequence logo of the 83 cleavage sites. (**J**) Cleavage of C-terminally HA-tagged RplE from cell lysates in the presence of *Ec*TIR metabolites as shown by western blot. GroEL is shown as a loading control.

cells, using the peptide-AMC cleavage assay as a reporter system to assess the activity of HPLC fractions (fig. S7). Initial purification in phosphate buffer (pH 8.0) showed that the molecule rapidly lost activity under these conditions, and we therefore purified it in water (pH 7.0). Liquid chromatography coupled with mass spectrometry (LC-MS) showed that the molecule has the same mass as the canonical cyclic ADP-ribose (cADPR) (Fig. 4C) and MS-MS analysis showed that the fragmentation pattern of the molecule was indistinguishable from that of cADPR (fig. S7E). However, the molecule had a different LC retention time and absorbed light at a different wavelength than cADPR, suggesting that the type IV Thoeris molecule is distinct from cADPR (Fig. 4C). Indeed, synthetic cADPR was unable to activate *Ps*Caspase (Fig. 4B).

We subjected the purified molecule to nuclear magnetic resonance (NMR) analysis. Data from 1D ^{1}H, 2D homonuclear COSY and TOCSY, and 2D heteronuclear ^{1}H-^{13}C HSQC and HMBC NMR experiments, showed that the molecule comprises two ribose moieties and an adenine base, supporting the notion that the molecule is a variant of cADPR (fig. S8). However, ribose carbon 1", which in the canonical cADPR is naturally found attached to N1 in the adenine ring, showed a 3-bond HMBC correlation to H8 in the adenine ring (Fig. 4D, inferred from the H8-C1" and H1"-C8 correlations in the HMBC spectrum). Moreover, similar intensities were observed for peaks correlating with position 8 on the adenine base and 1' and 1" in the two ribose moieties (H1'-C8 and H1"-C8, and H8-C1' and H8-C1"), indicating a symmetrical orientation of the two ribose moieties relative to carbon atom C8 of the adenine base (Fig. 4D). Given that ribose carbon 1' was verified as attached

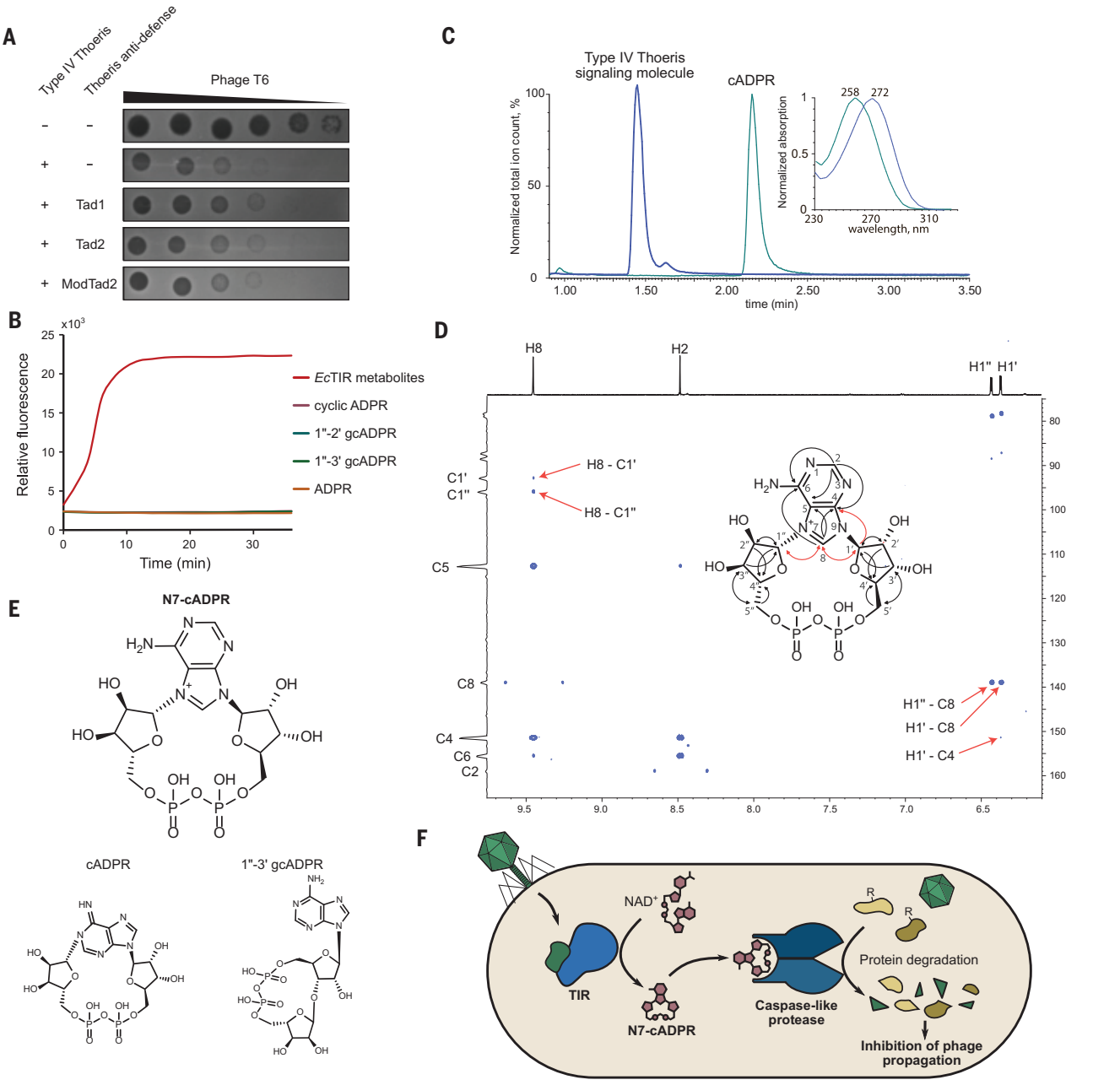

Fig. 4. Type IV Thoeris produces the immune signaling molecule N7-cADPR. (**A**) Plaque assay of phage T6 on cells co-expressing the type IV Thoeris system from *Pseudomonas* sp. 1-7 with RFP control, Tad1 from phage SBSphiJ7 (*12*), Tad2 from phage SPO1 (*32*), or Tad2 from *M. odoratus* (ModTad2) (*15*). None of the anti-defense proteins inhibit type IV Thoeris defense. (**B**) *Ps*Caspase reporter assays using metabolites derived from *Ec*TIR-expressing cells following phage infection, or using 100 μM of pure cyclic ADPR, 1"-2' gcADPR, 1"-3' gcADPR or ADPR. Only *Ec*TIR-derived metabolites activate *Ps*Caspase. (**C**) Chromatograms and UV-spectra (inset) of the type IV Thoeris signaling molecule (blue) and canonical cADPR (N1-cADPR, green). Both molecules have m/z = 540.0543 in negative ionization mode. (**D**) Correlations observed for N7-cADPR in the 2D ^{1}H-^{13}C HMBC NMR spectrum. Correlations between the adenine and the two ribose moieties are marked by red arrows both in the spectrum and on the molecule; other HBMC-derived correlations are shown by black arrows on the molecule. (**E**) Structure of N7-cADPR, compared with structures of canonical cADPR and 1"-3' gcADPR. (**F**) A model for the type IV Thoeris mechanism of immunity.

to N9 in the adenine base (H1'-C4 correlation), our results indicate that ribose carbon 1" is attached to nitrogen atom N7 in the adenine base (Fig. 4D). Altogether, our MS and NMR experiments indicate that the molecule that activates *Ps*Caspase is ADP-cyclo[N7:1"]-ribose (N7-cADPR), a molecule that, to our knowledge, has not been described before in natural systems (Fig. 4E). It was previously shown that N7-methylation of adenosine shifts the wavelength of the absorption maximum from 257 to 272 nm (*33*), which is in line with the shift in absorption that we observe in N7-cADPR as compared with cADPR (Fig. 4C).

Two types of Thoeris systems were previously studied in detail, and a third type (type III Thoeris) was suggested recently based on an operon architecture that contains TIR domains (*16*). In type I Thoeris, the effector protein ThsA harbors a SLOG domain that binds the signaling molecule gcADPR (*14*), and in type II Thoeris, the signaling molecule His-ADPR is perceived by a Macro domain found in the effector protein (*15*). In type IV Thoeris, the caspase-like protease effector encodes a C-terminal domain of unknown function (fig. S9A). Structural modeling (*34*) suggests that *Ps*Caspase forms a dimer in which the C-terminal domains are brought in close proximity to form a putative ligand-binding pocket (fig. S9B). When co-folding the *Ps*Caspase dimer with N7-cADPR, AlphaFold3 (*34*) confidently placed N7-cADPR within this pocket, predicting multiple residues in *Ps*Caspase to interact with N7-cADPR through hydrogen bonds (E255, Q284, R288, H299) or π-π stacking with the adenine base (W301) (fig. S9C). Mutations in any of these residues abolished defense against phage T6 (fig. S9D), together suggesting that the pocket formed by the C-termini of the *Ps*Caspase dimer is responsible for binding N7-cADPR to trigger the proteolytic activity of the caspase-like domain.

Discussion

Together, our data provide a model for the mechanism of type IV Thoeris (Fig. 4F). Once infection is sensed in the cell, the TIR-domain protein utilizes NAD^+ as a substrate and generates a cyclized ADPR molecule where the carbon previously connected to the nicotinamide ring becomes covalently attached to the N7 nitrogen atom in the adenine base. This N7-cADPR molecule specifically activates the caspase-like effector of the defense system which then indiscriminately cleaves cellular and potentially phage proteins after arginine residues, causing massive protein degradation in the cell and incapacitating the phage reproductive cycle (Fig. 4F). The phage-derived component that is sensed by type IV Thoeris as a signature for infection is currently unknown and awaits future study.

Our data show that the molecule N7-cADPR functions as an immune signaling molecule in bacteria. Past studies showed that immune signaling molecules tend to be shared between domains of life. For example, 2′3′ cyclic GMP-AMP functions as an immune signaling molecule in the human cGAS-STING pathway (*35*), as well as in defense systems of the CBASS family (*36*). Similarly, 3′3′ cyclic UMP-AMP, originally discovered as a signaling molecule in bacterial CBASS systems (*37*), was later shown to be produced by animal immune proteins in response to dsRNA stimulation (*38*). TIR-derived immune signaling molecules also have parallels between bacteria, animals, and plants. For example, 1"-3′ gcADPR, produced by type I Thoeris, was shown to also be produced by the plant immune protein BdTIR (*18*) and the human TIR-domain protein SARM1 (*39*), although the biological roles of this molecule in plants and humans are currently unclear. It is therefore anticipated that the molecule discovered here, N7-cADPR, could also be found to participate in immune signaling in multicellular eukaryotes in future studies.

Human caspases can function both as initiators of cell death, where they activate specific death-promoting proteins by proteolytic cleavage (*1*), or as executioners of cell death, where they cleave hundreds of proteins to promote apoptosis (*3*). Our findings strengthen the understanding that caspase-like proteins have similar roles in bacterial immunity. Bacterial caspase-like proteases were previously shown to cleave bacterial gasdermins into pore-forming effectors that execute a form of pyroptotic-like cell death (*5*), paralleling inflammatory caspases in humans (*1*, *2*). In type IV Thoeris immunity, the role of the caspase-like protease is analogous to executioner caspases, as it directly executes cell death by cleaving many cellular target proteins, likely shutting off essential processes in the cell and preventing viral replication. Recent work has shown that some type III CRISPR-Cas systems also co-opted caspase-like proteases as a part of their immune mechanism (*6*–*8*). In particular, a type III-B CRISPR-Cas system employs a cascade of proteolytic events, in which CRISPR-Cas signaling activates a SAVED-CHAT protease to specifically process *PCaspase*, a caspase-like promiscuous protease that cleaves multiple proteins possibly downstream of arginine residues (*8*). Our results point to a common molecular function of *PCaspase* and the type IV Thoeris caspase as arginine-specific promiscuous proteases responsible for executing cell death or dormancy. Caspase-like proteases were predicted to be associated with other families of defense systems such as CBASS (*40*) and Avs (*41*), but their roles in these systems are currently unknown. It is possible that these proteases mediate bacterial defense through a mechanism similar to that of *Ps*Caspase. Our results show that proteases of the caspase family are ancient modules in the toolbox of immune-related cell death machineries shared by bacteria, fungi (*42*), plants (*43*), and humans (*1*).

REFERENCES AND NOTES

1. N. Van Opdenbosch, M. Lamkanfi, *Immunity* **50**, 1352–1364 (2019).
2. J. Shi *et al*., *Nature* **526**, 660–665 (2015).
3. S. Nagata, *Annu. Rev. Immunol.* **36**, 489–517 (2018).
4. J. Asplund-Samuelsson, B. Bergman, J. Larsson, *PLOS ONE* **7**, e49888 (2012).
5. A. G. Johnson *et al*., *Science* **375**, 221–225 (2022).
6. C. Hu *et al*., *Science* **377**, 1278–1285 (2022).
7. J. Strecker *et al*., *Science* **378**, 874–881 (2022).
8. J. A. Steens *et al*., *Science* **383**, 512–519 (2024).
9. K. Takeda, S. Akira, *Int. Immunol.* **17**, 1–14 (2005).
10. K. Essuman, J. Milbrandt, J. L. Dangl, M. T. Nishimura, *Science* **377**, eabo0001 (2022).
11. M. K. Manik *et al*., *Science* **377**, eadc8969 (2022).
12. A. Leavitt *et al*., *Nature* **611**, 326–331 (2022).
13. G. Ofir *et al*., *Nature* **600**, 116–120 (2021).
14. G. Tamulaitiene *et al*., *Nature* **627**, 431–436 (2024).
15. D. Sabonis *et al*., TIR domains produce histidine-ADPR conjugates as immune signaling molecules in bacteria. bioRxiv 2024.01.03.573942 (2024); doi:10.1101/2024.01.03.573942.
16. D. F. van den Berg *et al*., *Cell Host Microbe* **32**, 1427–1443.e8 (2024).
17. S. Huang *et al*., *Science* **377**, eabq3297 (2022).
18. A. M. Bayless *et al*., *Sci. Adv.* **9**, eade8487 (2023).
19. A. Jia *et al*., *Science* **377**, eabq8180 (2022).
20. D. Yu *et al*., *Cell* **185**, 2370–2386.e18 (2022).
21. E. Maffei *et al*., *PLOS Biol.* **19**, e3001424 (2021).
22. F. Rousset, R. Sorek, *Curr. Opin. Microbiol.* **74**, 102312 (2023).
23. G. Hogrel *et al*., *Nature* **608**, 808–812 (2022).
24. B. R. Morehouse *et al*., *Nature* **608**, 803–807 (2022).
25. N. Tal *et al*., *Cell* **184**, 5728–5739.e16 (2021).
26. B. Koopal *et al*., *Cell* **185**, 1471–1486.e19 (2022).
27. J. Garb *et al*., *Nat. Microbiol.* **7**, 1849–1856 (2022).
28. A. Millman *et al*., *Cell Host Microbe* **30**, 1556–1569.e5 (2022).
29. M. Zaremba *et al*., *Nat. Microbiol.* **7**, 1857–1869 (2022).
30. Y. T. N. Yu, L. Snyder, *Proc. Natl. Acad. Sci. U.S.A.* **91**, 802–806 (1994).
31. H. R. Stennicke, G. S. Salvesen, *Methods Enzymol.* **322**, 91–100 (2000).
32. E. Yirmiya *et al*., *Nature* **625**, 352–359 (2024).
33. S. P. Assenza, P. R. Brown, *J. Chromatogr. A* **289**, 355–365 (1984).
34. Willmore, A. J. *et al*., *Nature* **630**, 493–500 (2024).
35. A. Ablasser *et al*., *Nature* **498**, 380–384 (2013).
36. U. Tak, A. T. Whiteley, Bacterial cGAS-like enzymes produce 2′,3′-cGAMP to activate an ion channel that restricts phage replication. bioRxiv [preprint] 2023.07.24.550367 (2023);
37. A. T. Whiteley *et al*., *Nature* **567**, 194–199 (2019).
38. Y. Li *et al*., *Cell* **186**, 3261–3276.e20 (2023).
39. J. Garb *et al*., *PLOS ONE* **19**, e0302251 (2024).
40. A. Millman, S. Melamed, G. Amitai, R. Sorek, *Nat. Microbiol.* **5**, 1608–1615 (2020).
41. L. A. Gao *et al*., *Science* **377**, eabm4096 (2022).
42. A. Daskalov, *iScience* **26**, 106793 (2023).
43. Q. Xu, L. Zhang, *Plant Signal. Behav.* **4**, 902–904 (2009).
44. I. A. Chen *et al*., *Nucleic Acids Res.* **47**, D666–D677 (2019).

ACKNOWLEDGMENTS

We acknowledge C. Katina for preparing protein samples for mass spectrometry, N. Sumbatyan for useful discussions, and all members of the Sorek lab for constructive criticism on the manuscript. **Funding:** F.R. was supported by the Clore Foundation postdoctoral fellowship and by the Dean of Faculty fellowship from the Weizmann Institute of Science. I.O. was supported by the Ministry of Absorption New Immigrant program. T. Scherf is the incumbent of the Monroy-Marks Research Fellow Chair. R.S. was supported, in part, by the European Research Council (grant ERC-AdG GA 101018520), the Israel Science Foundation (MAPATS grant 2720/22), the Deutsche Forschungsgemeinschaft (SPP 2330, grant 464312965), the Minerva Foundation with funding from the Federal German Ministry for Education and Research, the Ernest and Bonnie Beutler Research Program of Excellence in Genomic Medicine, a research grant from the Estate of Marjorie Plesset, the Institute for Environmental Sustainability (IES), the Center for Immunotherapy at the Weizmann Institute of Science,

and the Knell Family Center for Microbiology. M.I. and S.M. are supported by the Vera and John Schwartz Family Center for Metabolic Biology. **Author contributions:** Conceptualization: F.R., I.O., and R.S. Phage infection experiments: F.R. Cloning: F.R. and A.L. Production and purification of the signaling molecule and analytical chemistry data analysis: I.O. LC-MS experiments: A.H.F., M.I., and S.M. NMR analysis: T.S. EF-Tu cleavage experiments and cleavage sites identification: F.R. Protein mass spectrometry analysis: A.S. Design of the peptide-based reporter assay: G.A. Testing of Thoeris anti-defense proteins: S.S. Bioinformatic detection of Type IV Thoeris: F.R. Writing: F.R., I.O., and R.S. **Competing interests:** R.S. is a scientific cofounder and advisor of BiomX and Ecophage. Other authors declare that they have no competing interests. **Data and materials availability:** All data from the manuscript are available in the manuscript or in supplementary materials. Other materials are available upon request.

SUPPLEMENTARY MATERIALS

science.org/doi/10.1126/science.adu2262
Materials and Methods
Figs. S1 to S9
Tables S1 to S4
References (*45*–*58*)
MDAR Reproducibility Checklist

Submitted 29 October 2024; accepted 30 December 2024
10.1126/science.adu2262

ENERGETICS

Energetic constraints drive the decline of a sentinel polar bear population

Louise C. Archer[1]*, Stephen N. Atkinson[2], Nicholas J. Lunn[3], Stephanie R. Penk[1,4]†, Péter K. Molnár[1,4]

Human-driven Arctic warming and resulting sea ice loss have been associated with declines in several polar bear populations. However, quantifying how individual responses to environmental change integrate and scale to influence population dynamics in polar bears has yet to be achieved. We developed an individual-based bioenergetic model and hindcast population dynamics across 42 years of observed sea ice conditions in Western Hudson Bay, a region undergoing rapid environmental change. The model successfully captured trends in individual morphometrics, reproduction, and population abundance observed over four decades of empirical monitoring data. Our study provides evidence for the interplay between individual energetics and environmental constraints in shaping population dynamics and for the fundamental role of a single limiting mechanism—energy—underpinning the decline of an apex Arctic predator.

Understanding the processes that govern the spatiotemporal dynamics of populations is a fundamental objective in ecology (*1*). Long-term population studies have played important roles in providing sufficient data at the scales required to answer ecological questions about the factors that shape population dynamics (*2*, *3*). However, rapid global change means that patterns and correlations established under contemporary or historical conditions may be disrupted as populations become increasingly exposed to altered environmental states (*4*). To proactively conserve vulnerable species, more mechanistic insight is needed regarding the links between individuals and environments and how these processes scale to influence population-level responses (*5*). Despite repeated calls for mechanistic approaches to understanding populations (*4*, *6*–*8*), process-based studies that reveal mechanisms regulating wild populations remain a challenge. Gaps between theoretical and empirical studies persist for large carnivores, in particular, owing to a dearth of population data at appropriate multigenerational scales (*9*–*11*).

More mechanistic understanding is imperative in the Arctic, where warming is occurring faster than anywhere else on Earth (*12*), causing declines in sea ice (*13*), transforming ecosystems, and threatening the persistence of ice-dependent species (*14*). Polar bears (*Ursus maritimus*) are considered particularly at risk because they rely on sea ice as a platform to hunt seals, their primary food source (*15*). When sea ice melts during warmer months, polar bears are forced on land or to follow retreating ice away from productive continental shelf regions (*16*). During periods of diminished sea ice, individuals rely on their accumulated energy reserves because terrestrial foods are an energetically insufficient replacement (*17*), and deeper, unproductive waters provide few foraging opportunities for those that remain on retreating ice (*18*). Altered sea ice dynamics from climate warming are expected to lead to longer periods of food deprivation for most polar bear subpopulations. Observed declines in body condition (*19*–*21*), reproduction (*19*, *22*), survival (*23*, *24*), and abundance (*23*–*25*) indicate that responses to climate change are already being seen in several regions. Data deficiencies for most subpopulations and the lack of a mechanistic framework quantifying the effects of sea ice loss across the life cycle have hindered conservation. This knowledge gap is partially a result of logistical and financial limitations associated with studying a long-lived, wide-ranging marine mammal that occupies remote regions—limitations common to many imperiled large mammal species (*26*). More broadly, developing mechanistic models that accurately capture effects of environmental change across long timescales and multiple levels of organization (e.g., the joint responses of individual traits, demographic rates, and population dynamics) remains challenging (*7*).

Our objective was to derive a mechanistic model that could explain long-term dynamics in a population that is experiencing rapid environmental change. Given that this change fundamentally affects polar bears through reduced on-ice feeding periods and extended on-land fasting, and recognizing that survival and reproduction are constrained by an individual's ability to meet associated energetic costs (*27*), we focus on energy as the mediating link between environment, individuals, and populations (*5*). We developed an individual-based bioenergetic model based on fundamental physiological principles, which integrates energy acquisition and expenditure (feeding, somatic maintenance, movement, growth, and reproduction) across an individual's life cycle into a single energy budget (*28*) (Fig. 1). We parameterized this model for polar bears using primarily physiological data, considerably advancing on previous studies that had inferred the fasting limits of adult bears on land but could not be applied outside of the ice-free period or across longer timescales (*27*, *29*). Energetic fluxes, energy balance, and allocation to different processes are modeled across the life cycle as a function of an individual's physiological state—which in turn depends on sea ice availability and associated feeding opportunities—to give individual life history, including reproduction and death. Demographic rates and population dynamics emerge through time from the balance between reproduction and mortality across individuals.

We first evaluated the bioenergetic model under average sea ice conditions (calculated across 1979 to 2021) and found that it generated realistic dynamics in individual energetics, body mass, body length, and reproduction that were consistent with polar bear life history and ecology. Because we assumed negligible foraging without sea ice (*27*), energy intake from feeding was zero during the ice-free period and varied across the rest of year based on individual size and seasonal differences in prey availability. Annual cycles in energy balance emerged, where modeled bears switched from an energy deficit

[1]Laboratory of Quantitative Global Change Ecology, Department of Biological Sciences, University of Toronto Scarborough, Toronto, ON, Canada. [2]Independent Researcher, Cooks Creek, MB, Canada. [3]Wildlife Research Division, Science and Technology Branch, Environment and Climate Change Canada, Edmonton, AB, Canada. [4]Department of Ecology and Evolutionary Biology, University of Toronto, Toronto, ON, Canada.
***Corresponding author. Email: louise.archer@utoronto.ca**
†Present address: US Geological Survey Montana Cooperative Wildlife Research Unit, University of Montana, Missoula, MT, USA.

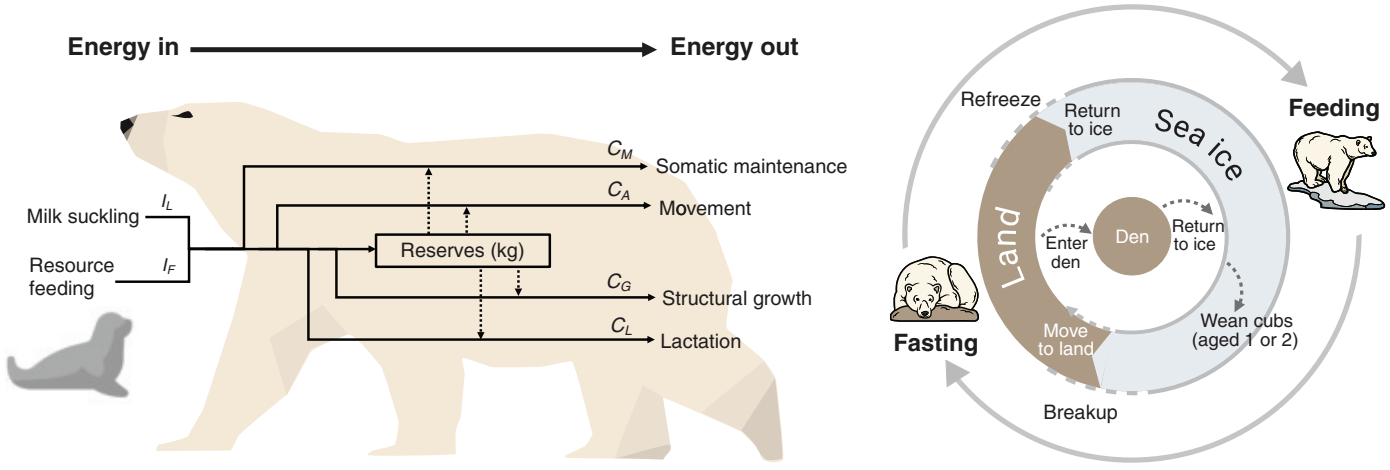

Fig. 1. Overview of key energetic processes (in megajoules per day) that form the polar bear bioenergetic model. Solid lines show the allocation of incoming energy across different processes, and dashed lines show where energy can be mobilized from reserve mass when required. The annual cycle for individuals is also shown, where bears switch between feeding on the sea ice and fasting on land in the summer, when sea ice melts and marine mammal prey become inaccessible. Depending on an individual's state, the time of year, and reproductive condition, the annual cycle may occasionally be punctuated by reproductive events (den entry, den emergence, and weaning of cubs), which do not necessarily occur every year. Pregnant adult females may enter a maternity den in the fall (if above a threshold body condition), give birth to one to three cubs, emerge from the den with their new cubs in spring, and return to the sea ice to feed and provide extended maternal care (including lactation) for up to 2.4 years.

during the ice-free period into energy surplus after freeze-up, when bears resumed feeding on marine prey (Fig. 2 and fig. S7). Feeding rates peaked during the seal pupping period from April to mid-May, averaging 51.6 MJ day^{-1} (SD ± 0.8) for adult females, which matched field-derived consumption estimates (51.6 to 54.2 MJ day^{-1}) (*30*–*32*), and remained high until breakup (48.6 ± 1.0 MJ day^{-1}). Feeding was lower upon return to the ice (32.2 ± 0.6 MJ day^{-1} in November to December), with the lowest feeding rates in midwinter (27.1 ± 1.3 MJ day^{-1} in January to March). Seasonality in energetic balance led to large oscillations in reserve mass (body mass that can be metabolized as a source of energy), where reserves peaked at breakup and were lowest at refreeze (Fig. 2). Oscillations in reserve mass were most pronounced early in the reproductive cycle. While denning, females lost on average 40% body mass, which agrees well with observed mass loss of 43% between autumn and spring for denning females (*33*). After den emergence and resuming on-ice feeding, females with "cubs of the year" regained 57 ± 19 kg before subsequently losing 31% body mass during the ice-free period (mass loss averaging 0.6 ± 0.04 kg day^{-1}). Oscillations dampened as females reduced investment in older cubs. Females with yearlings lost 22% body mass across the ice-free period (0.5 ± 0.03 kg day^{-1}), similar to solitary adult females (0.5 ± 0.05 kg day^{-1}, 20% body mass). Yearling cubs lost 17% body mass over the ice-free season (0.2 ± 0.02 kg day^{-1}), whereas average cub-of-the-year mass stayed approximately constant (gain of 0.02 ± 0.04 kg day^{-1}) because loss of reserve mass (0.1 kg day^{-1}) was offset by structural growth. Our mass loss rates (modeled across the entire ice-free period) were at the low end of empirically observed mass loss rates over shorter intervals (0.2 to 1.6 kg day^{-1} for adult females, 0.4 to 0.7 kg day^{-1} for yearlings, and 0.15 to 0.25 kg day^{-1} for cubs of the year) (*17*, *19*, *27*, *34*, *35*), likely because of nonlinear mass loss over longer periods. Sensitivity analyses indicated that the model was generally robust to variation in parameter values (tables S2 and S3). Parameters related to feeding had the strongest influence on model outputs (figs. S3 and S4), highlighting foraging and prey dynamics as areas for further study and monitoring. These processes likely have outsized impacts on individuals and populations and may be further influenced by environmental change, beyond the reductions in ice-based foraging considered in this work.

We next applied the bioenergetic model to reconstruct the dynamics of a sentinel population of polar bears in Western Hudson Bay, Canada, under climate warming and sea ice conditions observed across the past four decades. Western Hudson Bay is the most intensively studied subpopulation of polar bears, which has been subject to scientific research and monitoring efforts for around five decades (*36*, *37*). The subpopulation occupies the seasonal ice ecoregion (*16*), where sea ice disappears completely in the summer, forcing the entire population onshore. Progressively earlier breakup and later refreeze dates have extended the ice-free period in Western Hudson Bay by 9 to 10 days per decade since 1979 (*27*, *38*), which has coincided with declining metrics of polar bear population health (*15*, *19*) and a recently estimated population size that is approximately half the size of that in the 1980s through mid-1990s (*36*). To examine whether these observed changes could be mechanistically explained by sea ice loss, the resultant loss of feeding opportunities, and impacts on individual-level energetics, we ran simulations of our bioenergetic model over a 42-year period (1979 to 2021) using starting variables (population size, age, and sex structure) corresponding to empirical estimates from Western Hudson Bay for 1979 and with fluctuating sea ice breakup and refreeze dates that matched conditions in Hudson Bay derived from satellite imagery (*27*). We compare model hindcasts against 37 years of long-term empirical monitoring data (comprising 5116 measurements from 2892 polar bears captured during the ice-free period in Western Hudson Bay from 1979 to 2016) to first confirm that the bioenergetic model could reproduce observable empirical trends at multiple levels, including morphometrics and reproductive metrics. Given the importance of recruitment to population dynamics, we focus comparisons on adult females, yearlings, and cubs of the year.

Temporal changes in morphometric traits and reproductive indices

We used generalized linear models (GLMs) to summarize and compare temporal changes in morphometric traits and reproductive indices across the study period in model hindcasts and

the empirical data. Hindcasts captured important features of the empirical data, showing overall similar distributions and temporal dynamics in morphometric and reproductive indices across all age classes and sexes (figs. S8 and S9 and table S5). Body lengths, body masses, and body conditions of adult females, yearlings, and cubs of the year declined through time in both model hindcasts and empirical data (Fig. 3, A to C, and table S6). Overlap of Bayesian 95% credible intervals (fig. S10) indicated that hindcast rates of decline in length were weaker than empirical trends for adult females and cubs of the year but were similar for yearlings, which declined by 1.2 and 1.8 cm decade^{-1} in hindcasts and empirical data, respectively. Body mass declined similarly in hindcasts and empirical data for both adult females and yearlings (e.g., adult female mass declined by 9.6 and 10.5 kg decade^{-1} in hindcasts and empirical data, respectively). Body condition (measured as megajoules of reserve energy per kilogram of lean mass) also declined similarly in hindcasts and empirical data for adult females (by 5.3% and 4.6% decade^{-1}, respectively), with hindcast declines relatively stronger for yearlings and weaker for cubs of the year. Declines in morphometrics were a response to declining environmental conditions (diminished ice-based feeding time and extended fasting periods), with hindcasts also capturing positive observed effects of later sea ice breakup on body mass and body condition (Fig. 3, D and E, and table S7).

Changes in individual energetics scaled up to changes in reproductive indices, with hindcasts again mirroring empirical trends (Fig. 4, fig. S11, and table S8). Hindcast average litter size declined by 0.8% decade^{-1} [95% credible intervals (0.5, 1.2)] for cubs of the year [empirical = 3% (0.2, 5.6)] and by 6.3% decade^{-1} (5.8, 6.8) for yearlings [empirical = 4.5% (−0.8, 9.7)]. The hindcast proportion of females producing a litter declined [−0.035 decade^{-1} (−0.037, −0.033)] as did the number of dependent cubs per female [by 8.6% decade^{-1} (7.9, 9.2)], with weaker evidence for empirical declines [by −0.01 decade^{-1} (−0.03, 0.01) and by 4.6% decade^{-1} (−1.5, 10.3), respectively]. The proportion of females with cubs that were not lactating increased similarly in hindcasts [0.06 decade^{-1} (0.057, 0.064)] and in empirical data [0.08 decade^{-1} (0.03, 0.14)].

Vital rates and population dynamics emerge from individual energetic constraints and sea ice conditions

Having confirmed that the mechanistic model captured observed temporal trends in morphometric traits and reproductive indices and produced realistic functional relationships with

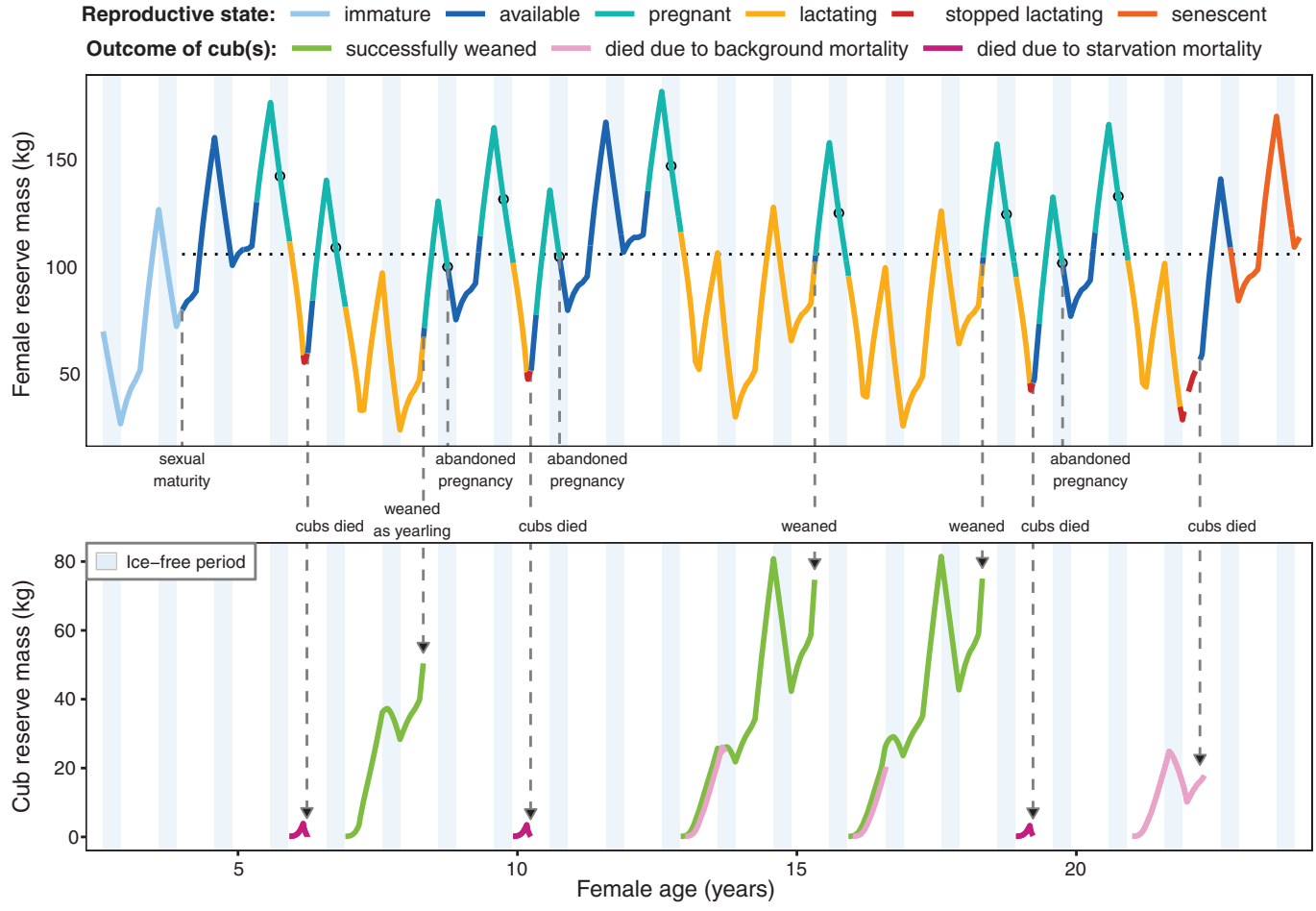

Fig. 2. An example time series of fluctuations in reserve mass across one modeled female polar bear's lifespan and for her dependent cubs, simulated under average sea ice conditions. (**Top**) Fluctuations in reserve mass for one female polar bear's lifespan. (**Bottom**) Fluctuations for her dependent cubs. The female was initiated as a 2 year old, with a body length of 1.79 m, a body mass of 157 kg, structural mass of 114 kg, and reserve mass of 43 kg. The possible reproductive states of the female are indicated by color, with life history events highlighted below the top panel. Open circles indicate the reserves of the female before potential den entry on 1 October, and the dotted horizontal line indicates the threshold body condition for denning and production of cubs. The fates of her cubs in the bottom panel are also indicated by color, where green indicates a cub that was successfully weaned (i.e., became independent), light pink indicates a cub that died owing to background (age-related) mortality, and dark pink indicates a cub that died from starvation mortality.

sea ice, we next aimed to determine how hindcast changes in individual energetics scaled to influence population vital rates. Reduced cub survival and recruitment have occurred alongside declines of several subpopulations (*23*, *24*, *39*), and changes in reproductive rates that emerged from hindcasts supported this. In addition to the declines in reproductive indices described above, life history traits of hindcast females further indicated reduced reproductive output: Although age at first litter production remained approximately stable, the hindcast age at which females first successfully weaned cubs increased slightly (fig. S12A and table S9). The interbirth interval increased more strongly over time [by 8.8% decade^{-1} (8.5, 9.0)], reflecting a change in the life history of Western Hudson Bay bears. Historically, offspring often became independent as yearlings [e.g., from 1966 to 1979, up to 80% of yearlings were independent (*19*)], in contrast to most other regions, where cubs separate from their mothers as 2 year olds (*37*). However, as sea ice has declined over the past four decades, early separation of cubs from their mothers has also become infrequent, with the observed proportion of independent yearlings dropping to <10% and the typical reproductive cycle extending from 2 to 3 years (*15*, *19*). By incorporating energy-dependent weaning in our model, a similar shift in the age of cub independence also emerged in hindcasts, where the average proportion of independent yearlings dropped to 9%, and the mean interbirth interval increased from ~2 years in the 1980s to 1990s to ~3 years in the 2000s (Fig. 4D and fig. S12B). Such emergent features underscore how altered individual-level energetics from environmental changes can scale up to affect vital rates: Reduced reproductive performance and altered life history traits ultimately led to a decline in the hindcast recruitment of yearlings to 2 year olds by 11.8% decade^{-1} (10.7, 12.9) since the 1980s (fig. S12C).

The bioenergetic model incorporated two sources of mortality: starvation-related mortality (from low energy reserves) and background mortality (related to aging and incidental death or harvest). Using GLMs to identify emergent patterns in hindcast mortality, we found that annual starvation mortality increased with duration of the ice-free period for adult females, yearlings, and cubs of the year (Fig. 5A). Consequently, starvation mortality increased across years (fig. S13), concurrent to a general trend toward a longer ice-free period (Fig. 5B), which acted to reduce the number of days that individuals spent feeding across the year and increased the number of days spent fasting (when energy balance was negative). Because annual survival was negatively correlated with starvation mortality (Pearson's correlation coefficient $r = -0.93$; $P < 0.001$), survival showed a corresponding decline with increasing ice-free period and ultimately declined across years

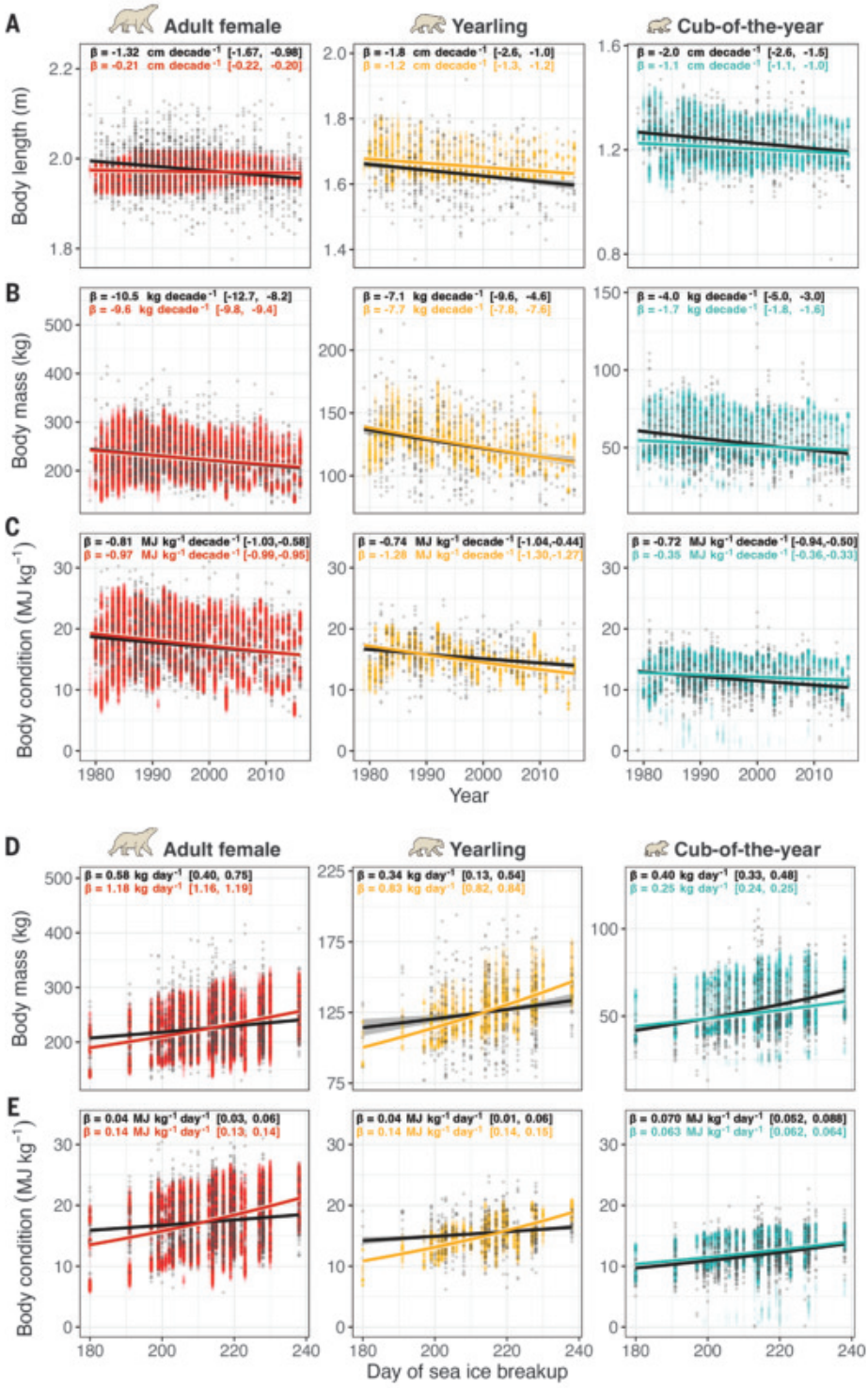

Fig. 3. Empirical and hindcast trends in morphometrics. (**A** to **C**) Comparison of temporal trends in individual body length (A), body mass (B), and body condition (C) from empirical data collected from polar bears in Western Hudson Bay across four decades with outputs from model hindcasts for the same period. (**D** and **E**) Relationships between day of sea ice breakup and body mass (D) and body condition (E) for the same period. Empirical data are shown as gray points, with the black lines showing the mean of the posterior predictions from GLMs. Outputs from model hindcasts are shown as red points (adult females), yellow points (yearlings), and teal points (cubs of the year), with respective lines showing the means of the posterior predictions from GLMs summarizing hindcasts. Parameter values and distributions of GLMs for empirical and hindcast data are available in tables S6 and S7. Also shown are the marginal effects of time and sea ice breakup, indicated by β.

for adult females, yearlings, and cubs of the year (fig. S14).

A particular strength of the mechanistic modeling framework is its ability to give insight into processes occurring at times of the year when opportunities for direct observation and empirical studies are rare. For example, the highest mortality rates in polar bears have generally been recorded for cubs of the year (*24*, *25*, *40*), in agreement with hindcasts. Our model further indicated that although starvation mortality for older bears was distributed toward the end of the ice-free period and after freeze-up, cub-of-the-year mortality showed two additional peaks: The highest mortality occurred after den exit (fig. S15A), when mothers were often in poor condition after protracted fasting and thus tended to either stop or greatly reduce their investment in lactation, leaving their new cubs vulnerable to starvation. Mortality also occurred shortly after breakup for cubs that survived their first few months out of the den but arrived onshore in poor body condition. From the mid-1990s, an additional spike in cub starvation mortality emerged in hindcasts toward the end of cubs' first year (fig. S15B) because earlier sea ice breakup limited cubs' ability to accumulate reserves after den emergence, whereas longer stretches on land caused mothers to reduce investment in lactation toward the end of the ice-free period, leading to some cub starvation (*41*). Elevated mortality continued even after bears returned to the ice at freeze-up and resumed feeding because unfavorable hunting conditions in early and mid-winter meant that modeled food intake was ~35 to 45% lower compared with spring feeding, and cubs of the year (and, to a lesser extent, adult females and yearlings) remained vulnerable to starvation until their energy reserves were gradually restored. Increased starvation mortality of cubs of the year, and resultant reduced recruitment into the yearling age class, may explain the relatively low abundance of yearlings observed in recent population surveys (*36*).

The changes in reproduction and mortality that emerged from hindcasts ultimately precipitated changes in the population size and an overall decline from 1979 to 2021 (Fig. 5C). Ranging between 906 and 1234 bears across the first 20 years, the hindcast population subsequently declined by 49% (95% confidence interval, 40 to 57%) across the next two decades. This trend mirrors empirical population estimates from mark-recapture studies and aerial surveys. Despite differences in empirical study designs (*23*), there is broad consensus that the population was increasing or stable from the 1970s through the mid-1990s, declining into the early 2000s, and followed by a period of stability or slight decline through the mid-2010s (*36*). After increasing from 1000 bears in 1979 to 1230 bears in 1995 (1112 to 1354), increased frequency of longer ice-free periods (relative to 1980s conditions) meant that our hindcast population declined by 19% to 993 bears in 2004 (880 to 1107), which corresponded closely with empirical estimates of 1233 bears (863 to 1643) in 1995 (*42*) and 935 bears (794 to 1076) in 2004 (*25*). By 2011, hindcasts predicted a population of 923 bears (793 to 1057), which falls between estimates from two separate studies of 1030 bears (754 to 1406) (*43*) and 806 bears (653 to 984) (*23*) in 2011. The most recent empirical population estimate was 618 bears (425 to 899) in 2021, closely aligning with our modeled estimate of 616 bears (497 to 751) (*36*). The emergence of realistic population-level trends from the process-based bioenergetic model—which operates at the individual level—is a strong indicator that the most important mechanisms linking polar bears to sea ice were captured (*44*).

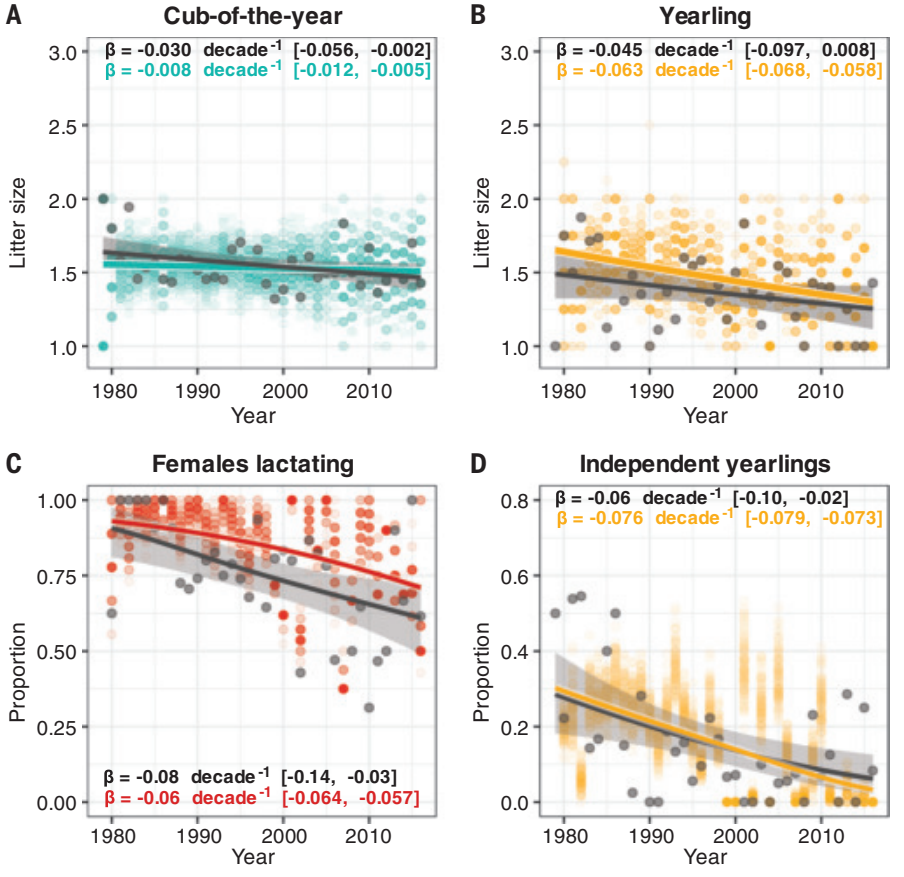

Fig. 4. Empirical and hindcast trends in reproductive metrics. (**A** to **D**) Temporal trends in the average litter size for cubs of the year (A) and yearlings (B), the proportion of females with offspring that are lactating (C), and the proportion of yearlings that are independent (D). Empirical data collected from polar bears in Western Hudson Bay across four decades are shown together with outputs from model hindcasts for the same period. Empirical data are shown as gray points, with the dark gray lines showing the means of the posterior predictions (shaded regions show the 95% credible intervals) from GLMs. Outputs from model hindcasts are shown as teal points in (A), as yellow points in (B) and (D), and as red points in (C), with respective solid lines showing the means of the posterior predictions from GLMs. Parameter values and distributions of GLMs for empirical and hindcast data are available in table S8. Also shown are the marginal effects of time (percentage point change), indicated by β.

Conclusions

Understanding population responses to change requires insight into proximate causes—i.e., the mechanisms that mediate environmental effects on individuals. A challenge in developing such mechanistic insight for long-lived mammals is ensuring that the model can predict independent real-world dynamics at appropriate temporal scales. Using a model developed on first principles of energetics (*28*) and validated against four decades of independent long-term population monitoring and capture data, we have demonstrated how observed population dynamics of a large carnivore are mediated by individual-level energy budgets, environmental change, and cascading demographic effects. The close match between model hindcasts and real-world data across multiple levels provides rare evidence for the role of a single fundamental mechanism (energetic limitation) in driving a

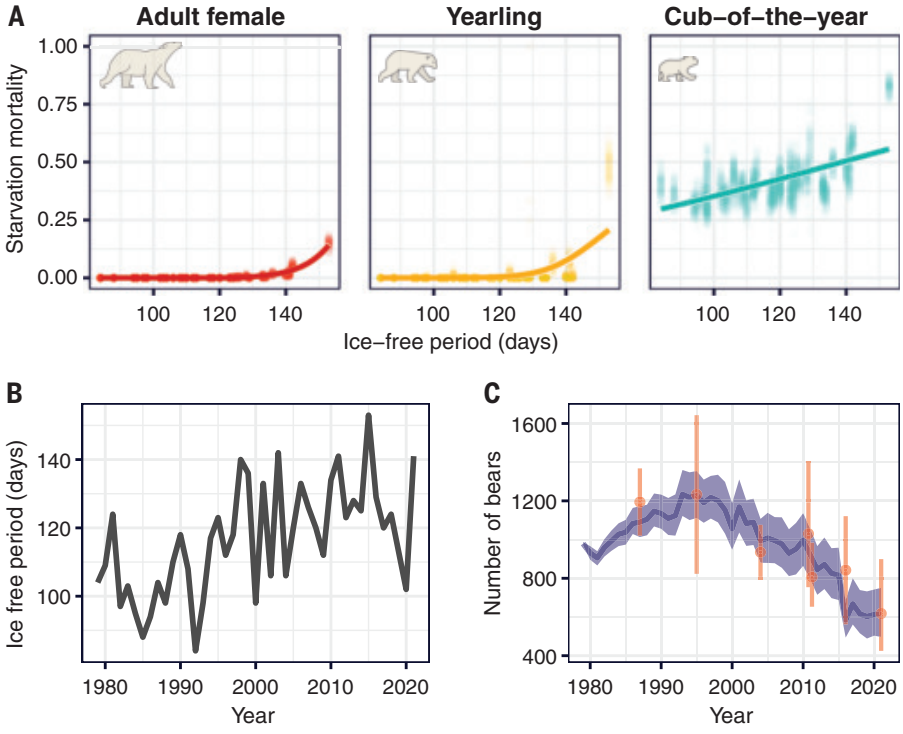

Fig. 5. Effects of sea ice conditions on population dynamics. (**A**) Relationship between the length of the ice-free period and starvation mortality of adult females, yearlings, and cubs of the year estimated from model hindcasts. Points represent output from model hindcasts, and lines represent the means of the posterior predictions from GLMs. Parameter values and distributions for GLMs are available in table S10. (**B**) Duration of the ice-free period in Western Hudson Bay across time. (**C**) Total population size estimated from hindcasts of the bioenergetic model, where the solid blue line is the mean number of bears across 100 simulations, and the shaded blue area is the 95% confidence interval, with the orange points and vertical bars indicating population estimates (means and 95% confidence intervals, respectively) from field studies (*23*, *25*, *36*, *42*, *43*, *50*).

population decline, adding weight to projections that continued warming risks the collapse of most polar bear subpopulations (*27*, *45*) and supporting evidence-based management, conservation decision-making, and policy development (*46*). Although our model was developed for polar bears, the framework is built around the unifying currency of energy and can be adapted to other species where environmental or anthropogenic factors constrain foraging time (*47*, *48*) or could be broadly applied to consider other global change stressors that affect energy acquisition or expenditure—e.g., altered movement rates in response to land use change (*49*).

REFERENCES AND NOTES

1. W. J. Sutherland *et al.*, *J. Ecol.* **101**, 58–67 (2013).
2. T. Clutton-Brock, B. C. Sheldon, *Trends Ecol. Evol.* **25**, 562–573 (2010).
3. A. Ozgul *et al.*, *Nature* **466**, 482–485 (2010).
4. B. Helmuth, J. G. Kingsolver, E. Carrington, *Annu. Rev. Physiol.* **67**, 177–201 (2005).
5. S. Tomlinson *et al.*, *Trends Ecol. Evol.* **29**, 280–290 (2014).
6. T. P. Dawson, S. T. Jackson, J. I. House, I. C. Prentice, G. M. Mace, *Science* **332**, 53–58 (2011).
7. A. S. A. Johnston *et al.*, *Proc. R. Soc. B* **286**, 20191916 (2019).
8. M. C. Urban *et al.*, *Science* **353**, eaad8466 (2016).
9. J. L. Atkins *et al.*, *Science* **364**, 173–177 (2019).
10. R. Bischof *et al.*, *Proc. Natl. Acad. Sci. U.S.A.* **117**, 30531–30538 (2020).
11. G. Passoni *et al.*, *Ecology* **105**, e4197 (2024).
12. E. Post *et al.*, *Sci. Adv.* **5**, eaaw9883 (2019).
13. D. Notz, J. Stroeve, *Science* **354**, 747–750 (2016).
14. K. L. Laidre *et al.*, *Conserv. Biol.* **29**, 724–737 (2015).
15. I. Stirling, A. E. Derocher, *Glob. Change Biol.* **18**, 2694–2706 (2012).
16. S. C. Amstrup *et al.*, *Nature* **468**, 955–958 (2010).
17. A. M. Pagano *et al.*, *Nat. Commun.* **15**, 947 (2024).
18. A. M. Pagano, T. C. Atwood, G. M. Durner, T. M. Williams, *Ecology* **101**, e02959 (2020).
19. A. E. Derocher, I. Stirling, *Can. J. Zool.* **73**, 1657–1665 (1995).
20. K. L. Laidre *et al.*, *Ecol. Appl.* **30**, e02071 (2020).
21. M. E. Obbard *et al.*, *Arct. Sci.* **2**, 15–32 (2016).
22. K. D. Rode, S. C. Amstrup, E. V. Regehr, *Ecol. Appl.* **20**, 768–782 (2010).
23. N. J. Lunn *et al.*, *Ecol. Appl.* **26**, 1302–1320 (2016).
24. J. F. Bromaghin *et al.*, *Ecol. Appl.* **25**, 634–651 (2015).
25. E. V. Regehr, N. J. Lunn, S. C. Amstrup, I. Stirling, *J. Wildl. Manage.* **71**, 2673–2683 (2007).
26. T. M. Williams, *Science* **383**, eadn9607 (2024).
27. P. K. Molnár *et al.*, *Nat. Clim. Chang.* **10**, 732–738 (2020).
28. R. M. Sibly *et al.*, *Methods Ecol. Evol.* **4**, 151–161 (2013).
29. P. K. Molnár, A. E. Derocher, G. W. Thiemann, M. A. Lewis, *Biol. Conserv.* **143**, 1612–1622 (2010).
30. P. K. Molnár, A. E. Derocher, T. Klanjscek, M. A. Lewis, *Nat. Commun.* **2**, 186 (2011).
31. A. M. Pagano *et al.*, *Science* **359**, 568–572 (2018).
32. I. Stirling, N. A. Øritsland, *Can. J. Fish. Aquat. Sci.* **52**, 2594–2612 (1995).
33. S. N. Atkinson, M. A. Ramsay, *Funct. Ecol.* **9**, 559–567 (1995).
34. J. P. Y. Arnould, M. A. Ramsay, *Can. J. Zool.* **72**, 1365–1370 (1994).
35. S. C. Polischuk, R. J. Norstrom, M. A. Ramsay, *Environ. Pollut.* **118**, 29–39 (2002).
36. S. N. Atkinson *et al.*, "2021 Aerial survey of the Western Hudson Bay polar bear subpopulation" (Government of Nunavut, Department of Environment, Wildlife Research Section, 2022).
37. M. A. Ramsay, I. Stirling, *J. Zool.* **214**, 601–633 (1988).
38. H. L. Stern, K. L. Laidre, *Cryosphere* **10**, 2027–2041 (2016).
39. M. E. Obbard *et al.*, *Arct. Sci.* **4**, 634–655 (2018).
40. A. E. Derocher, I. Stirling, *Can. J. Zool.* **74**, 1246–1252 (1996).
41. L. C. Archer, S. N. Atkinson, A. M. Pagano, S. R. Penk, P. K. Molnár, *Mar. Ecol. Prog. Ser.* **720**, 175–189 (2023).
42. N. J. Lunn, I. Stirling, D. Andriashek, G. B. Kolenosky, *Arctic* **50**, 234–240 (1997).
43. S. Stapleton, S. Atkinson, D. Hedman, D. Garshelis, *Biol. Conserv.* **170**, 38–47 (2014).
44. C. A. Gallagher *et al.*, *Biol. Rev.* **96**, 1868–1888 (2021).
45. J. Stroeve *et al.*, *Commun. Earth Environ.* **5**, 296 (2024).
46. S. C. Amstrup, C. M. Bitz, *Science* **381**, 949–951 (2023).
47. J. Luo, B. M. Siemers, K. Koselj, *Glob. Change Biol.* **21**, 3278–3289 (2015).
48. K. L. Laidre *et al.*, *Ecol. Appl.* **18**, S97–S125 (2008).
49. M. A. Tucker *et al.*, *Science* **359**, 466–469 (2018).
50. M. Dyck, M. Campbell, D. S. Lee, J. Boulanger, D. Hedman, "Aerial survey of the Western Hudson Bay polar bear sub-population 2016" (Government of Nunavut, Department of Environment, Wildlife Research Section, 2017).
51. L. Archer, Energetic constraints drive the decline of a sentinel polar bear population, dataset, Figshare (2025); https://doi.org/10.6084/m9.figshare.27974307.

ACKNOWLEDGMENTS

We thank and recognize the late Dr. Ian Stirling for his vision in establishing and leading Environment and Climate Change Canada's long-term research on polar bears in Western Hudson Bay and the many staff, students, and researchers who have contributed to it. This work also greatly benefited from data collected by the late Dr. Malcolm Ramsay (University of Saskatchewan), and we thank F. Messier for access to these data. We thank G. York for funding and advisory support. Polar bear icons used in figures were created by D. Fernandez Bellon (left panel in Fig. 1, Fig. 3, and Fig. 5) and Hey Rabbit (right panel in Fig. 1). **Funding:** This study was supported by a MITACS Elevate Fellowship (L.C.A.); Polar Bears International (L.C.A. and P.K.M.); Natural Sciences and Engineering Research Council of Canada (NSERC) discovery grant RGPIN-2016-06301 (P.K.M.); the Canada Foundation for Innovation (CFI) John R. Evans Leaders Fund grant 35341 (P.K.M.); the Ministry of Research, Innovation and Sciences (MRIS) Ontario Research Fund (P.K.M.); the Churchill Northern Studies Centre (N.J.L.); Environment and Climate Change Canada (N.J.L.); the Earth Rangers Foundation (N.J.L.); the Isdell Family Foundation (N.J.L.); Manitoba Conservation (N.J.L.); the Parks Canada Agency (N.J.L.); Quark Expeditions (N.J.L.); the Schad Foundation (N.J.L.); the World Wildlife Fund Arctic Programme (N.J.L.); and World Wildlife Fund Canada (N.J.L.).
Author contributions: Conceptualization: L.C.A., S.R.P., and P.K.M. Data curation: N.J.L. and S.N.A. Methodology: L.C.A., S.R.P., and P.K.M. Formal analysis: L.C.A. Visualization: L.C.A. Funding acquisition: L.C.A., P.K.M., and N.J.L. Supervision: P.K.M. Writing – original draft: L.C.A. Writing – review & editing: L.C.A., S.N.A., N.J.L., S.R.P., and P.K.M. **Competing interests:** The authors declare that they have no competing interests. **Data and materials availability:** No new data were collected for the study. Raw long-term monitoring data are presented throughout the paper and are also available from Environment and Climate Change Canada. Inputs, outputs, and code required to run the model and recreate the analyses are archived on Figshare (*51*).

SUPPLEMENTARY MATERIALS

science.org/doi/10.1126/science.adp3752
Materials and Methods
Supplementary Text
Figs. S1 to S16
Tables S1 to S10
References (*52*–*193*)
MDAR Reproducibility Checklist

Submitted 29 April 2024; accepted 20 December 2024
10.1126/science.adp3752

PHASE TRANSITIONS

Nondeterministic dynamics in the η-to-θ phase transition of alumina nanoparticles

Masaya Sakakibara[1], Minoru Hanaya[2], Takayuki Nakamuro[1]*, Eiichi Nakamura[1]*

Phase diagrams and crystallography are standard tools for studying structural phase transitions, whereas acquiring kinetic information at the atomistic level has been considered essential but challenging. The η-to-θ phase transition of alumina is unidirectional in bulk and retains the crystal lattice orientation. We report a rare example of a statistical kinetics study showing that for nanoparticles on a bulk $Al(OH)_3$ surface, this phase transition occurs nondeterministically through an ergodic equilibrium through the molten state, and the memory of the lattice orientation is lost in this process. The rate of the interconversion was found to be insensitive to the electron dose rate, and this process had a small Gibbs free energy of activation. These nondeterministic kinetics should be a key feature of crystal nucleation occurring in high-surface-energy regions of bulk crystals.

Crystal phase transitions are often irreversible and thus deterministic processes. For example, alumina (Al_2O_3) undergoes a series of irreversible first-order phase transitions with increasing temperature as it transforms from hydrated alumina [bayerite, α-$Al(OH)_3$] into the metastable η phase, the θ phase, and finally the most stable α phase previously reported (Fig. 1A) (*1*). The transitions involve a series of Al–O bond cleavages that increase in the aluminum atom coordination, from a 3:5 ratio of 4- and 6-coordinate in the η phase, an equal mix in the θ phase, to all 6-coordinate in the α-phase. Previous bulk crystallographic studies concluded that the orientation of the anion sublattice is retained during the η-to-θ transition, although the reasons for this were not fully understood (*2*, *3*).

To investigate this transformation further, we focused on surface regions where nucleation initiates the bulk phase transition. We studied nanosized particles (NPs) of alumina that formed on a bulk surface of α-$Al(OH)_3$ crystallites prepared at submicrometer scale on a spherical aggregate of an aminated carbon nanotube (*a*CNT) (Fig. 1B). The reactions were then monitored in situ with angstrom- and millisecond-resolution transmission electron microscopy (TEM) at 80 kV. At temperatures between 110 and 298 K, α-$Al(OH)_3$ dehydrated (*2*) to form an alumina melt. From this melt, a mixture of NPs formed that underwent various equilibria transitions (η-to-θ, θ-to-η, η-to-η, and θ-to-θ) through a molten state (ML) of alumina (Fig. 1C, 20.02 s and 35.60 s) under the influence of a high surface energy. The surface energy of alumina NPs with diameters smaller than ~4 nm makes ML as stable as crystalline states (*4*), as opposed to the bulk thermodynamics, where ML becomes the most stable only at 2300 K. Here, the η-to-η and θ-to-θ transitions refer to the NP changing its orientation relative to the bulk $Al(OH)_3$ substrate.

Thus, the η-to-θ phase transition of alumina, which is unidirectional in bulk, occurs nondeterministically through a rapid η/θ equilibrium that occurs through melting and recrystallization of NPs on the bulk $Al(OH)_3$ surface (Fig. 1, D and E). Also, we found that the memory of the lattice orientation was lost. For single NPs, the ratio of time spent in the η and θ forms converged after ~1 min at 298 K. This ratio matched the number of η and θ NPs formed when the equilibrium stopped as the NPs grew larger and the surface energy decreased. These observations conform to the ergodicity concept in statistical mechanics; that is, the system explores all parts of its available phase space versus becoming kinetically trapped (*5*–*7*).

The phase transition was driven thermally because of underlying high surface energy, as evidenced by the data showing that the phase transition rate, expressed as the observation time in seconds [k (s^{-1})], depended on the temperature of the sample stage but not the electron dose rate (EDR). The TEM observations indicated that the recrystallization step was rate limiting and occurred >100 times more slowly than the melting step, which took place in <3 ms at 298 K (*8*). Statistical kinetic analysis on individual NPs at 110 and 298 K provided a set of kinetic parameters of the η/θ interconversion, an Arrhenius frequency factor (A = 20.9 s^{-1}), an Arrhenius activation energy (E_a = 2.62 kJ mol^{-1}), a large negative activation entropy ($\Delta S^{\ddagger}$ = −230 J mol^{-1} K^{-1}), and a Gibbs free energy of activation ($\Delta G^{\ddagger}$ = 68.0 kJ mol^{-1}), indicating that the sluggishness of the recrystallization arises from entropic penalty (*9*, *10*). Not unexpectedly, the magnitude of the $\Delta G^{\ddagger}$ value was comparable to those of common organic chemical reactions taking place at room temperature. These data represent a rare demonstration of the capability of real-space TEM observation for elucidation of the mechanism of chemical events through statistical mechanical analysis (*11*, *12*).

These kinetics data obtained for NPs grown from $Al(OH)_3$ crystallites align with the thermodynamics of nanosized alumina polymorphs that Navrotsky *et al.* studied for NPs prepared by gas-phase condensation (*13*). The Navrotsky data, combined with the data that we present here, suggest that nondeterministic kinetics is a common feature of crystal nucleation in high-surface-energy regions of alumina crystals. The discrepancy between the lattice retention in bulk and the scrambling at the nanoscale suggests that the bulk experiment observations (*4*) result from an interplay between localized disorder in high-energy nanoregions and the overarching order imposed by the surrounding bulk crystal structure (*14*). Combined with the atomistic mechanism of bulk crystal disordering (*15*), this disparity challenges traditional views of phase transitions based on macroscopic analyses and underscores the necessity for caution when extrapolating macroscopic data to comprehend their atomistic mechanism. The observed kinetics and the EDR insensitivity indicate that the surface energy is more influential than has been generally assumed in the atomistic event on bulk surfaces and defects or in nanoscale materials that are often studied by high-resolution TEM (*16*).

Alumina nanoparticle formation on $Al(OH)_3$

We used single-molecule atomic-resolution time-resolved electron microscopy (SMART-EM) (*17*–*20*) to cinematographically analyze individual chemical events on single molecules or nanometer-sized specimens supported on CNTs in vacuum (*21*). The method provides the highest spatiotemporal resolution available for the given instrumentation, operating under high-vacuum and variable temperature and voltage conditions with a useful frame rate of 1000 frames per second (fps) (*15*, *22*, *23*). This capability was essential to study the faint contrast of aligned oxygen atoms in alumina NPs (*24*). In this context, we have developed a method to grow alumina NPs on the surface of α-$Al(OH)_3$ (Fig. 1C). By mixing a water-dispersible spherical aggregate of *a*CNT with an aqueous solution of $NaAlO_2$ (*25*) and allowing the mixture to stand at room temperature, we formed a thin crust of polycrystals of α-$Al(OH)_3$ on the ~100-nm-sized *a*CNT aggregate. Neither pristine CNT nor oxidized CNT produced 100-nm-sized solid crystals instead of a crust of α-$Al(OH)_3$ crystallites (fig. S3).

The average size of the α-$Al(OH)_3$ crystallites was 4.7 nm, as estimated by powder x-ray diffraction (fig. S2). The shell of the α-$Al(OH)_3$ polycrystals served as the seed for the alumina crystallization (compare with Fig. 1C). Thermogravimetric and differential thermal analysis

[1]Department of Chemistry, The University of Tokyo, Bunkyo-ku, Tokyo, Japan. [2]Graduate School of Science and Technology, Gunma University, Kiryu, Gunma, Japan.
*Corresponding author. Email: muro@chem.s.u-tokyo.ac.jp (T.N.); nakamura@chem.s.u-tokyo.ac.jp (E.N.)

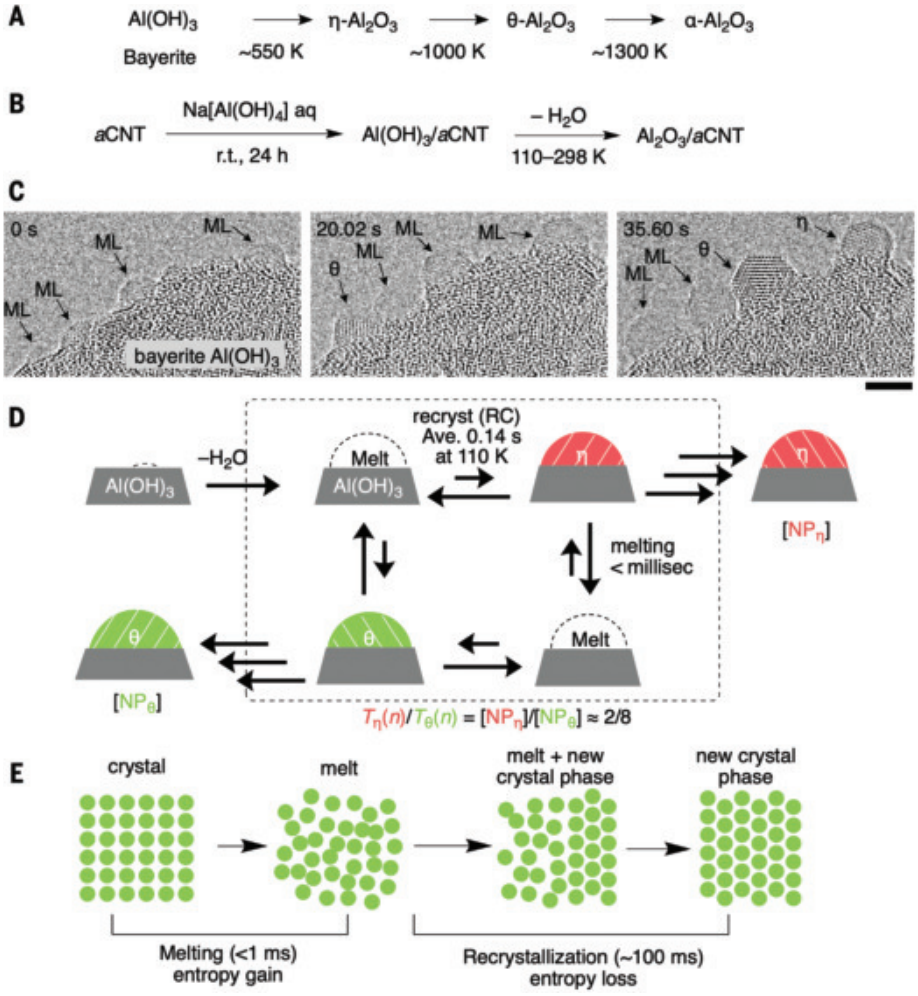

Fig. 1. Conversion of α-Al(OH)$_3$ to η and θ alumina. (**A**) The macroscale thermal transformation of α-Al(OH)$_3$ to α-Al$_2$O$_3$ is an irreversible phase transition. (**B**) Preparation of α-Al(OH)$_3$ on a spherical aggregate of *a*CNT (see text). (**C**) Representative TEM images (50 fps) of in situ formation of alumina NPs. The aggregates of ~100-nm-diameter α-Al(OH)$_3$ nanocrystallites formed on the surface of a spherical aggregate of *a*CNT. ML represents a molten state consisting of a mixture of melt and growing crystal, where we found few discernable lattices in the 50-fps images, and η and θ represent NP$_\eta$ and NP$_\theta$, respectively. The gray area at the top is a vacuum. See the supplementary materials for a low-magnification image of the Al(OH)$_3$/*a*CNT crystallites on the spherical aggregate of *a*CNT (fig. S1). Scale bar, 3 nm. (**D**) Summary of the ergodic equilibria of alumina NPs through melting and recrystallization of the melt that resulted in the loss of memory of lattice orientation (stripes). $T_\eta(n)/T_\theta(n)$ is defined as the ratio of time each NP spent in the NP$_\eta$-to-NP$_\theta$ state. [NP$_\eta$] and [NP$_\theta$] indicate the structural information after nucleation. (**E**) Schematic diagram of the observed mechanism of transformation mediated by the molten phase.

of the Al(OH)$_3$/*a*CNT samples showed a transformation sequence from α-Al(OH)$_3$ to η-Al$_2$O$_3$ at 520 K, then to θ-Al$_2$O$_3$ around 1000 K, and finally to α-Al$_2$O$_3$ at ~1300 K, consistent with transitions reported for bulk α-Al(OH)$_3$ (Fig. 1A and fig. S2) (*3*). The nanosized α-Al(OH)$_3$ crystallites dehydrated into a mixture of η-Al$_2$O$_3$ and θ-Al$_2$O$_3$ under the high-vacuum TEM observation (*26*), a process akin to the dehydrative production of α-alumina from nanosized boehmite [γ-Al(O)OH] at room temperature upon ball milling (*27*). As discussed below, the electron beam–mediated dehydration occurred on the order of minutes, whereas the thermal phase transitions of the NPs occurred in milliseconds (Fig. 2).

300-fps imaging of η/θ interconversion through melting and recrystallization

The transformation of an NP from the θ structure to the η structure at 298 K is shown as a series of images at 300 fps (3.33 ms per frame) in Fig. 2A. This transformation occurred in two steps, fast melting followed by rate-limiting crystal growth. We estimated that the θ structure disappeared in far less time than one frame, but likely in under 1 ms, because we observed only the η structure in the 30.0- to 33.3-ms frame and only the θ structure in the 33.3- to 36.7-ms frame. After the rapid melting in the 33.3-ms frame, we observed the slow formation of the η crystal from the melt (*28*). The recrystallization process required ~100 ms to complete, which is >100 times longer than the melting process. Note that the rate-limiting step of such a multistep reaction was identified visually rather than being determined by kinetic analysis.

In the 30.0-ms frame, we saw the θ phase on the top right part (Fig. 2A, green), which, in the 33.3-ms frame, has disappeared to produce a melt, and the η phase on the bottom left (Fig. 2A, red). The η-crystalline phase continued to expand toward the top right region, where we had seen the θ structure several milliseconds earlier. Using two-dimensional (2D) fast Fourier transform (FFT) analyses, we determined the orientation of the anion sublattices. The 30.0-ms frame (Fig. 2B, green square) corresponds to the θ phase with a lattice spacing of 2.3 Å, while the 33.3-ms frame (Fig. 2B, red square) represents the η phase with a lattice spacing of 1.9 Å.

The θ-to-η transformation was quantified by the change in intensities of the 2D FFT peaks (Fig. 2C). Compared with the instantaneous θ-to-η melt transition, the melt-to-η transition was far slower, as evidenced by the increase of the red-colored area of η-structure plotted in Fig. 2D. Here, we observed in situ the nucleation and crystal growth process on the nanoscale, as illustrated in Fig. 1E (*27*, *29*). The large difference in the rate constants between the crystal-to-melt and melt-to-crystal transitions suggested that the latter suffers an entropic penalty because it requires extensive atomic organization (*13*).

We analyzed the crystal lattice orientation before and after phase transitions and found that the orientation was randomized (Fig. 2, B and E), in contrast to the reported bulk observation (*4*). We measured the angles between the θ(310) and η(400) planes during three-phase transition events and obtained varied values of 1.8° (Fig. 2B), 43.1° (Fig. 2E, left), and 77.6° (Fig. 2E, right). These findings were consistent with the formation of a molten state in which substantial atomic relocations and extensive alternation of Al–O bonds took place (compare with Fig. 1E). Thus, the phase change at the nanoscale occurred through a reconstructive mechanism instead of by direct transformation from one crystal plane to a specific other plane, as occurs in martensitic transformation or cation diffusion within the anion sublattice (*30*). In good agreement with the reconstructive mechanism, we determined a highly negative entropy of activation of the recrystallization step (discussed below).

Interconversions of η and θ alumina at 110 K

We next performed statistical analysis to determine the energetics of the dynamics at 110 K.

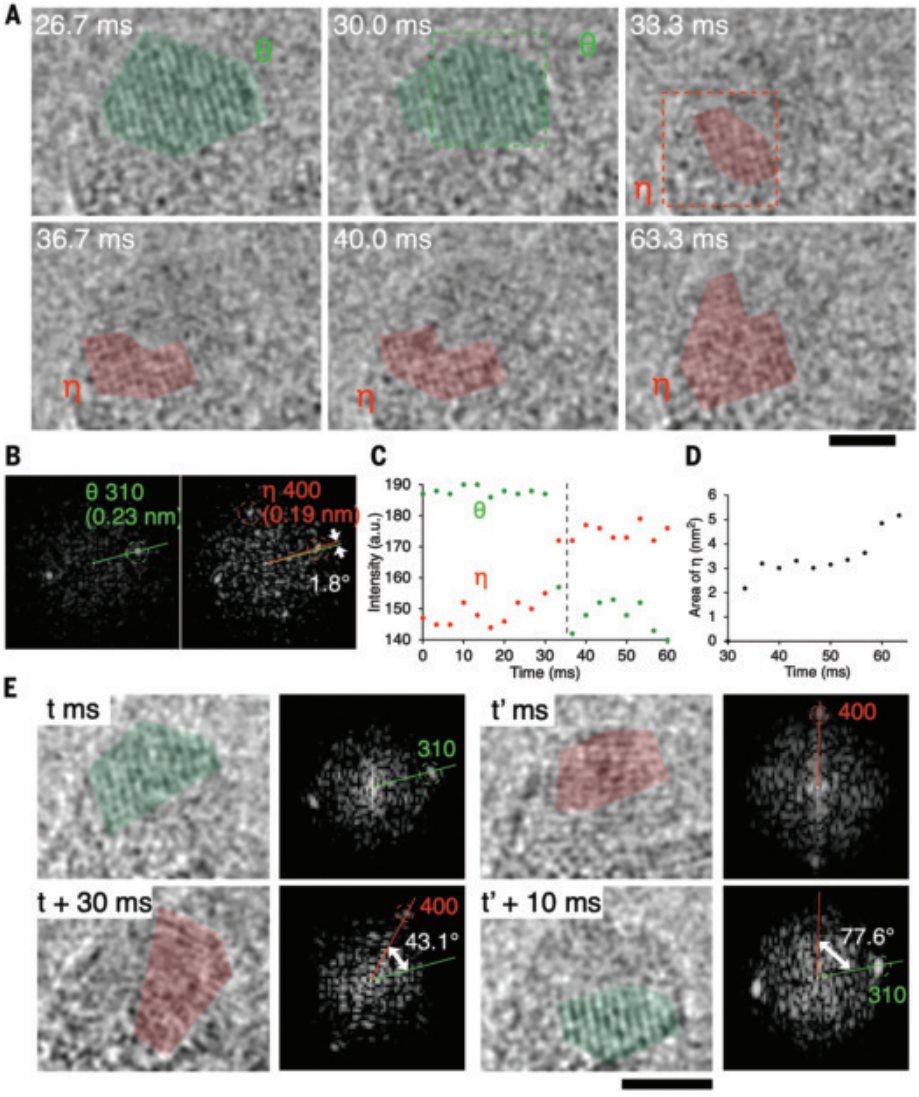

Fig. 2. Observation of phase transition by 300-fps imaging at 298 K. (**A** and **B**) Representative TEM images of a nucleating NP and their 2D FFT patterns (fig. S4 and movie S1). EDR = 2.2 × 10^6 e^- nm^{-2} s^{-1}, 80 kV, with the K3-IS camera. Scale bar, 2 nm. Local structures were classified into θ (green) and η (red) based on 2D FFT analysis. (**C**) Time evolution of the intensity of the strongest peaks in 2D FFT pattern for the θ (green) and η (red) phases. (**D**) Time course of the increase of the projected area of η crystal for the TEM image [e.g., the red area in (A)]. (**E**) Measurement of the angle between the θ(310) and η(400) planes before and after the transformation. For TEM images with 2D lattice fringes, the structure was assigned by comparing with simulated images in terms of both lattice spacing and symmetry. For TEM images with only a 1D lattice fringe, the frames with a 0.19-nm spacing [η(400)] are classified as η, and those with a 0.23-nm spacing of [θ(310)] are classified as θ.

We studied tens of NPs cinematographically at 110 K and 50 fps. Figure 3A illustrates an example observation of a single NP for 100 s (see also Fig. 1C). Small bulges on the $Al(OH)_3$/*a*CNT surface appeared first (*31*). Initially, up to a projected area of ~3 nm^2 (0 s), we saw no structural features. As the size of these bulges increased, the structure of the single NP fluctuated stochastically between η structures (22.46, 79.72, and 99.80 s) and θ structures (20.44 and 47.88 s) transforming through the ML (54.36 s and 56.76 s). The ML, which is a mixture of the melt and a growing crystal, produced no discernable lattice image in the 50-fps images.

We assigned the structure by 2D FFT analysis (fig. S6). During the course of 10 to 20 s, the NP frequently switched between η (Fig. 3B, red) and θ (Fig. 3B, green). The changes for 12.0 to 13.0 s and for 15.6 to 16.6 s indicated that the interconversions were stochastic at any given point (*32*, *33*). The observation of the ML (black) over several consecutive frames was the result of slow crystal growth, as discussed above. Although the lifetime of each state changed stochastically (*26*, *34*, *35*), an average over a sufficiently long time revealed that the ratio of the time the NP spent in NP_η to NP_θ (T_η/T_θ) reached a constant value, as discussed below.

As the electron beam–mediated $Al(OH)_3$-to-alumina conversion proceeded, the NP grew larger and its projected area increased from 2 to 8.5 nm^2 after 100 s (Fig. 3C, black dots), which was thousands of times slower than the thermal melting and recrystallization process (Fig. 2A). For the NP of projected area 3 to 6 nm^2, the two phases interconverted frequently with a frequency of 1.19 Hz, corresponding to a reaction rate constant k = 1.19 s^{-1}, or one event every 840 ms on average. This frequency gradually decreased, and the interconversion stopped when the reduced contribution of surface energy, observed as the projected area of the NPs, reached an average size of 7.88 nm^2 (Fig. 3D).

Figure 3E illustrates the "convergence of time averages," a basic aspect of statistical mechanical analysis. The T_η/T_θ ratio varied and the proportion of η changed appreciably from 0.05 to 0.45 in short observations (1 to 5 s) but converged to a constant value after 20 s. The convergence time constant (τ) was 9.0 s, indicating the time required for the deviation from the long-term average to reduce to e^{-1}. Therefore, time scales longer than τ = 9.0 s reflected statistically meaningful properties of the system. Figure 3F shows the frequency of alternation between the η and θ phases during 10-s intervals between 0 and 100 s. As the projected area of the NP slowly increased (black dots), the converged T_η/T_θ ratio averaged 0.17/0.83 between 10 and 70 s.

Figure 3G shows a finer-resolution series at ~82.72 s (purple line), when the projected area was 7.52 nm^2 and the η/θ interconversions ceased and stabilized as NP_η (T_η/T_θ = 1/0). This change indicated that the interconversion was quenched by a decrease in the surface energy. Figure 3H summarizes the duration of the ML (Fig. 3B, black bar) at 110 K, representing the time required for recrystallization: the average time of 0.14 s and the maximum time of 0.96 s. The final state of the 10 NPs that we studied in detail showed a ratio of [NP_η]/[NP_θ] = 2/8 (fig. S7). This value agreed with the T_η/T_θ = 0.17/0.83 discussed above. This observation of "equivalence of time and ensemble averages" evidenced the ergodicity of the η/θ interconversions.

Interconversions of η and θ alumina at 298 K

Statistical analysis of the behavior of individual alumina NPs at 110 K showed that the η/θ equilibrium follows the ergodic principle of statistical mechanics. This indicates that studying a single NP or several NPs over a

sufficiently long time provides statistically meaningful insights into the reaction mechanism. Therefore, we repeated the same set of experiments at 298 K and determined the kinetic and thermodynamic parameters of the η/θ equilibrium process.

Like the observations at 110 K, we saw reversible interconversions (Fig. 4A) between η (such as at 5.06 s), θ (such as at 27.72 s), and ML (such as at 37.62 s) at 298 K. Data from one of the 13 NPs examined are shown in Fig. 4, A to E. Over a period of 60 s, the projected area of the NP grew from 2 to 16 nm^2, and interconversions between the η and θ phases were observed over the 3- to 12.5-nm^2 range. The shape of the NP gradually changed with the η/θ structural transition. Analyzing changes between 33.84 and 33.88 s (Fig. 4B), we found that the orientation of the crystals shifted and the NP surface moved at a minimum rate of ~0.01 nm/ms. This shape flexibility was consistent with the melting and crystal growth mechanism and lattice scrambling in Fig. 2E. [We note in passing that higher-temperature (473 K) analysis was not possible because $Al(OH)_3$ was converted entirely to alumina before analysis, and atomic resolution imaging at a midtemperature (200 K) analysis was unfeasible because of instability of the view field caused by evaporation of liquid nitrogen (fig. S8).]

With EDR = 3.2×10^6 e^- nm^{-2} s^{-1} at 80 kV, the projected area increased from 2 to 16 nm^2 (Fig. 4C, black dots). The rate constant of the η/θ interconverting was k = 7.27 s^{-1}, or one event every 138 ms on average, measured over the 3- to 6-nm^2 range; this was 6.1 times more frequent than at 110 K. We also observed a "convergence of average" at 298 K, and the convergence time constant of τ = 1.6 s was 5.6 times shorter compared with that at 110 K (Fig. 4D). The converged T_η/T_θ ratio was 0.20/0.80 (Fig. 4E), which was slightly greater than that of 0.17/0.83 at 110 K.

The interconversion rate k was insensitive to the EDR for a NP of the same size (5 nm^2). As shown in Fig. 5A, the ERD variation at 298 K between 3.2 and 6.4×10^6 e^- nm^{-2} s^{-1} did not affect the rate constant of the interconversion to be k = 7.42 ± 0.08 (SE) s^{-1}, nor did the $T_\eta/(T_\eta + T_\theta)$ ratio, where k does change upon the temperature variation of the sample stage. This result indicated that the electron beam had negligible effects on the rate of the η/θ transition in the alumina NPs on bulk $Al(OH)_3$, where the high surface energy of the NP and the thermal energy from the stage drove the reaction. This result is also consistent with the observation that the rate-limiting step is the entropy-controlled recrystallization instead of the melting (Fig. 1E).

At 298 K, the increased thermal energy imparted to the particles allowed the interconversion between η and θ to continue beyond the

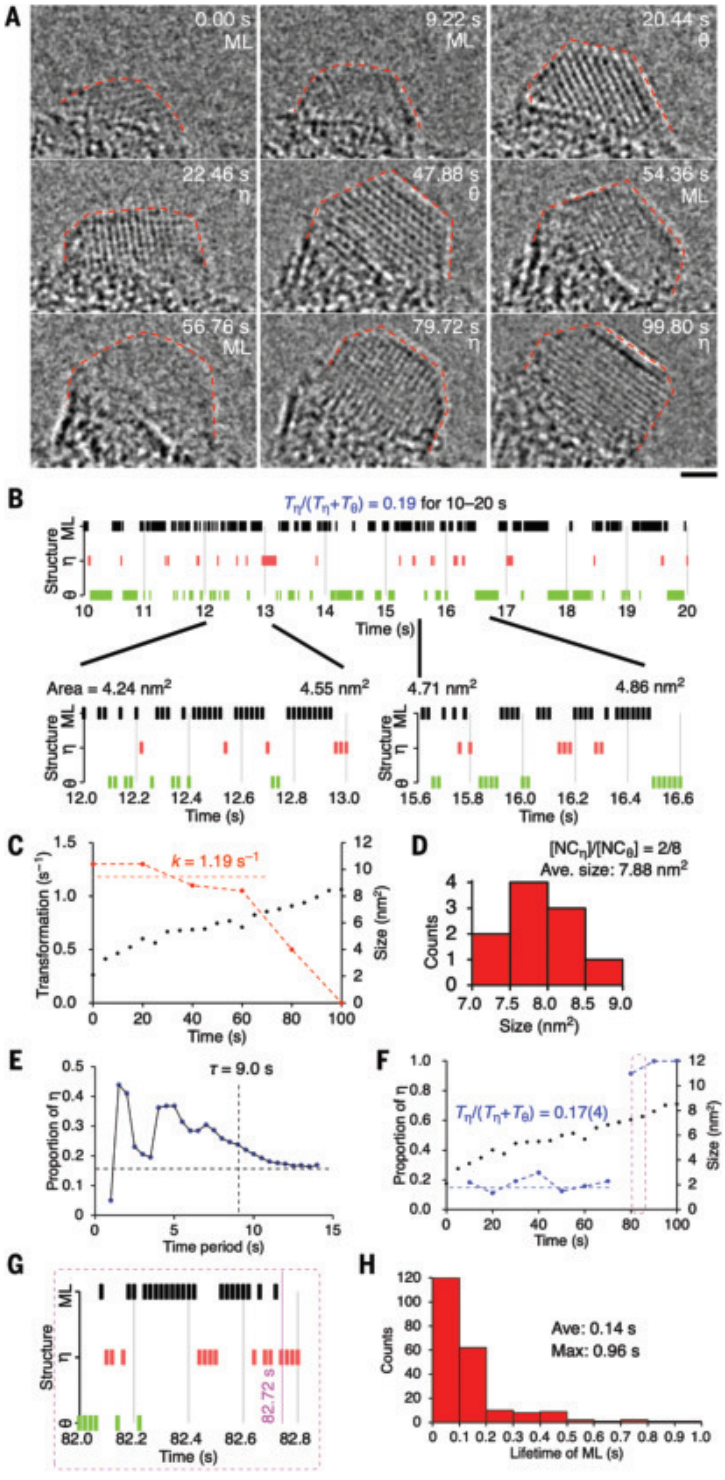

Fig. 3. Structural fluctuations of alumina NPs at 110 K. (**A**) Representative TEM images of an alumina NP at 50 fps. EDR = 2.9×10^6 e^- nm^{-2} s^{-1}. Scale bar, 1 nm. The gray top area is a vacuum, and the bottom is the α-$Al(OH)_3$ crystallite (fig. S5 and movie S2). (**B**) Time evolution of the structure of the NP during 10 to 20 s and its close-up versions. (**C**) Time-course analysis of the η/θ interconversion frequency (red) with the size of the NP (black). (**D**) Statistical analysis of the critical size of alumina for structural freezing. (**E**) Convergence of the η/θ ratio with extended averaging time. (**F**) Time-course analysis of the proportion of η structure (blue) during 10-s intervals between 0 and 100 s. (**G**) Close-up plot of the structure of the NP around 82.44 s. (**H**) Statistics of the lifetime of ML at 110 K.

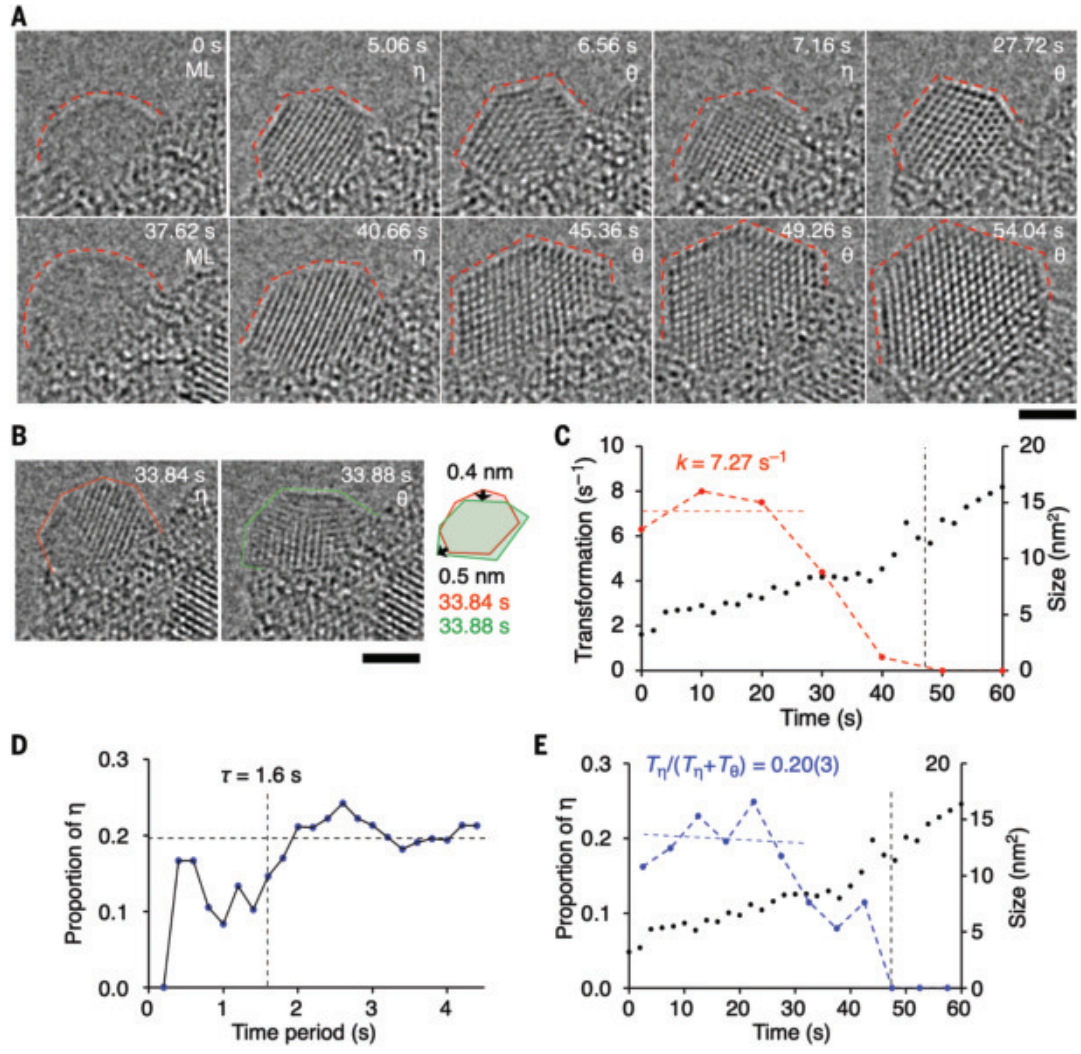

Fig. 4. Formation and structural fluctuation of alumina NPs at 298 K. (**A**) Representative TEM images of an alumina NP. At 50 fps, EDR = 3.2×10^6 e^- nm^{-2} s^{-1}, 80 kV. Scale bar, 1 nm (fig. S8 and movie S3). (**B**) Shape changes of the cluster during the interconversion. (**C**) Time-course analysis of the η/θ interconversion frequency (red) with the size of the NP (black). (**D**) Convergence of the η/θ ratio with extended averaging time at the diameter of ~3 nm. (**E**) Time-course analysis of the proportion of η structure (blue) with the averaging period of 5 s.

projected area of 8 nm^2. However, as the NP size increased, the interconversion frequency gradually dropped (Fig. 4C), and the interconversion completely stopped once the size reached 12.5 nm^2. This freezing size corresponded to ~150 Al_2O_3 units, ~1.5 times larger in volume than the ~100 Al_2O_3 units at 110 K. Note that the NP is seen here as a macromolecule made of 150 Al_2O_3 units. As the size increased, the T_η/T_θ ratio dropped to <1/9, eventually forming NPs composed entirely of the θ phase (Fig. 4A, 54.04 s). When the structures froze, all 13 NPs we studied were in the θ form (fig. S10), demonstrating the equivalence of time and ensemble averages at 298 K.

Discussion

In terms of crystal nucleation, the most important finding of this study was the stochastic appearance of the η and θ structures preceding the formation of a stable crystalline phase in the NP experiments. These events were driven by the surface and thermal energy, as evidenced by their insensitivity to EDR, much slower kinetics compared with electron beam–driven $Al(OH)_3$ dehydration, and the kinetic parameters discussed below. We suspect that this dominance of surface and thermal energy may be common for the nanoscale TEM observations, because we recently observed a similar occurrence in the nucleation of CsCl nanocrystals (*36*). To investigate this further, we conducted a quantitative statistical analysis of the ergodic equilibria under the 110 and 298 K conditions, studying single NPs for a period longer than the convergence time (τ). We estimated the energetics of η/θ interconversion in NPs of ~20 nm^3 using the temperature dependency of the T_η/T_θ ratio and the rate constant (k) obtained statistically for single NPs at 110 and 298 K (*37*). The increase of the T_η/T_θ ratio from 0.17/0.83 at 110 K to 0.20/0.80 at 298 K indicates that NP_η is thermodynamically less stable than NP_θ by ΔH = 0.29 kJ/mol. The differences in entropy and free energy associated with the η-to-θ interconversion were calculated from the equilibrium constant (Fig. 5C; for details, see figs. S11 and S12).

The η/θ interconversion rate, which reflects the energetics of the rate-limiting recrystallization step, increased from k = 1.19 s^{-1} at 110 K to k = 7.27 s^{-1} at 298 K, indicating an Arrhenius frequency factor of A = 20.9 s^{-1} and an activation energy (E_a) of 2.62 kJ mol^{-1} (Fig. 5B). We calculated $\Delta H^\ddagger$ = 0.14 kJ mol^{-1} using the equation $E_a = \Delta H^\ddagger + RT$, where RT = 2.48 kJ mol^{-1} is the thermal energy at 298 K. From $\Delta H^\ddagger$ and the Eyring equation, we calculated an entropy of activation, $\Delta S^\ddagger$ = −230 J mol^{-1} K^{-1}, an extremely large entropy loss due to recrystallization of the molten phase into η or θ phase. Using this dataset, we estimated the activation free energy of the η/θ interconversion to be $\Delta G^\ddagger$ = 68.0 kJ mol^{-1}, which in turn reproduces the observed rate constant k at 298 K (fig. S11 and Eqs. 1 to 6 in the supplementary materials). The recrystallization step suffered from an entropy decrease, whereas the melting step benefited from an entropy increase (compare

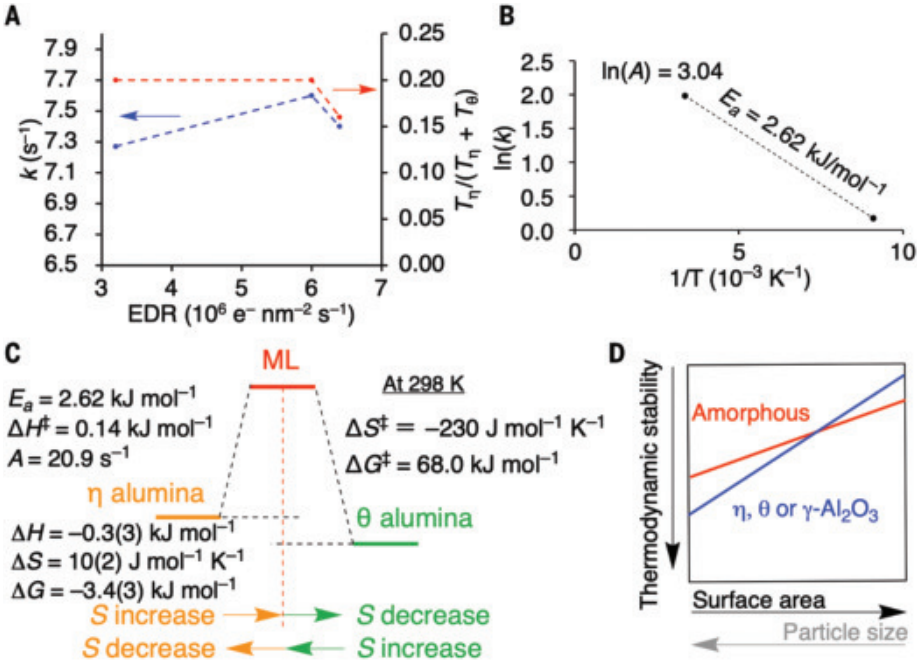

Fig. 5. Kinetics and thermodynamic analysis. (**A**) Insensitivity of k and the $T_\eta/(T_\eta + T_\theta)$ ratio to EDR at 298 K. (**B**) Arrhenius plot of the temperature dependence of k. (**C**) Energy diagram on statistical kinetics of individual NPs of ~20 nm^3 in volume. The energetic parameters are shown per mole of NPs. (**D**) Navrotsky's surface energy/stability diagram on alumina polymorphs (arbitrary scale). The crossing point reported for γ-alumina NPs corresponds to a volume of ~50 nm^3 (*17*). The crossing point determined in this study for the η- and θ-alumina NPs is ~20 nm^3.

with Fig. 2). Thus, the η-to-θ interconversion is a rare example of reactions that are controlled solely by the entropy barrier with virtually no enthalpy barrier.

The extremely small activation enthalpy ($\Delta H^\ddagger$ = 0.14 kJ mol^{-1}) of the η/θ equilibrium through the ML state suggests that the ML state and the η and θ crystalline state of the alumina NPs of ~20 nm^3 in volume have nearly the same enthalpy (Fig. 5C). This conclusion aligns with Navrotsky's thermodynamic data showing that the enthalpy difference becomes zero for amorphous alumina NPs and γ-alumina NPs at a volume of ~50 nm^3 (Fig. 5D) (*1*, *4*). The discrepancy in the volume between 20 and 50 nm^3 may have been caused by the presence of an $Al_2O_3/Al(OH)_3$ interface in the present study. In cases where E_a approaches zero, the accuracy of the derived activation parameters may become uncertain and reflect inherent limitations of the Arrhenius model, which assumes a clear exponential dependence of the rate constant on temperature.

The SMART-EM study of the alumina NP system provided a unique opportunity to perform a statistical mechanical analysis of the chemical kinetics. The observed crystal melting and recrystallization using real-space TEM imaging parallels our recent reciprocal space study on crystal melting (*20*). Through this comparison, we found that the electron beam drives the bulk disordering studied under electron diffraction (ED) conditions, whereas the nanoscale phase transition discussed herein is driven thermally because of the underlying high surface energy (*38*). Therefore, the former has a rate constant and Arrhenius frequency factor (A) with units of $(e^-)^{-1}$ nm^2, whereas the latter has units of s^{-1}. This difference, along with the temperature dependence of the reaction rate, as described by the Arrhenius equation, $k = A\exp(-E_a/RT)$, makes comparing the reaction rates between the two systems complex. Furthermore, our recent statistical mechanical kinetic studies of electron beam–driven reactions have revealed temperature- and voltage-dependent switching among multiple mechanisms (*15*, *16*). Our data underscore the importance of careful kinetic and thermodynamic studies to accurately infer mechanisms for the atomistic phenomena observed under TEM and ED conditions.

REFERENCES AND NOTES

1. I. Levin, D. Brandon, *J. Am. Ceram. Soc.* **81**, 1995–2012 (1998).
2. R.-S. Zhou, R. L. Snyder, *Acta Crystallogr. B* **47**, 617–630 (1991).
3. S. Ishizuka *et al.*, *Chem. Mater.* **28**, 8732–8741 (2016).
4. J. M. McHale, A. Auroux, A. J. Perrotta, A. Navrotsky, *Science* **277**, 788–791 (1997).
5. D. J. Smith, A. K. Petford-Long, L. R. Wallenberg, J.-O. Bovin, *Science* **233**, 872–875 (1986).
6. S. Iijima, T. Ichihashi, *Phys. Rev. Lett.* **56**, 616–619 (1986).
7. J.-Y. Li *et al.*, *Proc. Natl. Acad. Sci. U.S.A.* **121**, e2314797121 (2024).
8. B. J. Siwick, J. R. Dwyer, R. E. Jordan, R. J. D. Miller, *Science* **302**, 1382–1385 (2003).
9. D. Frenkel, *Physica A* **263**, 26–38 (1999).
10. R. K. Bowles, P. Harrowell, *J. Phys. Chem. B* **127**, 4126–4134 (2023).
11. S. Okada *et al.*, *J. Am. Chem. Soc.* **139**, 18281–18287 (2017).
12. D. Liu *et al.*, *Proc. Natl. Acad. Sci. U.S.A.* **119**, e2200290119 (2022).
13. A. H. Tavakoli *et al.*, *J. Phys. Chem. C.* **117**, 17123–17130 (2013).
14. P.-C. Chen *et al.*, *Nat. Nanotechnol.* **19**, 775–781 (2024).
15. D. Liu *et al.*, *Science* **384**, 1212–1219 (2024).
16. F. M. Alcorn, P. K. Jain, R. M. van der Veen, *Nat. Rev. Chem.* **7**, 256–272 (2023).
17. M. Koshino *et al.*, *Science* **316**, 853 (2007).
18. T. Ishikawa *et al.*, *J. Am. Chem. Soc.* **145**, 12244–12254 (2023).
19. E. Nakamura, *Acc. Chem. Res.* **50**, 1281–1292 (2017).
20. K. Harano, T. Nakamuro, E. Nakamura, *Microscopy (Oxf.)* **73**, 101–116 (2024).
21. T. Nakamuro, M. Sakakibara, H. Nada, K. Harano, E. Nakamura, *J. Am. Chem. Soc.* **143**, 1763–1767 (2021).
22. T. Shimizu, D. Lungerich, K. Harano, E. Nakamura, *J. Am. Chem. Soc.* **144**, 9797–9805 (2022).
23. M. Sakakibara, H. Nada, T. Nakamuro, E. Nakamura, *ACS Cent. Sci.* **8**, 1704–1710 (2022).
24. J. Xing *et al.*, *Proc. Natl. Acad. Sci. U.S.A.* **119**, e2114432119 (2022).
25. H. Isobe *et al.*, *Angew. Chem. Int. Ed.* **45**, 6676–6680 (2006).
26. T. Kogure, *J. Am. Ceram. Soc.* **82**, 716–720 (1999).
27. A. P. Amrute, Z. Łodziana, H. Schreyer, C. Weidenthaler, F. Schüth, *Science* **366**, 485–489 (2019).
28. Y. Jiang *et al.*, *Nat. Commun.* **14**, 104 (2023).
29. X. Peng *et al.*, *Nat. Commun.* **13**, 3601 (2022).
30. C. G. Bischak *et al.*, *Matter* **3**, 534–545 (2020).
31. J. Li, Y. Li, Q. Li, Z. Wang, F. L. Deepak, *Nanoscale Horiz.* **4**, 1302–1309 (2019).
32. S. Auer, D. Frenkel, *Nature* **409**, 1020–1023 (2001).
33. Y. Kimura, H. Niinomi, K. Tsukamoto, J. M. García-Ruiz, *J. Am. Chem. Soc.* **136**, 1762–1765 (2014).
34. J. Kotakoski, A. V. Krasheninnikov, U. Kaiser, J. C. Meyer, *Phys. Rev. Lett.* **106**, 105505 (2011).
35. S. Jeon *et al.*, *Science* **371**, 498–503 (2021).
36. M. Sakakibara, T. Nakamuro, E. Nakamura, *ACS Nano* **18**, 22325–22333 (2024).
37. S. S. Zumdahl, S. A. Zumdahl, D. J. DeCoste, *Chemistry* (Houghton Mifflin Harcourt, ed. 11, 2023), pp. 526–577.
38. J. Sun *et al.*, *Nat. Mater.* **13**, 1007–1012 (2014).

ACKNOWLEDGMENTS

We appreciate the thorough feedback provided by R. Clérac, M. Uwaha, D. Liu, and R. F. Egerton. M.S. thanks the Japan Society for the Promotion of Science (JSPS) and Forefront Physics and Mathematics Program to Drive Transformation (FoPM) for the fellowship. **Funding:** This work was supported by the Ministry of Education, Culture, Sports, Science and Technology (MEXT) (KAKENHI grant JP19H05459 to E.N.); JSPS (KAKENHI grants JP24H00447 to E.N. and JP23H04874 to T.N.); the JST PRESTO program (grant JPMJPR23Q6 to T.N.); and the Kazato Research Foundation (T.N.). **Author contributions:** Conceptualization: E.N., T.N.; Data acquisition: M.S.; Data analysis: M.S., T.N.; Funding acquisition: E.N., T.N.; Project administration: E.N., T.N.; Project supervision: E.N.; Writing–original draft: E.N., M.S., T.N.; Writing – review & editing: E.N., T.N., M.S., M.H. **Competing interests:** The authors declare no competing interests. **Data and materials availability:** All data necessary for evaluating the conclusions of this study are included in the main text or the supplementary materials.

SUPPLEMENTARY MATERIALS

science.org/doi/10.1126/science.adr8891
Materials and Methods
Supplementary Text
Figs. S1 to S12
Movies S1 to S3
References (*39*–*48*)

Submitted 24 July 2024; accepted 30 December 2024
10.1126/science.adr8891

MOLECULAR BIOLOGY

Structural basis of H3K36 trimethylation by SETD2 during chromatin transcription

Jonathan W. Markert, Jelly H. Soffers†, Lucas Farnung*

During transcription, RNA polymerase II traverses through chromatin, and posttranslational modifications including histone methylations mark regions of active transcription. Histone protein H3 lysine 36 trimethylation (H3K36me3), which is established by the histone methyltransferase SET domain containing 2 (SETD2), suppresses cryptic transcription, regulates splicing, and serves as a binding site for transcription elongation factors. The mechanism by which the transcription machinery coordinates the deposition of H3K36me3 is not well understood. Here we provide cryo–electron microscopy structures of mammalian RNA polymerase II–DSIF-SPT6-PAF1c-TFIIS-IWS1-SETD2-nucleosome elongation complexes, revealing that the transcription machinery regulates H3K36me3 deposition by SETD2 on downstream and upstream nucleosomes. SPT6 binds the exposed H2A-H2B dimer during transcription, and the SPT6 death-like domain mediates an interaction with SETD2 bound to a nucleosome upstream of RNA polymerase II.

The regulation of transcription in eukaryotes occurs in the context of chromatin, and the organization of chromatin plays a critical role in determining genome accessibility to the transcription machinery. A key mechanism of transcriptional regulation is achieved through histone modifications (*1*, *2*). For example, trimethylation of histone H3 lysine 36 (H3K36me3) is an essential histone mark associated with actively transcribed genes (*3*–*6*). It suppresses aberrant transcription initiation within gene bodies (*7*–*9*) and provides a recruitment platform for factors involved in chromatin maintenance, splicing, pre-mRNA processing, and DNA repair (*10*–*12*). Mutations of H3K36 have been linked to various cancers, including chondroblastomas, colorectal cancers, and head and neck squamous carcinomas (*13*).

H3K36me3 is primarily established by the histone methyltransferase SET [Su(var)3-9, Enhancer-of-zeste, and Trithorax] domain containing 2 (SETD2) in humans (*14*). SETD2 contains a catalytic SET domain that catalyzes the methylation of lysine residues using *S*-adenosyl methionine (SAM). Together with the SET domain, the N-terminally flanking associated-with-SET (AWS) and C-terminal post-SET domains are required for the catalytic activity and engage with the nucleosomal substrate to deposit H3K36me3 (*15*, *16*). SETD2 also contains an autoinhibitory domain (AID) (*17*) and a WW domain. During transcription elongation, SETD2 is recruited to the transcription machinery through an interaction of the SETD2 SRI (Set2 Rpb1 interaction) domain with the phosphorylated C-terminal domain (CTD) of the largest RNA polymerase II subunit, RPB1 (*18*–*21*). Additionally, SETD2 can interact with transcription elongation factors SPT6 and IWS1 (*22*).

Department of Cell Biology, Blavatnik Institute, Harvard Medical School, Boston, MA, USA.
*Corresponding author. Email: lucas_farnung@hms.harvard.edu
†Present address: Division of Biological and Biomedical Systems, School of Science and Engineering, University of Missouri, Kansas City, MO, USA.

How transcription and the deposition of H3K36me3 are coupled and how transcription elongation factors regulate this process remain unclear. To address this gap in knowledge, we investigated the relationship between transcription and SETD2 methyltransferase activity in a fully reconstituted system. Using a combination of biochemical and structural approaches, we provide a mechanistic basis for understanding how transcription and transcription elongation factors facilitate deposition of H3K36me3 and how this modification is restricted to actively transcribed regions. Our study visualizes transcription through chromatin and deposition of H3K36me3 on downstream and upstream nucleosome substrates, providing a basis for understanding the interplay between transcription and histone modifications.

Transcription stimulates H3K36me3 deposition by SETD2

To better understand the cotranscriptional basis of H3K36me3 deposition by SETD2, we established a biochemical assay that concurrently measures both RNA polymerase II elongation and H3K36me3 deposition (Fig. 1A and fig. S1). The RNA polymerase II–DSIF-SPT6-PAF1c-IWS1-SETD2 complex (DSIF, DRB sensitivity inducing factor; PAF1c, RNA polymerase II–associated factor 1 complex) was positioned on a nucleosomal substrate in the presence of adenosine triphosphate (ATP) (*23*) (see methods in the supplementary materials). Upon addition of SAM, TFIIS (transcription elongation factor II S), and the nucleoside triphosphates CTP, GTP, and UTP, RNA polymerase II extended the RNA primer into the nucleosomal substrate, and SAM allowed for the trimethylation of H3K36 by SETD2 (Fig. 1B). Reactions lacking nucleotide triphosphates (NTPs) did not extend the RNA (Fig. 1B). Reactions were stopped at different time points, and H3K36me3 was detected by Western blot analysis (Fig. 1B). When the transcription machinery did not extend into the nucleosome, limited amounts of H3K36me3 were detected. Similarly, no methylation was observed on a nucleosomal substrate in the absence of the transcription elongation complex (fig. S1C). In contrast, increased H3K36me3 amounts were present in the samples in which RNA polymerase II transcribed its substrate, demonstrating that transcription into the nucleosome facilitates H3K36me3 deposition (Fig. 1B). Our results suggest that transcriptional activity stimulates SETD2, whereas SETD2 does not appear to facilitate RNA polymerase II's traversal of nucleosomes (fig. S1, E to G, and data S1 and S2).

To clarify how SETD2 activity is stimulated and whether downstream-positioned or upstream-transferred nucleosomes can be methylated, we used multiple nucleosomal DNA constructs with stall sites 15 base pairs (bp −15) in front of the nucleosome and 27 bp (bp +27) or 115 bp (bp +115) within the nucleosome (methods; Fig. 1, C to E). The bp −15 and bp +27 constructs represent downstream nucleosomes. The bp +115 construct interrogates methylation of an upstream nucleosome (*24*). The transcription elongation complexes were positioned in front of the nucleosome (*25*) (Fig. 1C). Upon addition of TFIIS and CTP, GTP, and UTP, RNA polymerase II extended the RNA primer to the stall sites (bp −15, bp +27, or bp +115) (Fig. 1, D and E). As before, reactions lacking NTPs did not extend the RNA (Fig. 1D). Thirty minutes after transcription, SAM was added to the reactions to allow for H3K36me3 deposition by SETD2. Limited amounts of H3K36me3 were detected when the transcription machinery was positioned at bp −31 (no NTPs) or bp −15 (Fig. 1D), whereas increased H3K36me3 amounts were observed in the preparation in which RNA polymerase II had transcribed within a downstream nucleosome (bp +27) or a transferred upstream nucleosome (bp +115, most signal observed) (Fig. 1, D and E). Our results show that transcription into a nucleosomal substrate stimulates SETD2 activity and that SETD2 activity depends on unwrapped DNA from the histone octamer both on downstream and upstream nucleosomes. Our biochemical data indicate that the upstream nucleosome is the preferred target of SETD2 methyltransferase activity. Next, we used single-particle cryo–electron microscopy (cryo-EM) to elucidate the structures of SETD2 bound to downstream and upstream nucleosomal substrates.

Structure of the RNA polymerase II–DSIF-SPT6-PAF1c-TFIIS-IWS1-SETD2–downstream nucleosome transcription elongation complex

First, we prepared a chromatin transcription elongation complex with SETD2 on a downstream nucleosome for cryo-EM (Fig. 2 and figs. S1 and S2). We used the modified Widom 601 nucleosome substrate that permits transcription

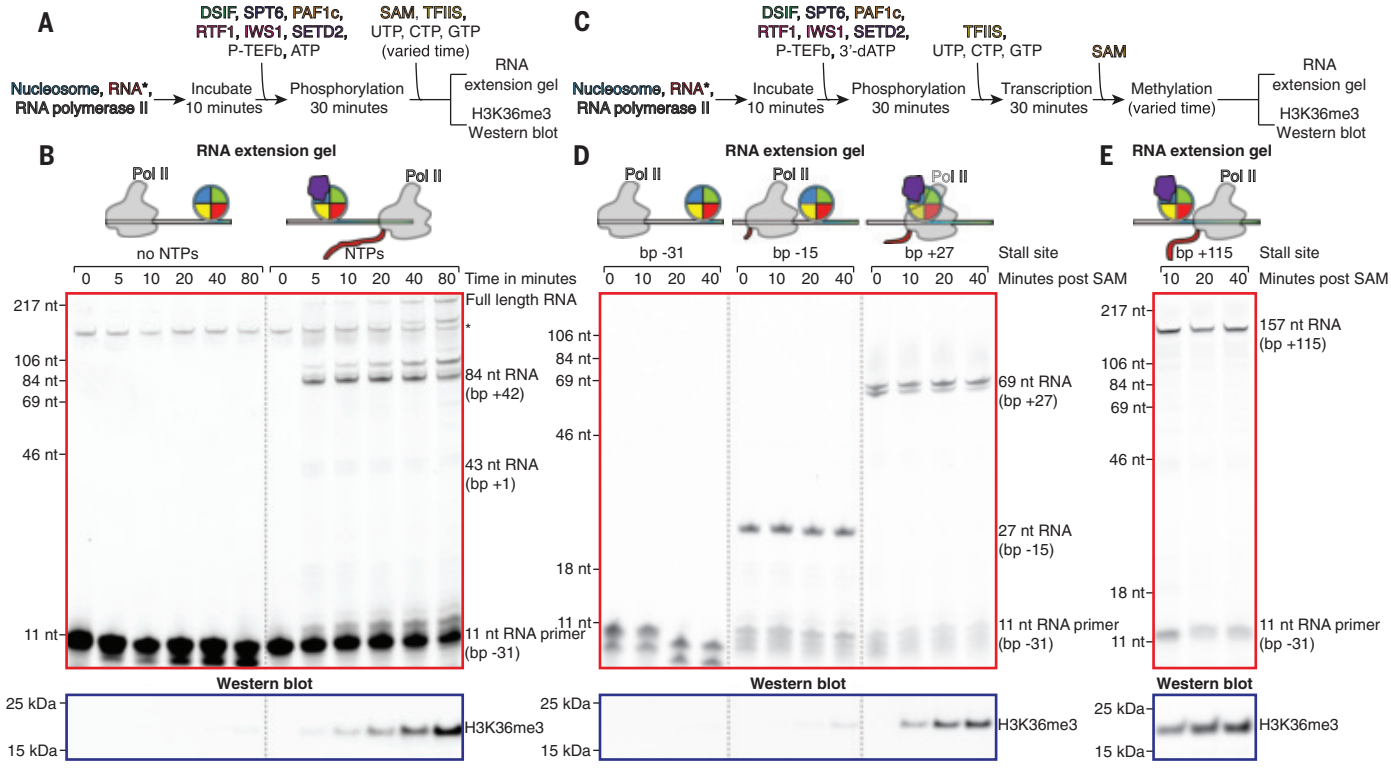

Fig. 1. Biochemical reconstitution of H3K36me3 deposition by SETD2 during transcription. (**A**) Schematic of RNA extension–coupled histone mark deposition assay in the presence of all NTPs. (**B**) Denaturing gel of RNA products and Western blot analysis reveal that transcription stimulates H3K36me3 deposition by SETD2. SETD2 concentration is 3.5 μM. nt, nucleotide. (**C**) Schematic of RNA extension–coupled histone mark deposition assay with pause sites (bp −31, bp −15, and bp +27). (**D**) Denaturing gel of RNA products and Western blot analysis reveal that transcription stimulates H3K36me3 deposition by SETD2 on a partially transcribed downstream nucleosome. SETD2 concentration is 3.5 μM. (**E**) Denaturing gel of RNA products and Western blot analysis reveal that transcription stimulates H3K36me3 deposition by SETD2 on upstream-transferred nucleosome (bp +115). SETD2 concentration is 700 nM. RNA extension gel and Western blot from (E) are the same as in fig. S13F.

elongation up to position bp +27 (figs. S1 and S2; methods) (*25*, *26*). To stabilize binding of SETD2, we incorporated the oncogenic H3K36M variant into the nucleosomal substrate (*15*, *16*). We collected two datasets, encompassing a total of 2,579,512 particles (fig. S3). Classification of the acquired cryo-EM data resulted in the structure of the RNA polymerase II–DSIF-SPT6-PAF1c-TFIIS-IWS1-SETD2 complex bound to a downstream nucleosome at an overall resolution of 2.9 Å (Fig. 2, figs. S3 to S7, tables S1 to S3, and movie S1). A composite map was assembled from masked refinements of RNA polymerase II, DSIF-SPT6-IWS1, PAF1c, TFIIS, and the nucleosome with local resolutions ranging from 2.9 to 12 Å (figs. S3 to S6). Known structures of the mammalian activated elongation complex including RNA polymerase II, DSIF, SPT6, and PAF1c, together with TFIIS, IWS1, and the nucleosome with bound SETD2, were placed into the cryo-EM reconstruction (*23*, *25*, *27*, *28*) and adjusted locally (methods; Fig. 2, A and B, and fig. S7).

In our structure, RNA polymerase II unwrapped ~55 bp of nucleosomal DNA from the histone octamer (Fig. 2C), and the RNA polymerase II active site is in a posttranslocated state at nucleosomal position bp +27 (fig. S7L). The DNA unwrapping facilitated SETD2 binding (*15*, *16*). SETD2 bound the transcribed nucleosome at superhelical location (SHL) +1 (see supplementary text in the supplementary materials). Additional density corresponding to IWS1 was located between SPT4, SPT5, and RPB1 (Fig. 2A) as in yeast Spn1 (*24*), and IWS1 appeared to influence unwrapping of nucleosomal DNA (supplementary text; fig. S8).

During cryo-EM data analysis, we observed a density next to SPT6. By using signal subtraction and extensive classifications, we identified a secondary nucleosome bound by a second SETD2 (methods; Fig. 2 and fig. S3). This secondary nucleosome was anchored to the transcription machinery by the second copy of SETD2 and SPT6 (Fig. 2). Modeling of B-DNA extending from the upstream DNA toward the secondary nucleosome suggests that this nucleosome could occupy the space of an upstream nucleosome (fig. S1B) (*24*).

Interaction of SETD2 with the downstream nucleosome

In our structure, SETD2 engaged the unwrapped downstream nucleosome (Fig. 2C). The AWS domain of SETD2 interacted with the H2A C-terminal tail and contacted the αN helix of histone H3 (fig. S9). The N-terminal tail of H3 projected into the SET domain to position H3K36M in the SETD2 active site (Fig. 2C and fig. S9) (*15*, *16*). Comparison of the transcribed nucleosome with a canonical nucleosome revealed that SETD2 binding is only permissible when DNA is unwrapped from the histone core (fig. S9). Nucleosome unwrapping alone did not enable SETD2 binding. A stalled transcription elongation complex at ~bp −5 showed unwrapped DNA but prevented SETD2-nucleosome association owing to a steric clash with RNA polymerase II (fig. S10). Thus, SETD2 binding on downstream nucleosomes occurred only when the elongation complex had moved past the nucleosomal entry site, consistent with our biochemical data.

Structure of the RNA polymerase II–DSIF-SPT6-PAF1c-TFIIS-IWS1-SETD2–upstream nucleosome transcription elongation complex

To determine SETD2 association with an upstream-positioned nucleosome, we generated substrates that positioned the elongation complex upstream of a nucleosome either by

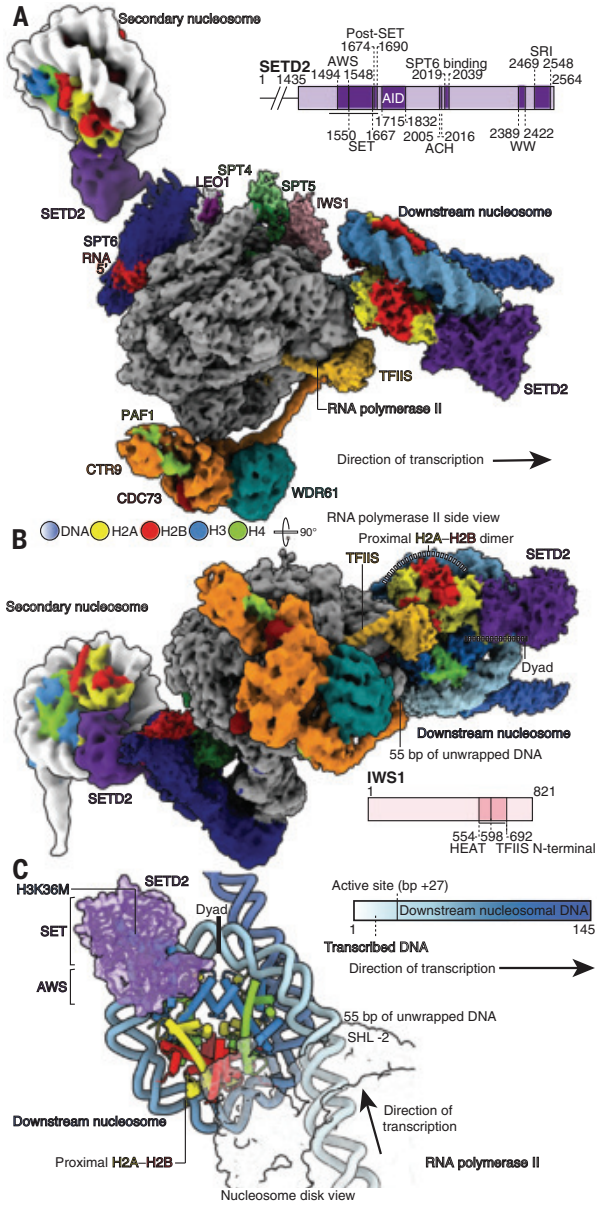

Fig. 2. Structure of RNA polymerase II–DSIF-SPT6-PAF1c-TFIIS-IWS1-SETD2–downstream nucleosome transcription elongation complex. (**A** and **B**) Two views of the SETD2-containing downstream nucleosome transcription elongation complex with a secondary nucleosome. Coulomb potential map is shown for map T. Secondary nucleosome is superposed on the basis of map N. Same color code is used throughout the figure. RTF1 and additional cryo-EM density binding the exposed H2A-H2B dimer are only visible at higher contour levels and are not shown. Domain architecture of SETD2 and IWS1. Modeled regions are indicated as solid black lines. (**C**) Interaction of SETD2 with the partially unwrapped downstream nucleosome.

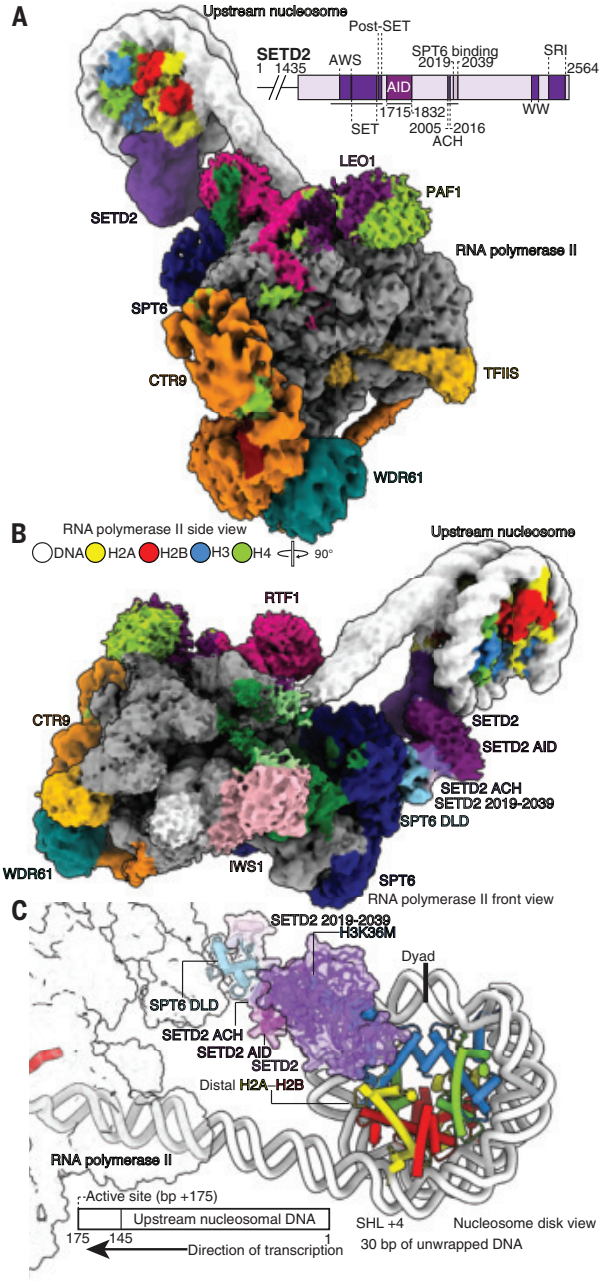

Fig. 3. Structure of RNA polymerase II–DSIF-SPT6-PAF1c-TFIIS-IWS1-SETD2–upstream nucleosome transcription elongation complex. (**A** and **B**) Two views of the SETD2-containing upstream nucleosome transcription elongation complex. Coulomb potential map is shown for map 9. (**C**) Interaction of SETD2 with the partially unwrapped upstream nucleosome.

transcription to nucleosomal bp +115 (*24*) or by a transcription bubble placed 20 or 30 bp from the upstream nucleosome. We assembled the complexes, cross-linked the samples, and subjected them to single-particle cryo-EM (fig. S2). We analyzed all data, and we obtained highly similar structures. We obtained the highest resolution reconstruction for the transcription elongation complex with a 30 bp upstream–positioned nucleosome and will discuss this structure in detail (fig. S11). We note that all upstream structures share these features, and we observed density for all transcription elongation factors (Fig. 3; figs. S7, S11, and S12; tables S4 to S6; and movie S2). For the 30 bp–upstream structure, 30 bp of DNA emerged from the upstream side of the RNA polymerase II cleft and connected to the nucleosome (Fig. 3, A and B). The nucleosome showed partial unwrapping of DNA, with SHL +4 to SHL +7 detached (Fig. 3C). SETD2 bound the partially unwrapped nucleosome, and SETD2 bound SPT6 by inserting a short conserved peptide motif (SETD2 residues 2019 to 2039)

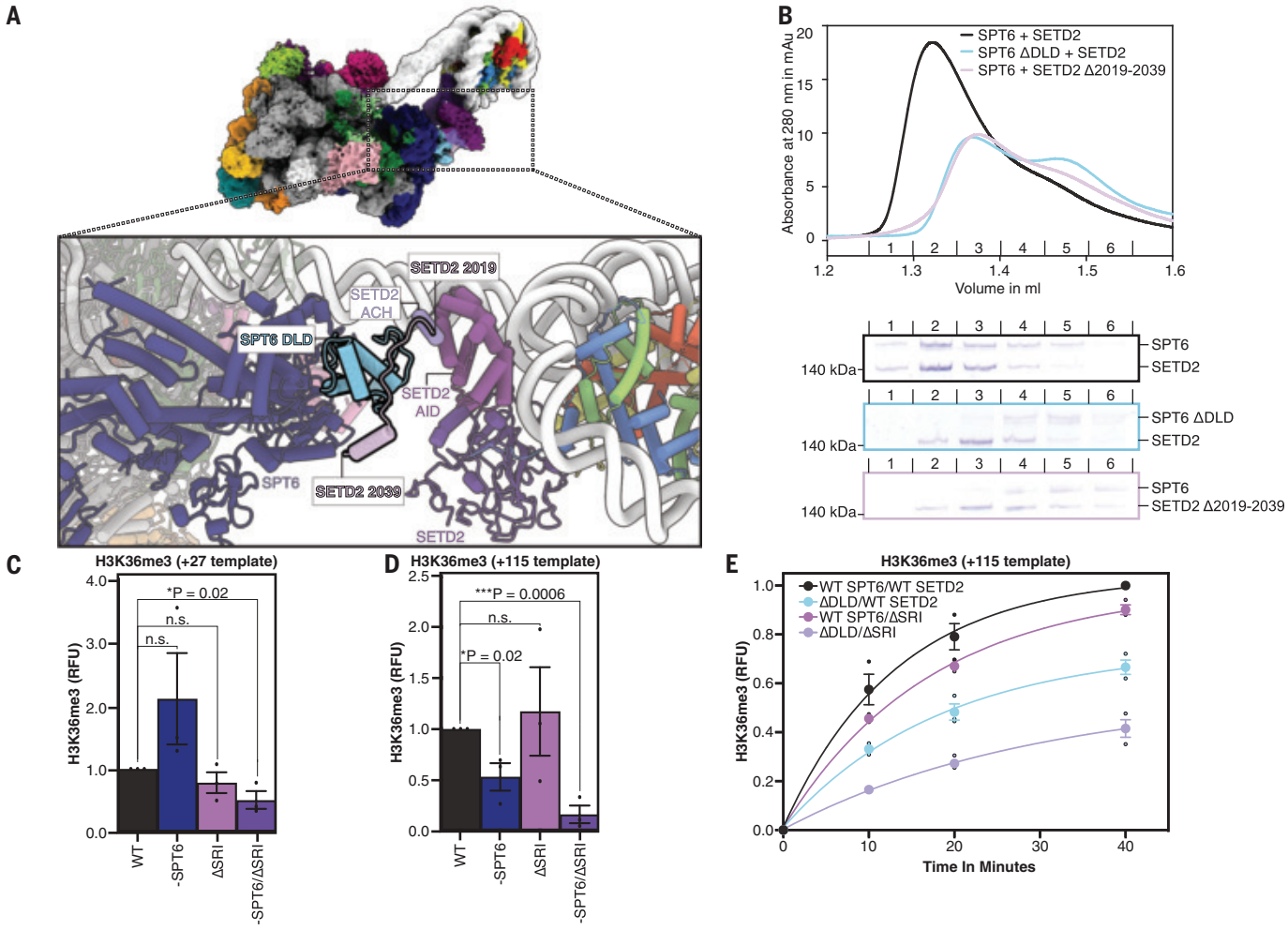

Fig. 4. Interactions of SETD2 with the upstream nucleosome and SPT6. (**A**) Interaction interface between the SPT6 DLD (light blue), the SETD2 SPT6 interacting region (pink), the SETD2 ACH (lilac), the SETD2 AID (purple), and the SETD2 SET and AWS domains (rebecca purple). (**B**) Size exclusion chromatography and SDS–polyacrylamide gel electrophoresis (SDS-PAGE) analysis confirms that the SPT6 DLD forms an interaction interface with SETD2. SETD2 residues 2019 to 2039 interact with SPT6. Gels and chromatogram are the same as from fig. S13C. (**C** and **D**) Quantification of RNA extension–coupled histone mark deposition assay shows that SPT6 and the SETD2 SRI domains play important roles for SETD2 activity on upstream nucleosomes. SETD2 concentration is 3.5 μM. Urea gel and Western blot are shown in fig. S20A (C). Quantification of wild-type (with SPT6 and with SETD2 SRI) is the same as in figs. S8E and S20F (C). Urea gel and Western blot are shown in fig. S20B (D). Quantification of wild type (with SPT6 and with SETD2 SRI) is the same as in figs. S8F and S20G (D). RFU, relative fluorescence units; n.s., not significant. (**E**) Time course of RNA extension–coupled histone mark deposition assay on the bp +115 upstream nucleosome construct with SPT6 ΔDLD and SETD2 ΔSRI establishes the importance of SPT6 and the SETD2 SRI domain for H3K36me3 deposition. Urea gel and Western blot are shown in fig. S20C (E). SETD2 concentration is 1.4 μM. Error bars represent standard error.

into a crevice formed by the SPT6 death-like domain (DLD; SPT6 residues 1056 to 1133) (fig. S7O), clarifying the genetic association of SETD2 with SPT6 (*29*, *30*). Directly preceding this peptide motif in SETD2 is a helix, which we call the AID complementary helix (ACH). The ACH bound the SETD2 AID (Fig. 3C). Tethered by the ACH, the AID itself was sandwiched between the nucleosome-bound SET domain and SPT6, allowing for engagement of the AWS and SET domains with the nucleosomal substrate (Fig. 3 and fig. S13). Notably, the AID was positioned differently in AlphaFold predictions of SETD2 alone, where it likely blocked nucleosomal binding (fig. S13, G to J). This suggests that the AID underwent a conformational switch upon binding to the nucleosome and SPT6, allowing the SET domain to engage with nucleosomal features such as the H2A binding surface.

The observed SETD2 configuration, including the SETD2-SPT6 and ACH-AID interactions, was robust across the different upstream nucleosome distances. The substrate with a nucleosome located 20 bp upstream from the active site showed similar densities to the 30-bp construct (figs. S2, S7, S14, and S15 and tables S7 to S9). Similar densities were also observed for the actively transcribed +115 substrate (fig. S9), although at lower resolution. Like the 20 and 30 bp upstream–positioned constructs, the bp +115 substrate showed densities for SETD2 on the transferred and partially unwrapped nucleosome (figs. S16 to S19).

From the actively transcribed bp +115 substrate, we obtained an additional structure. This structure represents a nucleosome reassembly intermediate, where the heterodimeric protein complex FACT binds a partially reassembled hexasomal intermediate on the upstream side. FACT stabilized the hexasomal intermediate and was additionally tethered to the elongation complex by an interaction with RTF1 (residues 267 to 302, interaction with SPT16 middle domain). SETD2 was only engaged to

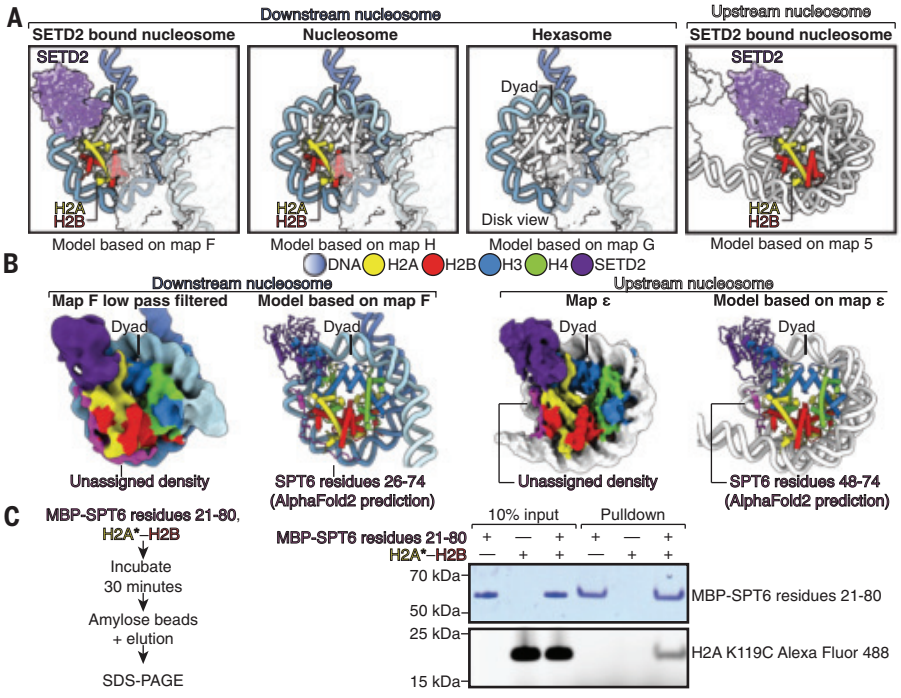

Fig. 5. Different nucleosome compositions and SPT6 N-terminal interaction with exposed H2A-H2B dimer. (**A**) Three different downstream nucleosomal populations were observed in the cryo-EM data with an intact histone octamer (SETD2 bound), an intact histone octamer (no SETD2 bound), and a hexasome (no SETD2 bound). For the upstream nucleosome, SETD2 binds the partially rewrapped histone octamer. (**B**) Unassigned density (magenta) is observed flanking the exposed H2A-H2B dimer on both partially unwrapped or partially rewrapped downstream and upstream nucleosomes, respectively. AlphaFold-Multimer predictions suggest binding of the SPT6 N terminus. (**C**) MBP-SPT6 residues 21–80 amylose bead pull-down assay shows binding to Alexa Fluor 488 fluorescently labeled H2A-H2B dimer. MBP-SPT6 residues 21–80 imaged using One-Step Blue (Coomassie stain) and H2A-H2B using the Alexa Fluor 488 fluorescent label, respectively.

the SPT6 DLD and not to the partially assembled upstream-transferred hexasome (supplementary text; figs. S16 to S19 and tables S10 to S12). Together, our structural data indicated that SETD2 can engage unwrapped downstream and upstream nucleosomes. During the transfer process, there appears to be a period when SETD2 was excluded from engaging the nucleosome by FACT but remained associated with the elongation complex through the SPT6 DLD. Upon further transcription and progression of nucleosome transfer, SETD2 could engage with the upstream nucleosome.

The SETD2 SRI domain and SPT6 DLD are important for H3K36me3 deposition

To further validate whether the SPT6 DLD is required for the binding of SETD2 (Fig. 4A), we purified an SPT6 mutant lacking the DLD (SPT6 ΔDLD; methods; fig. S1). We then performed size exclusion chromatography experiments with SPT6, SPT6 ΔDLD, SETD2, and SETD2 lacking the DLD-interacting region (SETD2 Δ2019–2039) to monitor SETD2 binding to SPT6. As expected, wild-type SPT6 and SETD2 bind each other, whereas SPT6 ΔDLD or SETD2 Δ2019–2039 prevent binding of SETD2 to SPT6 (Fig. 4B and fig. S13).

SETD2 is also recruited to actively transcribing RNA polymerase II through an interaction between its SRI domain and the RPB1 CTD (*18*–*21*). We therefore sought to verify the significance of the SRI domain and SPT6 in H3K36me3 deposition on downstream and upstream nucleosomes using our coupled transcription-histone mark deposition assay (Fig. 4, C and D). Compared with wild-type H3K36me3 deposition, the absence of either SPT6 or deletion of the SRI domain did not affect trimethylation of downstream nucleosomes. However, the combination of the absence of SPT6 and the ΔSRI mutant resulted in a slight reduction in trimethylation on the downstream nucleosome (Fig. 4C). For upstream nucleosomal substrates, the absence of SPT6 reduced H3K36me3 levels by half, whereas removal of the SRI domain alone did not affect H3K36me3 levels (Fig. 4D). The simultaneous removal of SPT6 and the SRI domain, however, led to a further reduction in H3K36me3 on the upstream substrate (Fig. 4D). To confirm that SPT6 influences upstream activity through its DLD interaction with SETD2, we monitored H3K36me3 deposition after removing the SPT6 DLD (Fig. 4E). This removal resulted in a loss of H3K36me3, with the greatest reduction observed when both the SPT6 DLD and the SETD2 SRI domain were removed (Fig. 4E). None of these mutations affected transcription by RNA polymerase II (fig. S20).

Because the SPT6 DLD domain bound SETD2 in a region that was directly adjacent to the SETD2 ACH, we decided to test whether the ACH was required for SETD2-dependent methylation. Indeed, deletion of the ACH led to a reduction in H3K36me3 deposition, with an additional removal of the SPT6 DLD domain resulting in only a slight additional decrease (fig. S13). Hence, SPT6 binding allowed the ACH to position SETD2 for H3K36me3 deposition on the upstream nucleosome (fig. S13, D, E, and G to J).

SPT6 stabilizes the exposed H2A-H2B dimer

Further classification of our downstream nucleosome cryo-EM data revealed two additional nucleosomal populations (Fig. 5A and fig. S4). The first population showed an intact histone octamer core that was not bound by SETD2, whereas the second additional population was identified as a hexasome missing the proximal H2A-H2B dimer and was also not associated with SETD2 (Fig. 5A and fig. S7, P to R). These observations suggest a dependence of SETD2 binding and H3K36me3 deposition on an intact H2A-H2B dimer on the SETD2-facing nucleosomal side (*15*, *31*, *32*).

Unwrapping of DNA during transcription or incomplete rewrapping during nucleosome transfer exposes the proximal or distal H2A-H2B dimers, respectively, and can lead to their loss (*28*). We observed additional cryo-EM density next to the exposed H2A-H2B dimer in the downstream- and upstream-positioned nucleosomes. The additional density covered the H2A-H2B DNA interaction surface and extended toward SETD2 (Fig. 5B and movie S3). The density was similar to that seen in FACT-nucleosome structures (*33*) (fig. S20, D and E). FACT, however, was not present in these particular reconstitutions. We used AlphaFold2 (*34*) to screen for binding partners of the H2A-H2B dimer. We found that the SPT6 N terminus (residues 21 to 80) is predicted to bind to the H2A-H2B dimer. The identified SPT6 N terminus accommodated the observed density in our reconstructions (Fig. 5B), consistent with observations that SPT6 is a histone chaperone (*35*, *36*). Accordingly, we did not observe any density for the SPT6 N terminus in our hexasome reconstruction. To validate binding of the SPT6 N terminus to the exposed dimer, we purified a maltose-binding protein (MBP)–tagged SPT6 construct containing SPT6 residues 21 to 80. We then performed

an amylose bead pulldown with the SPT6 construct and Alexa Fluor 488 fluorescently labeled H2A-H2B dimer (Fig. 5C). Indeed, the SPT6 construct interacted with the H2A-H2B dimer (Fig. 5C). Deletion of the identified SPT6 H2A-H2B interacting region did not have any effect on cotranscriptional H3K36me3 deposition (fig. S20, F and G).

Discussion

Here, we reveal that deposition of H3K36me3 is facilitated by transcriptional regulation of SETD2 binding to its nucleosomal substrate (fig. S21). Initially, SETD2 copies are recruited to the transcription machinery by the RPB1 CTD (*18*–*21*). Transcription into the nucleosomal substrate leads to DNA unwrapping and generates a nucleosomal substrate that is amenable to SETD2 binding in a window of ~50 bp. Transfer of the nucleosome to an upstream position then again generates a substrate amenable for SETD2 binding. SETD2 binding of the upstream nucleosome is directed by an interaction between the SPT6 DLD and SETD2 that is important for relief of SETD2 autoinhibition and H3K36me3 deposition, suggesting that the upstream nucleosome is the preferred target for H3K36me3 deposition. It remains possible that SETD2 could symmetrically modify both H3 tails on the upstream nucleosome.

Our structures showed that SETD2 only interacts with downstream nucleosomes that have a complete histone octamer (Fig. 5A). In contrast, we did not observe SETD2 binding to transcriptionally generated hexasomes or FACT-bound nucleosome transfer intermediates. This finding suggests that H3K36me3 may encode information regarding the histone content of transcribed nucleosomes at the time of methylation (*15*, *31*, *32*). Nucleosomes with a complete histone octamer undergo H3K36 trimethylation by SETD2, thereby facilitating the recruitment of various transcription elongation factors (*37*), chromatin remodelers (*38*), and other transcriptional regulators (*39*). When RNA polymerase II cotranscriptionally disrupts the nucleosomal structure during nucleosome transfer, and SETD2 is only associated with the transcription machinery through SPT6, H3K36me3 is only deposited after FACT dissociation on the upstream side.

Transcription through nucleosomes creates distinctive noncanonical nucleosomal configurations that are specifically recognized by various factors. Examples include the binding of factors such as the histone chaperone FACT (*24*, *33*, *40*) and Spt5 (*40*) or the activation of chromatin remodelers such as Chd1 (*40*) to facilitate transcription through chromatin. Our results show that this mechanism extends to histone-modifying enzymes such as SETD2. We additionally provide evidence that SPT6 binds nucleosomes (*41*) and may act as a H2A-H2B histone chaperone (*35*, *36*). We also resolve a nucleosome transfer intermediate where FACT and RTF1 cooperatively stabilize an upstream-positioned hexasomal structure. Together, RNA polymerase II transcription generates nucleosomal environments that tightly regulate and coordinate the activity of associated factors. Our work provides a framework to understand the action of histone-modifying enzymes during transcription.

REFERENCES AND NOTES

1. M. Smolle, J. L. Workman, *Biochim. Biophys. Acta* **1829**, 84–97 (2013).
2. B. Li, M. Carey, J. L. Workman, *Cell* **128**, 707–719 (2007).
3. D. Schaft *et al*., *Nucleic Acids Res.* **31**, 2475–2482 (2003).
4. T. Xiao *et al*., *Genes Dev.* **17**, 654–663 (2003).
5. A. Shilatifard, *Annu. Rev. Biochem.* **75**, 243–269 (2006).
6. N. J. Krogan *et al*., *Mol. Cell. Biol.* **23**, 4207–4218 (2003).
7. B. D. Strahl *et al*., *Mol. Cell. Biol.* **22**, 1298–1306 (2002).
8. M. J. Carrozza *et al*., *Cell* **123**, 581–592 (2005).
9. A. A. Joshi, K. Struhl, *Mol. Cell* **20**, 971–978 (2005).
10. E. J. Wagner, P. B. Carpenter, *Nat. Rev. Mol. Cell Biol.* **13**, 115–126 (2012).
11. S. X. Pfister *et al*., *Cell Rep.* **7**, 2006–2018 (2014).
12. M.-C. Keogh *et al*., *Cell* **123**, 593–605 (2005).
13. C. Lu *et al*., *Science* **352**, 844–849 (2016).
14. X.-J. Sun *et al*., *J. Biol. Chem.* **280**, 35261–35271 (2005).
15. S. Bilokapic, M. Halic, *Nat. Commun.* **10**, 3795 (2019).
16. Y. Liu *et al*., *Cell Discov.* **7**, 32 (2021).
17. Y. Wang, Y. Niu, B. Li, *Nucleic Acids Res.* **43**, 4881–4892 (2015).
18. K. O. Kizer *et al*., *Mol. Cell. Biol.* **25**, 3305–3316 (2005).
19. S. M. Fuchs, K. O. Kizer, H. Braberg, N. J. Krogan, B. D. Strahl, *J. Biol. Chem.* **287**, 3249–3256 (2012).
20. B. Li, L. Howe, S. Anderson, J. R. Yates 3rd, J. L. Workman, *J. Biol. Chem.* **278**, 8897–8903 (2003).
21. J. Li, D. Moazed, S. P. Gygi, *J. Biol. Chem.* **277**, 49383–49388 (2002).
22. S. M. Yoh, J. S. Lucas, K. A. Jones, *Genes Dev.* **22**, 3422–3434 (2008).
23. S. M. Vos *et al*., *Nature* **560**, 607–612 (2018).
24. H. Ehara, T. Kujirai, M. Shirouzu, H. Kurumizaka, S. I. Sekine, *Science* **377**, eabp9466 (2022).
25. M. Filipovski, J. H. M. Soffers, S. M. Vos, L. Farnung, *Science* **376**, 1313–1316 (2022).
26. P. T. Lowary, J. Widom, *J. Mol. Biol.* **276**, 19–42 (1998).
27. S. M. Vos, L. Farnung, A. Linden, H. Urlaub, P. Cramer, *Nat. Struct. Mol. Biol.* **27**, 668–677 (2020).
28. L. Farnung, M. Ochmann, G. Garg, S. M. Vos, P. Cramer, *Mol. Cell* **82**, 3126–3134.e7 (2022).
29. R. Gopalakrishnan, S. K. Marr, R. E. Kingston, F. Winston, *Nucleic Acids Res.* **47**, 3888–3903 (2019).
30. K. Cermakova, E. A. Smith, V. Veverka, H. C. Hodges, Biorxiv, 636084 (2019).
31. H.-N. Du, S. D. Briggs, *J. Biol. Chem.* **285**, 11704–11713 (2010).
32. H. Endo *et al*., *Genes Cells* **17**, 65–81 (2012).
33. Y. Liu *et al*., *Nature* **577**, 426–431 (2020).
34. J. Jumper *et al*., *Nature* **596**, 583–589 (2021).
35. L. McCullough, Z. Connell, C. Petersen, T. Formosa, *Genetics* **201**, 1031–1045 (2015).
36. A. Bortvin, F. Winston, *Science* **272**, 1473–1476 (1996).
37. M. M. Pradeepa, H. G. Sutherland, J. Ule, G. R. Grimes, W. A. Bickmore, *PLOS Genet.* **8**, e1002717 (2012).
38. J. C. VaryJr *et al*., *Mol. Cell. Biol.* **23**, 80–91 (2003).
39. A. Dhayalan *et al*., *J. Biol. Chem.* **285**, 26114–26120 (2010).
40. L. Farnung, M. Ochmann, M. Engeholm, P. Cramer, *Nat. Struct. Mol. Biol.* **28**, 382–387 (2021).
41. S. M. McDonald, D. Close, H. Xin, T. Formosa, C. P. Hill, *Mol. Cell* **40**, 725–735 (2010).

ACKNOWLEDGMENTS

We thank all members of the Farnung lab for support. We thank the Harvard Cryo-EM Center for Structural Biology at Harvard Medical School and X. Zhao from the Janelia CryoEM facility staff for support with data collection. We thank S. M. Vos for critical reading, resources, and input. We thank F. Steinruecke, K. Adelman, D. Moazed, S. Buratowski, and F. Winston for discussions. **Funding:** Smith Family Awards Program for Excellence in Biomedical Research (L.F.); Damon Runyon-Rachleff Cancer Innovator (L.F.); Rita Allen Foundation (L.F.); NIH New Innovator Award DP2-ES036404 (L.F.); DF/HCC SPORE DRP P50 CA101942 (L.F.); Cell Biology Education and Fellowship Fund, Harvard Medical School (J.W.M.). **Author contributions:** Conceptualization: J.W.M. and L.F. Methodology: J.W.M. and L.F. Investigation: J.W.M., J.H.S., and L.F. Visualization: J.W.M. and L.F. Funding acquisition: L.F. Project administration: L.F. Supervision: L.F. Writing – original draft: J.W.M. and L.F. Writing – review & editing: J.W.M. and L.F. **Competing interests:** The authors declare that they have no competing interests. **Data and materials availability:** The cryo-EM reconstructions and final models were deposited in the Electron Microscopy Data Bank (EMDB) and the Protein Data Bank (PDB). Maps, half maps, and masks for maps A, B, C, D, E, F, I, J, and T are deposited under EMD-47999, EMD-48000, EMD-48001, EMD-48002, EMD-48003, EMD-48004, EMD-48007, EMD-48008, and EMD-48041, respectively. Maps, half maps, and masks for maps H and S are deposited under EMD-48006 and EMD-48040, respectively. Maps, half maps, and masks for maps G and R are deposited under EMD-48005 and EMD-48039, respectively. Maps, half maps, and masks for maps N, O, and P are deposited under EMD-48012, EMD-48013, and EMD-48014, respectively. Maps, half maps, and masks for maps K, L, M, and Q are deposited under EMD-48009, EMD-48010, EMD-48011, and EMD-48038, respectively. Maps, half maps, and masks for maps 1, 2, 3, 4, 5, 6, 7, 8, and 9 are deposited under EMD-48015, EMD-48016, EMD-48017, EMD-48018, EMD-48019, EMD-48020, EMD-48021, EMD-48022, and EMD-48042, respectively. Maps, half maps, and masks for maps α, β, γ, δ, ε, ζ, η, and θ are deposited under EMD-48023, EMD-48024, EMD-48025, EMD-48026, EMD-48027, EMD-48028, EMD-48029, and EMD-48043, respectively. Maps, half maps, and masks for maps I, II, III, IV, and IX are deposited under EMD-48030, EMD-48031, EMD-48032, EMD-48033, and EMD-48044, respectively. Maps, half maps, and masks for maps V, VI, VII, VIII, and X are deposited under EMD-48034, EMD-48035, EMD-48036, EMD-48037, and EMD-48045, respectively. The RNA polymerase II–DSIF-SPT6-PAF1c-TFIIS-IWS1-SETD2-nucleosome, bp +27 model is deposited under PDB ID 9EGZ. The RNA polymerase II–DSIF-SPT6-PAF1c-TFIIS-IWS1-nucleosome, bp +27 model is deposited under PDB ID 9EGY. The RNA polymerase II–DSIF-SPT6-PAF1c-TFIIS-IWS1-hexasome, bp +27 is deposited under PDB ID 9EGX. The RNA polymerase II–DSIF-SPT6-PAF1c-TFIIS-IWS1-S1ETD2–30 bp upstream nucleosome model is deposited under PDB ID 9EH0. The RNA polymerase II–DSIF-SPT6-PAF1c-TFIIS-IWS1-SETD2–20 bp upstream nucleosome model is deposited under PDB ID 9EH1. The RNA polymerase II–DSIF-SPT6-PAF1c-TFIIS-IWS1-SETD2-FACT nucleosome upstream model is deposited under PDB ID 9EH2. All materials are available upon request and are subject to a material transfer agreement with Harvard University.

SUPPLEMENTARY MATERIALS

science.org/doi/10.1126/science.adn6319
Materials and Methods
Supplementary Text
Figs. S1 to S21
Tables S1 to S12
References (*42*–*56*)
MDAR Reproducibility Checklist
Movies S1 to S4
Data S1 and S2

Submitted 19 December 2023; resubmitted 11 June 2024
Accepted 30 November 2024
Published online 12 December 2024
10.1126/science.adn6319

INFLUENZA

Pre-exposure antibody prophylaxis protects macaques from severe influenza

Masaru Kanekiyo[1]*, Rebecca A. Gillespie[1], Kristine Cooper[2], Vanessa Guerra Canedo[1], Priscila M. S. Castanha[3], Amarendra Pegu[1]‡, Eun Sung Yang[1], Luke Treaster[4], Gabin Yun[4], Megan Wallace[3]§, Gwenddolen Kettenburg[3]¶, Connor Williams[5], Jeneveve Lundy[5], Stacey Barrick[5], Katherine O'Malley[5], Morgan Midgett[5], Michelle M. Marti[3], Hasitha Chavva[3], Jacqueline Corry[3]#, Benjamin R. Treat[3]**, Abby Lipinski[5]††, Lucia Ortiz Batsche[6]‡‡, Adrian Creanga[1], Isabella Ritter[7], Reagan Walker[7], Emily Olsen[3,5]§§, Amanda Laughlin[5]¶¶, Daniel R. Perez[6], John R. Mascola[1]##, Eli A. Boritz[1], Yueh-Ming Loo[8]***, Wade Blair[8]***, Mark Esser[8], Barney S. Graham[1]†††, Douglas S. Reed[5,9]†*, Simon M. Barratt-Boyes[3,9]†*

Influenza virus pandemics and seasonal epidemics have claimed countless lives. Recurrent zoonotic spillovers of influenza viruses with pandemic potential underscore the need for effective countermeasures. In this study, we show that pre-exposure prophylaxis with broadly neutralizing antibody (bnAb) MEDI8852 is highly effective in protecting cynomolgus macaques from severe disease caused by aerosolized highly pathogenic avian influenza H5N1 virus infection. Protection was antibody dose–dependent yet independent of Fc-mediated effector functions at the dose tested. Macaques receiving MEDI8852 at 10 milligrams per kilogram or higher had negligible impairment of respiratory function after infection, whereas control animals were not protected from severe disease and fatality. Given the breadth of MEDI8852 and other bnAbs, we anticipate that protection from unforeseen pandemic influenza A viruses is achievable.

Antibodies are a critical component of protective immunity against infectious diseases and have been utilized as prophylactic and therapeutic countermeasures for more than a century, including against the 1918 influenza pandemic (*1*, *2*). Prophylactic monoclonal antibody (mAb) treatment against respiratory virus infection is effective at preventing lower respiratory disease caused by respiratory syncytial virus (RSV) and has saved countless lives since palivizumab, an anti-RSV mAb, was first approved in 1998 (*3*). The initial success of mAbs in treating COVID-19 patients was undermined by the emergence of virus variants that allowed viral escape (*4*, *5*). This highlights the need for mAbs that target less mutable sites on the virus.

In past decades, the discovery of broadly neutralizing antibodies (bnAbs) against influenza virus has resulted in several promising candidates in human clinical trials for assessing protective efficacy in both prophylactic and therapeutic settings (*6*). Most bnAbs target the conserved supersite on the stem of the viral hemagglutinin (HA), featuring the hydrophobic groove encompassing the tryptophan at position 21 on the HA2 ($Trp21_{HA2}$) (*7*, *8*). Although these bnAbs have shown protective efficacy in preclinical studies and safety and tolerability in humans, efficacy in humans against seasonal influenza appears underwhelming (*9*, *10*) and remains incomplete (*9*, *11*, *12*).

We asked whether pre-exposure prophylaxis by a single infusion of one of the best-in-class bnAbs, MEDI8852 (*13*), would confer protection against severe lower respiratory tract influenza disease caused by a highly pathogenic avian influenza (HPAI) H5N1 virus infection in a cynomolgus macaque model (*14*, *15*). We also conducted a dose de-escalation study to determine the protective threshold for MEDI8852 and investigated whether Fc-mediated functions play a role in protection. Lastly, we performed high-throughput, single-genome sequencing of the virus in bronchoalveolar lavage (BAL) fluid to assess the potential for MEDI8852 to select for escape mutations. Our study lays the groundwork to evaluate promising bnAbs in a model relevant to humans and provides pragmatic insights into the use of MEDI8852 and potentially other bnAbs as a pre-exposure prophylaxis to confer protection from severe disease and death in the event of a zoonotic influenza pandemic.

Pharmacokinetics and protective efficacy of MEDI8852

To establish a pharmacokinetic profile, we administered MEDI8852 [human immunoglobulin G1 (IgG1)] intravenously at a concentration of 30 mg kg^{-1} body weight to three healthy adult cynomolgus macaques. The peak concentration (C_{max}) of MEDI8852 in sera reached 1000 μg ml^{-1} immediately after infusion, dropping to an average of 448 μg ml^{-1} at 3 days post infusion (DPI) with a subsequent slow linear decay, resulting in an estimated serum half-life ($T_{1/2}$) of 18.9 days (Fig. 1A). These values were similar to that of a human phase 1 study (dose range 250 to 3000 mg; C_{max} = 85 to 1110 μg ml^{-1}; and $T_{1/2}$ = 19.4 to 22.6 days) (*16*). Sera from animals receiving MEDI8852 were highly effective at neutralizing A/Vietnam/1203/2004 (H5N1) influenza virus in vitro, with an average 50% inhibitory dilution (ID_{50}) at 3 DPI of ~1:50,000 (Fig. 1A). At 3 DPI, the ratio of MEDI8852 and total macaque IgG in nasal swabs and BAL reached or exceeded that in serum in all animals (Fig. 1B). On the basis of these findings, we treated cynomolgus macaques with MEDI8852 (n = 6) or an irrelevant HIV-1–specific mAb, VRC01 (*17*, *18*) (n = 6), at 30 mg kg^{-1} by intravenous injection and challenged them at 3 DPI with small-particle aerosols of HPAI A/Vietnam/1203/2004 (H5N1) virus, which produces fulminant pneumonia

[1]Vaccine Research Center, National Institute of Allergy and Infectious Diseases, National Institutes of Health, Bethesda, MD, USA. [2]Biostatistics Facility, UPMC Hillman Cancer Center, University of Pittsburgh, Pittsburgh, PA, USA. [3]Department of Infectious Diseases and Microbiology, University of Pittsburgh, Pittsburgh, PA, USA. [4]Department of Diagnostic Radiology, University of Pittsburgh Medical Center, Pittsburgh, PA, USA. [5]Center for Vaccine Research, University of Pittsburgh, Pittsburgh, PA, USA. [6]Department of Population Health, University of Georgia, Athens, GA, USA. [7]Division of Laboratory Animal Resources, University of Pittsburgh, Pittsburgh, PA, USA. [8]Vaccine and Immune Therapies, AstraZeneca, Gaithersburg, MD, USA. [9]Department of Immunology, University of Pittsburgh, Pittsburgh, PA, USA.
***Corresponding author. Email: kanekiyom@nih.gov (M.K.); dsreed@pitt.edu (D.S.R.); smbb@pitt.edu (S.M.B.-B.)**
†These authors contributed equally to this work.
‡Present address: Generate:Biomedicines, Somerville, MA, USA.
§Present address: Q2 Lab Solutions, Durham, NC, USA.
¶Present address: Department of Ecology and Evolution, University of Chicago, Chicago, IL, USA.
#Present address: Department of Microbiology, Ohio State University, Columbus, OH, USA.
**Present address: Department of Infectious Diseases, St. Jude Children's Research Hospital, Memphis, TN, USA.
††Present address: Baylor College of Medicine, Houston, TX, USA.
‡‡Present address: Department of Microbiology and Immunology, Emory University School of Medicine, Atlanta, GA, USA.
§§Present address: Department of Microbiology and Immunology, Tulane National Primate Center, Tulane University, New Orleans, LA, USA.
¶¶Present address: University of Hawaii, Honolulu, HI, USA.
##Present address: ModeX Therapeutics, Weston, MA, USA.
***Present address: IntegerBio, Gaithersburg, MD, USA.
†††Present address: Department of Microbiology, Biochemistry, and Immunology, Morehouse School of Medicine, Atlanta, GA, USA.

progressing to acute respiratory distress syndrome (ARDS) within days of exposure in untreated macaques (*14*) (Fig. 1C). The concentration of inhaled aerosolized virus ranged from $10^{4.12}$ to $10^{5.96}$ plaque-forming unit (PFU), with the mean virus inoculum dose for each group approximating the 50% lethal dose of virus in this model of $10^{5.2}$ PFU (*15*) (Fig. 1D). Three of the control mAb-treated macaques were euthanized as a result of ARDS at 3 days post challenge (DPC) (macaque 97-20), 4 DPC (90-20), and 7 DPC (95-20) (animals

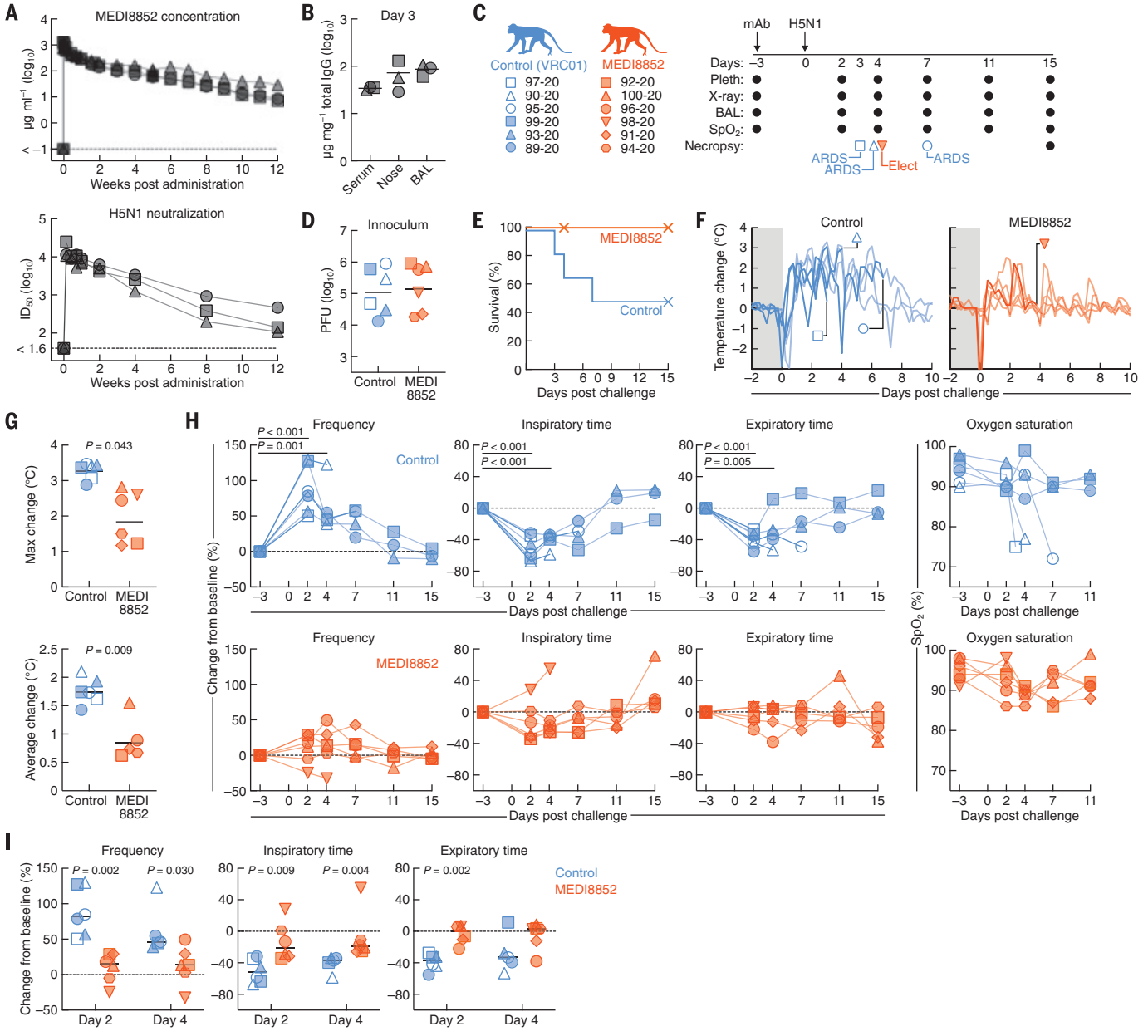

Fig. 1. Physiologic response to H5N1 infection after MEDI8852 prophylaxis. (**A**) Concentration of MEDI8852 mAb in the serum of three macaques at different points after administration and the concentration of the serum needed to neutralize 50% of the H5N1 infectivity (IC_{50}) at a given time point after administration. Horizontal dotted lines indicate the lower limit of detection. (**B**) Amount of MEDI8852 per unit of IgG in the serum, nose, and BAL 3 days after administration. Horizontal bars indicate the group mean. (**C**) Schematic of study. Animals were electively sacrificed at 15 DPC unless noted. (**D**) Inoculum given to control and MEDI8852-treated animals in log_{10} PFU. Closed symbols indicate animals that survived; open symbols indicate animals that succumbed to ARDS. Macaque 98-20, receiving MEDI8852, was electively sacrificed at a similar time point as controls with ARDS (4 DPC). Horizontal bars indicate the group geometric mean. (**E**) Kaplan-Meier survival curves for animals in the MEDI8852 and control groups. Animals that were censored are indicated as cross marks. (**F**) Temperature change from baseline in control and MEDI8852-treated animals. (**G**) Maximum and average temperature change in control and MEDI8852-treated animals. Horizontal bars indicate the group geometric mean. (**H**) Percent change in breath frequency, inspiratory time and expiratory time from baseline, and blood oxygen saturation in control and MEDI8852 animals. Within-group analyses were performed using paired *t* test. Horizontal dotted lines indicate the pre-challenge baseline (no change). (**I**) Percent change in breath frequency, inspiratory time, and expiratory time in control and MEDI8852-treated animals at 2 and 4 DPC. Between-treatment group analyses were performed using Mann-Whitney test, and within-group analyses were performed using paired *t* test. Horizontal dotted lines indicate the pre-challenge baseline (no change), and horizontal bars indicate the group median. Animal experiments were performed once, whereas virus quantification was performed at least twice with similar results.

who did not survive are indicated by open symbols in all figures). One MEDI8852-treated macaque (98-20) was electively sacrificed at 4 DPC to serve as a temporal control and censored in survival analysis. All other macaques were electively sacrificed at 15 DPC (Fig. 1, C and E). Body temperature as measured by radiotelemetry increased in all macaques after infection but had significantly greater duration and maximum and average temperature changes in control macaques (Fig. 1, F and G). Respiratory function as measured by plethysmography was significantly altered in control macaques, with breath frequency increasing by an average of 101% and inspiratory and expiratory times decreasing by 51 and 40%, respectively, by 2 DPC, reflecting severe lower respiratory tract disease (Fig. 1, H and I). These changes in respiratory parameters were similar in control macaques with and without progression to ARDS, although in macaques with ARDS the saturation of oxygen in blood dropped to <75%, warranting euthanasia. By contrast, MEDI8852-treated macaques maintained largely normal respiratory function over time with minimal average changes in breath frequency (~10%), inspiratory time (~−13%), and expiratory time (~−3%) at both 2 and 4 DPC (Fig. 1H and 1I). Collectively, these results establish that the pre-exposure prophylaxis of MEDI8852 confers protection from severe febrile and respiratory illnesses, ARDS, and fatality upon aerosolized H5N1 virus infection in a macaque model.

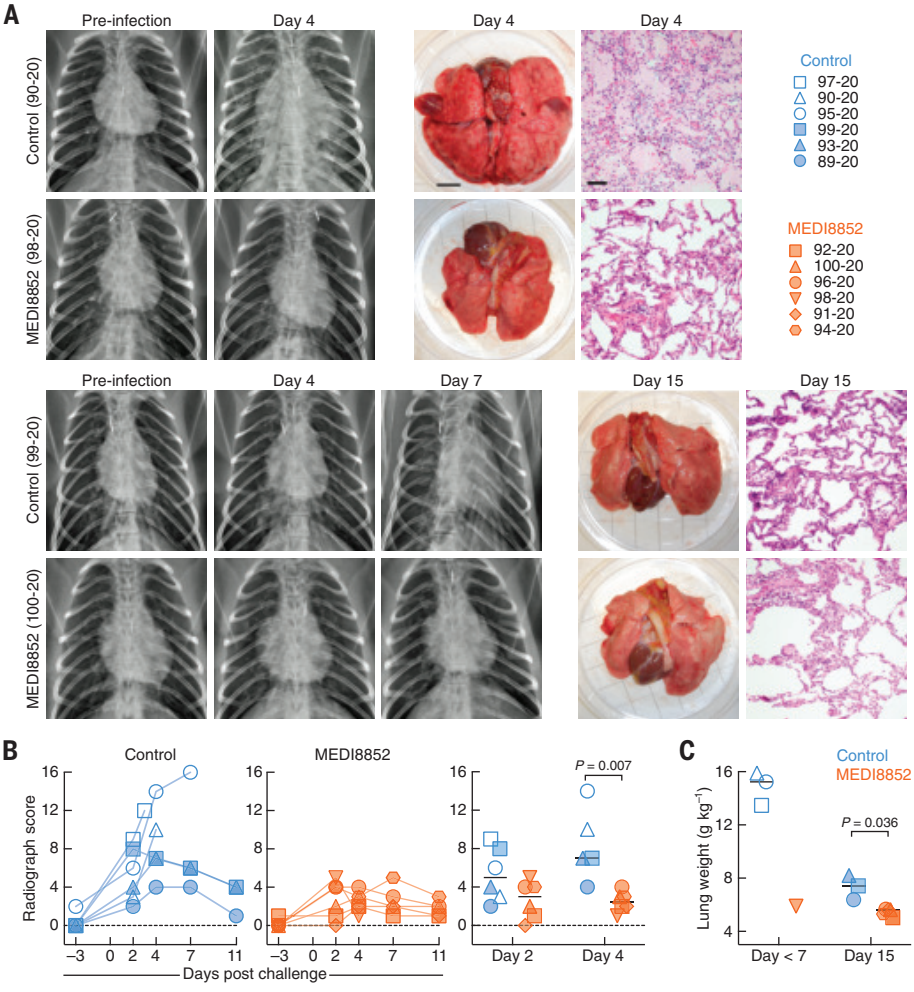

Fig. 2. Radiographic and pathologic response to H5N1 infection after MEDI8852 prophylaxis. (**A**) Chest radiographs, gross lung pathology, and hematoxylin and eosin micrographs of select control and MEDI8852 animals sacrificed at 4 or 15 DPC. (**B**) Radiographic scoring of x-rays from all control and MEDI8852-treated animals over time and at 2 and 4 DPC. Horizontal dotted lines indicate the lower limit of detection. (**C**) Lung gross weight at necropsy at between 3 and 7 DPC (left) and at 15 DPC (right) of control and MEDI8852-treated animals. Horizontal bars indicate the group median. Closed symbols indicate animals that survived; open symbols indicate animals that succumbed to ARDS. Between-treatment group analyses were performed using Mann Whitney test, and within-group analyses were performed using paired *t* test. Radiographs were independently evaluated blindly by two radiologists.

Characterization of MEDI8852-mediated protection in lungs

Severe influenza virus infection often leads to lower respiratory tract disease and viral pneumonia, especially in younger children, pregnant women, the elderly, and individuals with comorbidities (*19*). Control macaques all had diffuse radiographic changes, ranging from interstitial opacities alone to a predominance of alveolar opacities (Fig. 2A). Control macaques that progressed to ARDS had the most significant changes, with maximum radiograph scores of 9 to 16 (*20*) (Fig. 2B). Notably, macaque 97-20 had marked cardiomediastinal deviation to the right due to left lung consolidation at 3 DPC, and 95-20 had pneumothorax at 4 and 7 DPC (fig. S1). By contrast, MEDI8852-treated macaques had minimal although measurable radiographic changes upon infection, with two of six macaques reaching a maximum radiograph score of 5 (Fig. 2, A and B). When compared with the control macaques, radiograph scores in MEDI8852-treated macaques were significantly lower at 4 DPC (P = 0.007, Fig. 2B). At the necropsy, lungs from control macaques euthanized due to ARDS between 3 and 7 DPC were grossly enlarged, edematous, and hemorrhagic, with widespread intra-alveolar edema, septal thickening, and cellular infiltrates evident histologically, unlike the lungs from MEDI8852-treated macaques electively sacrificed at day 4 (Fig. 2, A and C). The lungs from the remaining control macaques sacrificed at 15 DPC were smaller, with limited intra-alveolar edema, septal thickening, and leukocyte infiltration. The lungs from MEDI8852-treated macaques electively euthanized at 15 DPC were significantly smaller than that of controls (P = 0.036, Fig. 2C) and had limited swelling and edema both grossly and histologically (Fig. 2A), demonstrating that MEDI8852 prophylaxis protects from viral pneumonia and lung damage induced by H5N1 infection.

Cellular, cytokine, and virologic responses in BAL

To evaluate cellular and inflammatory changes after H5N1 infection, we did serial BAL collections on all macaques. Before infection, the predominant cell type in BAL were CD163$^+$CD206$^+$ alveolar macrophages, with an average of 38 and 44% in control and MEDI8852-treated macaques, respectively (Fig. 3, A and B). In all control macaques, the percentage of alveolar macrophages dropped precipitously by an average of 73% by 2 DPC, concurrent with infiltration of CD163$^+$CD206$^-$ interstitial macrophages. The proportion of CD163$^-$MHC-II$^-$CD11b$^+$ neutrophils in BAL also increased from <1% to an average of 9.3% in control macaques by 2 DPC,

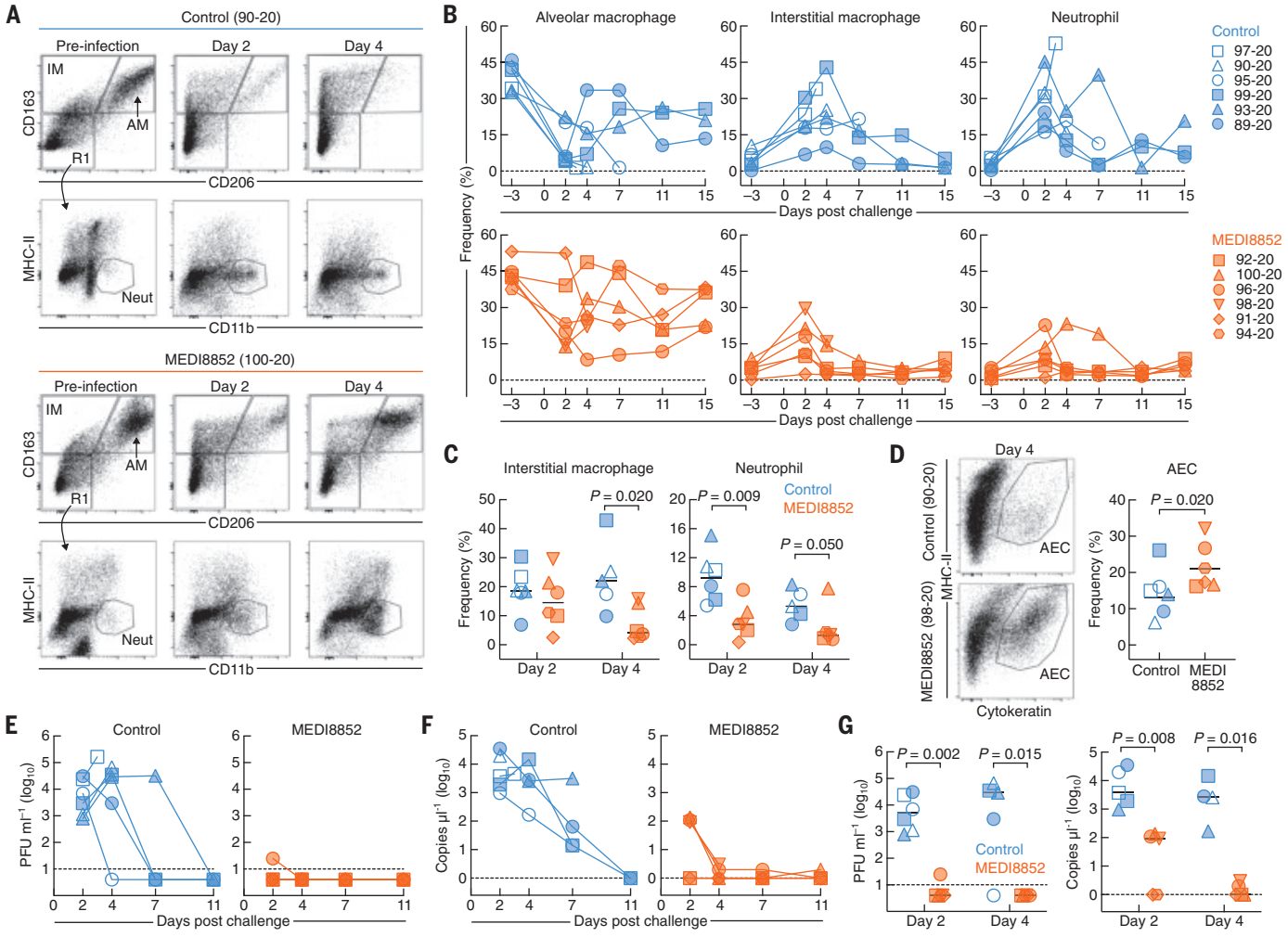

Fig. 3. Cellular and virologic response in BAL and lung to H5N1 infection after MEDI8852 prophylaxis. (**A**) Flow cytometry dot plots of BAL cells stained with antibodies to CD163, CD206, CD11b, and MHC-II at days −7, 2, and 4 from a control and a MEDI8852-treated animal to identify alveolar macrophages (AM), interstitial macrophages (IM), and neutrophils (Neut). (**B**) Percent of alveolar and interstitial macrophages and neutrophils in BAL from control and MEDI8852-treated animals over time. Closed symbols indicate animals that survived; open symbols indicate animals that succumbed to ARDS. Horizontal dotted lines indicate the lower limit of detection. (**C**) Percent of interstitial macrophages and neutrophils in BAL at 2 and 4 DPC. Horizontal bars indicate the group median. (**D**) (Left) Flow cytometry dot plots of lung-cell suspensions from a control and a MEDI8852-treated animal sacrificed at 4 DPC stained with antibody to cytokeratin to identify alveolar epithelial cells (AEC). (Right) Percent of lung cells that are AECs from lungs of all animals at sacrifice. Horizontal bars indicate the group median. (**E** and **F**) Titers of live virus (E) and viral RNA (F) in BAL supernatant of control and MEDI8852-treated animals over time. Horizontal dotted lines indicate the lower limit of detection. (**G**) Comparison of virus quantities in BAL supernatant of control and MEDI8852-treated animals measured by plaque assay (left) and digital polymerase chain reaction (dPCR) (right) at 2 and 4 DPC. Horizontal dotted lines indicate the lower limit of detection, and horizontal bars indicate the group median. Between-treatment group analyses were performed using Mann-Whitney test. Flow cytometry experiments were performed once, whereas viral quantification was performed at least twice with similar results. dPCR was performed once.

reflecting neutrophil recruitment to lungs. These changes in cell subsets were noted in all control macaques and were generally the greatest in macaques progressing to ARDS (Fig. 3, A and B). By contrast, the percentage of alveolar macrophages in MEDI8852-treated macaques was variable, ranging from 14 to 53% at 2 DPC, as was the proportion of interstitial macrophages. The percentage of neutrophils in MEDI8852-treated macaques was generally low, with an average of 2% of at 2 DPC (Fig. 3, A and B). Differences in frequencies of interstitial macrophages and neutrophils between control and MEDI8852-treated groups were significant (Fig. 3, B and C). At the level of lung tissue at necropsy, cytokeratin$^+$ alveolar epithelial cells were significantly lost in control macaques compared with MEDI8852-treated macaques (14.5 versus 21.7%, $P = 0.020$, Fig. 3D). Between the DPC-matched control and MEDI8852-treated macaques (90-20 and 98-20, respectively), the difference was even more drastic (6.3 versus 32.1%). In line with the observed cellular changes, several inflammatory cytokines and chemokines were significantly elevated in BAL fluid in control macaques, with levels of CXCL11, CXCL8, CCL11, and CCL4 increasing from sixfold (CCL4) to 175-fold (CXCL11) at 2 DPC. Of these, only CXCL8 was significantly elevated in MEDI8852-treated macaques (sixfold at 2 DPC). The concentration of CXCL8, CCL11, CCL4, and interleukin-1β were all significantly lower in MEDI8852-treated macaques than control macaques at either or both 2 and 4 DPC (fig. S2). Together, these data show that MEDI8852 prophylaxis protects lungs from loss of alveolar macrophages and alveolar epithelial cells, inhibits infiltration of interstitial macrophages and neutrophils, and limits the production of

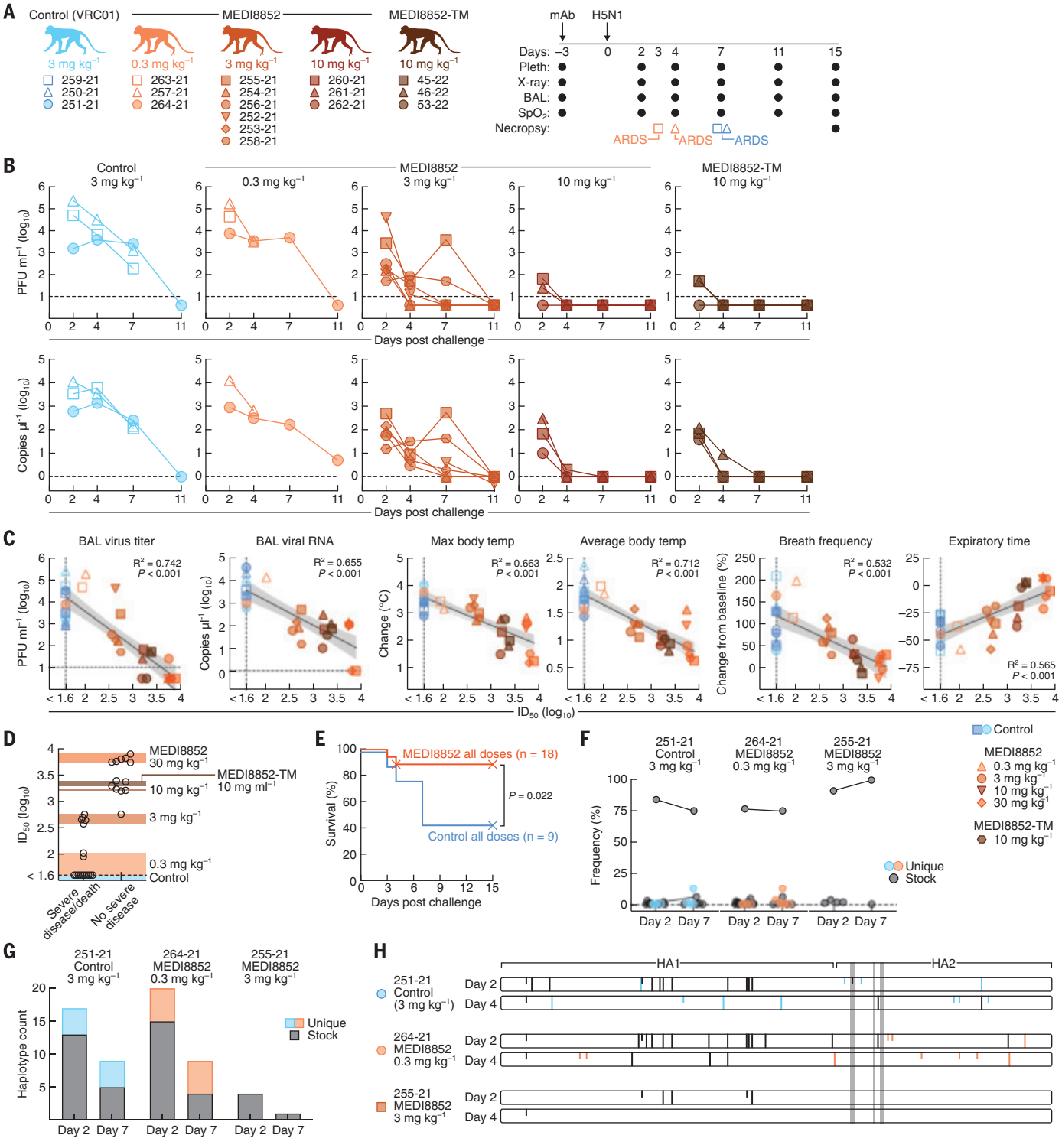

Fig. 4. Response to different MEDI8852 doses and virus sequencing. (**A**) Schematic of MEDI8852 titration study. Animals were sacrificed at 15 DPC unless noted. (**B**) Live virus titers (top) and viral RNA copies (bottom) in BAL supernatant of animals receiving control or MEDI8852 antibody at various doses over time. Horizontal dotted lines indicate the lower limit of detection. (**C**) Correlation between serum neutralizing ID_{50} titers (*x* axis) and each of the following parameters: BAL virus titers (2 DPC); BAL viral RNA copies (2 DPC); maximum temperature change, average temperature change, and breath frequency (2 DPC); and expiratory time (2 DPC). Correlation was estimated by simple linear regression, with 95% confidence intervals shaded in gray. Horizontal and/or vertical dotted lines indicate the lower limit of detection. (**D**) Serum neutralizing ID_{50} titers by severe disease or death status for control and MEDI8852-treated animals. Horizontal dotted lines indicate the lower limit of detection. (**E**) Survival curves of control and MEDI8852-treated animals at all dose levels. Animals that were censored are indicated as cross marks. Comparison of the Kaplan-Meier curves was made with log-rank (Mantel-Cox) test. (**F**) Frequencies of single-genome HA sequences in the three macaques with replication-competent virus detected in BAL at 7 DPC that matched

sequences detected in the challenge stock (black) or were unique to the animal (blue or orange). Symbols indicating sequences detected at both 2 DPC and 7 DPC are connected with line segments. Horizontal dotted lines indicate the lower limit of detection. (**G**) Counts of distinct HA sequences (haplotypes) detected in each macaque at 2 and 7 DPC. (**H**) Maps of minor variant nucleotide (short bars) and amino acid (long bars) polymorphisms detected in single-genome HA sequences from three macaques. Polymorphisms also detected in the challenge stock are indicated in gray, and polymorphisms that are unique to the animal are indicated in blue or orange. The position of the target epitope sequence for MEDI8852 is indicated with gray vertical bars. Animal experiments were performed once, whereas viral quantification was performed at least twice with similar results. dPCR was performed once. HT-SGS was performed at least twice with similar results.

inflammatory cytokines and chemokines upon H5N1 infection.

MEDI8852 prophylaxis inhibited viral replication in the treated macaques. In the control macaques, replication-competent virus was recovered from the BAL fluid of all six macaques at 2 DPC and four of the five macaques at 4 DPC (Fig. 3E). By contrast, only one BAL sample had detectable virus at 2 DPC in the MEDI8852-treated macaques, although the infused mAbs present in BAL might affect the readout (Fig. 3E). These data align well with the results from the viral RNA quantification by reverse transcription polymerase chain reaction of the BAL fluids (Fig. 3F). Differences in viral titers and viral RNA levels in BAL at both 2 and 4 DPC between treatment groups were significant (Fig. 3G). At the necropsy, replication-competent virus was recovered from all three regions of lung sampled from control macaques 97-20 and 90-20, sacrificed because of ARDS at 3 and 4 DPC, respectively, whereas a 100-fold-lower concentration of virus was recovered from only one region of lung of the MEDI8852-treated macaque 98-20, electively sacrificed at 4 DPC. Viral RNA was recovered from the lungs of five out of six macaques in each group at necropsy, with the highest viral quantity being in tissues from control macaques 97-20 and 90-20 (fig. S3A). Immunohistochemistry revealed loss of cytokeratin$^+$ alveolar epithelial cells and infiltration of CD163$^+$ interstitial macrophages with substantial viral nucleoprotein (NP) expression in both cell types in control macaque 90-20, sacrificed because of ARDS at 4 DPC. By contrast, MEDI8852-treated macaque 98-20, electively sacrificed at 4 DPC, had fewer NP-expressing epithelial cells and macrophages and substantially fewer interstitial macrophages in tissues, which is consistent with flow cytometry data. Lungs from control macaque 99-20 and MEDI8852-treated macaque 100-20, each sacrificed electively at 15 DPC, showed evidence of occasional NP-expressing epithelial cells and macrophages (fig. S3B). Collectively, these findings indicate that MEDI8852 prophylaxis resulted in virus suppression in the lungs.

Dose and Fc function dependency of MEDI8852

To assess the dose effect of MEDI8852, three additional groups of macaques with varying doses (10, 3, and 0.3 mg kg^{-1}) of MEDI8852 along with control mAbs (3 mg kg^{-1}) were infected with aerosolized H5N1 virus (Fig. 4A). The average serum concentration of MEDI8852 at 3 DPI was 130, 48, and 4 μg ml^{-1} for the 10, 3, and 0.3 mg kg^{-1} groups, respectively, which was proportionally lower than that of the 30 mg kg^{-1} group (448 μg ml^{-1} at 3 DPI). Upon infection, two of the three macaques each in the control and the lowest MEDI8852-treated group (0.3 mg kg^{-1}) succumbed to ARDS (open symbols), whereas all macaques in the 3 and 10 mg kg^{-1} groups survived (Fig. 4, A and B). Replication-competent virus titers, as well as viral RNA levels in BAL fluids, were higher in the control and the lowest MEDI8852-treated macaques (Fig. 4B). Although all six macaques in the 3 mg kg^{-1} group survived, they all had detectable virus as well as viral RNA in BAL fluids, which was different from higher-dose groups (10 and 30 mg kg^{-1}) (Fig. 3, E and F, and Fig. 4B).

To assess the potential role of antibody Fc-mediated effector functions in providing protection from morbidity and mortality caused by H5N1 infection in macaques, we tested an Fc variant called TM (*21*), which contains L234F (L234→F), L235E, and P331S substitutions (where L is lysine, F is phenylalanine, E is glutamic acid, P is proline, and S is serine) in the C_H2 domain within the Fc portion of the MEDI8852 (referred to hereafter as MEDI8852-TM). This TM variant results in a profound decrease in binding to FcγRI, FcγRIIa, FcγRIII, and complement C1q, while maintaining binding to FcγRn (*21*). Notably, the neutralizing activity of MEDI8852-TM was not different from that of MEDI8852, and both antibodies potently neutralized more recent panzootic 2.3.4.4b clade H5N1 viruses (*22*, *23*) as well (fig. S4). The pharmacokinetics of MEDI8852-TM and MEDI8852 in transgenic hFc-hFcRn mice (*24*) were also similar (9.5 ± 1.6 versus 9.6 ± 1.5 days, respectively) (fig. S4). We administered MEDI8852-TM at 10 mg kg^{-1} to three macaques (Fig. 4A). Average serum concentration of MEDI8852-TM was 144 μg ml^{-1} at 3 DPI, which was similar to the concentration of MEDI8852 when administered at the same 10 mg kg^{-1} dose (130 μg ml^{-1}), confirming that TM did not alter pharmacokinetics in macaques. All three MEDI8852-TM–treated macaques survived H5N1 challenge and had low or no detectable virus in BAL, analogous to MEDI8852-treated macaques at the same 10 mg kg^{-1} dose (Fig. 4B). These data show that at the dose of 10 mg kg^{-1}, protection acquired by MEDI8852 administration does not require Fc receptor function, although Fc receptor function may be important at the lower dose level, as shown in a mouse model (*25*, *26*).

Disease outcome prediction and protective threshold

We measured serum neutralizing activity against A/Vietnam/1203/2004 (H5N1) virus in all macaques at the time of challenge to determine correlations with disease outcomes (Fig. 4C). We found that serum neutralizing activity inversely correlated with viral burden in the BAL fluids, body temperature elevation, and breath frequency ($P < 0.0001$), and positively correlated with expiration time ($P < 0.0001$) (Fig. 4C). To set criteria for severe disease, we next used historical data from a total of 15 macaques infected with aerosolized H5N1 virus at the 50% lethal dose or higher (*15*). All of these macaques either succumbed to ARDS, had respiratory disease, or had transient fever (table S1), allowing us to estimate confidence intervals for the reference range of severe disease using both respiratory and temperature parameters (see materials and methods) (fig. S5). We found that all macaques receiving the control mAb (30 and 3 mg kg^{-1}, $n = 9$) and MEDI8852 at 0.3 mg kg^{-1} dose ($n = 3$) had severe disease upon H5N1 infection, with a minimum of at least one parameter crossing the boundary. Although all six macaques receiving MEDI8852 at 3 mg kg^{-1} dose survived, five of them met the criteria for severe disease. By contrast, none of the 12 macaques that received either MEDI8852 at 10 and 30 mg kg^{-1} or MEDI8852-TM at 10 mg kg^{-1} met the criteria for severe disease (fig. S5). By using the serum neutralizing ID_{50} and the disease outcome of these study macaques ($n = 30$), we identified a threshold for protection from severe disease or death (Fig. 4D). All animals with a serum neutralizing $ID_{50} > 10^{2.76}$ at the time of challenge were protected from severe disease or death, and all animals with values $< 10^{2.76}$ developed severe disease or succumbed to disease (materials and methods). According to our pharmacokinetics study, this translates into ~8 weeks of protection from severe disease or death by a single infusion of 30 mg kg^{-1} of MEDI8852 in macaques (Fig. 1A). When all the MEDI8852 groups (excluding the MEDI8852-TM group) were combined (0.3, 3, 10, and 30 mg kg^{-1}, $n = 18$) and compared with the combined control groups (3 and 30 mg kg^{-1}, $n = 9$), there was a statistical difference in survival rate ($P = 0.022$), demonstrating the survival benefit of MEDI8852 prophylaxis (Fig. 4E). Further, we examined the relationship between dose of MEDI8852 and survival as a continuous variable by using a proportional-hazards regression model. Animals in the control groups were

included in the model as receiving 0 mg kg^{-1} of MEDI8852. As expected, MEDI8852 was a significant predictor of survival ($P < 0.001$), according to the likelihood ratio test, with a 72% reduction in the hazard rate for each mg kg^{-1} increase in MEDI8852 dose.

Viral HA gene sequencing

To investigate whether MEDI8852 administration had promoted outgrowth of new variants in this setting, we used high-throughput, single-genome amplification and sequencing (HT-SGS) to analyze full-length HA gene sequences in three macaques that had transiently increased replication-competent virus in BAL at 7 DPC (Fig. 4B). At 2 DPC, the majority of HA sequences in macaques 251-21 (control), 264-21 (MEDI8852 0.3 mg kg^{-1}), and 255-21 (MEDI8852 3 mg kg^{-1}) exactly matched the predominant sequence from the challenge virus stock [n = 998 (84%), 1159 (75%), and 342 (91%) sequences, respectively] (Fig. 4F). Minor variant HA sequences were also detected in all three animals at 2 DPC. Whereas 251-21 and 264-21 showed 17 and 20 minor variants including several not detected in the challenge stock, respectively, 255-21 showed only 4 minor variants, all of which were present in the challenge stock (Fig. 4G). At 7 DPC, the predominant HA sequence from each animal [1,009 (75%), 1444 (91%), and 1726 (99%)] again matched the predominant stock sequence, with fewer distinct minor variant sequences detected than at 2 DPC. Among 1592 and 1734 HA sequences obtained at 7 DPC from 264-21 and 255-21, respectively, minor variants with mutations at the antibody target epitope were not detected (Fig. 4H). These findings indicate that MEDI8852 prophylaxis did not result in outgrowth of new virus sequence variants after infection and suggest that a tighter transmission bottleneck and reduced intrahost virus diversification occur with increasing antibody dose.

Discussion

We have shown the efficacy and feasibility of pre-exposure antibody prophylaxis for protecting from respiratory disease and death due to avian influenza virus infection in macaques, extending prior knowledge obtained in small animal models. These results not only provide further support for the bnAb prophylaxis as an effective influenza pandemic countermeasure but also shed light on the development of vaccines that elicit such bnAb responses to confer protection from pandemic influenza morbidity and mortality. Although we gave virus challenge at 3 DPI, the slow linear rate of mAb decay in sera indicates that protection from severe disease would extend to weeks beyond mAb infusion, providing a realistic preventative window in the face of an H5N1 outbreak. It is possible to further broaden the preventative window by extending the antibody half-life through well-known Fc mutations, such as LS (*27*) and YTE (*28*). We tested MEDI8852, which is one of the broadest and most potent bnAbs against influenza A viruses targeting the HA stem supersite (*13*) and has been shown previously to mediate pre- and postexposure protection as well as transmission blocking in mice and ferrets (*13*, *29*). Due to the evolutionary, anatomical, and physiological differences, as well as the impractical mode of infection used in small animal models, results from these prior studies inevitably have limited translational value. Our study represents a relevant, reflective, and predictive model for antibody-mediated protection from severe influenza in humans, overcoming the inherent limitations of other models. Although MEDI8852 is an engineered antibody matured in vitro, the parental antibody FY1 belongs to a public clonotype called the V_H6-1 + D_H3-3 class (*13*, *30*), which can be recurrently found in multiple individuals upon experimental vaccination with non-circulating influenza subtypes (*30*, *31*). We have shown that the key immunogenetic and structural characteristics of the human V_H6-1 + D_H3-3 class bnAbs are evolutionarily conserved in macaques, and similar bnAbs can be elicited through vaccination of HA stem–based immunogens in macaques (*32*). This validates the approach of empirically testing protective efficacy of HA stem–based universal influenza vaccine candidates that elicit human-like bnAb responses in the aerosolized H5N1 macaque disease model. It is of great interest to see whether the protective threshold determined for MEDI8852 in this study can be translated into vaccine-elicited polyclonal responses and if any contributions derive from non-neutralizing or weakly neutralizing antibodies through Fc-mediated effector functions.

Our results were consistent with an earlier study with antimatrix M2 antibody against pandemic H1N1 infection in macaques (*33*), showing no sign of antibody-mediated enhanced disease even in macaques with a subprotective dose of MEDI8852, albeit with a limited number of animals. Our macaque model reflects and recapitulates many aspects of human H5N1 influenza virus infection (*19*, *34*), although there are inevitable differences in our model compared with human cases, including the varying inhaled virus dose, preexisting influenza immunity, supportive treatment, and use of antivirals. These factors may contribute to the disease outcome and could be addressed in future studies. Furthermore, a derivative of MEDI8852 has recently failed to meet its efficacy endpoint in a phase 2 clinical trial as a prophylaxis, accentuating the difficulty in studying the protective efficacy against seasonal influenza in humans in the face of preexisting immunity (*9*). Nevertheless, our study fills the critical knowledge void between preclinical and human clinical studies, offering a distinctive efficacy outlook for bnAb prophylaxis against HPAI virus infection that is unattainable in controlled human clinical trials.

Recent advances in antibody discovery have yielded several exceptionally broadly cross-reactive and protective human mAbs that recognize viral neuraminidase (NA) (*35*–*37*). Although these mAbs do not block virus entry in in vitro neutralization assays, they do provide protection in both pre- and postexposure prophylaxis settings in mice and block transmission in guinea pigs (*38*), likely through blocking viral NA activity and thereby inhibiting virus egress and/or limiting the mobility of virus in mucus. The combination of these NA-targeting mAbs and HA-directed bnAbs would be expected to provide superior breadth and a further reduction in the risk of selecting for virus escape variants. Potential synergy between MEDI8852 and an anti-NA mAb, FNI9, has been reported (*37*), accentuating the utility of anti-HA and anti-NA antibody cocktail or bispecific and multispecific antibody approaches (*39*–*41*). Those data, plus our findings, suggest that single or combination mAb prophylaxis could be protective in a human outbreak or pandemic scenario with H5N1, including the recent panzootic 2.3.4.4b clade viruses (*22*, *23*) and potentially other avian influenza viruses. Although our study is limited in sample size compared with a human efficacy trial, we have shown that bnAb prophylaxis averted morbidity and mortality due to respiratory dysfunction—a hallmark of severe influenza in humans—in macaques infected with H5N1 influenza virus through the natural route of infection, with no evidence for selection of bnAb escape variants. Results in the present study pave the way for developing medical countermeasures against future influenza virus pandemics.

REFERENCES AND NOTES

1. F. Winau, R. Winau, *Microbes Infect.* **4**, 185–188 (2002).
2. B. S. Graham, D. M. Ambrosino, *Curr. Opin. HIV AIDS* **10**, 129–134 (2015).
3. *Pediatrics* **102**, 531–537 (1998).
4. D. Corti, L. A. Purcell, G. Snell, D. Veesler, *Cell* **184**, 3086–3108 (2021).
5. D. Focosi *et al*., *Lancet Infect. Dis.* **22**, e311–e326 (2022).
6. K. Sedeyn, X. Saelens, *Antiviral Res.* **170**, 104562 (2019).
7. N. C. Wu, I. A. Wilson, *Cold Spring Harb. Perspect. Med.* **10**, a038778 (2020).
8. S. Nath Neerukonda, R. Vassell, C. D. Weiss, *Vaccines* **8**, 382 (2020).
9. S. K. Tan *et al*., *Clin. Infect. Dis.* **79**, 1054–1061 (2024).
10. S. O. Ali *et al*., *Antimicrob. Agents Chemother.* **62**, e00694-18 (2018).
11. E. Sparrow, M. Friede, M. Sheikh, S. Torvaldsen, A. T. Newall, *Vaccine* **34**, 5442–5448 (2016).
12. J. H. Beigel, F. G. Hayden, *Cold Spring Harb. Perspect. Med.* **11**, a038463 (2021).
13. N. L. Kallewaard *et al*., *Cell* **166**, 596–608 (2016).
14. E. R. Wonderlich *et al*., *J. Immunol.* **198**, 1616–1626 (2017).
15. M. Kanekiyo *et al*., *iScience* **26**, 107830 (2023).
16. R. M. Mallory *et al*., *Biologicals* **50**, 81–86 (2017).
17. X. Wu *et al*., *Science* **329**, 856–861 (2010).
18. T. Zhou *et al*., *Science* **329**, 811–817 (2010).
19. T. T. Hien, M. de Jong, J. Farrar, *N. Engl. J. Med.* **351**, 2363–2365 (2004).
20. D. Toussie *et al*., *Radiology* **297**, E197–E206 (2020).

21. V. Oganesyan, C. Gao, L. Shirinian, H. Wu, W. F. Dall'Acqua, *Acta Crystallogr. D Biol. Crystallogr.* **64**, 700–704 (2008).
22. J. A. Pulit-Penaloza *et al*., *Emerg. Microbes Infect.* **13**, 2332667 (2024).
23. E. R. Burrough *et al*., *Emerg. Infect. Dis.* **30**, 1335–1343 (2024).
24. B. E. Low, G. J. Christianson, E. Lowell, W. Qin, M. V. Wiles, *MAbs* **12**, 1829334 (2020).
25. D. Corti *et al*., *Science* **333**, 850–856 (2011).
26. D. J. DiLillo, G. S. Tan, P. Palese, J. V. Ravetch, *Nat. Med.* **20**, 143–151 (2014).
27. J. Zalevsky *et al*., *Nat. Biotechnol.* **28**, 157–159 (2010).
28. P. R. Hinton *et al*., *J. Immunol.* **176**, 346–356 (2006).
29. C. I. Paules *et al*., *J. Infect. Dis.* **216**, 356–365 (2017).
30. M. G. Joyce *et al*., *Cell* **166**, 609–623 (2016).
31. S. F. Andrews *et al*., *Sci. Immunol.* **2**, eaan2676 (2017).
32. S. M. Moin *et al*., *Immunity* **55**, 2405–2418.e7 (2022).
33. A. Song *et al*., *Antiviral Res.* **111**, 60–68 (2014).
34. M. D. de Jong *et al*., *Nat. Med.* **12**, 1203–1207 (2006).
35. D. Stadlbauer *et al*., *Science* **366**, 499–504 (2019).
36. A. Yasuhara *et al*., *Nat. Commun.* **13**, 6602 (2022).
37. C. Momont *et al*., *Nature* **618**, 590–597 (2023).
38. J. Tan *et al*., *J. Virol.* **96**, e0142121 (2022).
39. A. F. Labrijn, M. L. Janmaat, J. M. Reichert, P. W. H. I. Parren, *Nat. Rev. Drug Discov.* **18**, 585–608 (2019).
40. H. Cho *et al*., *Sci. Transl. Med.* **13**, eabj5413 (2021).
41. N. S. Laursen *et al*., *Science* **362**, 598–602 (2018).
42. M. Kanekiyo, S. Barratt-Boyes, D. Reed, Source data for Pre-exposure antibody prophylaxis protects macaques from severe influenza disease, Version v1, Zenodo (2024); https://www.doi.org/10.5281/zenodo.14390998.

ACKNOWLEDGMENTS

The authors thank C. Case (Frederick National Laboratory for Cancer Research, Leidos Biomedical Research), S. Gupta, C. Lange, G. Alvarado, and K. Bok [Vaccine Research Center (VRC)] for project management; C. Wiley (University of Pittsburgh) for histopathological analysis; W. Adams, J. Gall, and the Vaccine Production Program (VRC) for providing VRC01; D. Scorpio, R. Woodward, and J.-P. Todd (VRC) for help with macaque study coordination; K. Foulds, M. Donaldson, A. Noe, D. Flebbe, E. Lamb, S. Andrew, S. Nurmukhambetova, S. Provost, and K. Giridhar (VRC) for macaque sample processing; J. Vetosick, B. Seliga, and S. Moldovan (University of Pittsburgh) for macaque observation, handling, and sample collection; J. Lamb, D. Hollingshead, and B. Thompson (University of Pittsburgh) for virus sequencing; and S. Andrews and R. Koup (VRC) for fruitful discussion.
Funding: This study was supported by the Vaccine Research Center, an intramural division of the National Institute of Allergy and Infectious Diseases (NIAID), NIH (M.K., J.R.M., and B.S.G.); NIAID, NIH (HHSN261201500003, D.S.R. and S.M.B.-B.); NIAID, NIH (grant R01AI154894, D.R.P., and contract 75N93021C00014, options 15A, 15B, and 17A, D.R.P.); NIH (award UC7AI180311) from NIAID supporting the operations of the University of Pittsburgh Regional Biocontainment Laboratory (RBL) within the Center for Vaccine Research (CVR). MEDI8852 is available from M.E. under a material agreement with AstraZeneca. All other materials are available from M.K. under a material agreement with NIAID. **Author contributions:** Conceptualization: M.K., R.A.G., K.C., J.R.M., B.S.G., D.S.R., and S.M.B.-B. Formal analysis: M.K., R.A.G., K.C., V.G.C., E.A.B., D.S.R., and S.M.B.-B. Investigation: M.K., R.A.G., K.C., V.G.C., P.M.S.C., A.P., E.S.Y., L.T., G.Y., M.W., G.K., C.W., J.L., K.O., M.M., M.M.M., H.C., C.W., J.C., B.R.T., A.Li., L.O.B., A.C., I.R., R.W., E.O., A.La., D.R.P., E.A.B., Y.-M.L., D.S.R., and S.M.B.-B. Resources: A.C., D.R.P., Y.-M.L., W.B., and M.E. Writing – original draft: M.K., R.A.G., K.C., D.S.R., and S.M.B.-B. Writing – review & editing: all authors. Visualization: M.K., K.C., D.S.R., and S.M.B.-B. Supervision: M.K., J.R.M., E.A.B., B.S.G., D.S.R., and S.M.B.-B. Project administration: R.A.G. and S.B. Funding acquisition: M.K., J.R.M., B.S.G., D.S.R., and S.M.B.-B.
Competing interests: Y.-M.L., W.B., and M.E. are previous or current employees of AstraZeneca and hold or may hold stock in AstraZeneca. AstraZeneca has filed patent applications (WO 2017/123685 A1) related to MEDI8852. All other authors declare no competing interests. **Data and materials availability:** All data in the manuscript or the supplementary materials are available as source data and can be found at Zenodo (*42*). HA sequences from this study are available at NCBI SRA Bioproject PRJNA1105641.

SUPPLEMENTARY MATERIALS

science.org/doi/10.1126/science.ado6481
Materials and Methods
Figs. S1 to S5
Tables S1 and S2
References (*43*–*51*)
MDAR Reproducibility Checklist

Submitted 13 February 2024; accepted 17 December 2024
10.1126/science.ado6481

NEUROSCIENCE

The time course and organization of hippocampal replay

Caitlin S. Mallory*, John Widloski, David J. Foster*

The mechanisms by which the brain replays neural activity sequences remain unknown. Recording from large ensembles of hippocampal place cells in freely behaving rats, we observed that replay content is strictly organized over multiple timescales and governed by self-avoidance. After movement cessation, replays avoided the animal's previous path for 3 seconds. Chains of replays avoided self-repetition over a shorter timescale. We used a continuous attractor model of neural activity to demonstrate that neuronal fatigue both generates replay sequences and produces self-avoidance over the observed timescales. In addition, replay of past experience became predominant later into the stopping period, in a manner requiring cortical input. These results indicate a mechanism for replay generation that unexpectedly constrains which sequences can be produced across time.

Neuronal activity sequences associated with wakeful experience are replayed offline within the mammalian hippocampus and cortex (*1*–*11*). During movement, the hippocampus carries information about an animal's current location (*12*), whereas in sleep (*1*, *2*, *13*, *14*) or awake immobility (*15*–*24*), it depicts spatial trajectories that relate to the animal's past behavior or predicted future (*25*). Although replay can recapitulate previously experienced firing patterns (*22*) ("forward replay"), it can also reverse the order of neurons within a sequence (*21*) ("reverse replay") or depict new paths that the animal has not yet taken (*17*, *20*, *26*, *27*). These diverse phenomena have been linked to varying behavioral functions—from memory consolidation and reward processing to spatial planning and inference (*25*, *28*, *29*). Yet, the mechanisms by which the brain selects specific neuronal sequences at different times have remained unclear. We measured large numbers of replay events in rats exploring multiple environments to reveal a principled evolution of replay content with respect to recent experience and ongoing reactivations.

We recorded the activity of ensembles of place cells from the bilateral dorsal hippocampus of rats running laps on a linear track (n = 11 rats) or navigating within an open arena (n = 6 rats) (Fig. 1, A and F). On the track, rats paused between laps to consume liquid food reward (mean ± SEM rewards per session: 53 ± 3, n = 52 sessions; Fig. 1, A and B). In the open arena, rats were rewarded on alternating trials at a consistent location that was learnable across the session, or a random location that was unpredictable (*16*, *17*) ("Home trials" and "Random trials"; mean ± SEM trials per session: 76 ± 5, n = 56 sessions; Fig. 1F). In some sessions (n = 39), rats were additionally required to circumnavigate transparent "jail" barriers (*16*). Large numbers of co-recorded cells (mean ± SEM cells per session: linear track = 82 ± 05; open arena: 309 ± 21) in conjunction with a memory-less, uniform-prior Bayesian decoding algorithm (*23*) allowed us to accurately decode the rat's position during movement (mean ± SEM positional decoding error per session, linear track: 2.9 ± 0.1 cm; open arena: 3.4 ± 0.2 cm). On the linear track, where place cells are directionally selective (*30*), we additionally decoded the animals' movement direction (Fig. 1A).

Decoding on a fine timescale revealed abundant replay during reward-associated immobility (materials and methods) (Fig. 1, A and G). On the linear track, replays were classified as forward if the decoded heading direction aligned with the direction of replay motion across the track, and reverse if they were opposite (i.e., a trajectory depicting the animal running backward) (*21*–*23*) (Fig. 1C). We restricted analysis to replays representing motion away from the animal's current location ("local," n = 849), which made up the majority of events (Fig. 1D) and represented forward movement along the rat's immediate future path or reverse movement along its immediate past path. Forward events occurred with slightly higher frequency than reverse events (Fig. 1, D and E). In the open arena, we observed two-dimensional (2D) trajectories across the environment (*16*, *17*) (Fig. 1H), many of which approximated the path taken immediately before or after stopping (Fig. 1G). To quantify the degree to which replays corresponded to adjacent behavior, we calculated the angular displacement between each replay event and

Department of Neuroscience, University of California, Berkeley, Berkeley, CA, USA.
*Corresponding author. Email: caitlinmallory@berkeley.edu (C.S.M.); davidfoster@berkeley.edu (D.J.F.)

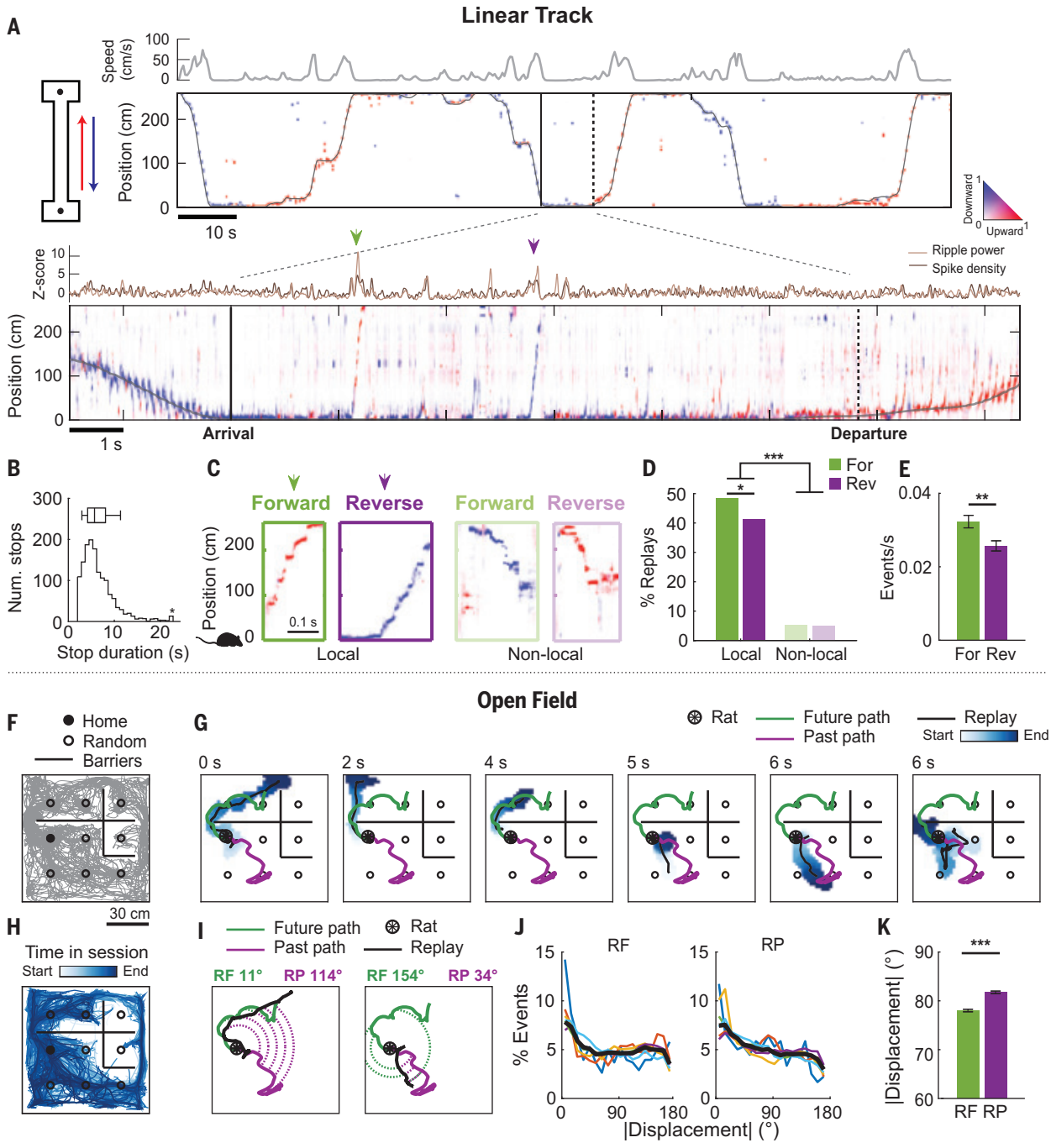

Fig. 1. Linear track and open field replay events. (**A**) Left: Schematic of the linear track. Circles: reward wells. Right: Posterior probability of position and running direction (400-ms bins). Gray: true position. Color indicates the estimated running direction. Inset: posterior probability during one stopping period (20-ms bins). (**B**) Stop durations. (**C**) Example replays. (**D**) Summary of replays within the first 10 s of stopping. Local replays (n = 849) versus nonlocal replays (n = 96), Z = 24.5, P < 0.0001. Forward local replays (n = 458) versus reverse local replays (n = 391), Z = 2.3, P = 0.021; two-tailed z-tests. (**E**) Replay rates per stopping period [mean ± SEM, n = 1642, Z = 2.7, P = 0.0058, Wilcoxon signed rank (WSR) test]. (**F**) Schematic of the open arena. Gray: behavioral trajectory. (**G**) Example replays from one trial, with time since stopping at top. Black: replay center of mass. Blues: replay posterior. Green and purple: rat's immediate future and past path, respectively (100 cm for each). (**H**) The center of mass of all replay events in the session. (**I**) Calculation of angular displacement from the immediate future (RF) or past path (RP) for two example replays. See also fig. S4. (**J**) Black: percentage of replays as a function of angular displacement from future or past paths. Colors: individual rats. (**K**) Mean ± SEM angular displacement from the immediate future or past path (n = 35,111 RF and 35,783 RP, Z = −9.54, P = 1.4e-21, WRS test). *P < 0.05, **P < 0.01, ***P < 0.001.

the animal's immediate past or future path, as previously (*17*) (Fig. 1I) (materials and methods). Smaller angular displacement indicates greater similarity between the traversed and replayed paths. Consistent with previous findings, replays were overall more tightly aligned to an animal's future path than its past (*16*, *17*) (Fig. 1, J and K).

Forward or prospective replays precede reverse or retrospective replays

We observed a consistent temporal order in the production of forward and reverse replays

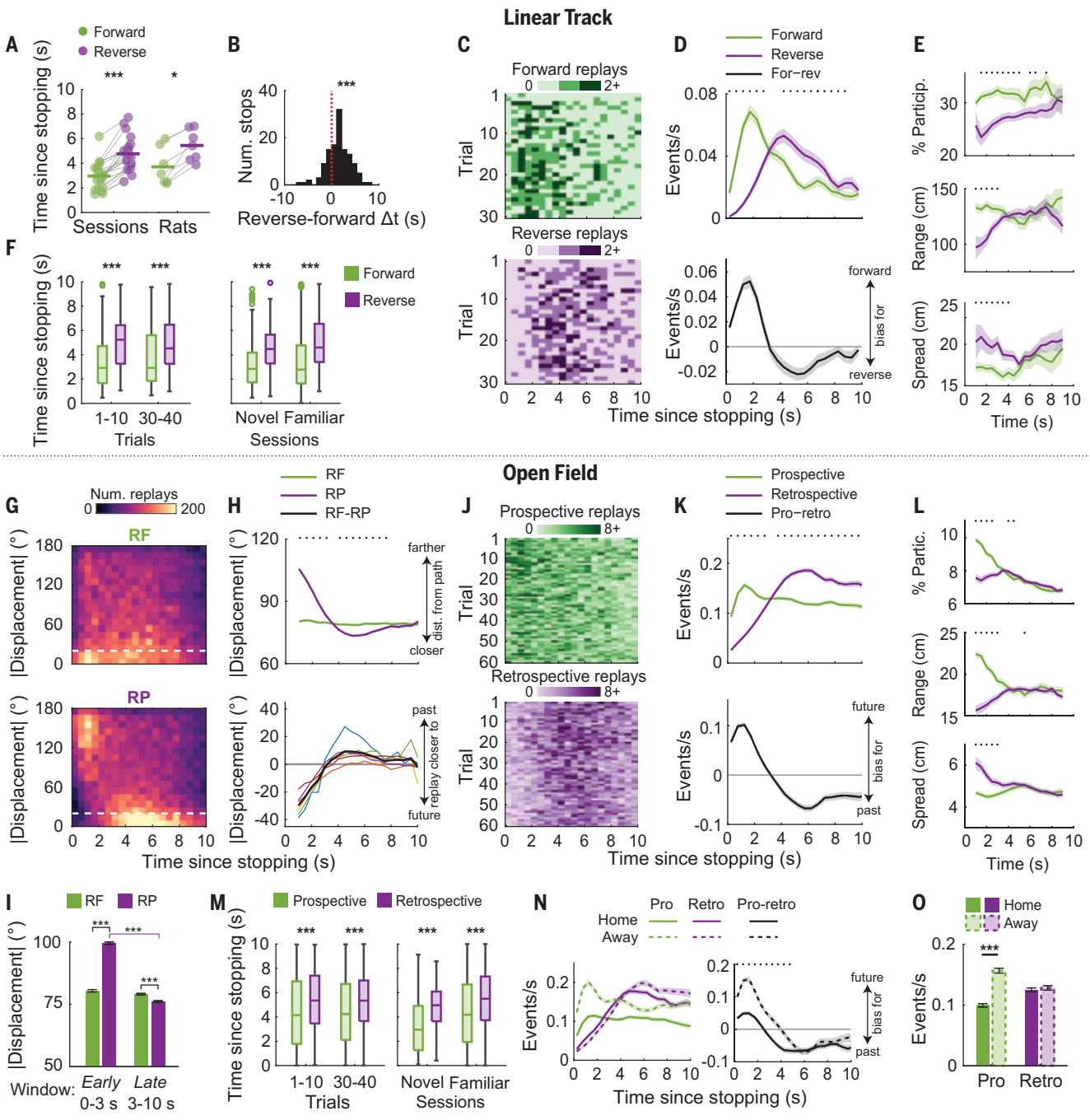

Fig. 2. Forward replay precedes reverse replay and prospective replay precedes retrospective replay. (**A**) Median replay time (n = 21 sessions, seven rats with at least five forward, five reverse replays; sessions: P = 6.0e-5; rats: P = 0.015, WSR). (**B**) Individual stops (n = 110, P = 2.5e-9, WSR). (**C**) Replay counts, summed across sessions. (**D**) Replay rates (max n = 1638 trials). (**E**) Replay properties (n = 458 forward replays and 391 reverse replays). Lower spread indicates higher precision. (**F**) Timing of replays occurring on early or late trials within a session, and in novel or familiar environments (trials 1 to 10: n = 47 forward replays and 61 reverse replays, P = 5.4e-4; trials 30 to 40: n = 98 forward replays and 83 reverse replays, P = 4.1e-5; Novel (first exposure): n = 150 forward replays and 106 reverse replays, P = 9.4e-9; familiar: n = 308 forward replays and 285 reverse replays, P = 1.8e-19, WRS). Box plots: median, interquartile range, and range. (**G**) Number of replays at varying angular displacements from the future (RF) or past path (RP), over time. (**H**) Top: mean ± SEM angular displacements from the future (RF) or past path (RP). Bottom: mean ± SEM difference in displacement (n = 36,677 replays). Colors: individual rats. Black: rat average. (**I**) Angular displacements within the Early or Late windows (n = 11,554 Early replays and 25,123 Late replays; interaction P = 1.0e-4, shuffle; Early, RF versus RP: P = 4.5e-193; Late, RF versus RP: P = 1.2e-10; RF, Early versus Late: P = 0.086; RP, Early versus Late: P = 2.0e-315; WRS). (**J**) Replay counts. (**K**) Replay rates (max n = 4269 trials). (**L**) Replay properties (n = 36,677 replays). (**M**) Timing of replays (trials 1 to 10: n = 637 prospective replays and 705 retrospective replays, P = 2.6e-9; trials 30 to 40: n = 661 prospective replays and 643 retrospective replays, P = 3.6e-11; novel: n = 70 prospective replays and 60 retrospective replays, P = 1.1e-4; familiar: n = 4752 prospective replays and 4951 retrospective replays, P = 4.3e-89; WRS). (**N**) Replay rates over time (n = 2147 Home trials and 2122 Away trials). (**O**) Trial averaged rates (interaction P = 1.4e-4, shuffle; prospective, Home versus Away: P = 9.5e-22; retrospective, Home versus Away: P = 0.59, WRS). Unless otherwise stated, plots show mean ± SEM. Dots above time course plots in panels (D), (E), (H), (K), (L), and (N) indicate time bins for which P < 0.05, WSR. *P < 0.05, ***P < 0.001

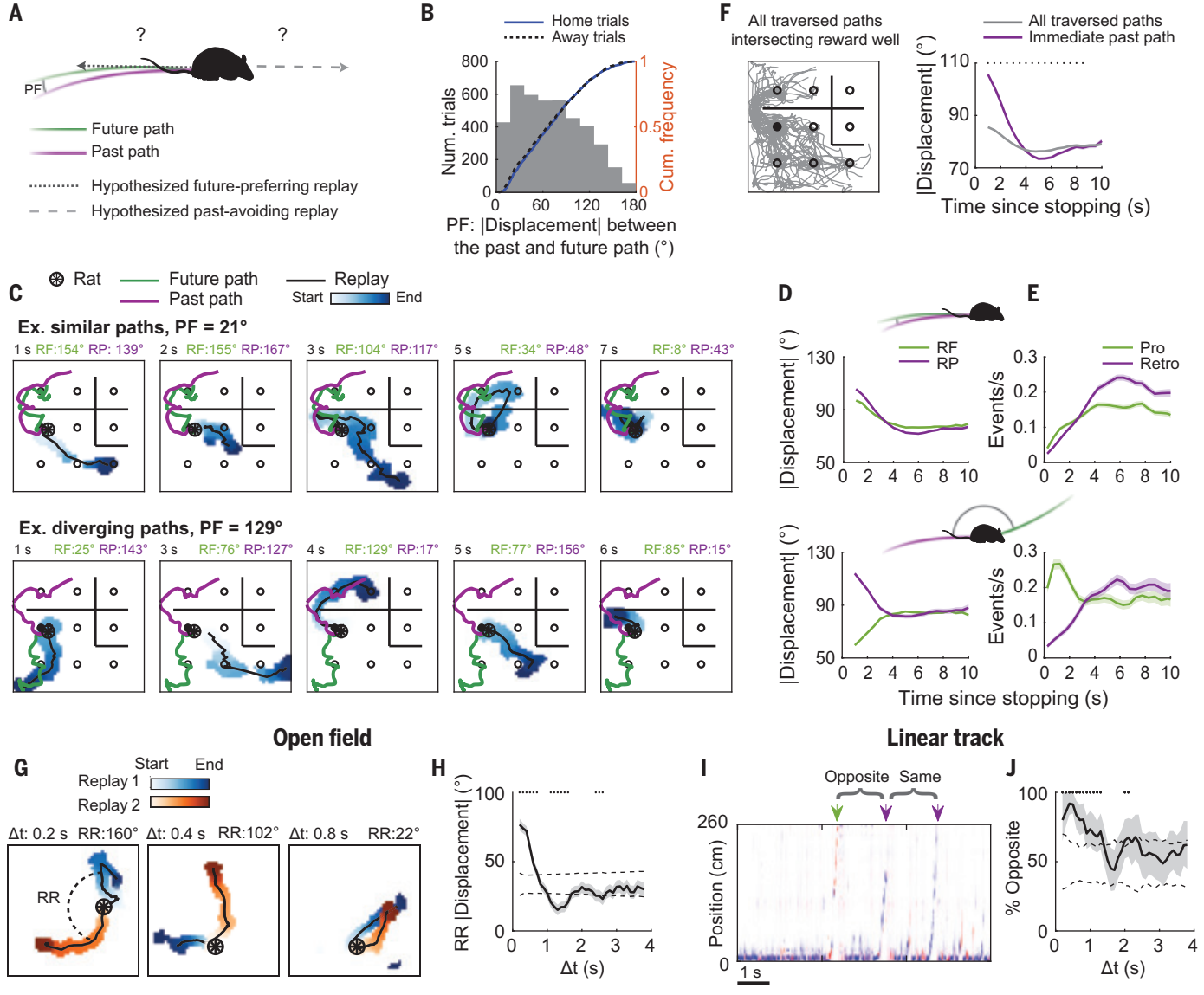

Fig. 3. Replay avoids recently traversed or reactivated spatial paths. (**A**) Hypothesized replays when the animal's past and future paths overlap. PF: Angular displacement between the past and future path. (**B**) Histogram of PF displacements for all trials (n = 4269; Home versus Away trials, P = 0.40, WRS). (**C**) Replays from example trials with similar (PF < 60°) or diverging (PF > 120°) past and future paths. Time since stopping denoted at top. (**D**) RP and RF: Angular displacements between replay and the past or future path, respectively. Top: On trials with similar paths, both RF and RP decreased over time [RF: r(16,109) = −0.12, P = 7.7e-57, RP: r(1,6109) = −0.19, P = 3.1e-128; Pearson's correlations]. Bottom: On trials with diverging paths, RF increased while RP decreased [RF: r(5,369) = 0.15, P = 1.7e-28, RP: r(5,369) = −0.17, P = 3.9e-35]. (**E**) Replay rates on trials with similar (top, max n = 1880) or diverging (bottom, max n = 619) paths. Prospective replay rate during the 0–3 s Early window was reduced for trials with similar paths (P = 2.5e-41, WRS test). (**F**) Left: All traversed paths intersecting one (filled) well. Right: Angular displacement of replays relative to the immediate past path or all other traversed paths (n = 36,677 replays). Dots indicate significant time bins (P < 0.05, WSR). (**G**) Example replay pairs. (**H**) Angular displacement between two replays (RR) as a function of the time between them (Δt). n = 42,345 replay pairs. Solid line, shading: mean ± SEM. Dashed lines: 2.5% and 97.5% quantiles obtained by permuting Δt. Dots indicate P < 0.05. (**I**) Example replay pairs. Green: forward. Purple: reverse. (**J**) Percentage of replay pairs depicting opposite content versus the time between the two replays (Δt). n = 389 replay pairs. Shaded region denotes the bootstrapped 95% confidence interval. Dashed lines: 2.5% and 97.5% quantiles obtained by permuting Δt. Dots, P < 0.05. (D) to (F) show mean ± SEM.

on the linear track (Fig. 2). Forward replays of the future path occurred shortly after stopping and almost always preceded reverse replays of the past {n = 458 forward replays and 391 reverse replays; median [interquartile range (IQR)] time since stopping, forward: 2.8 (1.7–4.6) s; reverse: 4.6 (3.4–6.4) s; Z = −10.8, P = 5.2e-27, Wilcoxon rank sum (WRS) test}. This forward-then-reverse ordering was evident across subjects, sessions, and individual stopping periods with multiple events (Fig. 2, A and B). The incidence rates of forward and reverse replays varied across the stopping period, and their difference revealed distinct temporal windows (~0 to 3 s, "early," and ~3 to 10 s, "late") marked by predominantly forward or reverse activity (Fig. 2, C and D). Theta power was strongly reduced during the early window (fig. S1), indicating that early

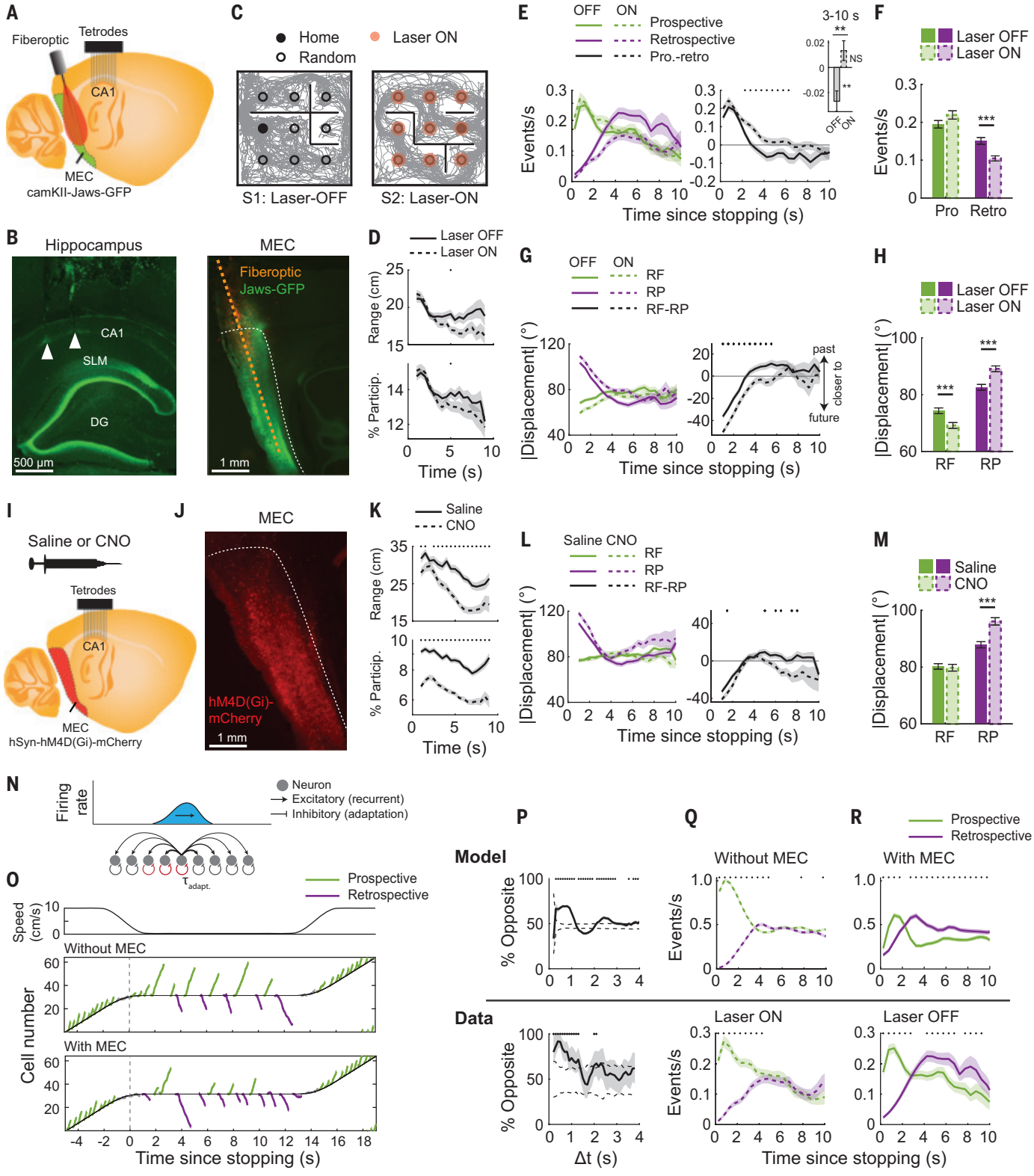

Fig. 4. MEC activity produces a bias toward retrospective replay. (**A**) Recording setup. (**B**) Histology. Arrows mark tetrodes. DG: dentate gyrus; SLM: stratum lacunosum-moleculare. (**C**) Behavioral paradigm. (**D**) Replay properties (n = 2778 laser OFF replays and 2761 laser ON replays). OFF versus ON within Late window: range, P = 0.0068; percent participation, P = 0.0063, WRS. (**E**) Replay rates (max n = 471 laser OFF trials and 484 laser ON trials). Inset: Late window retrospective bias (OFF, P = 0.0030, ON, P = 0.12, WSR; OFF versus ON, P = 0.0010, WRS). NS, not significant. (**F**) Replay rates per trial (interaction: P = 1.0e-4, shuffle; OFF versus ON, prospective: P = 0.20, retrospective: P = 1.0e-4; WRS). (**G**) Angular displacements between replay and the past (RP) or future path (RF) over time. (**H**) Average angular displacements (interaction: P = 1.0e-4, shuffle; OFF versus ON, RF: P = 2.4e-5, RP: P = 4.0e-7, WRS). (**I**) Recording setup. (**J**) Histology. (**K**), Replay properties (n = 2688 saline replays and 1922 CNO replays). Saline versus CNO within Late window: range, P = 3.4e-15; percent

participation, P = 1.1e-42; WRS. (**L**) Angular displacements over time. (**M**) Average angular displacements (interaction, P = 1.0e-4, shuffle; saline versus CNO, RF: P = 0.67, RP: P = 8.8e-7; WRS). (**N**) Recurrent network model. (**O**) Population activity during simulated track traversal. (**P**) Percentage of replay pairs depicting opposite content versus the time between the two replays (Δt). Top: The model produced self-avoiding (opposite) sequences at small time intervals. Bottom: Empirically observed self-avoidance (from Fig. 3J). Solid line, shading: mean ± SEM. Dashed lines: 2.5% and 97.5% quantiles obtained by permuting Δt. (**Q**) Top: Replay rates produced by the adaptation-only model. Bottom: Empirically observed rates with MEC inactive, from (E). (**R**) Top: Replay rates produced by the modified model with facilitating MEC input. Bottom: Empirically observed rates with MEC active, from (E). Unless otherwise stated, plots show mean ± SEM. Dots above time course plots in panels (D), (E), (G), (K), (L), (P), (Q), and (R) indicate time bins for which $P < 0.05$. $^{**}P < 0.01$, $^{***}P < 0.001$.

forward replays are distinct from theta sequences (*31*–*33*) seen during running. We obtained similar results when requiring replays to coincide with a sharp-wave ripple or applying alternative replay detection methods (fig. S2). Very few reverse replay events occurred in the early window, prompting us to inspect the quality of the sparse reverse events detected shortly after stopping. The percentage of cells participating, spatial range, and spatial precision of reverse replays were initially reduced compared with forward events, demonstrating that timing constrains both the quantity and quality of replay content (Fig. 2E). We observed the temporal segregation of forward and reverse replays even in rats with limited experience in an environment, indicating an intrinsically generated rather than learned organization (Fig. 2F). We did not observe consistent organization of replay content surrounding other behavioral transitions, emphasizing a particular significance of the run-to-rest junction (fig. S3).

In the open arena, replay of the immediate future or past behavior unfolded across time in a highly consistent manner (Fig. 2G). Throughout the entire stopping period, many replays corresponded to the future path (*16*, *17*) (Fig. 1K and Fig. 2G, top). By contrast, replays were maximally distant from the past path just after stopping and became tightly aligned around 4 s (Fig. 2G, bottom). On average, replays aligned more tightly to the future path during the early window, and more tightly to the past path during the late window (Fig. 2, H and I). The temporal dynamics of this transition were highly consistent across individual rats (Fig. 2H, bottom, and fig. S4). We next restricted analysis to events that tightly aligned with behavior, classifying replays as prospective if they fell within 20° of the future path and retrospective if they fell within 20° of the past path. The rate of prospective replays peaked shortly after stopping. The rate of retrospective replays was initially low but surpassed that of prospective replay after ~3 s (Fig. 2, J and K). Moreover, the quality of early retrospective replays was reduced (Fig. 2L), and the bias for prospective replays to precede retrospective replays was observable with little experience (Fig. 2M). Although the early prospective bias at first appeared weaker in the open field, separate analysis of Home and Away trials revealed higher rates of prospective replay on the latter, which precede memory-guided navigation (*17*) (Fig. 2, N and O).

Replay avoidance of recently traversed or reactivated paths

We wondered whether the predominance of prospective replay during the early window in part reflected a tendency of replay to avoid the immediate past (Fig. 3A). Consequently, we analyzed the subset of open field trials (Fig. 3B) in which the rat retraced its steps, which resulted in similar past and future paths (materials and methods) (Fig. 3C, top). If future preference dominated, early replays would be similar to both the future and past paths. However, if past avoidance dominated, we would expect early replays to avoid both the future and past paths (Fig. 3A). Replays clearly avoided both the (overlapping) past and future paths for the first ~3 s of stopping (Fig. 3, D and E, top). By contrast, when the past and future paths diverged, early replays avoided the past and aligned with the future (Fig. 3, D and E, bottom). We additionally quantified the tendency of replay to avoid the immediate past path to a greater degree than other potential paths intersecting the reward well at which the rat was positioned (Fig. 3F). Replays were more distant from the immediate past path than from other experienced paths for seconds after stopping (Fig. 3F).

We hypothesized that replay would avoid a recently reactivated path in the same manner it avoids a physically explored path. We looked for evidence of this phenomenon in the open arena by asking whether two replays that occur in close temporal proximity are more likely to depict dissimilar spatial trajectories. To quantify the spatial similarity of two replay events, we calculated their angular displacement (Fig. 3G) (materials and methods). The angular displacements between pairs of replays were maximal when the replays occurred in quick succession (Fig. 3H) and remained greater than chance for temporal distances up to ~1 s (significance assessed relative to "shuffles" in which the time between replay pairs was randomly permuted). Replays on the linear track showed a similar pattern of self-avoidance. We considered all events within a given stopping period and determined the percentage of replay pairs depicting opposing trajectories (i.e., forward followed by reverse, or reverse followed by forward; Fig. 3I). Replay pairs occurring within ~1 s of one another were more likely than chance to depict opposing content (Fig. 3J).

MEC biases hippocampal replay toward retrospective sequences

Thus far, the data suggest that replay direction is largely governed by avoidance of both recently traversed and reactivated spatial paths. Although this principle could potentially explain the early window of past avoidance, it remained unclear how replay of past experience becomes predominant later into the stopping period. We reasoned that a memory of experience could be provided by medial entorhinal cortex (MEC), a primary source of cortical input to hippocampus (*34*) that has been indirectly linked to reverse sequences (*35*). We thus monitored hippocampal replay during optogenetic inactivation of MEC. We expressed the inhibitory opsin Jaws (*36*) in bilateral MEC and delivered red light across the dorsal-ventral axis via tapered fiberoptics (*37*) (Fig. 4, A and B, and fig. S5). Two Jaws-expressing rats performed the open field navigation task. In experimental sessions (n = 12), light was delivered to MEC during reward consumption (Fig. 4C). Control sessions (n = 10) without light delivery were interleaved. Although the overall rates of spike density events, sharp-wave ripples, and replays were similar between MEC active or inactive trials (fig. S5), MEC inactivation reduced the spatial range (*38*) and cell recruitment of replays, particularly in the late window (Fig. 4D).

We next asked whether MEC inhibition alters hippocampal replay content. Notably, MEC inactivation decreased the rate of retrospective replays and eliminated the retrospective bias typically seen in the late window (Fig. 4 E and F, and figs. S5 and S6). Examining the angular displacement of replays relative to the rat's future or past path revealed similar effects: MEC inhibition increased the angular distance of replays from the past path, while decreasing the angular distance from the future path (Fig. 4, G and H). We confirmed these results in an additional animal expressing the inhibitory DREADD hSyn-hM4D(Gi)–MCherry in bilateral MEC (Fig. 4, I and J). Chronic inhibition via intraperitoneal injection of clozapine-*N*-oxide (CNO) reduced replays' range, cellular recruitment, and alignment to the past path (Fig. 4, K to M). We did not observe significant changes to task performance with MEC inhibition (fig. S7). MEC

inhibition during intermittent periods of reward consumption on the linear track did not influence the frequency of replay events but specifically decreased the quality of reverse replays (fig. S8).

Neuronal fatigue drives self-avoidance in a recurrent network

We also explored possible mechanisms underlying these phenomena using a simple network model that has been applied to replay (*16*, *39*–*43*). We simulated hippocampal place cell activity within a continuous attractor network, which supports a continuum of stable bump-like activity states (*44*–*46*) (Fig. 4N). To model neuronal fatigue, each neuron exhibited spike frequency adaptation, a form of slow timescale feedback inhibition (*47*, *48*), which destabilizes the activity bump and allows it to sweep across the network in the absence of external input (*16*, *39*–*43*, *49*–*51*). For simplicity, we simulated exploration of a 1D track and initiated sequences with a brief, place-specific input at the animal's current position (materials and methods) (Fig. 4O and fig. S9). We first confirmed that the neuronal fatigue was necessary to produce neuronal sequences (fig. S9). We next asked whether fatigue could explain the tendency of replays to avoid self-repetition (Fig. 3, G to J). During immobility, the model produced prospective and retrospective sequences that were self-avoiding over timescales consistent with our experimental findings (~1 s, Fig. 4P). We next sought to identify whether the same mechanism could explain the more prolonged replay avoidance of the previously traversed path (Fig. 3, A to F). At high running speeds, the model produced exclusively prospective sequences, consistent with theta sequences (*32*, *33*) (Fig. 4). Critically, as observed experimentally, the first replays to occur after stopping continued to propagate ahead of the animal, owing to the slow decay of the accumulated inhibition behind the animal [Fig. 4, O (top) and Q]. The duration over which early replays continued to avoid the past trajectory was directly related to the time constant of adaptation (fig. S9). We found that a time constant of 3 s well recapitulated the experimental results.

This adaptation-only model recapitulated the early window of past avoidance, but not the later window of past preference, shown experimentally to depend on MEC activity. We tested whether the late window of past preference could be recapitulated by including a facilitating input, presumed to arise from MEC, that accumulates in cells that are active during running and impinges on the circuit during immobility (materials and methods). As observed experimentally in the presence of MEC activity, retrospective replays became more frequent and indeed predominant once the experience-induced adaptation had dissipated [Fig. 4, O (bottom) and R]. Our model was limited to a single map for simplicity; however, place cells participate in multiple maps, raising the possibility of map-specific adaptation. Cells with strong firing in both running directions on the linear track participated in both early forward and later reverse replays, suggesting that neuronal fatigue is map specific (fig. S10).

Discussion

Other models of replay generation are less compatible with the organization revealed here. Early models proposed that reverse replays could result from a slowly decaying activity trace following experience (*21*, *22*, *24*). These models predict the highest rates of reverse replay immediately after stopping, in opposition to the observed window of past avoidance. Other models based on recurrent neural networks with asymmetric synaptic weights do not easily generate reverse sequences or predict replay self-avoidance (*52*, *53*). Outside of replay, models using neuronal fatigue have been proposed to underlie hippocampal sequences during movement, including behavioral timescale "episode" sequences (*49*, *54*) and theta sequences (*39*, *50*, *51*), raising the possibility that shared mechanisms operate across behavioral and sensory states. We note that the role played by spike frequency adaptation in our model, which has been observed in pyramidal cells of the rodent hippocampus (*48*), could also be played by presynaptic depression (*39*).

In addition to the organization that results from avoidance of previously traversed or reactivated paths, we show that cortical input can exert top-down control over the content of awake hippocampal replay. Because our experimental manipulations targeted MEC broadly, future work targeting specific layers (*38*) or projection-defined cell types (*55*) will be needed to elucidate the precise circuits through which MEC biases hippocampal replay content. MEC layer II is a likely candidate. First, inactivation of MEC layer III alone alters the length but not direction of replay in CA1 (*38*). Second, our hippocampal model of sequence generation is most consistent with the recurrent network architecture of area CA3, which receives direct MEC layer II input (*55*). We modeled the MEC-driven enhancement of retrospective replay as an excitatory input current onto cells recently activated through experience. Such enhancement could result from calcium-mediated synaptic facilitation (*56*, *57*) or persistent firing (*58*–*61*) within spatially selective MEC neurons (*62*–*65*). Alternatively, this drive could be provided by retrospectively biased MEC replay (*8*, *66*).

The organizing principles presented here may underlie previously reported phenomena, including the enhanced replay of paths not recently taken (*20*, *67*, *68*), or avoided entirely (*69*). They also offer a potential explanation for the variability among prior works relating replay to ongoing behavior, highlighting the need to consider the time of events relative to stopping (*18*, *25*). The strict temporal organization of replay affects several existing theories of awake replay function. It has been proposed that the temporal organization of awake replay reflects a role in reward learning (*70*), with reverse-going replays precipitated by reward discovery, and forwards-going replays precipitated by expectations of future movement, and with the explicit prediction that reverse replays should precede forwards. The direct contradiction with our results raises the possibility that awake replay is performing some other function, in addition to reward learning, perhaps related to planning (*22*, *71*). A simple planning account of replay appears at odds with our finding that replays avoid the future path if it coincides with the past; however, it remains possible that in these cases, the animal's decision was nevertheless informed by replays, as in other reported cases where replay moves into an area that is then avoided (*69*). Indeed, replay exhibits goal directedness in some spatial tasks beyond what would be predicted from merely avoiding recent behavioral trajectories [(*16*, *17*); although see (*68*)]. Finally, awake replay has been proposed to subserve memory consolidation—for example, by stabilizing hippocampal place cell maps (*72*, *73*). Self-avoidance may increase the diversity of replays, complementing the most recently behaviorally activated patterns, and perhaps also creating a temporal buffer between real and replayed experience, which could prevent interference between encoding and retrieval processes.

Refractory periods characterize neural circuits at multiple temporal and spatial scales (*74*–*76*). Here we describe a refractory period in the production of internally generated neural sequences, with implications for the temporal structure of episodic memory retrieval during a memory-guided navigation task. This structure may promote exploration of alternative trajectories, as well as the avoidance of overtraining on highly valued options, and more generally the broadening of internally generated training data to avoid bias and interference effects in network learning (*77*, *78*). This may reflect a general principle governing internally generated neural activity in multiple brain areas (*3*–*7*, *11*, *79*).

REFERENCES AND NOTES

1. W. E. Skaggs, B. L. McNaughton, *Science* **271**, 1870–1873 (1996).
2. A. K. Lee, M. A. Wilson, *Neuron* **36**, 1183–1194 (2002).
3. D. Ji, M. A. Wilson, *Nat. Neurosci.* **10**, 100–107 (2007).
4. A. Luczak, P. Barthó, S. L. Marguet, G. Buzsáki, K. D. Harris, *Proc. Natl. Acad. Sci. U.S.A.* **104**, 347–352 (2007).
5. D. R. Euston, M. Tatsuno, B. L. McNaughton, *Science* **318**, 1147–1150 (2007).
6. S. Fujisawa, A. Amarasingham, M. T. Harrison, G. Buzsáki, *Nat. Neurosci.* **11**, 823–833 (2008).
7. A. A. Wilber, I. Skelin, W. Wu, B. L. McNaughton, *Neuron* **95**, 1406–1419.e5 (2017).

8. J. O'Neill, C. N. Boccara, F. Stella, P. Schoenenberger, J. Csicsvari, *Science* **355**, 184–188 (2017).
9. A. P. Vaz, J. H. Wittig Jr., S. K. Inati, K. A. Zaghloul, *Science* **367**, 1131–1134 (2020).
10. Y. Liu, R. J. Dolan, Z. Kurth-Nelson, T. E. J. Behrens, *Cell* **178**, 640–652.e14 (2019).
11. J.-B. Eichenlaub *et al*., *Cell Rep.* **31**, 107581 (2020).
12. J. O'Keefe, L. Nadel, *The Hippocampus as a Cognitive Map* (Oxford Univ. Press, 1978).
13. M. A. Wilson, B. L. McNaughton, *Science* **265**, 676–679 (1994).
14. Z. Nádasdy, H. Hirase, A. Czurkó, J. Csicsvari, G. Buzsáki, *J. Neurosci.* **19**, 9497–9507 (1999).
15. J. D. Shin, W. Tang, S. P. Jadhav, *Neuron* **104**, 1110–1125.e7 (2019).
16. J. Widloski, D. J. Foster, *Neuron* **110**, 1547–1558.e8 (2022).
17. B. E. Pfeiffer, D. J. Foster, *Nature* **497**, 74–79 (2013).
18. H. F. Ólafsdóttir, F. Carpenter, C. Barry, *Neuron* **96**, 925–935.e6 (2017).
19. M. P. Karlsson, L. M. Frank, *Nat. Neurosci.* **12**, 913–918 (2009).
20. A. S. Gupta, M. A. A. van der Meer, D. S. Touretzky, A. D. Redish, *Neuron* **65**, 695–705 (2010).
21. D. J. Foster, M. A. Wilson, *Nature* **440**, 680–683 (2006).
22. K. Diba, G. Buzsáki, *Nat. Neurosci.* **10**, 1241–1242 (2007).
23. T. J. Davidson, F. Kloosterman, M. A. Wilson, *Neuron* **63**, 497–507 (2009).
24. J. Csicsvari, J. O'Neill, K. Allen, T. Senior, *Eur. J. Neurosci.* **26**, 704–716 (2007).
25. H. F. Ólafsdóttir, D. Bush, C. Barry, *Curr. Biol.* **28**, R37–R50 (2018).
26. H. F. Ólafsdóttir, C. Barry, A. B. Saleem, D. Hassabis, H. J. Spiers, *eLife* **4**, e06063 (2015).
27. H. Igata, Y. Ikegaya, T. Sasaki, *Proc. Natl. Acad. Sci. U.S.A.* **118**, e2011266118 (2021).
28. I. Stoianov, D. Maisto, G. Pezzulo, *Prog. Neurobiol.* **217**, 102329 (2022).
29. P. Schwartenbeck *et al*., *Cell* **186**, 4885–4897.e14 (2023).
30. B. L. McNaughton, C. A. Barnes, J. O'Keefe, *Exp. Brain Res.* **52**, 41–49 (1983).
31. A. M. Wikenheiser, A. D. Redish, *Nat. Neurosci.* **18**, 289–294 (2015).
32. D. J. Foster, M. A. Wilson, *Hippocampus* **17**, 1093–1099 (2007).
33. A. S. Gupta, M. A. A. van der Meer, D. S. Touretzky, A. D. Redish, *Nat. Neurosci.* **15**, 1032–1039 (2012).
34. N. L. M. Cappaert, N. M. Van Strien, M. P. Witter, in *The Rat Nervous System*, G. Paxinos, Ed. (Academic Press, ed. 4, 2015), chap. 20, pp. 511–573.
35. M. Wang, D. J. Foster, B. E. Pfeiffer, *Science* **370**, 247–250 (2020).
36. A. S. Chuong *et al*., *Nat. Neurosci.* **17**, 1123–1129 (2014).
37. F. Pisano *et al*., *Nat. Methods* **16**, 1185–1192 (2019).
38. J. Yamamoto, S. Tonegawa, *Neuron* **96**, 217–227.e4 (2017).
39. S. Romani, M. Tsodyks, *Hippocampus* **25**, 94–105 (2015).
40. A. D. Milstein, S. Tran, G. Ng, I. Soltesz, *J. Physiol.* **601**, 3241–3264 (2023).
41. A. Ecker *et al*., *eLife* **11**, e71850 (2022).
42. A. H. Azizi, L. Wiskott, S. Cheng, *Front. Comput. Neurosci.* **7**, 161 (2013).
43. J. J. Hopfield, *Proc. Natl. Acad. Sci. U.S.A.* **107**, 1648–1653 (2010).
44. A. Samsonovich, B. L. McNaughton, *J. Neurosci.* **17**, 5900–5920 (1997).
45. F. P. Battaglia, A. Treves, *Phys. Rev. E Stat. Phys. Plasmas Fluids Relat. Interdiscip. Topics* **58**, 7738–7753 (1998).
46. M. Tsodyks, T. Sejnowski, "Associate memory and hippocampal place cells" in vol. 6 of *International Journal of Neural Systems* (World Scientific, 1995), pp. 81–86.
47. J. Benda, A. V. M. Herz, *Neural Comput.* **15**, 2523–2564 (2003).
48. D. A. Henze, G. Buzsáki, *Neuroscience* **105**, 121–130 (2001).
49. V. Itskov, C. Curto, E. Pastalkova, G. Buzsáki, *J. Neurosci.* **31**, 2828–2834 (2011).
50. T. Chu *et al*., *eLife* **12**, RP87055 (2024).
51. J. Widloski, D. Foster, Spontaneous emergence of alternating hippocampal theta sequences in a simple 2D adaptation model. bioRxiv 2024.06.10.598313 [Preprint] (2024); https://doi.org/10.1101/2024.06.10.598313.
52. H. Sompolinsky, I. Kanter, *Phys. Rev. Lett.* **57**, 2861–2864 (1986).
53. M. V. Tsodyks, W. E. Skaggs, T. J. Sejnowski, B. L. McNaughton, *Hippocampus* **6**, 271–280 (1996).
54. E. Pastalkova, V. Itskov, A. Amarasingham, G. Buzsáki, *Science* **321**, 1322–1327 (2008).
55. T. Kitamura *et al*., *Science* **343**, 896–901 (2014).
56. N. Y. Masse, M. C. Rosen, D. J. Freedman, *Trends Cogn. Sci.* **24**, 242–258 (2020).
57. G. Mongillo, O. Barak, M. Tsodyks, *Science* **319**, 1543–1546 (2008).
58. M. Yoshida, E. Fransén, M. E. Hasselmo, *Eur. J. Neurosci.* **28**, 1116–1126 (2008).
59. T. T. G. Hahn, J. M. McFarland, S. Berberich, B. Sakmann, M. R. Mehta, *Nat. Neurosci.* **15**, 1531–1538 (2012).
60. A. V. Egorov, B. N. Hamam, E. Fransén, M. E. Hasselmo, A. A. Alonso, *Nature* **420**, 173–178 (2002).
61. R. Klink, A. Alonso, *J. Neurophysiol.* **77**, 1813–1828 (1997).
62. T. Solstad, C. N. Boccara, E. Kropff, M.-B. Moser, E. I. Moser, *Science* **322**, 1865–1868 (2008).
63. T. Hafting, M. Fyhn, S. Molden, M.-B. Moser, E. I. Moser, *Nature* **436**, 801–806 (2005).
64. K. Hardcastle, N. Maheswaranathan, S. Ganguli, L. M. Giocomo, *Neuron* **94**, 375–387.e7 (2017).
65. G. W. Diehl, O. J. Hon, S. Leutgeb, J. K. Leutgeb, *Neuron* **94**, 83–92.e6 (2017).
66. H. F. Ólafsdóttir, F. Carpenter, C. Barry, *Nat. Neurosci.* **19**, 792–794 (2016).
67. A. A. Carey, Y. Tanaka, M. A. A. van der Meer, *Nat. Neurosci.* **22**, 1450–1459 (2019).
68. A. K. Gillespie *et al*., *Neuron* **109**, 3149–3163.e6 (2021).
69. C.-T. Wu, D. Haggerty, C. Kemere, D. Ji, *Nat. Neurosci.* **20**, 571–580 (2017).
70. M. G. Mattar, N. D. Daw, *Nat. Neurosci.* **21**, 1609–1617 (2018).
71. M. F. Carr, S. P. Jadhav, L. M. Frank, *Nat. Neurosci.* **14**, 147–153 (2011).
72. D. Dupret, J. O'Neill, B. Pleydell-Bouverie, J. Csicsvari, *Nat. Neurosci.* **13**, 995–1002 (2010).
73. L. Roux, B. Hu, R. Eichler, E. Stark, G. Buzsáki, *Nat. Neurosci.* **20**, 845–853 (2017).
74. A. L. Hodgkin, A. F. Huxley, *J. Physiol.* **117**, 500–544 (1952).
75. H. Pashler, *Psychol. Bull.* **116**, 220–244 (1994).
76. J. C. Flores, K. Zito, A synapse-specific refractory period for plasticity at individual dendritic spines. *bioRxiv* 2024.05.24.595787 [Preprint] (2024); https://doi.org/10.1101/2024.05.24.595787.
77. T. L. Hayes *et al*., *Neural Comput.* **33**, 2908–2950 (2021).
78. L. Wittkuhn, S. Chien, S. Hall-McMaster, N. W. Schuck, *Neurosci. Biobehav. Rev.* **129**, 367–388 (2021).
79. W. Xu, F. de Carvalho, A. Jackson, *J. Neurosci.* **39**, 3698–3712 (2019).
80. C. Mallory, Zenodo (2024); https://doi.org/10.5281/zenodo.14237298.

ACKNOWLEDGMENTS

The authors thank S. Romani for helpful discussions; M. Kleinman, M. Plitt, and T. Elston for comments on the manuscript; and C. Walters for assistance in designing the Microdrive. **Funding:** National Institutes of Health grants NS113557 and MH103325 (D.J.F.); Howard Hughes Medical Institute Hanna H. Gray Fellowship (C.S.M.). **Author contributions:** Conceptualization: C.S.M., D.J.F. Conceptualization of model: J.W. Methodology: C.S.M., J.W. Investigation: C.S.M., J.W. Visualization: C.S.M. Funding acquisition: C.S.M., D.J.F. Writing – original draft: C.S.M. Writing – review and editing: C.S.M., J.W., D.J.F. **Competing interests:** The authors declare that they have no competing interests. **Data and materials availability:** The data analysis code is deposited at Zenodo (*80*). All (other) data needed to evaluate the conclusions of the paper are present in the paper or the supplementary materials.

SUPPLEMENTARY MATERIALS

science.org/doi/10.1126/science.ads4760
Materials and Methods
Figs. S1 to S10
References (*81*–*88*)
MDAR Reproducibility Checklist

Submitted 14 August 2024; accepted 2 December 2024
10.1126/science.ads4760

myIDP ScienceCareers
INDIVIDUAL DEVELOPMENT PLAN

Features in myIDP include:

- Exercises to help you examine your skills, interests, and values.
- 20 career paths with a prediction of which ones best fit your skills and interests.
- A tool for setting strategic goals with optional reminders to keep you on track.
- Articles and resources to guide you through the process.
- Options to save materials online and print them for further review and discussion.
- A certificate of completion for users that finish myIDP.

Start planning your future today!
myIDP.sciencecareers.org

In partnership with:

FASEB Federation of American Societies for Experimental Biology
UMASS University of Massachusetts Medical School
UCSF University of California San Francisco
UIC
BURROUGHS WELLCOME FUND

By **Anonymous**

A reluctant investigator

I was 3 months into graduate school when I realized my project was doomed. I had set out to build on the work of a previous student, but as I ran into roadblocks, it became increasingly clear that the previously published work was fundamentally flawed. The data didn't make sense; the results couldn't be replicated. I raised my concerns with my supervisor, but he was convinced there was a reasonable explanation. I clung to his reassurances for a time, assuming no one would publish something blatantly wrong. As weeks of digging and hoping turned into months, though, the cracks started to widen. Eventually it was undeniable: The paper was riddled with serious problems.

My supervisor was the corresponding author on the published paper, and when I told him he grew indignant. "I don't understand why you're making such a big deal out of this. Mistakes happen all the time. People mislabel things, they forget. Do you really think that in 5 years you could look me in the eye and say you're 100% confident in everything you did?" He leaned across the desk, his gaze stern, while discomfort washed over me.

"Yes," I answered, with more defiance than certainty. Honest mistakes were one thing—mislabeling a tube, losing track of a sample—but to my fresh, first-year grad student eyes, to publish an entire paper built on a mountain of mistakes was inconceivable.

"To publish an entire paper built on a mountain of mistakes was inconceivable."

I had heard stories of sloppy science, and worse. But I saw them as cautionary tales, not something I would have to personally grapple with during my first year of grad school. For the most part, I had been taught to view science as a domain of rigor and diligence, kept on track by the guardrails of both scientific scruples and peer review. But I was beginning to realize the people who did science were just that—people.

Because I couldn't build on the work, my supervisor instructed me to redo the original publication, eager for me to show the problems were no more than minor oversights. I painstakingly repeated the methods, which involved reanalyzing data. It was frustrating to not be setting out in a new scientific direction. But eventually, after I completed my exhaustive retracing of the original paper, I had something to show for my work.

With a knot in my stomach, I carefully presented a list of issues and mistakes to my supervisor. I told him about incorrect data analysis and experimental design, results that couldn't be replicated, and claims that were contradicted by the data. My supervisor's initial patience and silence slowly gave way to defensive interruptions. He dismissed some discrepancies as minor and insisted other errors weren't worth mentioning. Nobody likes the bearer of bad news, and I was aware I was risking my future. I'd need his support to continue in the program, and someday I would be turning to him for reference letters. But I couldn't back out now, and I was resolute on wanting the scientific record to be corrected.

I pushed for a complete retraction of the original paper. My supervisor instead lobbied for a small correction, an addendum to gloss over the errors. As the corresponding author, he was in communication with the journal. The journal editors convened a special meeting and reached their verdict: The issues were too systemic and serious for a simple correction. The only viable course was to retract the original publication and replace it with a paper describing my analyses. I felt vindicated and relieved: The errors were as serious as I thought, and I had been right to expose them.

Afterward, other faculty members commended me for standing up for research integrity. Their support, however, couldn't change the fact that I never wanted to have to choose between truth and peace again, especially not while existing under the thumb of my supervisor. I have maintained a good relationship with him through it all. But the experience was utterly exhausting and I understand why early-career researchers, if faced with a similar situation, might choose silence over speaking up. It's not easy to point out errors, especially when they're attached to the name of someone who holds great power over you. ■

The author is a Ph.D. student at a research intensive university in North America. Send your career story to SciCareerEditor@aaas.org.

ILLUSTRATION: ROBERT NEUBECKER

YOUR RESEARCH HAS ITS REWARDS.

Submit an essay by 3/15/25 to enter to win $25K.

The *Science* & PINS Prize seeks to recognize researchers who ask fundamental questions in the field of neuromodulation. It is awarded to scientists who conduct research at the intersection between engineering and clinical neurology to develop innovative neuromodulation approaches to advance our understanding of human health and disease or to guide therapeutic interventions.

To enter, just write a 1000-word essay about your research performed in the last three years. The Grand Prize winner will be presented a US$25,000 award, as well as have their essay published in *Science* magazine and online. A runner-up will have their essay published online.

For additional inquiries,
email SciencePINSPrize@aaas.org.

SCIENCE-PINS PRIZE FOR NEUROMODULATION
SCIENCE-PINS

SCIENCE.ORG/PINS